# UC Berkeley
## UC Berkeley Electronic Theses and Dissertations

**Title**

Soil Formation and Transport Processes on Hillslopes along a Precipitation Gradient in the Atacama Desert, Chile

**Permalink**

**Author**

Owen, Justine J.

**Publication Date**

2009

Peer reviewed|Thesis/dissertation

Soil Formation and Transport Processes on Hillslopes
along a Precipitation Gradient in the Atacama Desert, Chile

by

Justine Janet Owen

A dissertation submitted in partial satisfaction of the

requirements for the degree of

Doctor of Philosophy

in

Environmental Science, Policy, and Management

in the

Graduate Division

of the

University of California, Berkeley

Committee in charge:

Professor Ronald Amundson, Chair
Professor William E. Dietrich
Professor Celine Pallud
Professor Guillermo Chong Diaz

Fall 2009

Soil Formation and Transport Processes on Hillslopes along a
Precipitation Gradient in the Atacama Desert, Chile

by Justine Janet Owen

Abstract

Soil Formation and Transport Processes on Hillslopes
along a Precipitation Gradient in the Atacama Desert, Chile

by

Justine Janet Owen

Doctor of Philosophy in Environmental Science, Policy, and Management

University of California, Berkeley

Professor Ronald Amundson, Chair

The climate-dependency of the rates and types of soil formation processes on level landforms has been recognized and documented for decades.  In contrast, methods for quantifying rates of soil formation and transport on hillslopes have only recently been developed and the results suggest that these rates are independent of climate.  One explanation for this discrepancy is that hillslopes and their soil mantles are dynamic systems affected by local and regional tectonic effects.  Tectonics can change local or regional baselevel which affects the hillslope through stream incision or terrace formation at its basal boundary.  Another explanation is that in most of the world hillslope processes are biotic, and biota and their effects vary nonlinearly with climate.  The effects of both tectonics and life can obscure climatic effects.  Recent studies have been made to isolate the climatic effect on hillslope processes, but they are few and focus on humid and semiarid hillslopes.

In order to isolate the effects of boundary condition, precipitation, and life, I studied pairs of hillslopes in northern Chile in semiarid, arid, and hyperarid climates.  In each pair, one hillslope was bounded by an incising (bedrock-bedded), first-order channel, and the other was bounded by a low-slope, non-eroding surface.  This precipitation gradient spans the transition from biotic to abiotic landscapes.  The guiding framework for this study is a hillslope soil mass balance model in which the soil mass is controlled by the balance of soil production from bedrock and from atmospheric input, and soil loss through physical and chemical erosion.  My objectives were to quantify the components of the mass balance model, identify the processes driving soil production from bedrock and soil transport, and interpret this data in the context of climate and hillslope morphology.  In the field, I made observations of the processes driving soil formation and transport, surveyed the hillslopes to produce high-resolution topographic maps, and sampled soils and rock for chemical analysis and particle size analysis.  Dust collectors were erected to measure atmospheric input.  Bedrock and surface gravel samples were collected in order to calculate the rate of soil production from bedrock, the incision rate of the channels, the age of the non-eroding surfaces, and the exposure history of surface gravels using the concentrations of *in situ*-produced $^{10}Be$ and $^{26}Al$.  Rates of physical and chemical erosion were calculated using the soil mass balance model, based on the rate of soil production from bedrock,

the atmospheric deposition rate, and the concentrations of an immobile element in the soil, bedrock, and atmospheric input.  In addition, to understand the effect of precipitation on the landscape and to quantify the infiltration rate of the soil, sprinkling experiments were conducted in each climate region and infiltrometer measurements were made in the hyperarid region.

The effect of boundary condition on soil thickness was observed in all climate zones, with thicker soils on hillslopes with non-eroding boundaries compared to hillslopes bounded by channels.  However, the expected effect of boundary condition on the rates of soil production from bedrock, with slower erosion rates on hillslopes with non-eroding boundaries, decreased as precipitation decreased.  In contrast to previous work on wetter hillslopes which showed little climatic sensitivity, rates of soil production from bedrock increase with precipitation following a power law, from ~ 1 m My$^{-1}$ in the hyperarid region to ~ 40 m My$^{-1}$ in the semiarid region.  A geomorphic and pedologic threshold was observed at mean annual precipitation (MAP) ~100 mm, marked by changes in soil chemistry and thickness, types of erosion mechanisms, and rates of soil production.  In the semiarid region, where MAP = 100 mm, the hillslopes are soil-mantled with a relatively thick, chemically-weathered soil where MAP is high enough to support coastal desert vegetation.  Soil formation and transport is primarily through bioturbation.  As MAP decreases to 10 mm in the arid region, the hillslopes are nearly soil- and plant-free, and soil transport is through overland flow, rather than bioturbation. In the hyperarid region, where MAP is <2 mm, the hillslopes are mantled with salt-rich soils which are primarily derived from atmospheric input rather than bedrock erosion.  Soil transport is through overland flow and likely some salt shrink-swell.

The spatially-explicit physical erosion rates were used to test the applicability of four soil transport models.  Where bioturbation is active, soil transport is slope- and depth-dependent.  In the plant-free regions, soil transport is a function of slope and distance downslope.  The transport coefficients in the transport models increase several orders of magnitude with increasing MAP.  A comparison of these values with those determined on wetter hillslopes suggests that at MAP<100 mm, transport coefficients are a function of MAP.  Where MAP>100 mm, they are a function of the types of organisms driving bioturbation and other soil properties.  This threshold corresponds to the MAP below which there is a dramatic decrease in net primary productivity (NPP), and suggests that hillslope process rates are sensitive to MAP where the effect of life is small.

A unique feature on the hyperarid hillslopes was darkly-varnished, contour-parallel bands of gravels on the soil surface which I call "zebra stripes".  Based on cosmogenic radionuclide concentrations in surface gravel and bedrock, as well as salt deposition rates from the atmosphere and content in the soils, I propose that the salt-rich soils began accumulating >0.5-1 Ma and the zebra stripes formed in the last $10^3$-$10^5$ y.  The zebra stripe pattern has been preserved due to the self-stabilization of the gravels within the stripes and the continued absence of life (which would disturb the surface, as seen at the arid site).  The accumulation of the salt-rich mantle and the formation of zebra stripes suggest a profound climatic change occurred sometime between the late Pliocene and early Holocene.

The Atacama Desert provides a multi-million year-old experiment testing the effect of water and life on geophysical and geochemical processes.  In contrast with portions of the planet

where biota modulates soil production and erosion through complex and rapid feedbacks, this work shows that the absence of biota in the driest parts of the Atacama Desert results in the rates and mechanisms of geomorphic processes being extremely precipitation-sensitive. This unusual environment, for Earth, illuminates the uniqueness and complexity of a planet whose surface bears the indelible imprint of life.

# Table of Contents

*For Mom, Dad, Megan, and Lon,*
*for their enthusiasm and love*

# Chapter 1

## Introduction

The effect of climate and tectonics on landscape development is often mediated by processes forming and transporting the soil mantle. On hillslopes, these processes include soil production from the underlying bedrock, physical erosion, and chemical erosion. Quantifying these processes over relevant geologic timescales has previously been difficult, but is necessary in order to understand their dependence on climate, tectonics (through local boundary conditions such as an incising stream channel), topography, and soil characteristics (particularly soil thickness). New methods, including cosmogenic radionuclide (CRN)-derived erosion rates and geochemical mass balance modeling, have made quantification of soil production and transport more accessible. However, CRN-derived rates of hillslope soil production from bedrock have been measured mainly in humid to semiarid regions, and the hillslope geochemical mass balance model to only one hillslope. This dissertation applies these methods to arid to hyperarid hillslopes and provides some of the first data on hillslope soil formation and transport under these conditions. The study sites range from vegetated to nearly abiotic, thus the role life plays in soil and hillslope development is an important result in this work.

### Background

Soil persists on landscapes when production and erosion balance each other. Indeed, the persistence of both soils and mountains led James Hutton to recognize the dynamic nature of the Earth's surface (1795). Soil formation depends on many variables, which Hans Jenny (1941) condensed into five state factors: climate, organisms, topography, parent material, and time. Jenny (1941) cites numerous studies that used sequences of soils to quantify changes in soil characteristics due to variation in some state factor, such as climosequences and chronosequences. However, the chapter on the effect of topography on soil formation is the shortest and most limited in supporting citations. Jenny writes, "Topography as a soil-forming factor has not received the attention it deserves. It is true, of course, that a considerable amount of information on runoff and erosion in relation to slope is at hand, but it deals primarily with the removal and the destruction of soil and not with soil formation." (p.89) One of the primary reasons for this limited scope is the lack of methods by which soil formation could be quantified.

Hillslope soils are an important component of landscape development, in that they mediate the response of hillslopes to river and channel incision (which is often tectonically-driven through changes in base level). G.K. Gilbert (1877) was one of the first scientists to suggest that soil transport is a function of slope, rock mechanics, and climate, and that the thickness of the soil mantle affects the rate of erosion of the underlying bedrock (with thinner soils enabling faster bedrock erosion). These relationships provide the foundation for modern landscape modeling. To summarize, if the incision rate of a stream increases due to the uplift of rock relative to the stream's baselevel, the slope of the adjacent hillslope will steepen. Soil erosion will increase due to the steeper slope and thin the soil, which causes bedrock erosion to increase until it is equal to that of the incision rate of the channel.

In order to quantify and model the relationship between soil production, soil transport, and soil mass, a hillslope mass balance is often used (Carson and Kirkby, 1972; Dietrich et al.,

1995).  The primary input is often material eroded from the underlying bedrock, but other inputs include plant matter and atmospheric deposits of dust and/or solutes.  Soil loss occurs through physical erosion and chemical erosion.  In this thesis, I use the following:

$$\frac{\partial(\rho_s H)}{\partial t} = \underbrace{P}_{\substack{bedrock\\erosion}} + \underbrace{A}_{\substack{atmospheric\\deposition}} - \underbrace{\nabla \cdot \tilde{Q}_s}_{\substack{physical\\erosion}} - \underbrace{W}_{\substack{chemical\\erosion}} \tag{1}$$

$$\underbrace{\hspace{3cm}}_{\substack{soil\ production\\mechanisms}} \underbrace{\hspace{3cm}}_{\substack{soil\ loss\\mechanisms}}$$

where $\rho_s$ is the bulk density of the soil (M L$^{-3}$), $H$ is the slope-normal soil thickness (L), $P$ is the rate of soil production from bedrock (M L$^{-2}$ T$^{-1}$), $A$ is the deposition rate of silicate dust and salts from the atmosphere (M L$^{-2}$ T$^{-1}$), $\nabla \cdot \tilde{Q}_s$ is the physical erosion rate (the divergence of soil flux, $\tilde{Q}_s$) (M L$^{-2}$ T$^{-1}$), and $W$ is the chemical erosion rate(M L$^{-2}$ T$^{-1}$).  Previous work has ignored atmospheric input, and its inclusion in equation 1 is novel.

Most soil production on hillslopes is through the conversion of bedrock to soil ($P>A$) and is a complex biophysiochemical process.  The rate of bedrock erosion is dependent on the rock type (Onda, 1992), degree of fracturing (Molnar, 2007), degree of chemical weathering (Riebe et al., 2004; Dixon et al., 2009), types of processes driving the erosion (bioturbation, freeze-thaw, wetting and drying, etc.), and soil thickness.  Gilbert (1877) first hypothesized that rates of soil production from bedrock vary inversely with soil thickness, and CRN-derived  rates of $P$ in California and Australia (Heimsath et al., 1997, 1999, 2000; Wilkinson and Humphreys, 2005) demonstrate that $P$ decreases exponentially with increasing $H$:

$$P = P_0 e^{-\alpha H} \tag{2}$$

where $P_0$ is the bedrock erosion rate under zero soil cover and $\alpha$ is an empirical rate constant.  Equation 2 (a.k.a. "the soil production function", Heimsath et al., 1997) predicts that bare bedrock has the highest $P$.  However, a "humped" function, with maximum $P$ at some critical soil thickness (Carson and Kirkby, 1972; Dietrich et al., 1995; Furbish and Fagherazzi, 2001; Anderson, 2002), may be more reasonable, in that some soil is required to store water, support plants, and harbor burrowing animals, all of which increase $P$.  Work in Australia (Heimsath et al., 2006), South Africa (Heimsath et al., 2008), and Wyoming (Small et al., 1999) supports the humped function.

Physical erosion of soil is one of the best quantified components of the soil mass balance, due to the ease of short-term measurement and importance in agricultural areas.  Methods of quantifying physical erosion at the hillslope scale include local measurements such as the emplacement of rods that provide a reference point for soil movement over several years (Kirkby, 1967) and sediment traps (Krammes, 1960; Gabet, 2003).  At the watershed scale, sediment yields measured in streams can be averaged over the drainage area (Meade, 1988; Kirchner et al., 2001).  This work indicates that soil transport is a function of slope (Gilbert, 1877).  However, the form of the relationship is likely not consistent between hillslopes with different transport processes, climates, and bedrock types.  Several soil transport laws have been hypothesized but are difficult to test in the absence of spatially explicit soil flux rates.

In order to calculate physical and chemical erosion rates along a hillslope transect, which could be used to test soil transport laws, Yoo et al. (2007) developed a numerical approach using the concentration of an immobile (geochemically-conserved) element in the soil and its inputs, and the rates of soil production. This approach is based on a mass balance of an immobile element analogous to Equation 2:

$$\frac{\partial(\rho_s C_{is} h)}{\partial t} = C_{ir} P + C_{iA} A - \nabla \cdot \left( C_{is} \tilde{Q}_s \right) \tag{3}$$

where $C_{ir}$ is the concentration of an immobile element (usually Ti or Zr) in the rock [M M$^{-1}$], $C_{is}$ is the depth-averaged concentration in the soil [M M$^{-1}$], and $C_{iA}$ is the concentration in atmospheric deposition [M M$^{-1}$]. Note there is no $W$ term because the immobile element mass balance is not affected by chemical erosion. Assuming steady state and using an iterative process, both physical and chemical erosion rates can be calculated in a spatially explicit way (i.e., as a function of hillslope position) and related to factors such as slope, distance downslope, soil thickness, and soil production rates.

As noted above, soil flux, $\tilde{Q}_s$, is usually modeled as a function of slope, i.e. $\tilde{Q}_s = K \times f$(slope) where $K$ is a constant often called the transport coefficient. The factors controlling $K$ are likely to include climate, bedrock type, biota, and transport mechanisms. A few researchers have begun developing mechanistic models of physical erosion, constrained by values of $K$ (e.g., Gabet et al., 2000 and 2003; Yoo et al., 2005; Heimsath et al., 2005; Roering, 2008), but the studies are few and require more field data.

On many landscapes, $W$ is limited by the availability of fresh material (e.g., Dahlgren et al., 1997; Riebe et al., 2004; von Blanckenburg et al., 2004) such that it is positively correlated with $P$. $P$ has been shown to depend on many factors including tectonic setting (Riebe et al., 2001; von Blanckenburg et al., 2006); degree of rock fracturing (Molnar et al., 2007); and rock composition (Onda, 1992), which obscure any climatic effect. Reibe et al. (2003) defined a "chemical depletion factor" (CDF), a metric that would account for the co-variation of $W$ and $P$, and could reveal a climatic signature on chemical erosion. However, the CDF did not account for the input of chemically weathered material to the soil from upslope. To address this, Yoo et al. (2007) proposed an "extended chemical depletion factor" (ECDF), which has been modified here to include atmospheric input:

$$ECDF = \frac{W}{P+A} = \frac{1}{P+A} \left[ \left( 1 - \frac{C_{ir}}{C_{is}} \right) P + \left( 1 - \frac{C_{iA}}{C_{is}} \right) A + \left( \frac{\nabla C_{is}}{C_{is}} \right) \cdot \tilde{Q}_s \right]. \tag{4}$$

For a semiarid hillslope in Australia, Yoo et al. (2007) calculated a hillslope-averaged CDF that was 50% larger than the hillslope-averaged ECDF because the CDF did not account for the input of chemically-weathered soil from upslope. Additionally, the ECDF captured a switch from chemical loss at the top of the hillslope to chemical gain towards the base through the precipitation of clay. Thus far, the ECDF has been used in only one study, but clearly has the

potential to improve our understanding of the formation of hillslope soils as a continuous system and to provide an integrated view of chemical and physical processes.

**Unanswered Questions**

The methods described above have been developed within the last few decades or later and represent the state of the field of hillslope geomorphology. As a result, they have not yet been widely applied and many questions remain. These include, How widely applicable is the exponential soil production function? Where is the precipitation sensitivity in the hillslope soil mass balance model? Are the types and rates of hillslope formation processes different in the absence of life?

The main limitation to addressing these questions in the past was the lack of methods for quantifying $P$. For example, the rate of soil production from bedrock is required to test equation 2 against the humped soil production function and empirically derive values for $P_0$ and $\alpha$. CRN-derived rates of soil production from bedrock are increasingly common, but they are often not measured in conjunction with soil properties. As mentioned above, soil production functions have been tested on less than ten hillslopes globally (Heimsath et al., 1997, 1999; 2006, 2008; Small et al., 1999; Wilkinson and Humphreys, 2005), all of which are in semiarid to humid climates. The appeal of soil production functions is that, under certain conditions, one can model the distribution of soil thickness and the rates of soil production from bedrock across a hillslope needing only topographic data and the parameters in equation 2 (e.g., Dietrich et al., 1995; Heimsath et al., 1997, 1999; Saco et al., 2006). Once enough soil production functions have been parameterized, then these can be estimated for locations where only topographic data is available, such as remote areas on Earth or terrestrial planets like Mars. Thus, hillslopes in a variety of climates, with a variety of bedrock compositions, are of interest in order to understand the full range of soil production functions.

Despite the increasing database of CRN-derived erosion rates, clear evidence of a climatic impact remains elusive. For example, Riebe et al. (2004b) compiled erosion rates across 42 non-glaciated hillslopes encompassing a broad spectrum of mean annual temperatures (MAT: 2-25ºC) and mean annual precipitation rates (MAP: 25-420 cm/y). They found that erosion rates are not correlated with MAP or MAT. In another compilation, von Blanckenburg et al. (2006) had similar results: average catchment erosion rates across the globe were independent of MAP and MAT. Rather than indicating that soil production from bedrock is independent of climate, these findings suggest the influence confounding factors, primarily tectonic setting affecting local boundary conditions. Another possible confounding factor is that in some studies (eg. Riebe et al., 2004a) elevation gradients are used to create climosequences, but MAP and MAT often vary inversely along these transects. Without careful site selection, teasing apart the effects of precipitation, temperature, and boundary condition is difficult at best. Thus, a need exists for hillslope erosion rates that are considered in the context of their tectonic setting and topographic relief, among other factors.

Atmospheric input is often ignored in hillslope soil mass balances because it is usually much smaller than soil production from bedrock, essentially negligible in a bulk mass balance. However, atmospheric input can be very important geochemically. The oldest, wettest soils in Hawaii are prime examples, where atmospheric dust and solutes in rainfall provide Sr and K to

soils in which the local sources for these nutrients have been depleted or sequestered (Dymond et al., 1974; Vitousek et al., 1997; Kennedy et al., 1998). At the opposite end of the climate spectrum, soils in the Atacama Desert show substantial gain of atmospherically-derived sulfates, nitrates, and other soluble salts (Böhlke et al., 1997; Rech et al., 2003; Michalski et al., 2004; Ewing et al., 2006; Ewing et al., 2007). The rate of atmospheric input can be spatially and temporally consistent in some regions (Ewing et al., 2006). It is often only indirectly connected to climate, such as through desertification or precipitation.

Modeling spatially-explicit physical and chemical erosion rates is necessary to understand the factors controlling the rates of these processes. However, the approach described above has been applied to only two hillslopes, one in Australia (Yoo et al., 2007), and one in California (Yoo et al., 2009). It has also been applied, ignoring chemical erosion, on hillslopes in Australia and California (Heimsath et al., 2005). While this work has provided some insight to the variation of these processes across a hillslope, more data are needed to understand the variability of $K$, particularly in relation to climate. A particular challenge to hillslope soil modeling is that the effect of climate is not straightforward, primarily due to the contrasting effects of vegetation. Whereas roots and animals subsisting on the vegetation stir the soil (bioturbation) and produce net downslope transport, roots provide stability to the soil and plant canopies intercept rain and decrease its impact force. Currently, there is a lack of data on $K$ values for different hillslopes, but these are important for constraining mechanistic models of soil transport, such as those developed by Gabet et al.(2000 and 2003), Yoo et al. (2005), Heimsath et al. (2005), and Roering (2008).

In order to address some of these questions, I studied hillslopes in the Atacama Desert in northern Chile, at the hyperarid limit of life on Earth. The Atacama Desert is one of the driest locations on Earth, made famous by its extensive nitrate and copper deposits (Ericksen, 1981). Currently, life in the hyperarid core of the desert is limited to soil microbes (Navarro-González et al., 2003; Warren-Rhodes et al., 2006) and rare, transient birds. Thus, the Atacama is a unique opportunity to study hillslope soil processes in the absence of life. My field sites were selected in part to complement studies of soil temperature and moisture (McKay et al., 2003; McKay et al., 2009), microbiology (Navarro-González et al., 2003; Warren-Rhodes et al., 2006 and 2007), and soil chemistry (Quinn et al., 2005; Ewing et al., 2006, 2007, 2008). Some cosmogenic radionuclide work has been done in northern Chile, but with the objectives of dating non-eroding landforms or calculating the erosion rate of exposed bedrock or boulders (Dunai et al., 2005; Nishiizumi et al., 2005; Kober et al., 2007, 2009; Placzek et al., 2007; Evenstar et al., 2009). None has systematically examined erosion rates on soil-mantled hillslopes. Additionally, the west-east climosequences used by Kober et al. (2007) and Placzek et al. (2007), are even more poorly constrained than the north-south climosequence used here, and are complicated by greater co-variation of precipitation and temperature. By studying hillslopes along the north-south climosequence with similar bedrock compositions but varying boundary conditions, I sought to understand the effect of precipitation, boundary condition, and life on the types and rates of hillslope processes under semiarid to hyperarid conditions.

**Thesis Outline**

This thesis presents the first systematic study quantifying hillslope soil forming processes along a well-constrained precipitation gradient at the arid to hyperarid end of Earth's climatic

spectrum.  In Chapter 2, I compare rates of soil production from bedrock on hillslopes along a semiarid to hyperarid climosequence in northern Chile, and between hillslopes with different boundary conditions (actively incising channels or non-eroding landforms).  This chapter builds upon the compilations of erosion rates across different climates by Riebe et al. (2004b) and von Blanckenburg (2006).  However, unlike these previous studies, the boundary conditions of the hillslopes were well-constrained, the composition of the bedrock was uniform, and the variation in temperature was small relative to the variation in precipitation.  I also determine which soil production function, if any, applies on the hillslopes in each climate zone.  Along this climosequence, soil production and erosion mechanisms change from biotically-driven to salt-driven with decreasing MAP, and this change has pronounced impacts on the soil mass balance.  Average $H$ changes non-monotonically with MAP: it is thickest at the hyperarid and semiarid sites and nearly absent at the arid site.  Field observations and CRN data reveal distinct boundary condition effects on soil production rates from bedrock and soil thickness, with thinner soils on hillslopes bounded by channels compared to those bounded by non-eroding landforms, and a positive correlation between soil production from bedrock and precipitation.  Tests of the exponential and humped soil production functions within each climate zone show that while the exponential function appears to describe soil production from bedrock on the semiarid and arid hillslopes, neither applies in the hyperarid region.  I propose a MAP threshold ~100 mm, above which the rate of soil production from bedrock is a function of tectonics, life, and local boundary condition, and below which it is a function of precipitation.

In Chapter 3, I build on Chapter 2 and use the approach of Yoo et al. (2007) and soil chemistry data to quantify physical and chemical erosion on the hillslopes, calculate soil residence times, and calculate the ECDF values.  As in the previous chapter, this is the first time that these methods have been applied to abiotic, hyperarid hillslopes.  The shift from biotic to abiotic soil transport mechanisms is captured in the rates of the processes and the applicable soil transport law.  On gentle (non-landsliding) hillslopes in humid and semiarid climates, including the semiarid site in this study, soil transport is often primarily through bioturbation as burrowing and/or tree-throw.  As MAP decreases, soil transport shifts from biotic soil transport mechanisms to abiotic ones, particularly overland flow and possibly some salt shrink-swell. As proposed in Chapter 2, a geomorphic and pedologic threshold lies near MAP = 100 mm.  At this MAP, chemical erosion is low compared to more humid hillslopes, such that physical erosion is the primary soil loss mechanism but life still "drives" the landscape through bioturbation.  This landscape is sensitive to tectonically- or climatically-driven changes in boundary condition due to adequate water to drive stream incision and short hillslope soil residence times.  As MAP decreases, vegetation decreases and abiotic processes, especially overland flow, are increasingly important to soil transport.  Channels in arid regions are sensitive to MAP and unable to reach steady state with current base level.  At the hyperarid extreme: (1) soil production through atmospheric input is as important as that through bedrock erosion, (2) vegetation and biotically-driven geomorphic processes are absent, (3) the soils experience chemical gain rather than loss, and (4) hillslope soil processes are abiotic and extremely sensitive to MAP.   Though Dietrich and Perron (2006) found no topographic signature of life, the results presented here suggest that life has a distinct effect on the rates of hillslope soil processes.  One metric of this is the transport coefficient, which is sensitive to MAP where MAP < 100 mm, and sensitive to differences in vegetation and other soil properties where MAP > 100 mm.

In Chapter 4, I examine the contour-parallel bands of gravels found on the hyperarid hillslopes, which I call "zebra stripes", which are a unique feature of the Atacama Desert. Integrating satellite imagery, geologic mapping, and field observations, I find that zebra stripes are most likely produced by overland flow and preserved by the hyperarid conditions, self-stabilizing characteristics, and absence of life. I also propose a chronology for their formation, constrained with atmospheric deposition rates, soil chemistry, CRN-derived exposure ages of the surface gravels, and the climatic history of the Atacama Desert. CRN analysis indicates that atmospherically-derived salts and dust have floated the surface gravels and buried the bedrock for at least 0.5-1 My. The process is comparable to the formation of desert pavement found in arid regions throughout the world, but is unusual on hillslopes, particularly for such a long period of time. The regional occurrence of zebra stripes, their distribution on hillslopes, and the soil and rock properties associated with them suggest that the zebra stripes were produced by overland flow. Though overland flow capable of mobilizing gravels is likely possible under modern climate conditions, I propose that the zebra stripes formed centuries or millennia ago and have been preserved by their self-stabilization and the absence of other disturbances, particularly life.

Lastly, in Chapter 5, I summarize the conclusions of Chapters 2-4 and highlight the importance of the precipitation threshold at which pedologic and geomorphic processes shift from biotic to abiotic.

**References**

Anderson RS. 2002. Modeling the tor-dotted crests, bedrock edges, and parabolic profiles of high alpine surfaces of the Wind River Range, Wyoming. Geomorphology 46: 35-58.

Böhlke JK, Ericksen GE, Revesz K. 1997. Stable isotope evidence for an atmospheric origin of desert nitrate deposits in northern Chile and southern California, USA. Chemical Geology 136: 135-152.

Carson, M.A., Kirkby, M.J. 1972. Hillslope Form and Process. University Press, Cambridge [Eng.].

Dietrich WE, Reiss R, Hsu ML, Montgomery DR. 1995. A process-based model for colluvial soil depth and shallow landsliding using digital elevation data. Hydrological Processes 9: 383-400.

Dixon JL, Heimsath AM, Amundson R. 2009. The critical role of climate and saprolite weathering in landscape evolution. Earth Surface Processes and Landforms. DOI: 10.1002/esp.1836.

Dunai TJ, Gonzalez-Lopez GA, Juez-Larre J, Carrizo D. 2005. Preservation of (early) Miocence landscapes in the Atacama Desert, northern Chile. Geochimica et Cosmochimica Acta 69: A161-A161.

Dymond, J., Biscaye, P. E., and Rex, R. W., 1974, Eolian origin of mica in Hawaiian soils: Geological Society of America Bulletin, v. 85, p. 37–40.

Ericksen GE. 1981. Geology and origin of the Chilean nitrate deposits. Geological Society Professional Paper 1188. United States Government Printing Office: Washington.

Evenstar LA, Hartley AJ, Stuart FM, Mather AE, Rice CM, Chong G. 2009. Multiphase development of the Atacama Planation Surface recorded by cosmogenic $^3$He exposure ages: Implications for uplift and Cenosoic climate change in western South America. Geology 37: 27-30.

Ewing S, Michalski G, Thiemens M, Quinn R, Macalady J, Kohl S, Wankel S, Kendall C, McKay CP, Amundson R. 2007. Rainfall limit of the N cycle on Earth. Global Biogeochemical Cycles 21: GB3009.

Ewing SA, Sutter B, Owen JJ, Nishiizumi K, Sharp W, Cliff SS, Perry K, Dietrich WE, McKay CP, Amundson R. 2006. A threshold in soil formation at Earth's arid-hyperarid transition. Geochimica et Cosmochimica Acta 70: 5293-5322.

Ewing, S.A., Yang., W., DePaolo, D.J., Michalski, G., Kendall, C., Stewart, B.W., Thiemens, M., Amundson, R. 2008. Non-biological fractionation of stable Ca isotopes in soils of the Atacama Desert, Chile. Geochimica et Cosmochimica Acta 72: 1096-1110.

Furbish DJ, Fagherazzi S. 2001. Stability of creeping soil and implications for hillslope evolution. Water Resources Research 37: 2607-2618.

Gabet EJ. 2000. Gopher bioturbation: field evidence for nonlinear hillslope diffusion. Earth Surface Processes and Landforms. 25(13):1419–28.

Gabet EJ, Reichman OJ, Seabloom EW. 2003. The effects of bioturbation on soil processes and sediment transport. Annual Review of Earth and Planetary Sciences 31: 249-73.

Gilbert, G.K. 1877. Geology of the Henry Mountains (Utah). U.S. Geographical and Geological Survey of the Rocky Mountains Region, Washington, D.C.

Heimsath AM, Chappell J, Dietrich WE, Nishiizumi K, Finkel RC. 2000. Soil production on a retreating escarpment in southeastern Australia. Geology 28: 787-790.

Heimsath AM, Chappell J, Finkel RC, Fifield K, Alimanovic A. 2006. Escarpment erosion and landscape evolution in southeastern Australia. In Tectonics, Climate, and Landscape Evolution, Willett SD, Hovius N, Brandon MT, Fisher DM (eds). Geological Society of America Special Paper 398, Penrose Conference Series;173-190.

Heimsath AM, Chappell J, Hancock GR, Fink D, Fifield K. 2008. Eroding Australia: Slowly. Geochemica Cosmochemica Acta 72: A363.

Heimsath AM, Dietrich WE, Nishiizumi K, Finkel RC. 1997. The soil production function and landscape equilibrium. Nature 388: 358-361.

Heimsath AM, Dietrich WE, Nishiizumi K, Finkel RC. 1999. Cosmogenic nuclides, topography, and the spatial variation of soil depth. Geomorphology 27: 151-172.

Heimsath AM, Dietrich WE, Nishiizumi K, Finkel RC. 2001. Stochastic processes of soil production and transport: Erosion rates, topographic variation and cosmogenic nuclides in the Oregon Coast Range. Earth Surface Processes and Landforms 26: 531-552.

Heimsath AM, Furbish DJ, Dietrich WE. 2005. The illusion of diffusion: Field evidence for depth-dependent sediment transport. Geology 33: 949-952.

Hutton, J. 1795. Theory of the earth. Edinburgh.

Jenny, H. 1941. Factors of soil formation. New York: McGraw-Hill. pp. 281.

Kennedy MJ, Chadwick OA, Vitousek PM, Derry LA, Hendricks D. 1998. Replacement of weathering with atmospheric sources of base cations during ecosystem development, Hawaiian Islands Geology 26:1015–8.

Kirchner, J.W., Finkel, R.C., Granger, D.E., Clayton, J.L., King, J.G., Megahan, W.F. 2001. Mountain erosion over 10 yr, 10 k.y., and 10 m.y. time scales. Geology 29(7): 591-594.

Kirkby, M.J. 1967. Measurement and theory of soil creep. Journal of Geology 75(4): 359-378.

Kober F, Ivy-Ochs S, Schlunegger F, Baur H, Kubik PW, Wieler R. 2007. Denudation rates and a topography-driven rainfall threshold in northern Chile: Multiple cosmogenic nuclide data and sediment yield budgets. Geomorphology 83: 97-120.

Krammes, J.S. 1960. Erosion from mountain side slopes after fire in southern California. Research Note No. 171, Pacific Southwest Forest and Range Experimental Station, USDA, Berkeley, CA.

McKay, C.P., Friedmann, E.I., Gomez-Silva, B., Caceres-Villanueva, L., Andersen, D.T., Landheim, R., 2003. Temperature and moisture conditions for life in the extreme arid region of the Atacama Desert: 4 years of observations including the El Nino of 1997–98. Astrobiology 3, 393–406.

McKay, C.P., Molaro, J.L., Marinova, M.M. 2009. High-frequency rock temperature data from hyper-arid desert environments in the Atacama and the Antarctic Dry Valleys and implications for rock weathering. Geomorphology 110: 182-187.

Meade, R.H. 1988. Movement and storage of sediment in river systems. in Lerman, A., and Meybeck, M., eds. Physical and chemical weathering in geochemical cycles. Dordrect, Netherlands. Kluwer Academic Publishers: 165-179.

Michalski G, Böhlke J, Thiemens M. 2004. Long term atmospheric deposition as the source of nitrate and other salts in the Atacama Desert, Chile: New evidence from mass-independent oxygen isotopic compositions. Geochimica et Cosmochimica Acta 68: 4023-4038.

Molnar P, Anderson RS, Anderson SP. 2007. Tectonics, fracturing of rock, and erosion. Journal of Geophysical Research-Earth Surface 112(F3).

Nishiizumi K, Caffee MW, Finkel RC, Brimhall G, Mote T. 2005. Remnants of a fossil alluvial fan landscape of Miocene age in the Atacama Desert of northern Chile using cosmogenic nuclide exposure age dating. Earth and Planetary Science Letters 237: 499-507.

Onda Y. 1992. Influence of water storage capacity in the regolith zone on hydrological characteristics, slope processes, and slope form. Zeitschrift Fur Geomorphologie 36: 165-178.

Navarro-Gonzalez R, Rainey F, Molina P, Bagaley D, Hollen B, de la Rosa J, Small A, Quinn R, Grunthaner F, Caceres L, Gomez-Silva B, McKay CP. 2003. Mars-like soils in the Atacama Desert, Chile, and the dry limit of microbial life. Science 302: 1018-1021.

Quinn, R., Zent, A., Grunthaner, F., Ehrenfreund, P., Taylor, C., Garry, J. 2005. Detection and characterization of oxidizing acids in the Atacama Desert using the Mars Oxidation Instrument, Planetary Space Science, 53, 1376–1388.

Placzek C, Matmon A, Granger D, Quade J, Caffee MW. 2007. Erosion rates in the Atacama Desert, northern Chile (~24ºS) from multiple cosmogeic nuclides. Geological Society of America, Abstracts with Programs 39: 513.

Rech J, Quade J, Hart W. 2003. Isotopic evidence for the source of Ca and S in soil gypsum, anhydrite and calcite in the Atacama Desert, Chile. Geochimica et Cosmochimica Acta 67: 575-586.

Riebe CS, Kirchner JW, Finkel RC. 2004a. Erosional and climatic effects on long-term chemical weathering rates in granitic landscapes spanning diverse climate regimes. Earth and Planetary Science Letters 224: 547-562.

Riebe CS, Kirchner JW, Finkel RC. 2004b. Sharp decrease in long-term chemical weathering rates along an altitudinal transect. Earth and Planetary Science Letters 218: 421-434.

Roering JJ. 2008. How well can hillslope evolution models "explain" topography? Simulating soil transport and production with high-resolution topographic data. Geological Society of America Bulletin 120: 1248-1262.

Saco, P.M., Willgoose, G.R., Hancock, G.R. 2006. Spatial organization of soil depths using a landform evolution model. Journal of Geophysical Research 111: F02016.

Small EE, Anderson RS, Hancock GS. 1999. Estimates of the rate of regolith production using $^{10}$Be and $^{26}$Al from an alpine hillslope. Geomorphology 27: 131-150.

Vitousek PM, Chadwick OA, Crews T, Fownes J, Hendricks DM, Herbert D. 1997. Soil and ecosystem development across the Hawaiian Islands. GSA Today 7(9):1–8.

von Blanckenburg F. 2006. The control mechanisms of erosion and weathering at basin scale from cosmogenic nuclides in river sediment. Earth and Planetary Science Letters 242: 223-239.

Warren-Rhodes, K.A., Dungan, J.L., Piatek, J., Stubbs, K., Gómez-Silva, B., Chen, Y., McKay, C.P. 2007. Ecology and spatial pattern of cyanobacterial community island patches in the Atacama Desert, Chile. Journal of Geophysical Research 112: G04S15.

Warren-Rhodes K, Rhodes K, Pointing S, Ewing S, Lacap D, Gomez-Silva B, Amundson R, Friedmann E, McKay C. 2006. Hypolithic cyanobacteria, dry limit of photosynthesis, and microbial ecology in the hyperarid Atacama Desert. Microbial Ecology 52: 389-398.

Wilkinson MT, Humphreys GS. 2005. Exploring pedogenesis via nuclide-based soil production rates and OSL-based bioturbation rates. Australian Journal of Soil Research 43: 767-779.

Yoo K, Amundson R, Heimsath AM, Dietrich WE. 2005. Process-based model linking pocket gopher (Thomomys bottae) activity to sediment transport and soil thickness. Geology 33: 917-920.

Yoo K, Amundson R, Heimsath AM, Dietrich WE, Brimhall GH. 2007. Integration of geochemical mass balance with sediment transport to calculate rates of soil chemical weathering and transport on hillslopes. Journal of Geophysical Research-Earth Surface: 112(F2).

# Chapter 2

## The Sensitivity of Hillslope Soil Production to Precipitation

**Abstract**

Decoupling the impacts of climate and tectonics on hillslope erosion rates is a challenging problem. Hillslope erosion rates are well known to respond to changes in hillslope boundary conditions (e.g. channel incision rates) through their dependence on soil thickness, and precipitation is an important control on soil formation. Surprisingly though, compilations of hillslope denudation rates suggest little precipitation sensitivity. To isolate the effects of precipitation and boundary condition, we measured rates of soil production from bedrock and described soils on hillslopes along a semiarid to hyperarid precipitation gradient in Northern Chile. In each climate zone, hillslopes with contrasting boundary conditions (actively incising channels vs. non-eroding landforms) were studied.

Both geochemical and geomorphic thresholds were observed at the biotic-abiotic transition. Hillslope erosion shifts from relatively fast, biologically-driven processes to extremely slow, salt-driven processes, while channel incision shifts from tectonically-controlled to climate-controlled. Contrary to studies in humid regions, rates of soil production from bedrock increase with precipitation following a power law, from ~ 1 m $My^{-1}$ in the hyperarid region to ~ 40 m $My^{-1}$ in the semiarid region. The effect of boundary condition on soil thickness was observed in all climate zones (thicker soils on hillslopes with stable boundaries compared to hillslopes bounded by active channels), but the expected effect on the rates of soil production from bedrock (slower erosion rates on hillslopes with stable boundaries) decreased as precipitation decreased. The biotic-abiotic threshold also marks the precipitation rate below which denudation rates are no longer a function of soil thickness. Our work shows that hillslope processes become sensitive to precipitation as life and the ability of the landscape to respond to tectonics disappear.

## 1. Introduction

How does precipitation affect the mechanisms and rates of geomorphic processes on soil-mantled, gentle (non-landsliding) hillslopes? The imprint of precipitation and its associated biota on soil formation processes has been recognized for more than a century (e.g. Jenny, 1941, and references therein), but only recently have the rates of hillslope soil production and transport been quantifiable using cosmogenic radionuclides (CRN). Despite an ever-growing database of CRN-derived denudation rates (denudation rate refers to the rate of physical and chemical erosion of material, usually assumed to equal the rate of soil production from bedrock), evidence of precipitation-dependence remains elusive. Riebe et al. (2004a) compiled 42 denudation rates for 14 gentle, non-glaciated hillslopes spanning a broad spectrum of mean annual temperatures (MAT: 2-25ºC) and mean annual precipitation (MAP: 250-4200 mm $y^{-1}$). Denudation rates were not correlated with MAP or MAT. In another compilation, von Blanckenburg et al. (2006) found catchment-averaged denudation rates (calculated using stream sediment CRN concentrations) at sites across the globe were independent of MAP and MAT.

No clear linkage between denudation rate and precipitation or temperature has been observed, and large variations in the measured denudation rates in any given climate suggest that

other factors, such as tectonics, bedrock characteristics (particularly fracturing), and the co-variation of precipitation and temperature, may be obscuring the precipitation signal.  Riebe et al. (2001) found hillslopes bounded by faulting-affected river canyons erode faster compared to hillslopes bounded by low-relief surfaces (indicative of less incision).  They concluded that tectonic uplift, through its effect on channel incision rates (i.e. local boundary condition) and subsequent hillslope response, is the primary control on denudation rates.  This was confirmed by von Blanckenburg et al. (2006) who showed that variation in tectonic setting (affecting hillslope boundary conditions through channel incision response to uplift) obscures any MAP or MAT signal.  Alternatively, Molnar et al. (2007) argue that it is not the uplift rate but the disintegration of bedrock due to tectonics that influences erosion rates.  Selby (1980) proposed a classification system for rock mass strength to address the effect of jointing and residual stress on hillslope geomorphology.  Hillslope erosion may also be bedrock-dependent due to small variations in mineralogy or grain size (e.g., Onda, 1992), which are often ignored.  However, no study has attempted to account for degree of fracturing or grain size in addition to precipitation and boundary condition.  Temperature may obscure the role of precipitation, particularly when elevation gradients are used to create climosequences (eg. Riebe et al., 2004b; Dixon et al., 2009).  Precipitation and temperature often vary inversely of each other with elevation and so their individual effects upon process rates are difficult to separate (e.g. Dahlgren et al., 1997).  Without careful site selection, teasing apart the effects of precipitation, temperature, bedrock, and boundary condition may be difficult.

Here we examine hillslopes in northern Chile (primarily in the Atacama Desert) at the dry end of the Earth's precipitation spectrum to quantify the response of hillslope processes to increasing aridity and differing boundary conditions.  This study was motivated by our observations of large variations in soil thickness and chemistry (Ewing et al., 2006) along the precipitation gradient in this region, particularly at the threshold for plant growth.  Along a precipitation gradient, on hillslopes with different boundary conditions but with similar bedrock types, tectonic uplift rates, and MAT, we examined the thickness and chemical nature of the soil mantle, identified the mechanisms of bedrock erosion and soil transport, and quantified bedrock erosion rates (both the rates of hillslope soil production from bedrock and local channel incision rates).  We find that our sites reveal systematic differences in soil thickness and bedrock erosion due to boundary condition as expected.  However, at these low MAPs the rates of soil production from bedrock decrease with decreasing MAP, in contrast to previous work (Riebe et al., 2004a; von Blanckenburg et al., 2006).  This decreases coincides with changes in the mechanisms of soil production and soil transport.  When we compare these observations with findings in more humid settings, we find a critical MAP-threshold below which soil production from bedrock is precipitation-dependent, and above which soil production from bedrock is controlled by the complex interaction of other factors including tectonic uplift, biota, and MAT.

## 2. Theoretical Framework

The relationship between hillslope soil processes, boundary conditions, and precipitation can be approached through a mass balance.  The components of the mass balance are described below and their potential response to boundary conditions and precipitation are described.  Two components of the mass balance, the rate of soil production from bedrock and the steadiness of soil mass, can be evaluated using CRN analysis.  Throughout this paper, "soil" refers to the physically disturbed, chemically altered material subject to transport downslope; "saprolite"

refers to chemically altered bedrock which is not physically disturbed (the rock fabric is preserved) and may underlie the soil on some hillslopes; and "weathered rock" refers to rock which has been fractured but is otherwise undisturbed.

## 2.1. Hillslope soil mass balance and the soil production function

The mass of the hillslope soil mantle (the mobile mantle over weathered rock or saprolite) is determined by the balance between soil erosion and soil production (Fig. 1). This can be expressed as the difference between soil inputs and outputs per unit area of hillslope:

$$\frac{\partial(\rho_s H)}{\partial t} = \underbrace{\underbrace{P}_{\substack{production \\ from \\ bedrock}} + \underbrace{A}_{\substack{atmospheric \\ deposition}}}_{\substack{soil\ production \\ mechanisms}} - \underbrace{\underbrace{\nabla \cdot \tilde{Q}_s}_{\substack{physical \\ erosion}} - \underbrace{W}_{\substack{chemical \\ erosion}}}_{\substack{soil\ loss \\ mechanisms}} \tag{1}$$

where $\rho_s$ is the bulk density of the soil (M L$^{-3}$), $H$ is the slope-normal soil thickness (L), $P$ is the rate of soil production from bedrock (M L$^{-2}$ T$^{-1}$), $A$ is the deposition rate of silicate dust and salts from the atmosphere (M L$^{-2}$ T$^{-1}$), $\nabla \cdot \tilde{Q}_s$ is the rate of physical erosion (the divergence of soil flux, $Q_s$) (M L$^{-2}$ T$^{-1}$), and $W$ is the rate of chemical erosion (M L$^{-2}$ T$^{-1}$). Here $P$ is called the "rate of soil production from bedrock" rather than the "soil production rate" because both $P$ and $A$ are rates of soil production. Bedrock often undergoes some mass loss by chemical processes before being converted to soil (Anderson et al., 2002; Dixon et al., 2009), but this effect is not accounted for here.

Hillslopes evolve in response to their boundary conditions. A slope-dependent soil transport law, $Q_s = f(\nabla z)$ where $\nabla z$ is slope, enables "communication" between the boundary condition at the base of the slope and the soils upslope from it (Fernandes and Dietrich, 1997). The expression for $Q_s$ reflects the erosion processes involved and may include a combination of the following expressions (Braun et al., 2001). Soil creep (e.g. freeze-thaw and shrink-swell) and biologically-driven transport (e.g. tree throw and animal burrowing) are either a function of slope, $\nabla z$, $Q_s = -K\nabla z$, or of the depth-slope product, $Q_s = -K_h H \nabla z$ (where $K$ and $K_h$ are empirical "transport coefficients") (Heimsath et al., 1997; Braun et al., 2001; Heimsath et al., 2005; Heimsath et al., 2006; Yoo et al., 2007). On sufficiently steep slopes, soil flux may increase non-linearly with slope (e.g. Roering et al.,1999; Roering, 2008). Where overland flow is important, soil flux is also a function of drainage area (or length from the upslope divide). Transport laws for this process are less established, but $Q_s = -K_w A^m \nabla z^n$ is commonly assumed, where $A$ is upslope area and $K_w$, $m$, and $n$ are empirical constants (e.g. Dietrich et al., 2003). In any of these cases, an increase in slope increases soil flux and the stronger the hillslope curvature ($\nabla^2 z$) the greater the physical erosion rate.

Increased erosion will thin the soil, which will tend to increase $P$ (Dietrich et al., 2003; Dietrich and Perron, 2006). The hypothesis that rates of soil production from bedrock vary inversely with soil thickness originated with Gilbert (1877), and CRN-derived rates of $P$ in California and Australia (Heimsath et al., 1997, 1999, 2000; Wilkinson and Humphreys, 2005) demonstrate that $P$ decreases exponentially with increasing $H$:

$$P = P_0 e^{-\alpha H} \tag{2}$$

where $P_0$ is the bedrock erosion rate under zero soil cover and $\alpha$ is an empirical rate constant. Equation 2 (a.k.a. the soil production function) predicts that bare bedrock has the highest $P$. However, a "humped" function, with maximum $P$ at some critical soil thickness (Carson and Kirkby, 1972; Dietrich et al., 1995; Furbish and Fagherazzi, 2001; Anderson, 2002), may be more reasonable, in that some soil is required to store water, support plants, and harbor burrowing animals, all of which increase $P$. Work in Australia (Heimsath et al., 2006), South Africa (Heimsath et al., 2008), and Wyoming (Small et al., 1999) supports the humped function.

Regardless of the "shape" of the soil production function, the combination of depth-dependent bedrock erosion and slope-dependent soil flux produces a feedback between physical erosion and $P$ such that $P$ is sensitive to varying channel incision rates. If incision rates increase at the hillslope boundary, steepening slopes will increase physical erosion, thinning the soil, increasing $P$, and driving the coupled soil erosion-hillslope form-soil thickness to a new equilibrium (e.g., Penck, 1953; Dietrich et al., 1995). Early modeling experiments incorporating slope-dependent soil flux (but not thickness-dependent $P$) illustrated the impact of downslope boundary conditions on the shape of the hillslope (Kirkby, 1971; Ahnert, 1987; Armstrong, 1987; Anderson and Humphrey, 1989; Fernandes and Dietrich, 1997). Other models have included the effects of soil thickness on hillslope response (Ahnert, 1970; Furbish and Fagherazzi, 2001; Furbish, 2003; Mudd and Furbish, 2004; Mudd and Furbish, 2007). These models show that a constant incision rate can produce steady-state soil thicknesses in the upslope positions, whereas the cessation of incision leads to progressive upslope deviation from steady-state.

Precipitation is not explicitly expressed in the equations above. However, it is likely included in $K$ in the soil flux equations, a constant that may also incorporate geologic and biotic effects. In the soil production function, $P_0$ should be mostly dependent on bedrock characteristics but could reflect precipitation sensitivity, as could $\alpha$. Indeed, an interesting question is how precipitation (and resulting biota) impacts $K$, $P_0$, and $\alpha$, and how these might affect $W$ (Riebe et al., 2004a; Dixon et al., 2009), but that is beyond the scope of this work.

## 2.2. Cosmogenic radionuclide analysis

CRN produced *in situ* in rock are used to calculate bedrock denudation rates, determine if local soil mass has been approximately constant (soil steady-state), and constrain the age of land surfaces. CRN are produced near the Earth's surface by cosmic rays, and the rate of production decreases exponentially with increasing depth (e.g., Lal, 1991). The concentration of CRN in a rock reflects the time during which it has been near the surface, and is controlled by the rates of erosion and deposition above it. If rates of erosion and deposition are constant, such that the overlying soil is in steady state, and CRN production and erosion are also in steady state, then the CRN concentration reflects the rate of the conversion of weathered rock to soil, or $P$ in equation 1. This is often called the "denudation rate", because, if $A$ is ignored, a steady-state soil mass balance requires that $P$ is equal to the rate of soil loss ($\nabla \cdot \tilde{Q}_s + W$ in equation 1). In this paper, because of the influence of $A$, we will avoid using "denudation rate" and refer to the erosion rate calculated from CRN concentrations as $P$. At steady state, weathering of rock (e.g.

saprolitization) should keep pace with bedrock erosion. However, we have no measurements or observations as to whether this is occurring in our field areas.

The steady-state concentration of a CRN, $C$ (atom g$^{-1}$), in the bedrock at the soil-weathered bedrock interface is:

$$C = P_c \left( \frac{1}{\lambda + \frac{\rho_r P}{\Lambda}} \right) \qquad (3)$$

where $P_c$ is the CRN production rate (atom g$^{-1}$ y$^{-1}$)(corrected for overlying soil mass), $\lambda$ is the decay constant ($\lambda = \ln 2 / t_{1/2}$ y$^{-1}$, where $t_{1/2}$ is the half-life of the CRN), $\rho_r$ is the bulk density of the bedrock (g cm$^{-3}$), $P$ is the maximum rate of soil production from bedrock (cm y$^{-1}$), and $\Lambda$ is the mean attenuation length of cosmic ray interaction (g cm$^{-2}$) (Lal and Arnold, 1985). Equation 3 can be rearranged to solve for $P$:

$$P = \frac{\Lambda}{\rho_r} \left( \frac{P_c}{C} - \lambda \right) \qquad (4)$$

Though $P$ is in units of cm y$^{-1}$ here, it can be converted to a mass flux for use in equation 1 by multiplying by the sample density. The four requirements in this steady-state calculation are: (1) $P$ must be constant, (2) the soil mass must be constant ($\rho_s \partial h/\partial t = 0$), (3) the time the bedrock has been exposed to cosmic rays, $t$, is long enough that $t >> (\lambda + \rho_r P \Lambda^{-1})^{-1}$, and (4) the bedrock must have zero initial concentration of the CRNs being measured.

Pairs of CRN, such as [26]Al and [10]Be produced in quartz, are often analyzed because they have different response times to perturbations in steady-state conditions. A comparison of their concentrations in a sample can, under certain conditions, reveal deviation from steady state that would not be recognized with a single nuclide. In steady state, the production rate ratio of [26]Al and [10]Be in quartz is 6.7 (Nishiizumi et al., 2007 after Nishiizumi et al., 1989). At steady state, the ratio decreases with decreasing erosion rate, reaching a minimum of 3.5 when erosion is zero. The ratio also decreases with increasing exposure time, approaching 3.5 with infinite exposure time. If the ratio is below the steady-state line on a [10]Be-[26]Al/[10]Be evolution diagram, then the sample has experienced a complex exposure history ($\partial h/\partial t \neq 0$), non-uniform erosion, or experimental error (e.g., Lal, 1991; Nishiizumi, 1991). Discretion is required to interpret data from slowly eroding, ancient landscapes.

The minimum exposure age of a sample, $t$ (y), can be calculated if there is no inheritance of CRN in the sediment and simple exposure of the sample:

$$t = -\frac{1}{\lambda} \ln \left( 1 - \frac{C\lambda}{P_c} \right) \qquad (5)$$

16

This approach has been used extensively to calculate the ages of stable landforms, such as fluvial terraces in the Atacama (e.g., Nishiizumi et al., 2005). Equation 5 defines the minimum exposure age because no erosion is assumed. Potential complications with this approach include movement of the target material on the surface and non-zero erosion (e.g., Evenstar et al., 2009), which may produce a non-zero initial CNR content or change the orientation of the rock to cosmic ray flux. Field observations and the evaluation of $^{26}Al/^{10}Be$ isochrones can often determine if these complications are significant.

## 3. Study area

Northern Chile (Fig. 2a) was selected for our study area because a large, long-term precipitation gradient, from semiarid to hyperarid, exists over a region with relatively spatially-uniform uplift and areas of similar bedrock. The Atacama Desert spans a region from southern Peru into northern Chile. It is primarily located in a north-south trending valley, the Central Depression, bounded on the west by the Coastal Cordillera and on the east by the pre-Andean ranges. The Central Depression becomes increasingly discontinuous south of about 26ºS, though the general features of the Coastal Cordillera and pre-Andean ranges remain in place (Mortimer, 1973). The Central Depression disappears entirely near 27ºS and the topography to the south is continuously hilly to mountainous from the sea to the Andes. The southern boundary of the Atacama is subject to debate. Rundel et al. (1991) suggest the present-day border lies at La Serena and the Rio Elqui (~30ºS) based on a shift in vegetation from semiarid coastal scrub to succulent desert communities, but the nearly lifeless zone for which the Atacama is renowned ends near the latitude of Chañaral (~26.3ºS).

## 3.1. Climate and Biota

Present-day MAP decreases exponentially with decreasing latitude, from ~100 mm at 29ºS to ~1 mm in the Central Depression between 20 and 26ºS, the core of the Atacama Desert (Ericksen, 1981, Fig. 2b). South of ~21ºS, winter Pacific Westerlies are the source of rainfall to the Coast Range and Central Depression, whereas north of ~21ºS the summer Atlantic Easterlies are dominant (Houston, 2006). Regardless of its source, rainfall in the Central Depression may fail to occur for decades to centuries (Ericksen, 1981; Vargas et al. 2006). Fog is a significant source of moisture at elevations below ~1000 m near the coast (Rundel et al., 1991). Geochemical evidence suggests that dry conditions have persisted at least periodically since the middle to late Miocene (Alpers and Brimhall, 1988; Sillitoe and McKee, 1996; Hartley and Chong, 2002; Dunai et al., 2005; Nishiizumi et al., 2005; Clarke, 2006; Houston, 2006; Kober et al., 2007), and possibly much earlier (Hartley et al., 2005; Clarke, 2006; Evenstar et al., 2009). Recent research in the southern Pacific suggests that the present Pacific circulation (El Niño-Southern Oscillation, ENSO) was emplaced near the end of the Pliocene (Ravelo et al., 2004), and may signal the onset of the present episode of hyperaridity.

Within this long (at least 2 to 9 My) period of aridity have been episodes of more pluvial conditions. Offshore sediment deposits between 24ºS and 44ºS indicate that the position of the Southern Westerlies has occasionally moved north, as much as 5º latitude from its current position, in the last 80 ka (Lamy et al., 2000; Hebbeln et al., 2007). Other short term variations have been recorded in paleowetland deposits (Rech et al., 2003) and rodent middens (Betancourt et al., 2000; Latorre et al., 2002; Latorre et al., 2003). These short periods of elevated precipitation have been of insufficient magnitude and duration to remove or chemically alter

highly water-soluble and biologically-reactive compounds such as nitrate which have been accumulating since the beginning of the Pliocene (Ewing et al., 2007). Thus, present regional trends in rainfall are largely indicative of post-Pliocene climate conditions.

In the Central Depression and Coastal Cordillera, systematic shifts in biota occur with latitude due to the changes in MAP (Fig. 2c). The hyperarid north (~19-23ºS) is a nearly abiotic landscape (Navarro-González et al., 2003; Warren-Rhodes et al., 2006) with no vascular plants. Biota increases with increasing latitude, such that around 26ºS there are scattered fog-adapted plants, and by ~29ºS there is a succulent desert scrub ecosystem (Rundel et al., 1991).

## 3.2. Geologic Setting

Bedrock in the Atacama Desert is a complex mixture of volcanic, plutonic, and metasedimentary rock due multiple volcanic episodes and long-term plate convergence (Ericksen, 1981). A thick sequence of fluvial sediments with interbedded ash-flow tuffs known as the Atacama Gravels was deposited coincidentally with the onset of Andean uplift (beginning in the Oligocene) and continued until the late Miocene (Ericksen, 1981). This widely-distributed Miocene deposit blanketed much of the region from the foothills of the pre-Andean ranges, through the Central Depression, and into the Coastal Cordillera. Up to several hundred meters of this sediment has been locally removed since the Miocene, but Quaternary reworking of sediment is extremely limited despite continuing regional uplift (Fig. 2d). Many low hills (<200 m relief) in the Central Depression, possibly including the hillslopes at the north end of our study transect, were likely completely or partially buried by the Atacama Gravels and have been re-exposed by post-Miocene erosion (Nester, 2008; R. Amundson). However, arid conditions have limited erosion (see below), therefore, the general shapes of some hillslopes, particularly in the hyperarid core of the desert, were likely achieved in the Miocene or earlier and have since been only slightly altered. Many topographic features are likely relicts of a wetter past that are being slowly reworked under arid to hyperarid conditions.

Landform change since the Miocene has been remarkably slow. CRN-derived calculations of bedrock and boulder erosion rates in the northern part of the pre-Andean range are generally <2 m My$^{-1}$ (Nishiizumi et al., 2005). Along an west-east transect from the Coastal Cordillera into the Andes, Kober et al. (2007) found that CRN-derived erosion rates of exposed bedrock on hilltops and boulders increased with increasing precipitation by several orders of magnitude. However, this transect spanned a change in altitude of 4000 m and bedrock varied between granite and rhyolite, such that both temperature and bedrock varied in addition to precipitation. Placzek et al. (2007), working along an east-west transect near 23ºS, found that erosion rates of boulders, surface gravels, and channel sediments are less than 1 m My$^{-1}$ in the most hyperarid regions, but increased by up to two orders of magnitude with increasing elevation. Boulders provide a minimum erosion rate for the landscape because bare rock outcrops and boulders may experience little chemical weathering (e.g., Carson and Kirkby, 1972; Oberlander, 1972). Average hillslope $P$ may therefore provide a better estimate of the landscape erosion rate because it is more sensitive to precipitation and basal boundary condition.

Soils on non-eroding alluvial surfaces show extreme sensitivity to MAP in their salt composition and concentration (Ewing et al., 2006), in the degree of chemical weathering (Ewing et al., 2006; Amundson et al., 2007), and in the abundance of microbial life (Navarro-

18

González et al., 2003; Warren-Rhodes et al., 2006).  Gypsum, anhydrite, halite, carbonate, iodate and borate are found in alluvial soils in the northern part of the Atacama, above ~24ºS (Ericksen, 1981; Ewing et al., 2006), due in part to the deposition of material derived from marine and volcanic sources in the region (Böhlke et al., 1997; Rech et al., 2003; Michalski et al., 2004).  As precipitation increases, the salt content of alluvial soils decreases and organic matter increases (Ewing et al., 2006).

Uplift of the Coastal Cordillera between 22 and 33ºS has averaged about 0.2 mm $y^{-1}$ over the last 100 to 800 ky (Fig. 2d).  The long profiles of rivers cutting through the Coastal Cordillera at these latitudes have convex or straight regions near the coast, indicative of a geomorphic system out of equilibrium with baselevel (Mortimer, 1980).  Hypsometric curves (the cumulative fraction of total area vs. normalized elevation) of the land surface of the Atacama Desert are generally convex (Montgomery et al., 2001), a pattern consistent with a landscape where fluvial incision is unable to match tectonic uplift.  This suggests that inland hillslopes are isolated from current marine baselevel and local channel incision may differ greatly from uplift rate.

## 4.  Methods
### 4.1.  Site Selection
Pairs of gentle, non-landsliding, convex hillslopes were selected in three climate regions: 1) hyperarid, 2) arid, and 3) semiarid (Fig. 2, Table 1), all of which receive precipitation from the west.  In each pair, one hillslope is bounded by an actively incising channel (currently bedrock-bedded) and the other is bounded by a stable landform (e.g., upper stream terrace, pediment, or alluvial fan) (Figs. 2 and 3).  These are referred to as the "active hillslope" and "stable hillslope", respectively.  This nomenclature is not meant to imply that the stable hillslope is not eroding, only that its boundary is currently inactive and isolates the hillslope from local base level conditions.

The precipitation gradient spans two orders of magnitude (Fig. 2b).  The semiarid site is about 20 km inland from La Serena, where MAP = 119 mm (based on 80 years of data, Worldclimate, 2009) but ranges from 10 to 410 mm (Kalthoff et al., 2006).  Nocturnal dew inputs and fog events likely contribute another 5-10 mm $y^{-1}$ of moisture (Kalthoff et al., 2006).  The arid site is near Chañaral, where MAP is 9.5 mm (based on 53 years of data, WorldClimate, 2009).  MAP is highly variable, with periods of 5 to 7 years with no precipitation interrupted by large events up to 65 to 80 mm (Rundel et al., 1996).  Fog inputs at the arid site are frequent, due to the local connection to the coast *via* an east-west trending valley, and important, given the presence of fog-adapted vegetation.  In the hyperarid region, MAP is < 2 mm and most years have zero measurable rainfall (McKay et al., 2003).  Fog input is modest due to the elevation and distance inland (Cáceres et al., 2007).  MAP is likely not the best metric for geomorphically important precipitation because in arid regions, erosion is often driven by large, rare events (e.g., Coppus and Imeson, 2002, and references therein).  However, it is the only precipitation metric available in this little-studied area.

Mean annual temperature (MAT) decreases slightly from north to south (Table 1).  At the driest site, MAT is about 17ºC, ranging from 32ºC during the day in summer to 0ºC at night in winter (McKay et al., 2003).  MAT at the arid site is about 16ºC, ranging from 27ºC to 11ºC

(Rundel et al., 1996). The semiarid site is somewhat cooler with a MAT of 13.5ºC, ranging from 21ºC to 8ºC (Squeo et al., 2006). Along the study transect, rainfall increases by two orders of magnitude with increasing latitude while temperature decreases by a factor of about 0.76. Thus, from a first order perspective the largest climate signal is precipitation.

Fog input varies between sites. The ideal experimental set up would be sites of equal distance from the coast and at similar elevations, because geography controls fog occurrence in the Atacama Desert (Rech et al., 2003). However, because analysis of $^{26}$Al and $^{10}$Be requires quartz, the semiarid and arid sites are lower in elevation (377 and 687 masl, respectively) and closer to the coast (15 km and 21 km, respectively) than the hyperarid site (1167 masl, 50 km to coast) due to the limited extent of granitic bedrock in these regions. Because this serves to enhance the precipitation gradient, we feel it does not compromise the interpretation of our results.

The parent material is fairly uniform between the sites (Table 1). The hyperarid hillslopes are underlain by the Unidad Herradura, a fine-grained, amphibole and biotite-containing granodiorite of middle Cretaceous age (Marinovic et al., 1992). This is the most mafic and fine-grained bedrock of the three sites. In the arid region, bedrock is of the Pluton Cerros del Vetado, a 217 Ma, coarser-grained monzogranite with several andesitic to basaltic dikes that follow regional fracture patterns but do not appear to strongly control topographic development (Godoy and Lara, 1998). The hillslopes considered in this work do not have dikes. Lastly, bedrock at the semiarid site is the Pluton Santa Gracia, a biotite and amphibole-containing monzogranite with a grain size similar to that of the arid site. It contains no mafic dikes and is estimated to be at least 100 Ma by K-Ar dating (Emparan and Pineda, 2000).

## 4.2. Field Observations and Analyses

On each hillslope,10 to 40 soil pits were excavated, five to six of which formed a slope-parallel transect extending from the ridge top (or as close to the ridge top as possible) to the bottom of the hillslope (Fig. 4). Soil thickness was measured in all excavations, with the base of the soil defined as the transition to unexpanded or unperturbed bedrock textures at the semiarid and arid sites, and as the transition to >85% rock fragments at the hyperarid sites. The soils along the downslope transect were described for color, organic matter content, structure, porosity, and consistence following the methods of Schoenenberger et al. (2002) and were sampled by horizon for analysis of chemical composition, bulk density, and particle size. Evidence of the processes converting saprolite or bedrock to soil and transporting the soil downslope was recorded. Topographic surveys of each hillslope were made using a Trimble GPS and analyzed with Golden Surfer Software (v. 8.0). Vegetation density was measured along three transects on each hillslope by calculating the length fraction of a 50-m measuring tape underlain by vegetation.

Samples of bedrock (fresh, weathered, or altered to saprolite) were collected for CRN analysis. Saprolite at the soil-saprolite interface (at the semiarid sites) or fractured bedrock at the soil-bedrock interface (at the arid and hyperarid sites) was collected from excavations along the downslope transects to calculate $P$. Three additional samples were collected near the transect on the semiarid active hillslope (Table 2). Exposed bedrock from channels adjacent to the active hillslopes was collected to measure local incision rate. Quartz pebbles on the surface of the

terrace bounding the semiarid hillslope were collected and processed as an amalgamated sample to determine the exposure age of the stable boundary. Weathered bedrock from excavations in the pediplain surrounding the arid hillslopes was collected to determine the rate and uniformity of pediplain lowering.

The samples for CRN analysis were processed using methods described in Kohl and Nishiizumi (1992). Briefly, the samples are ground to pass through a 0.5 mm sieve. The quartz mineral grains are isolated through a series of acid dissolutions then dissolved and processed to isolate Be and Al. $^{10}$Be/$^9$Be and $^{26}$Al/$^{27}$Al were measured by accelerator mass spectrometry (AMS) at the Lawrence Livermore National Laboratory Center for Accelerator Mass Spectrometry (by Robert Finkel) and at the Purdue Rare Isotope Measurement Laboratory (by Marc Caffee) and normalized to the Nishiizumi et al. (2007) $^{10}$Be AMS standard and the Nishiizumi (2003) $^{26}$Al AMS standard, respectively. Accordingly, the $^{10}$Be half-life of 1.36 My and the $^{26}$Al half-life of 0.705 My were used. Erosion rates and exposure ages were calculated based on the scaling functions of Lal (1991) and assuming 2.5% muon contribution. Production rates (at sea level and high latitude) of 5.1 atoms $^{10}$Be g quartz$^{-1}$ y$^{-1}$ and 34.1 atoms $^{26}$Al g quartz$^{-1}$ y$^{-1}$ were used (Nishiizumi et al., 2007) and corrected for soil cover using modern soil thickness and bulk density.

Rock samples from the bedrock-soil interface were thin-sectioned by Spectrum Petrographics, Inc. (Vancouver, WA) or by the Department of Earth and Planetary Sciences at the University of California, Berkeley. Samples from the hyperarid and arid sites were impregnated with epoxy and then cut using a waterless technique to preserve any salt within the rock fragments. The samples were imaged on a Leo 430 Scanning Electron Microscope-Energy Dispersive X-Ray Spectrometer (SEM-EDS) in the Department of Earth and Planetary Science at the University of California, Berkeley.

## 5. Results

Both boundary condition and MAP exert control on landscape development and in order to tease apart their contributions the results from each climate region are presented separately before a site-to-site comparison is made. For each site we describe the soils, identify the processes of soil formation and transport, and quantify the rate of soil production.

### 5.1. Semiarid hillslopes

The semiarid hillslopes provide useful reference points because the climate is wet enough to support vegetation and animals as well as drive chemical weathering. Thus, the soil production and transport processes are similar to those found in previous studies of semiarid to humid hillslopes (e.g., Heimsath et al., 1999; Yoo et al., 2005). The availability of water, $CO_2$, and organic matter in the soil facilitates deep weathering, and hand excavations could not reach unweathered bedrock. Thick, red clay films surround in-place mineral grains in the saprolite and weathered bedrock. Carbonate and other salts were undetectable in the soils. The soil surface is coarse sand and fine gravel which overlies a dense, finer-textured soil interwoven with roots. Cacti and shrubs cover 32% of the soil surface (Figs. 2a-b) and their roots, though concentrated in the upper tens of centimeters of the soil, extend into the top of the saprolite (Fig. 5). Despite the large amount of bare ground, the coarse surface limits rainsplash and minimizes overland flow except for a few, anthropogenically disturbed areas where trails had been eroded tens of cm

deep. The vegetation supports small burrowing mammals and insects, as well as introduced grazers (including mules, horses, and goats). A population of native grazers likely existed prior to ranching (Wheeler, 1995). Chemical weathering (as evidenced by clay films and soil reddening) weakens the bedrock and leads to some chemical erosion, while bioturbation (as evidenced by burrows and root traces) disrupts the weathered bedrock, converts it to soil, and transports it downslope. Wetting and drying of the soil likely produces some soil creep due to shrinking and swelling (Kirkby, 1967). Bioturbation and soil creep are depth-dependent (e.g. Kirkby, 1967; Gabet et al., 2003; Yoo et al., 2005) and slope-dependent (Heimsath et al., 1999; Braun et al., 2001; Yoo et al., 2007). Thus, hillslopes with different boundary conditions should have different rates of soil production from bedrock and soil thicknesses.

The active hillslope is bounded by a small tributary which joins the Quebrada de Santa Gracia and Rio Elqui (the major drainage from the Andes at this latitude), eventually draining to La Serena Bay (~20 km downstream). The Quebrada de Santa Gracia is a gravel-bedded, braided river that rarely flows (the last major flood event was in 1997 during a strong El Niño year (Pérez, 2005)). Based on sediment records from the bay, this region, like most of the Chilean coast, experienced periods of uplift and transgression during the Miocene (Le Roux et al., 2006). Over the last 2.1 My, the bay has experienced uplift relative to sea level of ~80 m $My^{-1}$ (Le Roux et al., 2005). The channel adjacent to the active hillslope has a CRN-derived erosion rate of 34±1.7 m $My^{-1}$ (Tables 1, 2), less than half of the average uplift rate during the Pleistocene. The difference between the incision rate at the base of the active hillslope and the regional uplift rate suggests that the hillslope is not adjusted to marine base level. The stable hillslope is located on the other side of the ridge from the active one and bounded by the highest of a series of stream terraces along the Quebrada de Santa Gracia (Figs. 2b, 3a). An amalgamated sample of quartz pebbles from the surface of the terrace had an average minimum exposure age (using equation 3) of 220±110 ky. The $^{26}Al/^{10}Be$ ratio of this sample is low (Fig. 6a) indicating a complex exposure history. This is not unexpected because the sampled gravels were small and mobile, and thus have probably moved since the formation of the terrace. Additionally, bioturbation could have buried and brought to the surface some of the pebbles. The CRN calculation gives a minimum exposure time, so it is likely that the uppermost terrace has been in place at least 150 ky.

Slope-normal soil thickness on the active hillslope increases downslope from 6.7 to 27 cm, with an average of 14.5±6.7 cm (n=30) (Fig. 6b). Deviations from constant soil thickness are sometimes interpreted as evidence of deviation from steady state, but this applies only if soil flux is solely dependent on slope. Other expressions of soil flux are compatible with non-uniform soil thickness on steady-state hillslopes (e.g. Furbish, 2003), and expected for many biotic hillslopes (Heimsath et al., 2005). $^{26}Al/^{10}Be$ ratios and $^{10}Be$ concentrations measured in almost all of the saprolite samples indicate that the exposure time has been too short to test for steady-state (i.e., they plot to the left of the erosion window in Fig. 6a). A few of the samples (SGA-1, SGA-2, and SGA-4, Table 2) have $^{26}Al/^{10}Be$ ratios that are high, falling above the erosion window in Figure 6a. These could be due to an overestimate of $^{26}Al$ caused by a processing error, though the samples are close to the erosion window within error.

Slope-normal soil thickness on the stable hillslope increases slightly downslope (Fig. 6b), with an average of 23.2±6.4 cm (n=25). While average soil thickness is higher than on the active

hillslope, soil thickness was expected to increase more dramatically with distance downslope given the stable boundary condition. The absence of major soil accumulation at the base may be due to the uniformly low gradient across the hillslope (averaging 0.19±0.03, vs. 0.39±0.06 on the active hillslope, Fig. 4f) and its location upslope from the concave transition from hillslope to terrace (Fig. 4a). $^{26}$Al/$^{10}$Be ratios in saprolite are lower (average 6.1) than the steady-state ratio and might indicate some soil thickening.

As expected for a bioturbation-dominated hillslope, $P$ decreases exponentially with increasing soil thickness, with $P = 40.07e^{-0.0402H}$ ($r^2$=0.34) if all the data points except SGA-1 are considered ($H$ is in cm as in Heimsath et al., 1997) (Fig. 6c). The topmost excavation (SGA-1) is excluded because it has either too low $P$ for its current soil thickness or too thin a soil for the calculated $P$ to fit the trend. Though there are some boulders on the hillslope, they are not concentrated in a way suggesting varying bedrock composition has produced the lower $P$ at the top of the hill. The soil thickness is likely too low, despite its consistency with the general trend in Figure 6a, for two reasons. First, $P$ on the stable hillslope increases upslope but is lower at the crest (SGS-1) than the uppermost pit on the active hillslope (SGA-1) (Table 2). This suggests that the upper part of the hillslope has not adjusted to present boundary conditions on either side. Second, a trail follows the ridge dividing the two transects (but favors the side towards the active slope), resulting in deep, slope-parallel rilling along parts of the ridge which has likely thinned the soil. Guanacos (coastal cameloids similar to llamas) have occupied the area for thousands of years (Wheeler, 1995) and create trails, but these trails do not show anywhere near the same degree of erosion based on our few observations. Humans arrived in Chile 12 kya, and settled in the Coquimbo region no earlier than ~6 kya (Mostny, 1972). An agricultural culture developed in the Elqui valley ~2 kya (Mostny, 1972) and the region has been inhabited ever since. If humans were responsible for the formation of the trail, then the removal of soil from the ridge is a geologically recent phenomenon and may not have yet affected erosion rates, depending on the response time of $P$ to changes in $H$.

The trends in Figures 5a and 5c suggest $P$ values on the active hillslope should monotonically increase with distance from the channel as soil thickness decreases. However, $P$ varies parabolically away from the channel (Fig. 6d), increasing from ~17 m My$^{-1}$ next to the channel to ~37 m My$^{-1}$ along the shoulderslope and backslope and then decreasing at the top to ~20 m My$^{-1}$. The main culprit disrupting the trend is SGA-1, and its exclusion produces a trend in $P$ vs. distance downslope that varies as expected. A remaining issue is the channel incision rate, which is high compared to the $P$ values of soil excavations adjacent to it, but comparable to $P$ in excavations 15 to 35 m from the ridge crest (Fig. 6d). We assumed no soil cover for the calculation of the channel incision rate, but if there was additional mass in the channel that is periodically removed, then the incision rate would be lower (Muzikar, 2008). Channel fill is not consistent with field observations, but the channel bedrock is fractured and, in contrast to the granular disintegration of the bedrock on the hillslope, appears to weather into cobble-size fragments. Spalling of a slab of channel bedrock 15 cm-thick would lower the calculated incision rate to ~25 m My$^{-1}$ which is more consistent with the erosion rates of excavations closest to the channel. Though $H$ and $P$ on the active hillslope are mutually adjusted, the pattern of $H$ and $P$ across the hillslope indicate the hillslope has recorded transient boundary conditions.

Values of *P* are slower on the stable hillslope than the active hillslope. They are nearly constant (averaging 10.7±1.5 m My$^{-1}$), except for the uppermost excavation (SGS-1: 13.23±0.34 m My$^{-1}$) (Fig. 6d). The consistency of *H* and *P* over the hillslope suggest that it may be in a relict steady state, adjusted to an incision rate of ~10 m My$^{-1}$, and the effect of the stable boundary condition has not propagated significantly upslope.

In summary, the soils and the rates of soil production from bedrock on the active hillslope have recorded variations in channel incision, whereas the stable hillslope may be eroding near steady state, but it is a steady state adjusted to a previous boundary condition, and the present stable boundary has yet to produce much of an effect.

## 5.2. Arid hillslopes

The arid hillslopes lie in the biotic-to-abiotic transition zone and have only sparse soil cover (generally ≤ 3 cm) and biota (Figs. 2c-d). The soil cover, where present, is dominated by coarse sand and fine gravels that abruptly overlie fractured bedrock (Fig. 7a). Road cuts in the area reveal bedrock joint systems extending at least 6 m deep (Fig. 7b). The bedrock shows almost no evidence of chemical weathering (only a few reddish rinds are detectable in thin section), but accumulations of gypsum and halite in microfractures are detectable with EDS (Fig. 7c). Vertical fractures in the near-surface bedrock are filled with fine, reddish-brown dust. The dust is loose in the fractures and does not form films on the rock fragment faces. Based on observations during a fog event, we hypothesize that the dust acts as a wick, transporting fog water and atmospherically-derived salt into the bedrock. Bedrock fragments extend vertically into the soil, but unlike the fractures a few cm deeper, the upper ends of these fragments are rounded and slightly chemically altered (Fig. 7d). This rounding may be due to granular disintegration driven by fog condensation and salt deposition on the surface. Thus, an important mechanism of bedrock erosion may be granular disintegration by chemical and salt-driven physical weathering. However, bioturbation may also contribute to rock fracturing, as described below.

Despite the arid climate, soil transport appears to be through bioturbation and overland flow. Vegetation covers 6% of the ground surface and is comprised of shrubs and cacti which subsist on fog water and tend to grow in convergent areas (Figs. 2b-c). Roots and root traces were found in dust-filled fractures across the hillslopes suggesting that over long timescales the bioturbative effect of vegetation is dispersed over the entire hillslope (Fig. 7d). Guanaco paths crisscross the hills, and this trampling dislodges bedrock fragments and mobilizes them downslope. Although burrowing lizards and insects are present in the region, they are found only on the plains surrounding the hills and not on the hills themselves due to the shallow soil cover. Small-scale surface gravel sorting on the hillslopes (Fig. 8) suggests that rare overland flow events may transport material downslope. In any case, the mechanisms transporting the soil are likely slope-dependent.

The hillslopes are located on an expansive pediplain grading to the Quebrada de Peralilla. About 1 km from the ocean, the Peralilla drops over a cliff formed by a fault in the Tegrillo fault system (Grocott and Taylor, 2002). The fault has created a knickpoint which has not propagated upchannel, isolating the study site from present day sea level (similar to the hanging valleys of Wobus et al., 2006). The pediplain is covered with a network of shallow (<1 m-deep) channels.

CRN concentrations in saprolite from excavations on the pediplain (samples CHS-06-PP in an interfluve, CHA-06-PP from the side of a shallow channel, and CHS-7 near the transition from the stable hillslope to the pediplain) give bedrock erosion rates from 0.63 to 2.5 m My$^{-1}$, with higher rates in the channels. $^{26}$Al/$^{10}$Be ratios in the pediplain samples are mostly below the erosion window (Fig. 9a), which is expected if the channels are sweeping across the pediplain and driving non-steady erosion.

Despite the overall erosion of the pediplain, hillslopes with differing boundary conditions were identified. The active hillslope is bounded by a bedrock-bedded channel with an incision rate of 3.7±0.1 m My$^{-1}$ (Figs. 2c, 3c), and the erosion appears to be near steady state, within error (Fig. 9a). The stable hillslope faces away from the Peralilla (upslope along the pediplain), and small channels split around the hillslope, leaving a non-eroding wedge at the base of the slope (Figs. 2d, 3d). A sample from an excavation in this wedge (CHS-7) had the lowest $P$ value calculated for the region (0.63±0.14 m My$^{-1}$). The $^{26}$Al/$^{10}$Be ratio of this sample is the second lowest and records a substantial decrease in erosion rate. Though this is not a perfect "stable" boundary, it should produce similar adjustments in hillslope soil thickness and the rate of soil production from bedrock (e.g., Fernandes and Dietrich, 1997).

The active hillslope is convexo-planar, whereas the stable hillslope is convexo-concave (Fig. 4g). Correspondingly, average $H$ is slightly thinner on the active hillslope (2 cm, n=40) compared to the stable one (4.6 cm, n=25). $H$ is almost constant on the active hillslope and the convexo-planar section of the stable hillslope, but increases in the concave section of the stable hillslope (Fig. 9b). Though $H$ is low, the difference in trends between the two hillslopes is significant and indicative of slope-dependent soil transport and boundary condition forcing.

Values of $P$ are negatively correlated with $H$ despite the limited range of $H$, with $P = 3.15e^{-0.136H}$ (r$^2$= 0.62) using data from both hillslopes (Fig. 9c). This $H$-dependence supports the hypothesis that bedrock erosion is driven by bioturbation and salt processes. The active hillslope has nearly constant $P$, with a slight decrease from 2.9±0.2 m My$^{-1}$ at the crest to 2.4±0.1 m My$^{-1}$ at the base, whereas $P$ values on the stable hillsllope decrease more, from 1.9±0.2 m My$^{-1}$ at the crest to 1.2±0.1 m My$^{-1}$ towards the pediplain (Fig. 9d). The incision rate of the channel bounding the active hillslope is 3.7±0.1 m My$^{-1}$, higher than the hillslope and suggesting that current incision rates have not been transmitted upslope. $^{26}$Al/$^{10}$Be ratios on both hillslopes are below the steady-state erosion window, though there is more scatter in the stable hillslope data (Fig. 9a) which is consistent the hypothesis that the active hillslope is more likely to be near steady state, while the stable hillslope should be progressively deviating from steady state. These ratios suggest erosion rates and/or soil thicknesses have not been constant, which is not surprising given 1) the nature of the bounding pediplain (where erosion rate varies between 0.87-2.5 m My$^{-1}$, samples CHS-PP and CHA-PP in Table 2) and 2) the likely loss of soil with aridification in the past (discussed below).

In summary, the active hillslope is close to being in equilibrium, though not with its present boundary, whereas the stable hillslope shows partial response to its boundary. Both have $P$ values substantially lower than the semiarid hillslopes. The low $^{26}$Al/$^{10}$Be ratios may record the stripping of the soil mantle at some point, possibly in response to increasing aridity.

### 5.3. Hyperarid hillslopes

The soils on the hyperarid hillslopes are similar to soils on the adjacent alluvial fans in that they have accumulated atmospherically-deposited salts and are completely free of vegetation.  Thus, hillslope processes are very different compared to the other sites.  The soils on the hillslopes are a mixture of gypsum, nitrate, halite, and fine silicate dust, plus bedrock fragments ranging from sand to cobble size (Figs. 10a-b).  The bedrock fragments are angular and lack evidence of chemical weathering.  Soils are comprised of a thin (~1-2 cm) surface layer of loose, fine-grained, silicate-rich material which is underlain by salt-rich, vesicular horizons with weak polygonal structure, which overlie increasingly salt-cemented, gravel-rich horizons (Figs. 10a-b).  Road cuts reveal deep (>4m) fracture systems that are permeated with gypsum and halite.  Determining the location of the soil-bedrock interface was a challenge, and while we considered the base of the horizon with polygonal structure development (above where rock fragment content exceeds 85%) as the relevant soil depth over geologic time, on the stable hillslope the depth to this contact varied substantially (often >20 cm).  The polygonal soil structure is likely developed through the shrinking and swelling of soil salts due to changes in soil moisture.  Across the stable hillslope, sand-filled cracks, tens of cm wide, penetrate to the soil-bedrock interface (Fig. 10b).  Though some cracking in northern Chile may be linked to earthquakes (Loveless et al., 2005), shrink-swell events are more likely causes because the material filling many of the cracks is layered, indicative of progressive crack opening and in-filling.  The wetting events driving soil shrink-swell must be extremely rare, given the preservation of salts in the soils.

Biotic processes are essentially absent (Figs. 2e-f), instead salt-driven processes and overland flow dominate.  Salt pries apart the rock using pre-existing fractures (Fig. 10c) and eventually "lifts" bedrock fragments into the soil column through salt growth and shrink-swell (due to hydration-dehydration and/or temperature oscillations).  Crystallization pressures of gypsum and halite have been modeled to be more than adequate to fracture rock (Winkler and Singer, 1972; Steiger, 2005), and many experimental studies support this (e.g. Rodrigues-Navarro and Doehne, 1999; Cardell et al., 2003; Viles and Goudie, 2007).  The polygonal soil structure indicates that salt shrink-swell is important in soil transport.  Transport by clay shrink-swell is slope-dependent (e.g. Fleming and Johnson, 1975), and, though no work has been done on salt-driven soil transport it is likely also slope-dependent.  Sorting of surface gravels into contour-parallel bands (Fig. 3f) suggest that discontinuous overland flow occurs during extremely rare precipitation events.  Thus, it is likely that soil transport is slope-dependent but in a more complicated way than on the other hillslopes.

The active hillslope is located in an internally-drained basin which has been disconnected from marine base level since about the Pliocene.  The incision rate of the channel bounding this hillslope is, therefore, controlled by climate, relict topography, and local base level.  The erosion rate of the channel bedrock is $1.7\pm0.5$ m My$^{-1}$.  In contrast, the stable hillslope is abutted by Miocene to Holocene alluvium accumulating in an internally-drained basin filled with salar deposits (Marinovic et al., 1992).  The length of the hillslopes differs significantly (Fig. 4h), such that the shorter hillslope should have a faster response to changes in boundary condition than the longer one.

On the active hillslope, $H$ increases slightly with distance downslope and averages 5.5 cm (n=43) (Fig. 11a). There are a few places on the hillslope where $H$ is greater, up to 24 cm, and these coincide with rare, hydrothermally-altered zones in the bedrock. Bedrock in these zones disintegrates into much finer pieces compared to the unaltered bedrock. On the stable hillslope, only seven soils could be excavated to the base of the soil due to the degree of salt cementation and their higher $H$ (average = 57 cm). The difference in $H$ between the hillslopes appears to be due to the different boundary conditions, but $P$ values suggest otherwise.

Values of $P$ are nearly uniform on the active hillslope, ranging from 0.84 to 1.2 m My$^{-1}$ (Table 2), with the fastest rate closest to the channel (Fig. 11b). The hillslope $P$ are slower than in the channel, but the channel erosion rate calculation may be high because field observations suggest that the channel is not consistently sediment-free. It may be slowly filled with material which is periodically excavated during the rare large storm events. If channel erosion is recalculated assuming ~50 cm of fill (based on a smoothed topographic map) most of the time, the revised rate is ~1.3 m My$^{-1}$ and is similar to hillslope erosion. The ranges of $P$ and $H$ are too narrow to determine a relationship between the two, and including data from the stable hillslope does not help. The $^{26}$Al/$^{10}$Be ratios plot in the steady state erosion window, within error (Fig. 11c), suggesting that the active hillslope is near steady-state despite the extremely slow rates of bedrock erosion and soil development.

Values of $P$ are lower on the stable hillslope, ranging from 0.18±0.11 to 1.5±1.5 m My$^{-1}$ (Fig. 11b, Table 2). The error for many of these samples is large, primarily due to difficulties in measuring $^{26}$Al/$^{27}$Al in the high-Al quartz. $^{10}$Be/$^{26}$Al ratios on the stable hillslope (average ~3.8) are lower than on the active hillslope and show more scatter (Fig. 11c). The $^{10}$Be/$^{26}$Al ratios of the hillslope bedrock likely indicate long-term burial by atmospherically-derived salt and dust coupled with very low (approaching zero) erosion rates. The retention of atmospheric inputs is increased by low soil flux on the gentler stable hillslope (gradient ranges from 0.13 to 0.36, vs. 0.34 to 0.65 on the active hillslope) (Fig. 4h). $P$ values calculated using present-day $H$ will be too high because burial increases the shielding of the bedrock from cosmic rays, decreasing CRN production rates. Present-day bedrock erosion on the stable hillslope may be near zero. Erosion rates are so low that hillslope morphology is essentially unchanged from pre-Miocene conditions and soil processes are responding to these paleofeatures, discussed further below.

Hillslope bedrock erosion was hypothesized to be $H$-dependent because the frequency of salt shrink-swell at the soil-bedrock interface likely decreases with increasing $H$. Our results suggest there is a soil thickness above which $P$ appreciably declines. However, equation 2 does not seem to apply, nor is there enough data to identify the soil thickness threshold. $H$ is a function of hillslope morphology (thicker on gentler slopes, thinner on steeper ones), suggesting soil transport is slope-dependent. $P$ values are a factor of 2 slower than on the arid hillslopes and a factor of 10 slower than on the semiarid hillslopes, indicating that precipitation is an important control.

## 6. Discussion

Our data reveal systematic changes in soil thickness and the rate of soil production from bedrock due to both boundary condition and climate. Below we discuss the relationship between soil thickness and climate, and how a legacy of climate change may or may not be recorded on

the hillslopes.  We then consider the co-evolution of $H$ and $P$, and find that the effects of climate and boundary condition are coupled.  Lastly, we compare our results with those from semiarid to humid hillslopes and identify a precipitation-dependent geomorphic threshold.

Though consistent differences in $H$ with hillslope boundary condition were observed, they were not as large as the variation with MAP (Table 1).  Average $H$ changes non-monotonically with MAP: it is thickest at the hyperarid and semiarid sites and nearly absent at the arid site (Table 1).  Soil production and erosion mechanisms change from biotically-driven to salt-driven with decreasing MAP, and this change has pronounced impacts on the soil mass balance.  Because the entire region has experienced increasing aridity for the last 2 to 9 Ma, the variation in $H$ along the precipitation gradient may mirror the development of the soil mantle on the currently hyperarid hillslopes.  On an alluvial fan near the hyperarid hillslope, root fragments are found deep in the soil and provide evidence of semiarid conditions prior to ~2 Ma (Ewing et al., 2006).  During this semiarid period, the hillslopes were likely mantled with chemically weathered soil and supported vegetation and burrowing animals, similar to the semiarid site.  The lack of any remnant chemically-altered soil or bedrock on the hillslopes today, despite the slow erosion rates, suggests that the landscape was stripped of this material prior to the onset of hyperarid conditions.  The removal of saprolite during aridification has been invoked as the formation mechanism of granitic boulder slopes in the Mojave Desert (Oberlander, 1972).  The resulting landscape is similar to the arid hillslopes today, which are so dry that bedrock erosion cannot sustain a soil mantle against soil erosion, but wet enough that salt cannot accumulate.  During the transition from semiarid to arid, vegetation loss would have destabilized the soil while decreased chemical weathering of the bedrock would have made bedrock erosion more difficult for the remaining biota.  This may have resulted in a system where soil erosion exceeded soil production such that the hillslope became weathering-limited and the soils were thin, if present at all.  Consistent with this theory, $^{26}Al/^{10}Be$ ratios in bedrock/saprolite samples are slightly low on the arid hillslopes, indicative of variations in $H$ and $P$.  $P$ values of 1.5-3.0 m $My^{-1}$ (equivalent to those on the arid hillslopes) would remove bedrock with a non-steady state CRN signature (the uppermost ~65 cm) in less than 1 My, so the variations in $H$ and $P$ at the arid site must have occurred during the last 0.5-1 My for this signal to be preserved.  As the climate further aridified, vegetation would have disappeared completely while salt would have begun to accumulate, eventually producing the current salt and gravel-rich soil mantle.  The changes in $P$ and $H$ appear to be recorded in the low $^{26}Al/^{10}Be$ ratios in the hyperarid hillslope bedrock.

One challenge in interpreting CRN-derived $P$ values is that, as a result of their different erosion rates, they integrate over different timescales (i.e., $P$ values at the semiarid hillslopes integrate over ~40 ky, whereas $P$ values at the hyperarid hillslopes integrate over >600 ky).  However, part of the appeal of the Atacama Desert precipitation transect used in this work is that it has been in place for several million years.  Though the soil production rates are calculated over different timescales, the differences between those timescales are expected to be small compared to the precipitation difference along the gradient.

The shift from thick and chemically-weathered soils, to nearly absent soils, to thick and salty soils with decreasing MAP occurs regardless of boundary condition and demonstrates the profound impact climate has on the development of soils.  It also suggests a positive correlation between MAP and $K$ (or similar transport coefficient), particularly since hillslope gradients are

similar on the active hillslopes. However, the similarity between the active hillslope $P$ values and the incision rates of their respective channels supports that channel incision is an important control on $P$ and the soil mass balance. If $P$ and $H$ on the active hillslopes were unable to respond to faster channel incision due to precipitation-limitations, we would expect topographic discontinuities (cliffs) at the hillslope-channel transition as evidence of geomorphic disequilibrium. Instead, the hillslopes transition smoothly to the channels. Channel incision rates are well below the regional uplift rate, even in the semiarid region, indicating they are not adjusted to current tectonic uplift. Instead, they increase with increasing MAP which suggests that their ability to adjust to marine base level is precipitation-limited.

Based on the observations above, hillslope soils and $P$ values are affected by MAP in multiple ways, through the processes acting on the hillslopes and through the incision rates of the adjacent channels. We have proposed that the active hillslopes are near steady state, having fairly constant $H$ and uniform lowering rates. If this is the case, the time required for a hillslope to respond to changes in boundary conditions can be estimated. As an approximation for the time required for a change in incision rate to affect $P$ values all the way up the adjacent hillslope (the response time, $T_R$), we assume soil flux can be expressed as $Q_s = -K \nabla z$, such that $T_R \approx X^2 K^{-1}$, where $X$ is the total length of the hillslope (Furbish and Fagherazzi, 2001). Using $K$ values calculated by J. Owen (unpublished data) for total soil loss, $T_R$ on the active hillslopes decreases with increasing MAP, from ~2.1 My (hyperarid, $X$=14m), to ~1.7 My (arid, $X$=19 m), to ~0.84 My (semiarid, $X$=50 m). Given that the most recent episode of aridification occurred ~2 Ma, these estimates suggest the arid and hyperarid active hillslopes could be near steady state. They also could explain the trend in $P$ values on the semiarid active hillslope (Fig. 6c). Because this hillslope has a relatively short $T_R$, it will be more sensitive to short-term variations in channel incision. The terracing along the Quebrada de Santa Gracia indicates that local incision rates have not been steady over the last ~0.3 My. Therefore, $P$ values on the active hillslope may reflect partial hillslope adjustment to various incision rates over the last ~0.8 My. Similarly, the semiarid and arid stable hillslopes show only partial adjustment to their boundary conditions. The hyperarid stable hillslope is ~10 times longer than the active hillslope and thus has a much longer response time. On the upper portions of the hillslope, $P$ and $H$ have not "felt" the onset of the stable boundary condition at the base. Instead, they are developing in response to the only slightly altered pre-Miocene morphology of the hillslope, and this is likely the case in most of the hyperarid core of the Atacama Desert. Thus, while boundary conditions cause differences in $H$ (for all the hillslopes) and $P$ (except for the hyperarid hillslopes), the degree and rate of hillslope response is precipitation-dependent.

In order to put our results in a global context, $P$ calculated using similar methods to ours (i.e. from samples of the soil-bedrock interface) on other non-landsliding, granitic hillslopes were compiled and plotted against MAP (Figure 12). Along the precipitation gradient in this study, $P$ increases with increasing MAP following a power law relationship, (for active hillslopes $P = 0.44(MAP)^{0.90}$, $r^2$=0.97, Fig. 12), and the variation between climatic regions is greater than variations within a climatic region (i.e. due to boundary condition). In contrast, for MAP>100 mm, there is no correlation between $P$ and MAP, and the variation at a given MAP varies by an order of magnitude. Our semiarid data plot within the variance of the data from more humid regions, but our arid and hyperarid data plot significantly below. The source of the variance in $P$ is generally attributed to variations in tectonic uplift, though bedrock characteristics and

temperature may also be important factors. Our results suggest that for semiarid and humid landscapes the effect of precipitation is trumped by the response of biotic hillslopes to boundary conditions. Biota plays the dual role of 1) loosening bedrock and dispersing soil downslope, and 2) stabilizing the soil (particularly plants) by holding it together by root strength, shielding it from raindrop impacts, and slowing overland flow. Biotic landscapes are typically transport-limited (Gilbert, 1877; Carson and Kirkby, 1972). Thus, the humid landscapes may record multiple factors effective over varying spatial and temporal scales and this produces large variability in $P$. The arid site in this study marks the transition from biotic to abiotic hillslope processes, where soils that are no longer supported by roots are stripped from the hillslope by trampling and rare overland flows. Meanwhile, $P$ lags in the absence of significant chemical weathering, such that the hillslopes are weathering (soil production)-limited (Gilbert, 1877; Carson and Kirkby, 1972). At the extreme, hyperarid channel incision and $P$ are controlled primarily by precipitation and perhaps slightly by relict topography. Though the thick soils on the hyperarid stable hillslope would suggest the landscape is transport-limited, they are not the result of soil production from bedrock out-pacing soil transport, as the term usually implies. Thus, it may be more useful to consider the landscape as precipitation-limited, a combination of transport-limited and production-limited. This demarcates a new geomorphic threshold: as MAP decreases, the hillslopes transition from transport-limited, to production-limited, to precipitation-limited.

The surprising discovery here is that increasing aridity, and concurrent decreases in biota, produce systematic and dramatic decreases in the rate of soil production from bedrock. There appears to be a threshold below which MAP is the dominant control on $P$ (precipitation-limited), and above which other factors (tectonic setting, biota, and/or chemical weathering) dominate.

## 7. Conclusions

This work provides the first evidence for precipitation-dependent hillslope soil production from bedrock and quantifies the effect of boundary condition on hillslope erosion rates. Counter to observations from more humid regions, the rate of soil production from bedrock decreases following a power law as precipitation decreases from semiarid to hyperarid, and this trend is observed regardless of boundary condition. At our study sites, geomorphic processes shift from relatively fast and biotically-driven in the semiarid south, to slow and abiotic (salt-driven) in the hyperarid north. Hyperarid hillslopes, with their exceedingly low soil production and soil erosion rates, approach (but do not reach) the role of passive accumulators of atmospheric input. Because the region receives occasional precipitation, soil thickness is still a function of hillslope gradient but rates of soil production from bedrock are largely independent of soil thickness.

The Atacama Desert provides a multi-million year-old experiment testing the effect of water and life on geophysical and geochemical processes. In contrast with portions of the planet where biota modulates soil production and erosion through complex and rapid feedbacks (Yoo et al., 2005), the absence of biota in the driest parts of the Atacama Desert results in the rates and mechanisms of geomorphic processes being extremely precipitation-sensitive. This unusual environment, for Earth, illuminates the uniqueness and complexity of a planet whose surface bears the indelible imprint of life.

30

**References**

Ahnert F.1970. Functional relationships between denudation, relief, and uplift in large, mid-latitude drainage basins. *American Journal of Science*, **268**: 243-263.

Ahnert F. 1987. Approaches to dynamic equilibrium in theoretical simulations of slope development. Earth Surface Processes and Landforms. *Earth Surface Processes and Landforms*, **12**: 3-15.

Alpers CN, Brimhall GH. 1988. Middle Miocene climatic change in the Atacama Desert, Northern Chile - Evidence from supergene mineralization at La Escondida. *Geological Society of America Bulletin* **100**: 1640-1656.

Amundson R, Ewing S, Michalski G, Thiemens M, Kendall C, Nishiizumi K, McKay C, Chong G. 2007. The climatic and biotic thresholds on soil elemental cycling along an arid to hyperarid rainfall gradient. *Geochimica et Cosmochimica Acta* **71:** A22-A22.

Anderson RS. 2002. Modeling the tor-dotted crests, bedrock edges, and parabolic profiles of high alpine surfaces of the Wind River Range, Wyoming. *Geomorphology* **46:** 35-58.

Anderson SP, Dietrich WE, Brimhall GH. 2002. Weathering profiles, mass-balance analysis, and rates of solute loss: Linkages between weathering and erosion in a small, steep catchment. *GSA Bulletin* **114**: 1143-1158.

Anderson RS, Humphrey NF. 1989. Interaction of weathering and transport processes in the evolution of arid landscapes. *Quantitative Dynamic Stratigraphy*: 349-361.

Armstrong AC. 1987. Slopes, boundary conditions, and the development of convexo-concave forms – some numerical experiments. *Earth Surface Processes and Landforms* **12**: 17-30.

Betancourt JL, Latorre C, Rech JA, Quade J, Rylander KA. 2000. A 22,000-year record of monsoonal precipitation from Northern Chile's Atacama Desert. *Science* **289:** 1542-1546.

Böhlke JK, Ericksen GE, Revesz K. 1997. Stable isotope evidence for an atmospheric origin of desert nitrate deposits in northern Chile and southern California, USA. *Chemical Geology* **136:** 135-152.

Braun J, Heimsath AM, Chappell J. 2001. Sediment transport mechanisms on soil-mantled hillslopes. *Geology* **29:** 683-686.

Cáceres L, Gómez-Silva B, Garró X, Rodríguez V, Monardes V, McKay CP. 2007. Relative

humidity patterns and fog water precipitation in the Atacama Desert and biological implications. *Journal of Geophysical Research* **112**: G04S14. doi:10.1029/2006JG000344.

Cardell C, Rivas T, Mosquera M, Birginie J, Moropoulou A, Prieto B, Silva B, Van Grieken R. 2003. Patterns of damage in igneous and sedimentary rocks under conditions simulating sea-salt weathering. *Earth Surface Processes and Landforms* **28:** 1-14.

Carson MA, Kirkby MJ. 1972. Hillslope Form and Process. University Press, Cambridge [Eng.].

Clarke JDA. 2006. Antiquity of aridity in the Chilean Atacama Desert. *Geomorphology* **73:** 101-114.

Coppus R, Imeson AC. 2002. Extreme events controlling erosion and sediment transport in a semi-arid sub-Andean valley. *Earth Surface Processes and Landforms* **27**: 1365–75.

Dahlgren RA, Boettinger JL, Huntington GL, Amundson RG. 1997. Soil development along an elevational transect in the western Sierra Nevada, California. *Geoderma* **78**, 207-236.

Dietrich WE, Reiss R, Hsu ML, Montgomery DR. 1995. A process-based model for colluvial soil depth and shallow landsliding using digital elevation data. *Hydrological Processes* **9**: 383-400.

Dietrich WE, Bellugi DG, Sklar LS, Stock JD, Heimsath AM, Roering JJ. 2003. Geomorphic transport laws for predicting landscape form and dynamics; Prediction in Geomorphology. *Geophysical Monograph* **135:** 103-132.

Dietrich WE, Perron, JT. 2006. The search for a topographic signature of life. *Nature* **439:** 411-418.

Dixon JL, Heimsath AM, Amundson R. 2009. The critical role of climate and saprolite weathering in landscape evolution. *Earth Surface Processes and Landforms*. DOI: 10.1002/esp.1836.

Dunai TJ, Gonzalez-Lopez GA, Juez-Larre J, Carrizo D. 2005. Preservation of (early) Miocence landscapes in the Atacama Desert, northern Chile. *Geochimica et Cosmochimica Acta* **69:** A161-A161.

Emparan C, Pineda G. 2000. La Serena – La Higuera. Region de Coquimbo. Servicio Nacional de Geología y Minería. Geologic map No. 18, 1:100,000, Santiago.

Encinas A, Hervé F, Villa-Martínez R, Nielsen SN, Finger KL, Peterson DE. 2006. Finding of a Holocene marine layer in Algarrobo (33º 22' S), central Chile. Implications for coastal uplift. *Revista Geologica de Chile* **33**: 339-345.

Ericksen GE. 1981. Geology and origin of the Chilean nitrate deposits. Geological Society

Professional Paper 1188. United States Government Printing Office: Washington.

Ewing S, Michalski G, Thiemens M, Quinn R, Macalady J, Kohl S, Wankel S, Kendall C, McKay CP, Amundson R. 2007. Rainfall limit of the N cycle on Earth. *Global Biogeochemical Cycles* **21**: GB3009.

Ewing SA, Sutter B, Owen JJ, Nishiizumi K, Sharp W, Cliff SS, Perry K, Dietrich WE, McKay CP, Amundson R. 2006. A threshold in soil formation at Earth's arid-hyperarid transition. *Geochimica et Cosmochimica Acta* **70**: 5293-5322.

Fernandes NF, Dietrich, WE. 1997. Hillslope evolution by diffusive processes: The timescale for equilibrium adjustments. *Water Resources Research* **33**: 1307-1318.

Fleming RW, Johnson AM. 1975. Rates of seasonal creep of silty clay soil. *The Quarterly Journal of Engineering Geology,* **8**: 1-29.

Furbish DJ. 2003. Using the dynamically coupled behavior of land-surface geometry and soil thickness in developing and testing hillslope evolution models. *Prediction in geomorphology*: 169-181.

Furbish DJ, Fagherazzi S. 2001. Stability of creeping soil and implications for hillslope evolution. *Water Resources Research* **37:** 2607-2618.

Gabet EJ, Reichman OJ, Seabloom EW. 2003. The effects of bioturbation on soil processes and sediment transport. *Annual Review of Earth and Planetary Sciences* **31**: 249-73.

Gilbert GK. 1877. Geology of the Henry Mountains (Utah), U.S. Geographical and Geological Survey of the Rocky Mountains Region, Washington, D.C.

Godoy E, Lara L. 1998. Hojas Chañaral y Diego de Almagro, Región de Atacama. Servicio Nacional de Geología y Minería, Geologic map of Chile No. 5-6, 1:100,000, Santiago.

Grocott J, Taylor GK. 2002. Magmatic arc fault systems, deformation partitioning and emplacement of granitic complexes in the Coastal Cordillera, north Chilean Andes (25º30'S to 27º00'S). *Journal of the Geological Society* **159:** 425-442.

Hartley AJ, Chong G. 2002. Late Pliocene age for the Atacama Desert: Implications for the desertification of western South America. *Geology* **30:** 43-46.

Hartley AJ, Chong G, Houston J, Mather AE. 2005. 150 million years of climatic stability: evidence from the Atacama Desert, northern Chile. *Journal of the Geological Society* **162:** 421-424.

Hebbeln D, Lamy F, Mohtadi M, Echtler H. 2007. Tracing the impact of glacial-interglacial climate variability on erosion of the southern Andes. *Geology* **35:** 131-134.

Heimsath AM, Chappell J, Dietrich WE, Nishiizumi K, Finkel RC. 2000. Soil production on a retreating escarpment in southeastern Australia. *Geology* **28**: 787-790.

Heimsath AM, Chappell J, Finkel RC, Fifield K, Alimanovic A. 2006. Escarpment erosion and landscape evolution in southeastern Australia. In Tectonics, Climate, and Landscape Evolution, Willett SD, Hovius N, Brandon MT, Fisher DM (eds). Geological Society of America Special Paper 398, Penrose Conference Series;173-190.

Heimsath AM, Chappell J, Hancock GR, Fink D, Fifield K. 2008. Eroding Australia: Slowly. *Geochemica Cosmochemica Acta* **72:** A363.

Heimsath AM, Dietrich WE, Nishiizumi K, Finkel RC. 1997. The soil production function and landscape equilibrium. *Nature* **388:** 358-361.

Heimsath AM, Dietrich WE, Nishiizumi K, Finkel RC. 1999. Cosmogenic nuclides, topography, and the spatial variation of soil depth. *Geomorphology* **27:** 151-172.

Heimsath AM, Dietrich WE, Nishiizumi K, Finkel RC. 2001. Stochastic processes of soil production and transport: Erosion rates, topographic variation and cosmogenic nuclides in the Oregon Coast Range. *Earth Surface Processes and Landforms* **26:** 531-552.

Heimsath AM, Furbish DJ, Dietrich WE. 2005. The illusion of diffusion: Field evidence for depth-dependent sediment transport. *Geology* **33:** 949-952.

Houston J. 2006. Variability of precipitation in the Atacama desert: Its causes and hydrological impact. *International Journal of Climatology* **26**, 2181-2198.

Jenny H. 1941. Factors of Soil Formation. McGraw-Hill Book Company, Inc.: New York.

Kalthoff N, Fiebig-Wittmaack M, Meissner C, Kohler M, Uriarte M, Bischoff-Gauss I, Gonzales E. 2006. The energy balance, evapo-transpiration and nocturnal dew deposition of an arid valley in the Andes. *Journal of Arid Environments* **65:** 420-443.

Kirkby MJ. 1967. Measurement and theory of soil creep. *Journal of Geology* **75**, 359-378.

Kirkby MJ. 1971. Hillslope process-response models based on the continuity equation. *Institute of British Geographers Special Publication* **3**: 15-30.

Kober F, Ivy-Ochs S, Schlunegger F, Baur H, Kubik PW, Wieler R. 2007. Denudation rates and a topography-driven rainfall threshold in northern Chile: Multiple cosmogenic nuclide data and sediment yield budgets. *Geomorphology* **83:** 97-120.

Kohl CP, Nishiizumi K. 1992. Chemical isolation of quartz for measurement of *in situ*-produced cosmogenic nuclides. *Geochimica et Cosmochimica Acta* **56:** 3583-3587.

Lal D. 1991. Cosmic-ray labeling of erosion surfaces – *in situ* nuclide production-rates and

erosion models. *Earth and Planetary Science Letters* **104:** 424-439.

Lal D, Arnold JR. 1985. Tracing quartz through the environment. *Proceedings of the Indian Academy of Science(Earth Planetary Science Section)* **94**: 1-5.

Lamy F, Klump J, Hebbeln D, Wefer G. 2000. Late Quaternary rapid climate change in northern Chile. *Terra Nova* **12:** 8-13.

Latorre C, Betancourt JL, Rylander KA, Quade J. 2002. Vegetation invasions into absolute desert: A 45 000 yr rodent midden record from the Calama-Salar de Atacama basins, northern Chile (lat 22º-24ºS). *Geological Society of America Bulletin* **114:** 349-366.

Latorre C, Betancourt JL, Rylander KA, Quade J, Matthei O. 2003. A vegetation history from the arid prepuna of northern Chile (22-23º S) over the last 13,500 years. *Palaeogeography, Palaeoclimatology, Palaeoecology* **194**: 223-246.

Le Roux JP, Gomez C, Venegas C, Fenner J, Middleton H, Marchant M, Buchbinder B, Frassinetti D, Marquardt C, Gregory-Wodzicki KM, Lavenu A. 2005. Neogene-Quaternary coastal and offshore sedimentation in north central Chile: Record of sea-level changes and implications for Andean tectonism. *Journal of South American Earth Sciences* **19**: 83-98. DOI:10.1016/j.jsames.2003.11.003

Le Roux JP, Olivares DM, Nielsen SN, Smith ND, Middleton H, Fenner J, Ishman SE. 2006. Bay sedimentation as controlled by regional crustal behavior, local tectonics and eustatic sea-level changes: Coquimbo Formation (Miocene-Pliocene), Bay of Tongoy, central Chile. *Sedimentary Geology* **184:** 133-153. DOI: 10.1016/j.sedgeo.2005.09.023.

Leonard EM, Wehmiller JF. 1992. Low uplift rates and terrace reoccupation inferred from mollusk aminostratigraphy, Coquimbo Bay area, Chile. *Quaternary Research* **38:** 246-259.

Loveless JP, Hoke GD, Allmendinger RW, Gonzalez G, Isacks BL, Carrizo DA. 2005. Pervasive cracking of the northern Chilean Coastal Cordillera: New evidence for forearc extension. *Geology* **33:** 973-976.

Marinovic, N.; Smoje, I.; Maksaev, V.; Hervé, M., Mpodozis, C. 1992. Hoja Aguas Blancas, Región de Antofagasta. Servicio Nacional de Geología y Minería, Geologic map of Chile No. 70, 1:100,000, Santiago.

Marquardt C, Lavenu A, Ortlieb L, Godoy E, Comte D. 2004. Coastal neotectonics in Southern Central Andes: uplift and deformation of marine terraces in Northern Chile (27º S). *Tectonophysics* **394**: 193-219.

McKay CP, Friedmann EI, Gomez-Silva B, Caceres-Villanueva L, Andersen DT, Landheim R. 2003. Temperature and moisture conditions for life in the extreme arid region of the Atacama Desert: Four years of observations including the El Niño of 1997-1998.

*Astrobiology* **3:** 393-406.

Michalski G, Böhlke J, Thiemens M. 2004. Long term atmospheric deposition as the source of nitrate and other salts in the Atacama Desert, Chile: New evidence from mass-independent oxygen isotopic compositions. *Geochimica et Cosmochimica Acta* **68:** 4023-4038.

Molnar P, Anderson RS, Anderson SP. 2007. Tectonics, fracturing of rock, and erosion. *Journal of Geophysical Research-Earth Surface* **112(F3)**.

Montgomery DR, Balco G, Willett SD. 2001. Climate, tectonics, and the morphology of the Andes. *Geology* **29:** 579-582.

Mortimer C. 1973. The Cenozoic history of the southern Atacama Desert, Chile. *Journal of the Geological Society of London* **129**: 505-526.

Mortimer C. 1980. Drainage evolution in the Atacama Desert of northern Chile. *Revista Geológica de Chile* **11**: 3-28.

Mostny G. 1972. Prehistoria de Chile. Editorial Universitaria: Santiago, Chile.

Mudd SM, Furbish DJ. 2004. Influence of chemical denudation on hillslope morphology. *Journal of Geophysical Research-Earth Surface* **109:** F02001.

Mudd SM, Furbish DJ. 2007. Responses of soil-mantled hillslopes to transient channel incision rates. *Journal of Geophysical Research-Earth Surface* **112:** F02S18.

Muzikar P. 2008. Cosmogenic nuclide concentrations in episodically eroding surfaces: Theoretical results. *Geomorphology* **97:** 407-413.

Navarro-Gonzalez R, Rainey F, Molina P, Bagaley D, Hollen B, de la Rosa J, Small A, Quinn R, Grunthaner F, Caceres L, Gomez-Silva B, McKay CP. 2003. Mars-like soils in the Atacama Desert, Chile, and the dry limit of microbial life. *Science* **302:** 1018-1021.

Nester PL. 2008. Basin and paleoclimate evolution of the Pampa del Tamargual forearc valley, Atacama Desert, Northern Chile. PhD thesis. Cornell University.

Nishiizumi K. 2003. Preparation of $^{26}$Al AMS standards. *Nuclear Instruments & Methods in Physics Research Section B* **B223-224**: 388-392.

Nishiizumi K, Caffee MW, Finkel RC, Brimhall G, Mote T. 2005. Remnants of a fossil alluvial fan landscape of Miocene age in the Atacama Desert of northern Chile using cosmogenic nuclide exposure age dating. *Earth and Planetary Science Letters* **237:** 499-507.

Nishiizumi K, Imamura M, Caffee MW, Southon JR, Finkel RC, McAninch J. 2007. Absolute calibration of $^{10}$Be AMS standards. *Nuclear Instruments & Methods in Physics Research*

*Section B* **258**: 403-413.

Nishiizumi K, Kohl CP, Arnold JR, Klein J, Fink D, Middleton R. 1991. Cosmic ray produced $^{10}$Be and $^{26}$Al in Antarctic rocks: exposure and erosion history. *Earth and Planetary Science Letters* **104**: 440-454.

Nishiizumi K, Winterer EL, Kohl CP, Klein J. 1989. Cosmic ray production rates of $^{10}$Be and $^{26}$Al in quartz from glacially polished rocks. *Journal of Geophysical Research* **94**: 17,907-17,915.

Oberlander TM. 1972. Morphogenesis of granitic boulder slopes in Mojave Desert, California. *Journal of Geology* **80**: 1-20.

Onda Y. 1992. Influence of water storage capacity in the regolith zone on hydrological characteristics, slope processes, and slope form. *Zeitschrift Fur Geomorphologie* **36:** 165-178.

Ortlieb L, Zazo C, Goy JL, Hillaire-Marcel C, Ghaleb B, Cournoyer L. 1996. Coastal deformation and sea-level changes in the northern Chile subduction area (23ºS) during the last 330 ky. *Quaternary Science Reviews* **15:** 819-831.

Ota Y, Miyauchi T, Paskoff R, Koba M. 1995. Plio-Quaternary marine terraces and their deformation along the Altos de Talinay, North-Central Chile. *Revista Geológica de Chile* **22:** 89-102.

Penck W. 1953. Morphological analysis of land forms. Czech H, Boswell KC (trans). Macmillan: London.

Pérez Valdivia CA. 2005. Cambio climático: Vulnerabilidad, adaptación y rol institucional. Estudio de casos en el Valle de Elqui. PhD thesis, Universidad de La Serena, Chile.

Placzek C, Matmon A, Granger D, Quade J, Caffee MW. 2007. Erosion rates in the Atacama Desert, northern Chile (~24ºS) from multiple cosmogeic nuclides. *Geological Society of America, Abstracts with Programs* **39:** 513.

Quezada J, Gonzalez G, Dunai T, Jensen A, Juez-Larre J. 2007. Pleistocene littoral uplift of northern Chile: Ne-21 age of the upper marine terrace of Caldera-Bahia Inglesa area. *Revista Geologica de Chile* **34**: 81-96.

Ravelo AC, Andreasen DH, Lyle M, Lyle AO, Wara MW. 2004. Regional climate shifts caused by gradual global cooling in the Pliocene epoch. *Nature* **429:** 263-267.

Rech J, Quade J, Hart W. 2003. Isotopic evidence for the source of Ca and S in soil gypsum, anhydrite and calcite in the Atacama Desert, Chile. *Geochimica et Cosmochimica Acta* **67:** 575-586.

Riebe CS, Kirchner JW, Finkel RC. 2004a. Erosional and climatic effects on long-term chemical weathering rates in granitic landscapes spanning diverse climate regimes. *Earth and Planetary Science Letters* **224:** 547-562.

Riebe CS, Kirchner JW, Finkel RC. 2004b. Sharp decrease in long-term chemical weathering rates along an altitudinal transect. *Earth and Planetary Science Letters* **218:** 421-434.

Riebe CS, Kirchner JW, Granger DE, Finkel RC. 2001. Strong tectonic and weak climatic control of long-term chemical weathering rates. *Geology* **29:** 511-514.

Rodriguez-Navarro C, Doehne E. 1999. Salt weathering: Influence of evaporation rate, supersaturation and crystallization pattern. *Earth Surface Processes and Landforms* **24:** 191-209.

Roering JJ. 2008. How well can hillslope evolution models "explain" topography? Simulating soil transport and production with high-resolution topographic data. *Geological Society of America Bulletin* **120:** 1248-1262.

Roering JJ, Kirchner JW, Dietrich WE. 1999. Evidence for nonlinear, diffusive sediment transport on hillslopes and implications for landscape morphology. *Water Resources Research* **35:** 853-870.

Rundel PW, Dillon MO, Palma B, Mooney HA, Gulmon SL, Ehleringer JR. 1991. The phytogeography and ecology of the coastal Atacama and Peruvian deserts. *Aliso* **13**: 1-49.

Rundel PW, Dillon MO, Palma P. 1996. Flora and vegetation of Pan de Azucar National Park in the Atacama Desert of northern Chile. *Gayana Botánica* **53**: 295-315.

Saillard M, Hall SR, Audin L, Farber DL, Herail G, Martinod J, Regard V, Finkel RC, Bondoux F. 2009. Non-steady long-term uplift rates and Pleistocene marine terrace development along the Andean margin of Chile (31ºS) inferred from Be-10 dating. *Earth and Planetary Science Letters* **277:** 50-63.

Schoenenberger PJ, Wysocki DA, Benham EC, Broderson WD. 2002. Field book for describing and sampling soils. Natural Resources Conservation Service, National Soil Survey Center: Lincoln, NE.

Selby MJ. 1980. A rock mass strength classification for geomorphic purposes: with tests from Antarctica and New Zealand. *Zeitschrift für Geomorphologie* **24**: 31-51.

Sillitoe RH, McKee EH. 1996. Age of supergene oxidation and enrichment in the Chilean porphyry copper province. *Economic Geology and the Bulletin of the Society of Economic Geologists* **91**: 164-179.

Small EE, Anderson RS, Hancock GS. 1999. Estimates of the rate of regolith production using [10]Be and [26]Al from an alpine hillslope. *Geomorphology* **27**: 131-150.

Squeo FA, Aravena R, Aguirre E, Pollastri A, Jorquera CB, Ehleringer JR. 2006. Groundwater dynamics in a coastal aquifer in north-central Chile: Implications for groundwater recharge in an arid ecosystem. *Journal of Arid Environments* **67:** 240-254.

Steiger M. 2005. Crystal growth in porous materials - I: The crystallization pressure of large crystals. *Journal of Crystal Growth* **282:** 455-469.

Vargas G, Rutllant J, Ortlieb L. 2006. ENSO tropical-extratropical climate teleconnections and mechanisms for Holocene debris flows along the hyperarid coast of western South America (17º-24º S). *Earth and Planetary Science Letters* **249:** 467-483.

Viles H, Goudie A. 2007. Rapid salt weathering in the coastal Namib Desert: Implications for landscape development. *Geomorphology* **85:** 49-62.

von Blanckenburg F. 2006. The control mechanisms of erosion and weathering at basin scale from cosmogenic nuclides in river sediment. *Earth and Planetary Science Letters* **242:** 223-239.

Warren-Rhodes K, Rhodes K, Pointing S, Ewing S, Lacap D, Gomez-Silva B, Amundson R, Friedmann E, McKay C. 2006. Hypolithic cyanobacteria, dry limit of photosynthesis, and microbial ecology in the hyperarid Atacama Desert. *Microbial Ecology* **52:** 389-398.

Wheeler JC. 1995. Evolution and present situation of the South-American *Camelidae. Biological Journal of the Linnean Society* **54:** 271-295.

Wilkinson MT, Humphreys GS. 2005. Exploring pedogenesis via nuclide-based soil production rates and OSL-based bioturbation rates. *Australian Journal of Soil Research* **43:** 767-779.

Winkler E, Singer P. 1972. Crystallization pressure of salts in stone and concrete. *Geological Society of America Bulletin* **83:** 3509-3513.

Wobus CW, Crosby BT, Whipple KX. 2006. Hanging valleys in fluvial systems: Controls on occurrence and implications for landscape evolution. *Journal of Geophysical Research-Earth Surface*: **111(F2)**.

Worldclimate.com, accessed Nov. 18, 2009.

Yoo K, Amundson R, Heimsath AM, Dietrich WE. 2005. Process-based model linking pocket gopher (*Thomomys bottae*) activity to sediment transport and soil thickness. *Geology* **33:** 917-920.

Yoo K, Amundson R, Heimsath AM, Dietrich WE, Brimhall GH. 2007. Integration of geochemical mass balance with sediment transport to calculate rates of soil chemical weathering and transport on hillslopes. *Journal of Geophysical Research-Earth Surface*: **112(F2)**.

**Table 1.** Summary of hillslope boundary conditions, soil thicknesses, and denudation rates.

| | Semiarid | Arid | Hyperarid |
|---|---|---|---|
| MAP (mm y$^{-1}$)[a] | 119 | 9.5 | <2 |
| MAT (ºC) (average, range)[b] | 13.5, 21-8 | 16, 27-11 | 17, 32-0 |
| plant density (% area) | 32 | 6 | 0 |
| bedrock | monzogranite | monzogranite | granodiorite |
| incision rate of active boundary (m My$^{-1}$) | 34 ± 1.7 | 3.7 ± 0.1 | 1.7 ± 0.5 |
| age of stable boundary surface (My) | 0.25 ± 0.11 | 0.63 ± 0.14[c] | Pliocene- Holocene |
| average slope-normal soil thickness (cm) (active/stable) | 14.6 ± 6.7 / 23.2 ± 6.4 | 2.0 ± 3.4 / 4.6 ± 4.6 | 5.5 ± 3.5 / 76 ± 22 |
| average rate of soil production from bedrock (m My$^{-1}$) (active/stable) | 26 ± 7.2 / 10 ± 1.7 | 2.6 ± 0.2 / 1.5 ± 0.4 | 0.95 ± 0.10 / 0.65 ± 0.51 |
| geomorphic processes | bioturbation, chemical weathering | bioturbation, salt shrink-swell | salt shrink-swell |

[a]Semiarid and arid MAP data from Worldclimate (2009), hyperarid MAP from McKay et al. (2003) which is in general agreement with the Worldclimate (2009) data for Antofagasta, the nearest town.
[b]MAT data from Squeo et al. (2006), Rundel et al. (1996), and McKay et al. (2003), for the semiarid, arid, and hyperarid sites, respectively.
[c] Arid stable boundary condition is given as the erosion rate of the pediplain adjacent to the stable hillslope (m My$^{-1}$).

**Table 2.** Summary of CRN measurements and topographic data. [10]Be and [26]Al errors account for AMS analysis and do not include the uncertainty of the production rates or half lives of the CRN. Erosion rates were calculated assuming rock density = 2.5 g cm$^{-3}$ and saprolite density = 1.5 g cm$^{-3}$. *For SGS-Q, the values are minimum exposure ages in ky, rather than erosion rates. NA = not available or not applicable.

| sample ID | sample type | distance downslope (m) | CRN sample depth (cm) | slope-normal soil thickness (cm) | soil bulk density (g cm$^{-3}$) | slope | [10]Be (atom g$^{-1}$) | +/- | [26]Al (atom g$^{-1}$) | +/- | [26]Al/[10]Be | +/- | [10]Be erosion rate (m My$^{-1}$) | [26]Al erosion rate (m My$^{-1}$) | average erosion rate (m My$^{-1}$) | +/- |
|---|---|---|---|---|---|---|---|---|---|---|---|---|---|---|---|---|
| *Hyperarid Active (24.13°S, 69.99°W, 1170 masl)* | | | | | | | | | | | | | | | | |
| YH-05-16c | hillslope bedrock | 0 | 4.5 | 4.2 | 0.80 | 0.40 | 4.64E+06 | 2.10E+05 | 2.50E+07 | 1.33E+06 | 5.39 | 0.38 | 0.95 | 0.95 | 0.95 | 0.05 |
| YH-17-4 | hillslope bedrock | 2.5 | 5 | 4.7 | 0.81 | 0.34 | 5.14E+06 | 6.30E+04 | 2.67E+07 | 7.70E+05 | 5.19 | 0.16 | 0.83 | 0.85 | 0.84 | 0.02 |
| YH-18-4 | hillslope bedrock | 5.0 | 24 | 21.6 | 0.81 | 0.49 | 4.78E+06 | 8.23E+04 | 2.46E+07 | 7.77E+05 | 5.14 | 0.19 | 0.91 | 0.97 | 0.94 | 0.04 |
| YH-19-C | hillslope bedrock | 8.8 | 9 | 7.6 | 0.60 | 0.62 | 4.63E+06 | 5.79E+04 | 2.61E+07 | 9.15E+05 | 5.64 | 0.21 | 0.95 | 0.88 | 0.91 | 0.05 |
| YH-20-C | hillslope bedrock | 12.2 | 7 | 5.9 | 0.79 | 0.65 | 4.11E+06 | 6.90E+04 | 2.17E+07 | 6.35E+05 | 5.28 | 0.18 | 1.1 | 1.2 | 1.1 | 0.1 |
| YH-05-44b | channel bedrock | 14.6 | 0 | 0 | NA | NA | 3.57E+06 | 8.85E+04 | 1.47E+07 | 8.93E+05 | 4.11 | 0.27 | 1.3 | 2.1 | 1.7 | 0.5 |
| *Hyperarid Stable (24.13°S, 69.99°W, 1170 masl)* | | | | | | | | | | | | | | | | |
| ORH-06-4 | hillslope bedrock | 21.6 | 36 | 35.6 | 2.17 | 0.14 | 1.14E+07 | 1.97E+05 | 5.59E+07 | 2.67E+06 | 4.92 | 0.25 | 0.29 | 0.20 | 0.25 | 0.06 |
| ORH-06-3 | hillslope bedrock | 34.9 | 57 | 56.5 | 2.32 | 0.13 | 1.20E+07 | 5.09E+05 | 6.31E+07 | 7.80E+06 | 5.27 | 0.69 | 0.26 | 0.10 | 0.18 | 0.11 |
| ORH-06-13 | hillslope bedrock | 44.9 | 70 | 68.2 | 1.04 | 0.23 | 9.73E+06 | 3.98E+05 | 3.67E+07 | 2.63E+06 | 3.77 | 0.31 | 0.39 | 0.65 | 0.52 | 0.18 |
| ORH-2-4 | hillslope bedrock | 54.7 | 9 | 8.7 | 0.55 | 0.27 | 7.15E+06 | 8.19E+04 | 2.21E+07 | 9.62E+05 | 3.10 | 0.14 | 0.66 | 1.5 | 1.1 | 0.6 |
| ORH-06-18 | hillslope bedrock | 65.6 | 75 | 71.7 | 0.55 | 0.31 | 1.05E+07 | 3.67E+05 | 3.95E+07 | 4.48E+06 | 3.76 | 0.45 | 0.34 | 0.55 | 0.44 | 0.15 |
| ORH-1-5 | hillslope bedrock | 87.7 | 57 | 53.6 | 1.08 | 0.36 | 9.33E+06 | 2.18E+05 | 1.49E+07 | 1.22E+06 | 1.59 | 0.14 | 0.42 | 2.5 | 1.5 | 1.5 |
| ORH-06DC9 | hillslope bedrock | 98.3 | 85 | NA | 1.24 | NA | 1.06E+07 | 3.34E+05 | 3.07E+07 | 4.32E+06 | 2.89 | 0.42 | 0.32 | 0.87 | 0.60 | 0.39 |
| ORH-05-RC | hillslope bedrock | 129.2 | 80 | NA | 1.22 | NA | 1.27E+07 | 3.10E+05 | 5.69E+07 | 2.02E+06 | 4.50 | 0.19 | 0.22 | 0.17 | 0.19 | 0.03 |
| *Arid Active (26.28°S, 70.49°W, 687 masl)* | | | | | | | | | | | | | | | | |
| CH-1 | hillslope bedrock | 0 | 2.5 | 2.4 | 1.32 | 0.21 | 1.44E+06 | 3.40E+04 | 8.01E+06 | 3.11E+05 | 5.57 | 0.25 | 2.7 | 3.0 | 2.9 | 0.2 |
| CH-2 | hillslope bedrock | 2.3 | 2 | 1.9 | 1.20 | 0.40 | 1.38E+06 | 3.25E+04 | 7.72E+06 | 3.60E+05 | 5.61 | 0.29 | 2.9 | 3.1 | 3.0 | 0.2 |
| CH-3 | hillslope bedrock | 6.3 | 2 | 1.8 | 1.15 | 0.51 | 1.37E+06 | 3.29E+04 | 7.73E+06 | 2.76E+05 | 5.63 | 0.24 | 2.9 | 3.1 | 3.0 | 0.2 |
| CH-4 | hillslope bedrock | 10.7 | 4 | 3.6 | 1.16 | 0.51 | 1.56E+06 | 4.47E+04 | 8.98E+06 | 5.11E+05 | 5.76 | 0.37 | 2.4 | 2.6 | 2.5 | 0.1 |
| CH-5 | hillslope bedrock | 14.3 | 2 | 1.7 | 1.07 | 0.67 | 1.65E+06 | 4.63E+04 | 9.10E+06 | 3.18E+05 | 5.53 | 0.25 | 2.3 | 2.6 | 2.4 | 0.2 |
| CH-6 | hillslope bedrock | 17.3 | 3.5 | 3.1 | 1.42 | 0.53 | 1.59E+06 | 7.30E+04 | 9.29E+06 | 4.70E+05 | 5.85 | 0.40 | 2.4 | 2.5 | 2.4 | 0.1 |
| CH-7 | channel bedrock | 19.1 | 0 | 0 | NA | NA | 1.10E+06 | 2.79E+04 | 6.61E+06 | 3.39E+05 | 6.00 | 0.34 | 3.6 | 3.8 | 3.7 | 0.1 |
| *Arid Stable (26.28°S, 70.49°W, 670 masl)* | | | | | | | | | | | | | | | | |
| CHS-1 | hillslope bedrock | 0 | 2 | 1.9 | 1.96 | 0.27 | 2.00E+06 | 4.53E+04 | 1.08E+07 | 4.48E+05 | 5.39 | 0.26 | 1.8 | 2.0 | 1.9 | 0.1 |
| CHS-2 | hillslope bedrock | 3.1 | 3.5 | 3.3 | 1.26 | 0.36 | 1.99E+06 | 4.62E+04 | 9.69E+06 | 2.87E+05 | 4.88 | 0.18 | 1.9 | 2.3 | 2.1 | 0.3 |
| CHS-3 | hillslope bedrock | 6.4 | 2.5 | 2.4 | 1.19 | 0.31 | 2.00E+06 | 4.90E+04 | 1.18E+07 | 3.53E+05 | 5.89 | 0.23 | 1.8 | 1.8 | 1.8 | 0.0 |
| CHS-4 | hillslope bedrock | 11.6 | 3 | 2.8 | 1.19 | 0.36 | 2.99E+06 | 5.84E+04 | 1.33E+07 | 4.32E+05 | 4.45 | 0.17 | 1.1 | 1.5 | 1.3 | 0.3 |
| CHS-5 | hillslope bedrock | 19.8 | 4 | 3.9 | 1.06 | 0.25 | 3.06E+06 | 8.56E+04 | 1.55E+07 | 4.57E+05 | 5.06 | 0.21 | 1.1 | 1.2 | 1.1 | 0.1 |
| CHS-06-7 | low erosion surface | 35.3 | 11 | 10.9 | 1.5 | 0.11 | 4.98E+06 | 8.47E+04 | 2.10E+07 | 1.06E+06 | 4.21 | 0.22 | 0.53 | 0.73 | 0.63 | 0.14 |
| CHA-PP | pediplain channel | NA | 11 | NA | 0 | NA | 2.09E+06 | 8.47E+04 | 6.90E+06 | 4.23E+05 | 3.30 | 0.24 | 1.7 | 3.4 | 2.5 | 1.2 |
| CHS-PP | pediplain interfluve | NA | 44 | NA | 0 | NA | 3.39E+06 | 1.01E+05 | 1.97E+07 | 1.05E+06 | 5.80 | 0.35 | 0.93 | 0.81 | 0.87 | 0.09 |

**Table 2 continued.**

| sample ID | sample type | distance downslope (m) | CRN sample depth (cm) | slope-normal soil thickness (cm) | soil bulk density (g cm⁻³) | slope | $^{10}$Be (atom g⁻¹) | +/- | $^{26}$Al (atom g⁻¹) | +/- | $^{26}$Al/$^{10}$Be | +/- | $^{10}$Be erosion rate (m My⁻¹) | $^{26}$Al erosion rate (m My⁻¹) | average erosion rate (m My⁻¹) | +/- |
|---|---|---|---|---|---|---|---|---|---|---|---|---|---|---|---|---|
| *Semiarid Active (29.77°S, 71.08°W, 377 masl)* | | | | | | | | | | | | | | | | |
| SGA-1 | hillslope saprolite | 7.7 | 7 | 6.7 | 1.35 | 0.29 | 2.74E+05 | 6.59E+03 | 2.04E+06 | 1.68E+05 | 7.45 | 0.64 | 23 | 18 | 20 | 1.7 |
| SGA-2 | hillslope saprolite | 15.4 | 10 | 9.4 | 1.70 | 0.36 | 1.79E+05 | 5.00E+03 | 1.30E+06 | 8.10E+04 | 7.25 | 0.50 | 35 | 32 | 33 | 2.3 |
| SGA-3 | hillslope saprolite | 25.4 | 15 | 13.8 | 1.50 | 0.42 | 1.96E+05 | 5.48E+03 | 1.10E+06 | 7.29E+04 | 5.61 | 0.40 | 32 | 37 | 35 | 2.7 |
| SGA-4 | hillslope saprolite | 33.2 | 14 | 13.0 | 1.40 | 0.40 | 1.72E+05 | 4.66E+03 | 1.22E+06 | 5.74E+04 | 7.08 | 0.39 | 36 | 34 | 35 | 1.9 |
| SGA-06-28 | hillslope saprolite | 38.2 | 22 | 20.3 | 1.50 | 0.41 | 2.54E+05 | 1.29E+04 | 1.28E+06 | 9.98E+04 | 5.04 | 0.47 | 24 | 32 | 28 | 5.3 |
| SGA-06-17 | hillslope saprolite | 44.4 | 17 | 15.9 | 1.51 | 0.38 | 2.94E+05 | 2.06E+04 | 1.75E+06 | 1.15E+05 | 5.95 | 0.57 | 21 | 23 | 22 | 1.5 |
| SGA-06-16 | hillslope saprolite | 49.6 | 24 | 22.2 | 1.49 | 0.41 | 3.64E+05 | 2.04E+04 | 2.27E+06 | 1.55E+05 | 6.25 | 0.55 | 17 | 17 | 17 | 0.8 |
| SGA-5 | hillslope saprolite | 50.2 | 30 | 27.0 | 1.38 | 0.48 | 3.45E+05 | 9.02E+03 | 2.36E+06 | 2.16E+05 | 6.84 | 0.65 | 18 | 17 | 17 | 1.7 |
| SGA05-14b | channel bedrock | 59.2 | 0 | 0 | NA | N/A | 1.13E+05 | 8.09E+03 | 7.08E+05 | 4.67E+04 | 6.24 | 0.61 | 33 | 35 | 34 | 1.7 |
| *Semiarid Stable (29.78°S, 71.08°W, 400 masl)* | | | | | | | | | | | | | | | | |
| SGS-1 | hillslope saprolite | 12 | 37 | 36.6 | 1.43 | 0.15 | 4.69E+05 | 1.18E+04 | 2.97E+06 | 2.43E+05 | 6.33 | 0.00 | 13 | 13 | 13 | 0.3 |
| SGS-2 | hillslope saprolite | 22.9 | 15 | 14.7 | 1.49 | 0.21 | 5.56E+05 | 1.62E+04 | 3.88E+06 | 2.57E+05 | 6.98 | 0.00 | 11 | 9.9 | 10 | 0.3 |
| SGS-3 | hillslope saprolite | 36.8 | 22 | 21.4 | 1.38 | 0.23 | 6.73E+05 | 2.46E+04 | 3.64E+06 | 2.42E+05 | 5.40 | 0.41 | 8.9 | 11 | 9.8 | 1.2 |
| SGS-22b | hillslope saprolite | 48.3 | 25 | 24.6 | 1.46 | 0.18 | 6.48E+05 | 1.73E+04 | 3.61E+06 | 2.25E+05 | 5.56 | 0.38 | 9.3 | 11 | 10 | 1.0 |
| SGS-21 | hillslope saprolite | 70.5 | 25 | 24.6 | 1.46 | 0.18 | 6.28E+05 | 1.57E+04 | 3.82E+06 | 3.14E+05 | 6.09 | 0.52 | 9.6 | 10 | 9.8 | 0.3 |
| SGS-Q | non-eroding surface | >100 | 0 | 0 | NA | 0.09 | 1.59E+06 | 3.33E+04 | 5.22E+06 | 2.33E+05 | 3.29 | 0.16 | 300* | 150* | 220* | 110* |

**Figure 1.** A diagram of a hillslope soil profile showing inputs and outputs as described in equation 1. Soil production from bedrock can be calculated using cosmogenic radionuclides if the soil is at steady state (i.e. production from bedrock and soil mass have been constant).
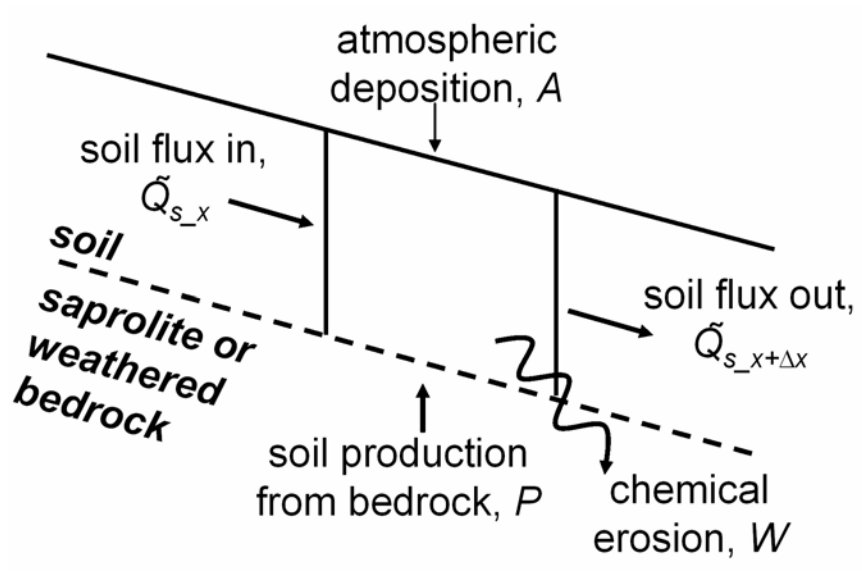
**Figure 2.** (a) A shaded relief map showing site locations (created with GeoMapApp v.1.7.8). Only in the hyperarid region were the two hillslopes sufficiently apart (~70 km) to necessitate separate markers on the map. (b) Average mean annual precipitation (MAP) increases with longitude (Worldclimate.com). (c) Plant density (measured in this study) follows MAP and increases with longitude. (d) Coastal uplift rates have been uniform across the study area in the Holocene. Uplift data compiled from Leonard and Wehmiller (1992), Ota et al. (1995), Ortlieb et al. (1996), Marquardt et al. (2004), Le Roux et al. (2005, 2006), Encinas et al. (2006), Quezada et al. (2007), and Saillard et al. (2009).

45
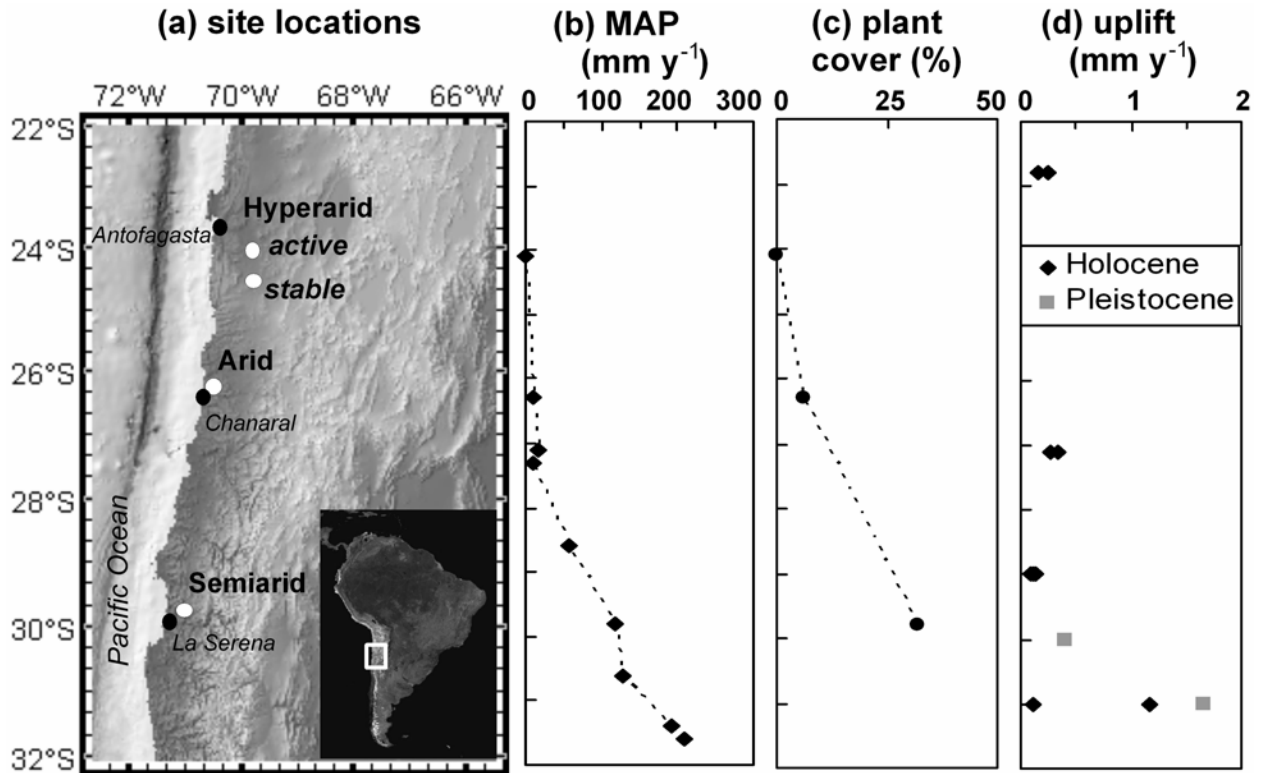
**Figure 3.** A pair of hillslopes with contrasting boundary conditions (actively incising channel vs. non-eroding landform) was studied within each climate zone (semiarid, arid, and hyperarid). (a) The semiarid active hillslope, looking up-transect from the channel. (b) The semiarid stable hillslope viewed from the bounding terrace. The arid active (c) and stable (d) hillslopes, looking up-transect. The hyperarid active (e) and stable (f) hillslopes, looking up-transect.



45
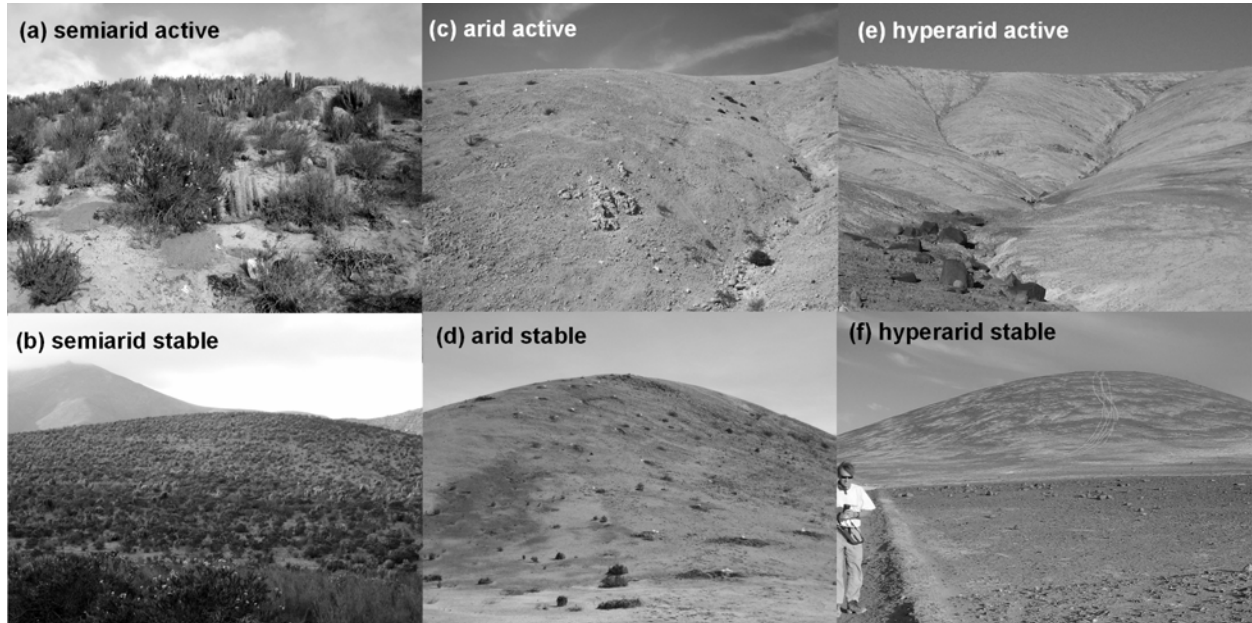
**Figure 4.** Topographic maps of the semiarid (a), arid active (b), arid stable (c), hyperarid active (d), and hyperarid stable (e) hillslopes showing the locations of the sampled soil excavations. Each map has a different scale, but the contour interval is always 1 m. The differences in local relief, hillslope length, and slope between the hillslopes are clearer in elevation profiles of the semiarid (f), arid (g), and hyperarid (h) hillslopes. Squares mark the sampled excavations. The elevations in (f), (g), and (h) were normalized by subtracting the elevation of the boundary condition (i.e., channel or terrace) from the actual surface elevation.
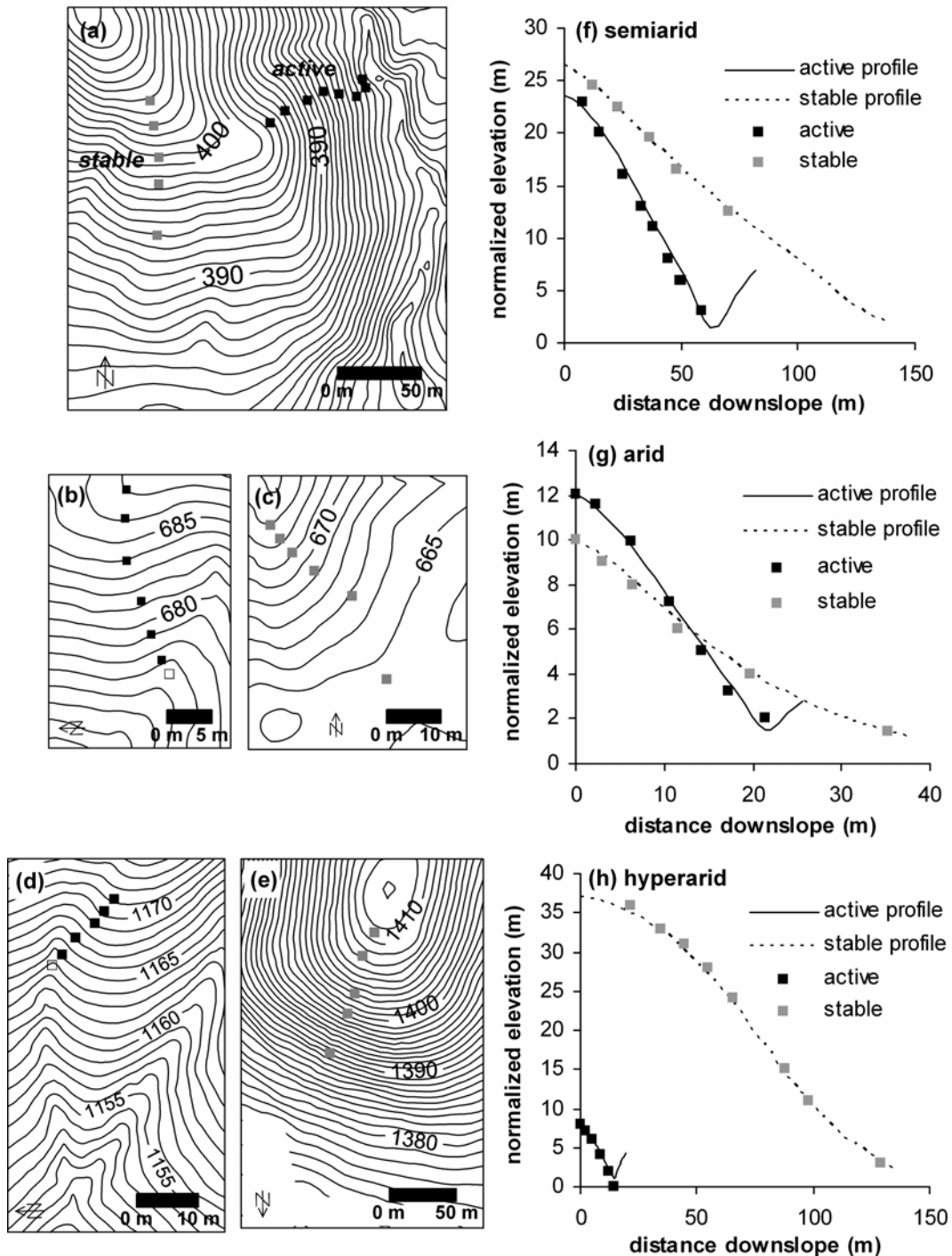
**Figure 5.** A soil profile on the semiarid active hillslope. Bioturbation is apparent in roots, root traces, and burrows extending to the soil-saprolite boundary, which are the main processes converting the saprolite into soil. The dashed white line marks the approximate boundary between the soil and saprolite. Note that the saprolite is not considered part of the soil because it has not been physically transported.
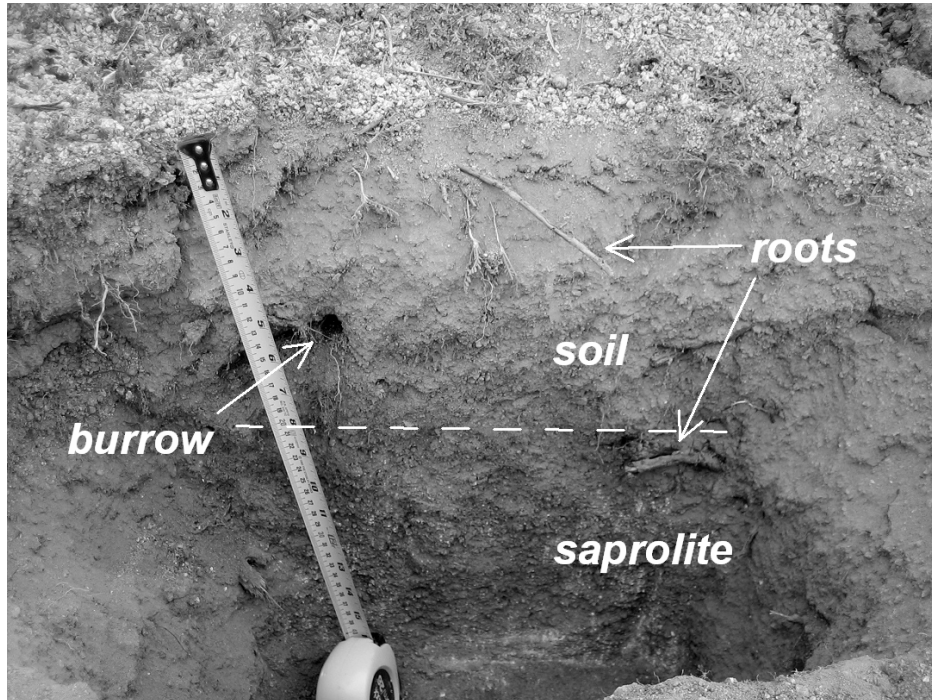
**Figure 6.** Semiarid hillslopes data. Error bars are AMS analytical error. (a) Cosmogenic radionuclide data from both the active and stable hillslope plot on the far left of the diagram, indicating that the exposure time has been short and the soil production rates derived from this data are minimum values. Several points plot in the "impossible zone", but are not far from the erosion window if we consider the additional uncertainty inherent in the production rates. Data plotting below the erosion window have experienced a complex exposure history including changes in the overlying soil thickness or the rate of soil production from bedrock. The sample from the terrace adjacent to the stable hillslope is an amalgamated sample of several gravels, which have experienced a complex exposure history. (b) Slope-normal soil thickness increases with distance downslope on the active hillslope but is essentially constant on the stable hillslope. Soil thickness is greater on the stable hillslope than active hillslope. (c) The rate of soil production from bedrock on the semiarid hillslopes is correlated to slope-normal soil thickness. If all data points except SGA-1 (circled in grey) are considered, $P = 40.07e^{-0.0402H}$ with $r^2=0.34$. SGA-1 is excluded due to geologically recent disturbance to the soil thickness. (d) The rate of soil production from bedrock varies parabolically with distance downslope on the active hillslope but is nearly constant on the stable hillslope.
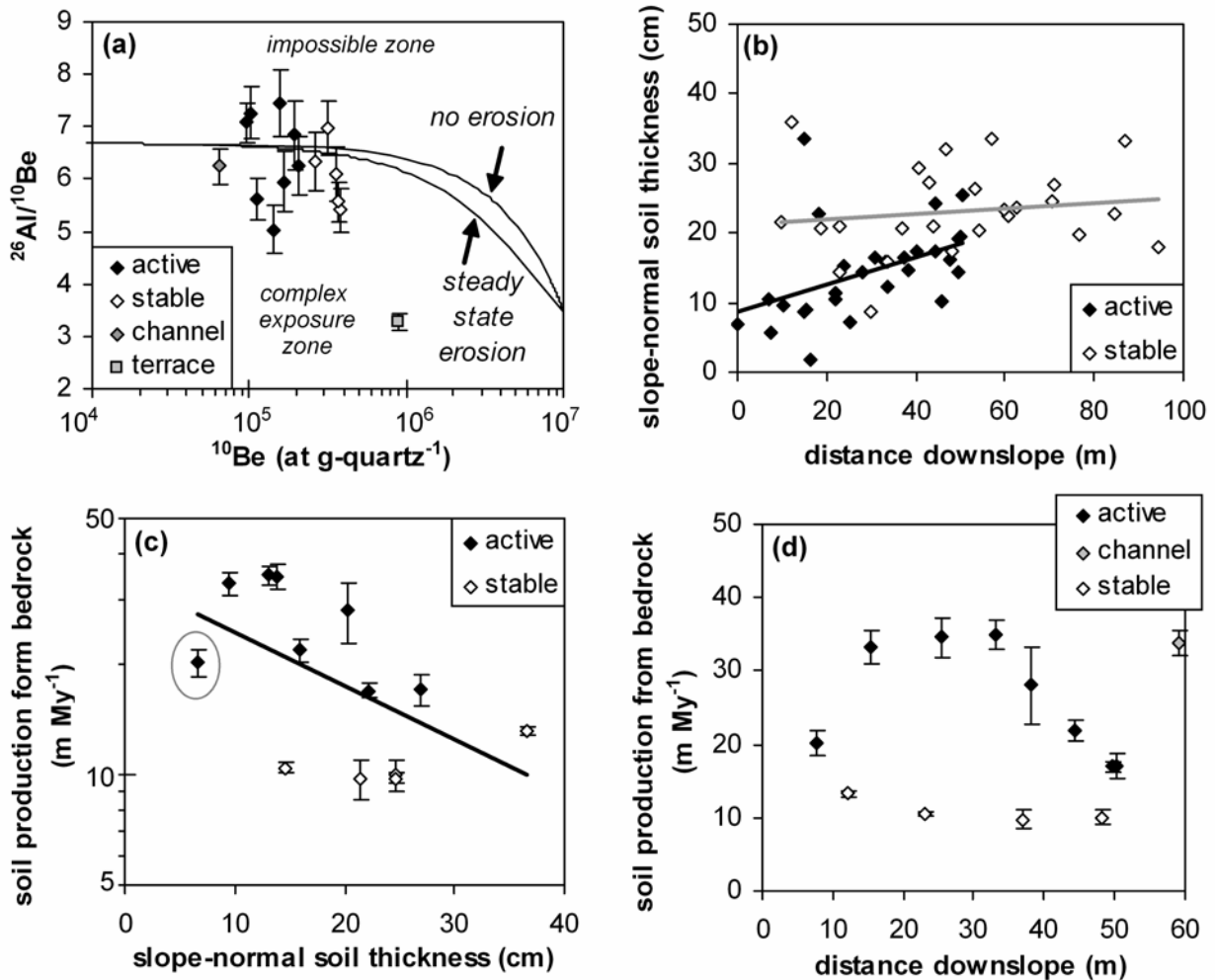
**Figure 7.** (a) An example of a soil profile at the arid site showing the thin, sandy soil underlain by fractured bedrock. (b) A nearby road cut showing the deep fracturing in the bedrock. (c) An EDS image showing salt accumulation in microcracks in the bedrock. (d) The exposed soil-bedrock interface showing the rounding of the tops of the bedrock fragments below the soil and root traces extending into the dust-filled cracks.
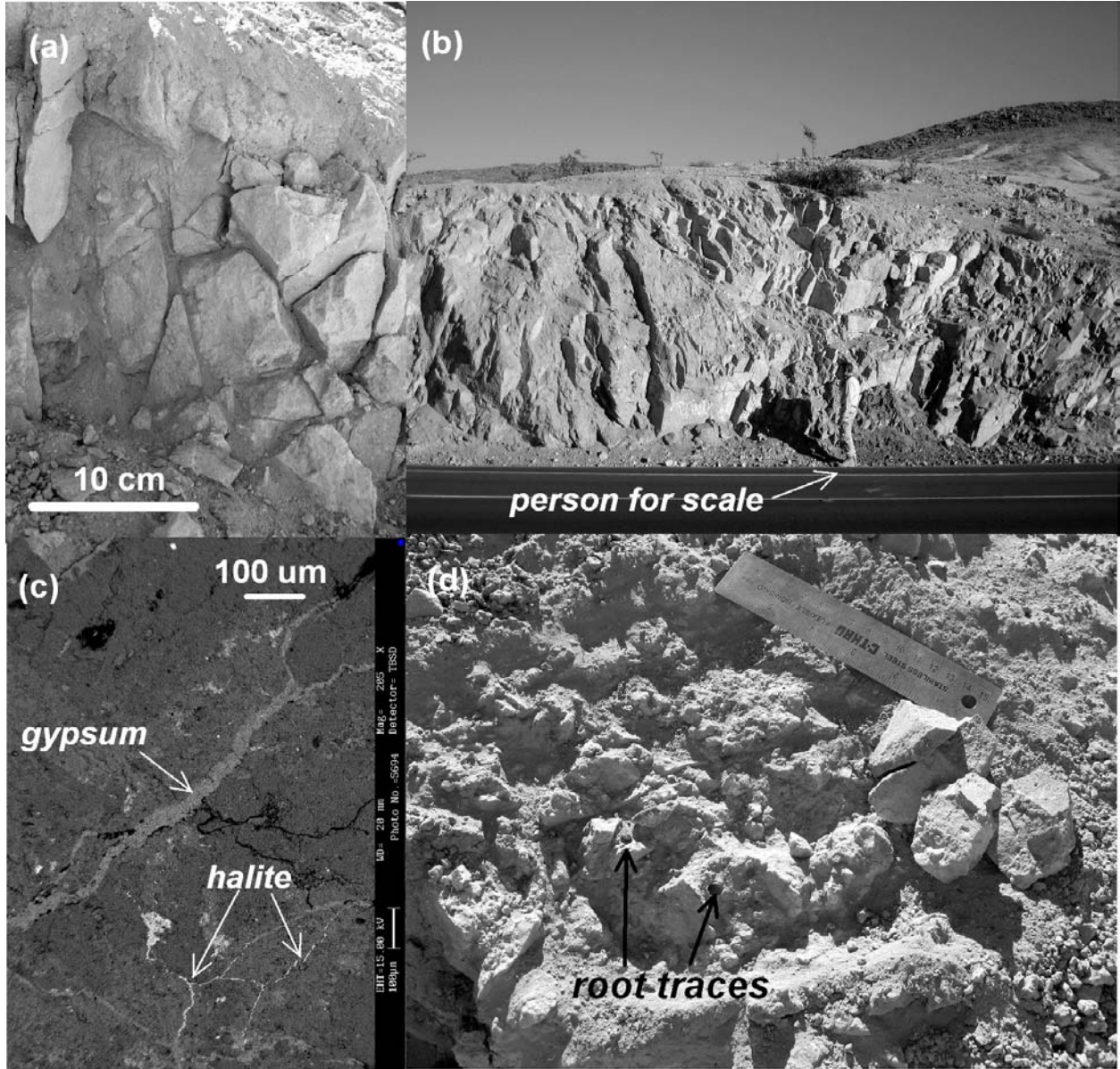
**Figure 8.** Surface-gravel sorting on a hillslope near the arid site, highlighted by the colonization of coarse gravels by dark-colored lichens.
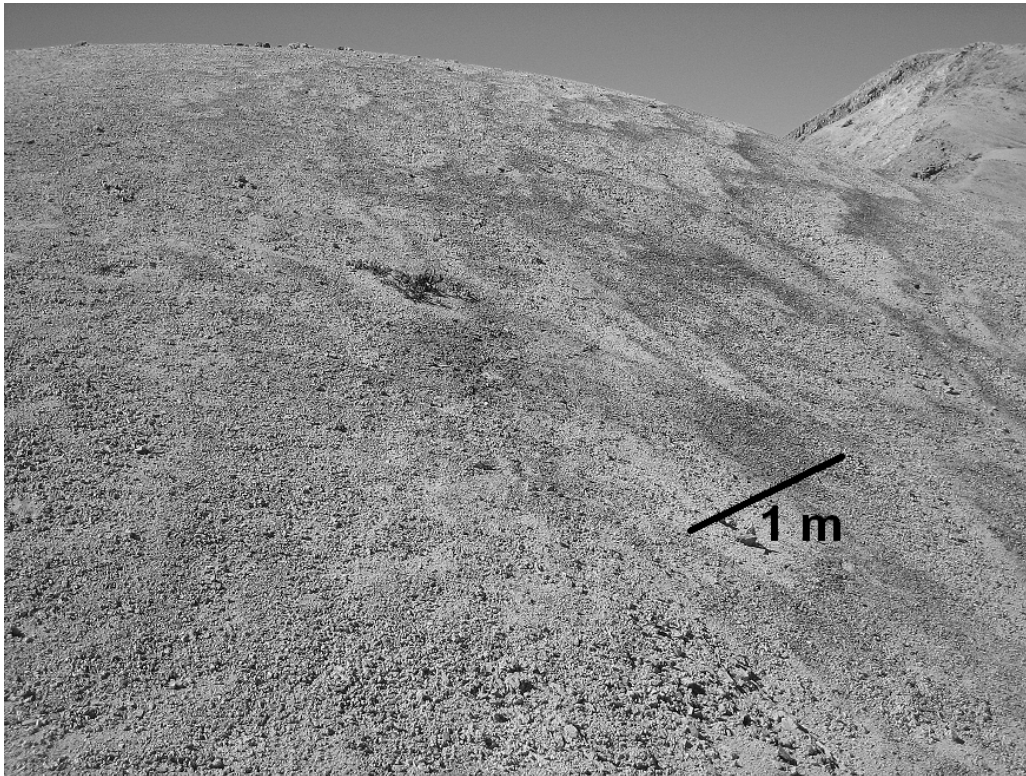
**Figure 9.** Arid hillslopes data.  Error bars are AMS analytical error. (a) Soil thickness is nearly constant with distance downslope on the active hillslope, whereas it increases on the stable hillslope.  (b) Using data from both hillslopes, the rate of soil production from bedrock is correlated to soil thickness on the arid hillslopes, where the trend line is $P = 3.29e^{-0.159H}$, $r^2 = 0.72$. (c) The rate of soil production from bedrock is similar on the two hillslopes and varies little with distance downslope.  (d) The rate of soil production from bedrock is nearly constant with distance downslope on the active hillslope.  It decreases slightly on the stable hillslope, likely indicating the propagation of lower erosion rates upslope in response to the low-erosion boundary condition.
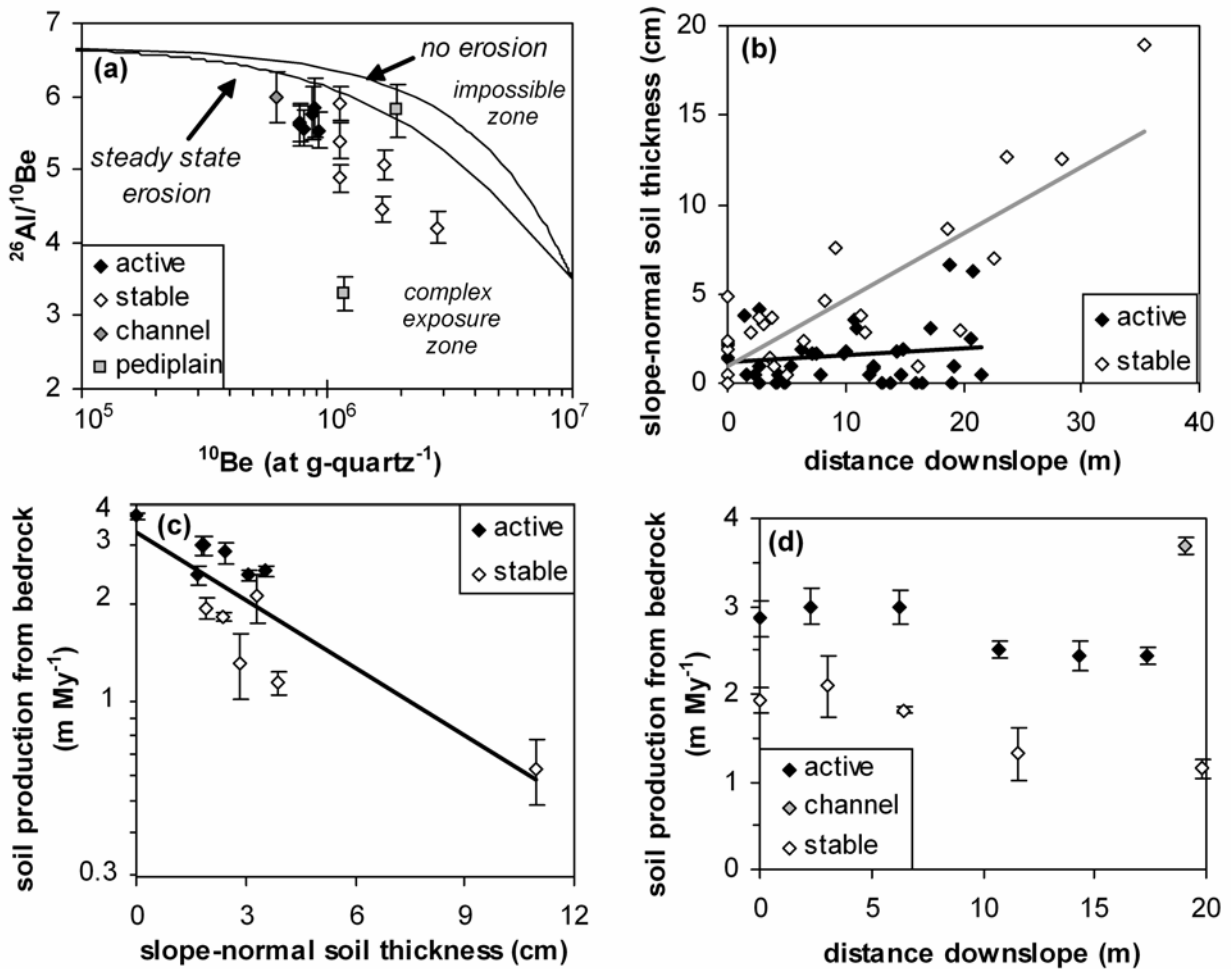
**Figure 10.** (a) A soil profile on the hyperarid active hillslope (pen is 15 cm long). (b) A soil profile near the summit of the hyperarid stable hillslope (excavation is 1 m deep). Angular, grey bedrock fragments are suspended in the white, gypsum-rich soil. The vertical feature on the right is a sand-filled crack. (c) EDS image of a rock fragment from the bedrock-soil interface on the active hillslope. The vertical crack is filled with both light grey halite and dark grey nitrate. The texture of the salt along the borders of the crack suggests episodes of dissolution and re-precipitation.
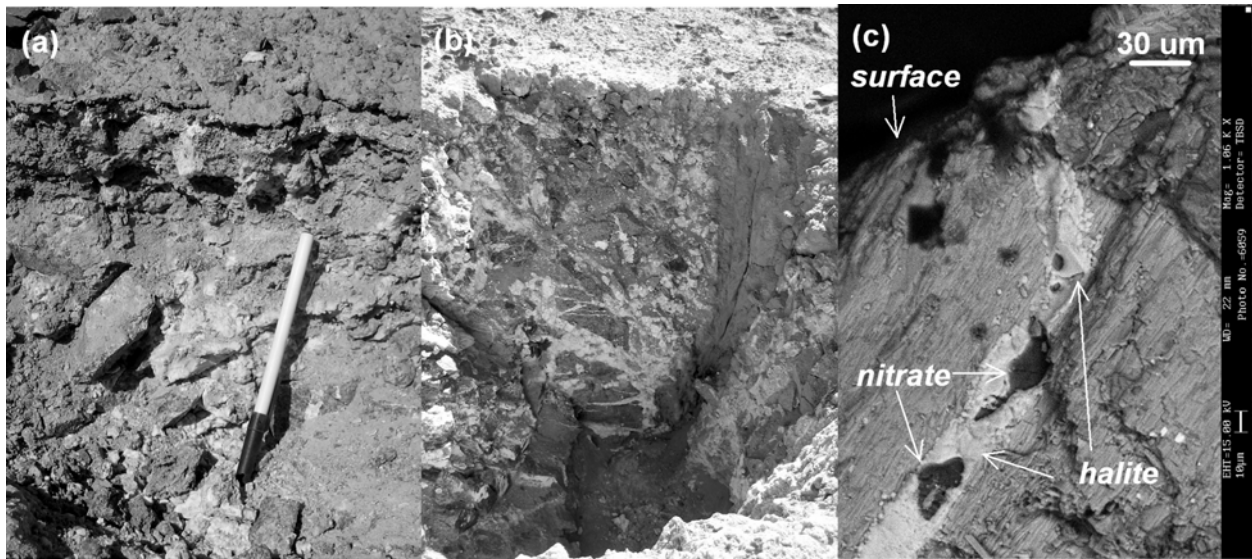
**Figure 11.** Hyperarid hillslopes data. Error bars are AMS analytical error. (a) Soil thickness is constant on the active hillslope but increases with distance downslope on the stable hillslope. (b) The rate of soil production from bedrock is nearly uniform with distance downslope on the active hillslope, showing a slight increase towards the channel, whereas they are consistently lower on the stable hillslope. (c) Samples from the active hillslope plot within the steady state erosion window, whereas the channel sample plots in the complex exposure zone. As expected, samples from the stable hillslope show more scatter and are more likely to be below the steady state erosion window.



53
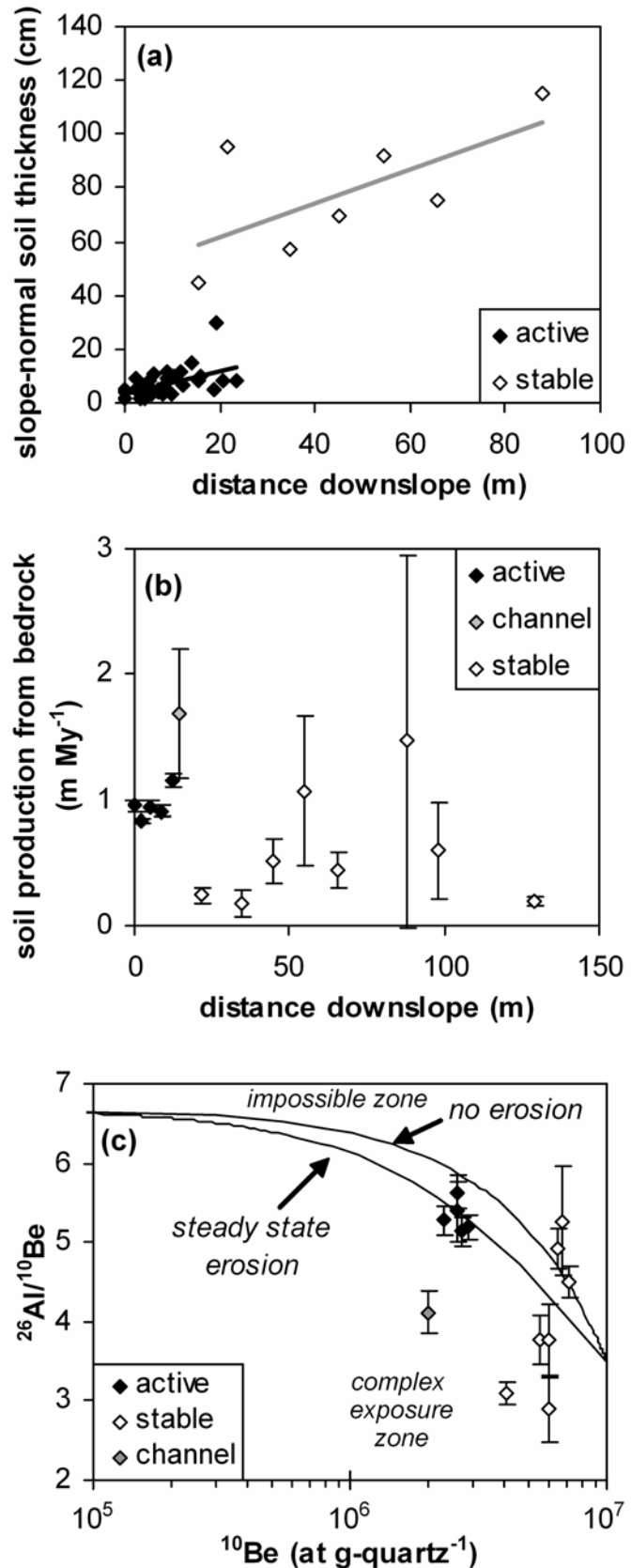
**Figure 12.** Rates of hillslope soil production from bedrock as a function of MAP. Data are limited to soil production rates calculated by measuring CRN in granitic bedrock at the soil-bedrock interface, except for the Riebe et al. (2004) data which were calculated from hillslope soils. In a well-mixed system, soil production rates calculated from the soil should be similar to rates calculated from bedrock. The black trendline is through the data from active hillslopes in this study. MAT ranges from 11 to 16ºC, except for the Riebe et al. (2004) samples which range from 3 to 25ºC.
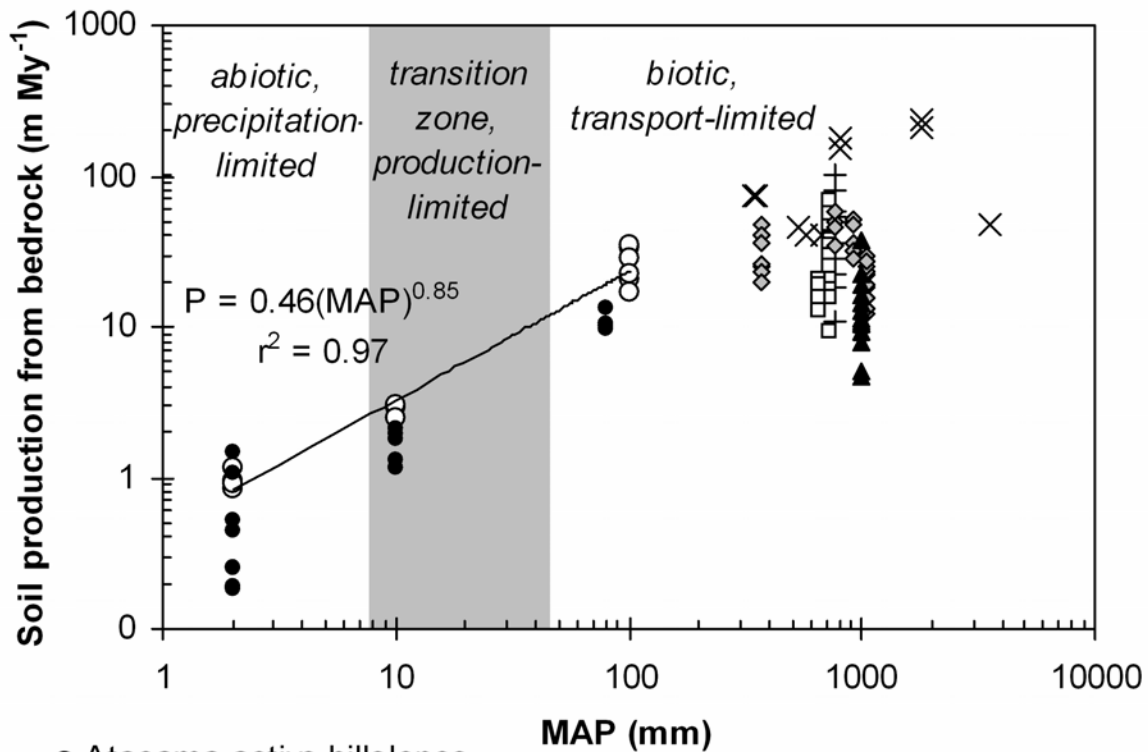
# Chapter 3

## The Effect of Precipitation on Physical and Chemical Erosion Rates
## on Hillslopes in Northern Chile

**Abstract**

The coupling between hillslope soil processes and precipitation is complex and poorly constrained.  Here we examine three granitic hillslopes along a precipitation gradient in northern Chile and use a soil mass balance model, in combination with soil chemistry, to calculate position-dependent soil erosion and soil residence time.  The model uses the rate of soil production from bedrock (calculated from cosmogenic radionuclides), atmospheric input (measured using dust collectors), and the concentration of a chemically-immobile element in the soil, bedrock, and atmospheric input to calculate both physical erosion and chemical erosion along the hillslopes.

A geomorphic and pedologic threshold was observed around a mean annual precipitation (MAP) of 100 mm, which is marked by changes in soil chemistry and erosion mechanisms.  In Chile, where MAP = 100 mm, the hillslopes are mantled with a relatively thick, chemically-weathered soil and covered with coastal desert vegetation.  Soil formation and transport is primarily through bioturbation.  As MAP decreases to 10 mm,  the hillslopes become nearly soil- and plant-free, and soil transport is through overland flow, rather than bioturbation. Where MAP is ~1 mm, the hillslopes are mantled with salt-rich soils which are primarily derived from atmospheric input rather than bedrock erosion.  Soil transport is through overland flow and likely some salt shrink-swell.  In contrast to previous work on wetter hillslopes, hillslope bedrock erosion rates were strongly correlated with MAP.  As a result, soil erosion and soil residence times were also MAP-dependent.

The spatially-explicit physical erosion rates were used to test the applicability of four soil transport models and calculate transport coefficients.  Where bioturbation occurs, soil transport is slope- and depth-dependent.  In the plant-free regions, soil transport is a function of slope and distance downslope.  A comparison of the transport coefficients with those determined on wetter hillslopes suggests that at MAP<100 mm, transport coefficients are a function of MAP.  Where MAP>100 mm, they are a function of the types of organisms driving bioturbation and other soil properties.  This threshold corresponds to the MAP below which there is a dramatic decrease in net primary productivity (NPP), and suggests that hillslope process rates are sensitive to MAP where the effect of life is small.

This work is the first investigation of the rates of physical and chemical erosion (calculated over entire hillslopes rather than at individual points) along a precipitation gradient that extends into hyperarid regions.  Because the study spans the biotic-abiotic transition in hillslope processes, it provides unique insight to the effect of climate and vegetation on them.

## INTRODUCTION

At hillslope sites around the world, soil production rates and chemical erosion rates appear to be insensitive to both precipitation and temperature (Riebe et al., 2004; von Blanckenburg et al., 2006).  This observation is surprising because climate is well known to

affect an array of soil processes on gentle or level landforms (e.g., Jenny, 1941) and to affect watershed- to continental-scale chemical erosion (e.g., White and Blum, 1995; Dupré et al., 2003; Syvitski and Milliman, 2007). Chemical weathering and erosion is affected by climate through the temperature-dependence of dissolution reactions acting on minerals (e.g., White et al., 1999), as well as the intensity of the hydrologic cycle (i.e., the turnover of soil porewater and transport of solutes to fluvial systems, Kump et al, 2000). The effect of precipitation on soils can be profound given long enough timescales, with near total chemical loss under high precipitation rates, and significant expansion through the accumulation of atmospherically-derived salt under hyperaridity (Amundson et al., 2007). Observation of climatic effects on soils can be complicated if precipitation and temperature vary inversely (e.g., Dahlgren et al., 1997; Dixon et al., 2009). On hillslopes, chemical erosion prepares the underlying rock for incorporation into the soil, and a positive correlation between chemical erosion and soil production from bedrock is well known (e.g., Riebe et al., 2004). The decoupling of hillslope soil production from climate seems inconsistent with observations of hillslope chemical erosion.

Climate determines the presence and type of vegetation and animal life which can be important factors in soil formation. Vegetation is thought to enhance chemical weathering and erosion through the production of organic acids (e.g., Kump et al., 2000), and possibly through its effect on microclimate. On hillslopes, vegetation increases physical erosion and soil production from bedrock through root growth and tree throw, but also stabilizes the soil through root strength, protection from rainfall impacts, and the impedance of overland flow (Greenway, 1987; Gabet et al., 2003). The relative importance of these different effects depends on the type of vegetation present, and is therefore a function of climate. Similarly, animals can also have a strong bioturbative effect, through burrowing or trampling (e.g., Yair, 1995; Govers and Poesen, 1998; Gabet et al., 2003; Yoo et al., 2005), and the presence and type of animals is determined by climatic and ecological factors. Therefore, biotic landscapes would be expected to have a positive, though potentially complex, relationship with climate.

What is responsible for the discrepancy between the observations of individual hillslopes and those of soils and continent-scale fluxes? Are there places on Earth where climate does exert a first order impact on these physical and chemical processes? In order to address these questions, we examined three hillslopes along a rainfall gradient at the dry-end of the Earth's rainfall spectrum. Using cosmogenic radionuclide-derived rates of soil production from bedrock, soil chemistry data, and a mass balance model to calculate physical and chemical erosion rate, we found that as decreasing rainfall begins to limit life, there are fundamental changes in the mechanisms and rates of hillslope processes. Our observations suggest that on most of Earth, life modulates hillslope soil processes and obscures the effect of precipitation. However, below a mean annual precipitation (MAP) of ~100 mm, the landscape transitions from biotic to abiotic and hillslope processes become extremely sensitive to precipitation.

**THEORY**

**Hillslope soil mass balance**
The soil mantle on gentle, convex hillslopes is determined by the balance between inputs into the soil and outputs:

$$\frac{\partial(\rho_s h)}{\partial t} = \phi - E \tag{1}$$

where $\rho_s$ is the depth-integrated bulk density of the soil [M L$^{-3}$], $h$ is the soil thickness [L], $t$ is time, $\phi$ is the rate of soil production [M L$^{-2}$ T$^{-1}$] (generally equal to the rate of bedrock erosion), and $E$ is the rate of soil erosion [M L$^{-2}$ T$^{-1}$] (Carson and Kirkby, 1972; Dietrich et al., 1995).

Equation 1 can be expanded to include specific processes that contribute to soil production and soil erosion. For example, atmospheric deposition of salt and dust, while small compared to soil production though bedrock erosion in humid environments, can be an important source of soil material in persistently arid systems. The potential role of atmospheric deposition in hillslope soil formation has been recognized (e.g., Kirkby, 1990; Mudd and Furbish, 2006) but has rarely been examined in the field. Atmospheric input is an important mechanism of soil formation in the Atacama Desert (Ewing et al., 2006) so in this work atmospheric deposition and bedrock erosion are treated as individual mechanisms of soil production. Likewise, soil erosion occurs through both physical and chemical processes. For simplicity, a two-layer model involving (1) soil and (2) bedrock or saprolite (whichever immediately underlies the soil) is used. Bedrock often undergoes some mass loss by chemical processes before being converted to soil (Anderson et al., 2002; Dixon et al, 2009), but this effect is not accounted for here because we are focused on losses in the soil mantle. A more process-specific mass balance is:

$$\frac{\partial(\rho_s h)}{\partial t} = \underbrace{\underbrace{P}_{\substack{\text{bedrock}\\\text{erosion}}} + \underbrace{A}_{\substack{\text{atmospheric}\\\text{deposition}}}}_{\substack{\text{soil production}\\\text{mechanisms}\\(\phi\ from\ Eq.1)}} - \underbrace{\underbrace{\nabla\cdot\tilde{Q}_s}_{\substack{\text{physical}\\\text{erosion}}} - \underbrace{W}_{\substack{\text{chemical}\\\text{erosion}}}}_{\substack{\text{soil loss}\\\text{mechanisms}\\(E\ from\ Eq.1)}} \tag{2}$$

where $P$ is the rate of soil production from bedrock [M L$^{-2}$ T$^{-1}$], $A$ is the rate of atmospheric deposition of silicate dust and salts [M L$^{-2}$ T$^{-1}$], $\nabla\cdot\tilde{Q}_s$ is the physical erosion rate [M L$^{-2}$ T$^{-1}$] (the divergence of depth-integrated soil flux, $\tilde{Q}_s$ [M L$^{-1}$ T$^{-1}$]), and $W$ is the chemical erosion rate [M L$^{-2}$ T$^{-1}$] (the other terms were described in Eq. 1). If the rate of soil production is greater than or equal to the rate of soil erosion, then the hillslope is soil-mantled and is "transport-limited" (Carson and Kirkby, 1972). If the combined loss mechanisms exceed production, then the hillslope lacks soil cover and is "weathering-limited" (Carson and Kirkby, 1972). The presence or absence of soils on a hillslope is thus a simple but powerful distinguishing characteristic of the sediment mass balance.

$P$ and $A$ can be measured using methods described below, but direct measurements of physical erosion and chemical erosion are difficult. However, if a hillslope is at steady state, such that soil inputs equal outputs, then there are only two unknowns in equation 2: physical and chemical erosion. Yoo et al. (2007) developed a numerical approach to calculate physical and chemical erosion rates using the concentration of an immobile (geochemically-conserved)

element in the soil and its inputs, and the rates of soil production.  This approach begins with a mass balance of an immobile element analogous to equation 2:

$$\frac{\partial (\rho_s C_{is} h)}{\partial t} = C_{ir} P + C_{iA} A - \nabla \cdot \left( C_{is} \tilde{Q}_s \right) \tag{3}$$

where $C_{is}$ is the depth-averaged concentration of an immobile element, $i$ (usually Ti or Zr), in the soil [M M$^{-1}$], $C_{ir}$ is the concentration in the rock [M M$^{-1}$], and $C_{iA}$ is the concentration in atmospheric deposition [M M$^{-1}$].  Note there is no $W$ term because the immobile element mass balance is not affected by chemical weathering.  For steady-state soils, equations 2 and 3 can be combined and solved for W:

$$W = \underbrace{\left( 1 - \frac{C_{ir}}{C_{is}} \right) P + \left( 1 - \frac{C_{iA}}{C_{is}} \right) A}_{W_\phi} + \underbrace{\left( \frac{\nabla C_{is}}{C_{is}} \right) \cdot \tilde{Q}_s}_{W_S} \tag{4}$$

Where $W_\Phi$ represents the chemical erosion of soil inputs and $W_S$ represents the chemical erosion of the soil as it is transported downslope.  Additionally, a steady-state expression for $\tilde{Q}_s$ can be written:

$$\left. \left| \tilde{Q}_s \right| \right|_{x+\Delta x} = \int_x^{x+\Delta x} (P + A - W) dx + \frac{l_x}{l_{x+\Delta x}} \left| \tilde{Q}_s \right|_x \tag{5}$$

where $|\tilde{Q}_s|_x$ is the soil flux at distance $x$ from the ridge [M L$^{-1}$ T$^{-1}$], $l_x$ is the width of a contour line bounded by two water flow lines [L], and the ratio ($l_x/l_{x+\Delta x}$) is 1 for planar slopes and less than one on divergent slopes.  We assume that at $x = 0$, $\tilde{Q}_s = 0$.  $W$ and $\tilde{Q}_s$ are solved iteratively by first assigning an arbitrary value for $\tilde{Q}_s$ in equation 4 to solve for $W$, then inserting this $W$ into equation 5 to solve for a new $\hat{Q}_s$, which is inserted back into equation 4.  Equations 3, 4, and 5 are identical to those derived by Yoo et al. (2007) except for the addition of atmospheric input terms.  This approach requires that the soil observations are located along a topographic transect oriented perpendicular to slope in order to provide chemical continuity along the hillslope.  As a result, this calculation reveals the spatial-dependency of $W$ and $\nabla \cdot \tilde{Q}_s$ (i.e., how soil transport varies with distance downslope).

**Analysis of Chemical and Physical Erosion Rates**
As mentioned in the introduction, neither $W$ nor $P$ have been shown to be dependent on climate, likely due to the overriding importance of other factors (Riebe et al., 2004; von Blanckenburg et al., 2006).  However, several approaches may help uncover climatic effects.  Here we review how chemical and physical erosion rates are compared and analyzed.

On many landscapes, $W$ is limited by the availability of fresh material (e.g., Dahlgren et al., 1997; Riebe et al., 2004; von Blanckenburg et al., 2004) such that it is positively correlated

with $P$. $P$ has been shown to depend on many factors including tectonic setting (Riebe et al., 2001; von Blanckenburg et al., 2006); degree of rock fracturing (Molnar et al., 2007); and rock composition (Onda, 1992), which obscure any climatic effect. Thus, Reibe et al. (2003) defined a "chemical depletion factor" (CDF), a metric that would account for the co-variation of $W$ and $P$, and could reveal a climatic signature on chemical erosion. In a steady-state soil, the CDF is,

$$CDF = \frac{W}{\phi} = \left(1 - \frac{C_{ip}}{C_{is}}\right). \tag{6}$$

In 42 samples from 14 sites spanning a wide range of climates, $W$ was proportional to $\Phi$, and though $W$ and $\Phi$ showed little climate-dependence individually, the CDF was positively correlated with both MAP and mean annual temperature (MAT) (Riebe et al., 2004).

The Riebe data are point measurements on hillslopes, but CDF values can vary by an order of magnitude over the length of a hillslope (Riebe et al., 2004; Yoo et al., 2007). Additionally, equation 6 assumes that soil production from bedrock is the only input to a hillslope soil and ignores lateral transport of soil and atmospheric deposition. To address these missing processes in the CDF and downslope variation, Yoo et al. (2007) derived what they called an "extended" CDF (ECDF) which includes the lateral component of chemical weathering, $W_S$ derived from equation 4. The ECDF has been modified here to include atmospheric input:

$$ECDF = \frac{W}{\phi} = \frac{1}{P+A}\left[\left(1 - \frac{C_{ir}}{C_{is}}\right)P + \left(1 - \frac{C_{iA}}{C_{is}}\right)A + \left(\frac{\nabla C_{is}}{C_{is}}\right)\cdot\tilde{Q}_s\right]. \tag{7}$$

The values of ECDF and CDF along hillslopes can be significantly different, with the exception of hillslope summits where they are identical due to the limited lateral transport of soil. For a semiarid hillslope in Australia, Yoo et al. (2007) calculated a hillslope-averaged CDF that was 50% larger than the hillslope-averaged ECDF because the CDF did not account for the input of chemically-weathered soil from upslope. Additionally, the ECDF captured a switch from chemical loss at the top of the hillslope to chemical gain towards the base through the precipitation of clay. Thus far, the ECDF has been used in only one study, but clearly has the potential to improve our understanding of the formation of hillslope soils as a continuous system and to provide an integrated view of chemical and physical processes.

The along-slope physical erosion rates calculated with equations 4 and 5 can be used to constrain the applicable transport law, related to the mechanisms driving physical erosion. The four soil transport laws considered here are: (1) slope-dependent, (2) slope- and depth-dependent, (3) critical slope-dependent, and (4) slope- and length-dependent. Below, each is discussed.

A simple, widely applied soil transport model is the linear, slope-dependent, "diffusion-like" transport model:

$$\tilde{Q}_s = -K_S\nabla z, \tag{8}$$

where $K_S$ is an empirical rate coefficient [$L^2 T^{-1}$] and $\nabla z$ is the slope gradient (Culling, 1963). In the absence of chemical erosion, equation 8 implies that a hillslope at steady-state will have constant curvature, a distinct condition that does not occur with the other models considered below. Though appealing in its simplicity, it may have limited applicability (Carson and Kirkby, 1972; McKean et al., 1993; Roering et al., 1999; Heimsath et al., 2005; Roering, 2008), particularly because the processes involved in soil creep (bioturbation, shrink-swell, freeze-thaw) are often limited to an active surface layer, such that soil transport increases with the thickness of that active layer.

Bioturbation and soil creep are both slope-dependent (Heimsath et al., 1999; Braun et al., 2001; Yoo et al., 2005) and may be depth-dependent (e.g. Kirkby, 1967; Gabet et al., 2003; Yoo et al., 2005), so a more descriptive transport law is

$$\tilde{Q}_s = -K_h H \nabla z, \qquad\qquad (9)$$

where $K_h$ is another rate coefficient [$L\ T^{-1}$] and $H$ is the slope-normal soil thickness [L] (Furbish, 2003). This formulation assumes that $\tilde{Q}_s$ increases linearly with soil thickness, which is reasonable for soils in which the transport processes are limited by the thickness of the soil (e.g., shallow bedrock). However, this results in a very large $\tilde{Q}_s$ for thick soils, which may not be reasonable if the transport processes are concentrated near the surface (e.g. Kirkby, 1967; Carson and Kirkby, 1972 and references therein). Field and laboratory experiments suggest that $\tilde{Q}_s$ decreases exponentially with increasing soil thickness (Kirkby, 1967; Fleming and Johnson, 1975; Gabet et al., 2003; Roering, 2004; Roering, 2008). Models based on these experiments are appealing in their direct treatment of soil mechanics, but are sensitive to the parameterization of the soil mechanics. Parameterization can be fairly straightforward in well-studied humid regions, but it is challenging or impossible where the processes are poorly constrained, such as the Atacama Desert. Here we test a linear relationship with soil thickness and treat $K_h$ as a depth-integrated value for simplicity (Heimsath et al., 2005). This is acceptable as long as the soil thicknesses do not exceed the depth over which soil transport processes are active.

The critical slope, $S_c$, soil transport model incorporates $S_c$ as a way to capture the nonlinear nature of some soil transport at high slope gradients (Roering, 2008). Written to include $H$,

$$\tilde{Q}_s = \frac{-K_c H \nabla z}{1 - \left( |\nabla z| / S_c \right)^2}, \qquad\qquad (10)$$

where $K_c$ is another transport coefficient [$L\ T^{-1}$] (Roering, 1999, 2008). Equation 10 implies that as $\nabla z$ approaches $S_c$, soil flux becomes infinite. This has the effect of producing a convexo-planar hillslope profile which is more common in some areas than the constant-curvature profile produced by equation 8. The formulation of equation 10 is slightly different from that of Roering (2008) in that the relationship with soil thickness is linear, rather than exponential. As discussed above, the exponential relationship requires information about the mechanics of soil transport which are often unavailable. Again, as long as the soil thicknesses do not exceed the depth over which soil transport processes are active, this is a reasonable simplification. $S_c$ is a function of the processes acting on the slope and soil properties, and is not the same as the

"threshold" angle or angle of repose, which are related to the mechanical properties of the soil (Roering, 1999). This model was used to describe soil flux in the Oregon Coast Range (Roering, 2008) and was better able to replicate hillslope morphology and soil thickness, where equations 7 and 8 were unsatisfactory.

Finally, overland flow, which is advective rather than "diffusive", is commonly modeled as a non-linear function of upslope drainage area (or distance downslope, $x$, if it is proportional to drainage area, Hack, 1957) and slope:

$$\widetilde{Q}_s = -K_w x^m (\nabla z)^n , \tag{11}$$

where $K_w$ is another transport coefficient with units dependent on $m$ and $n$, and $m$ and $n$ are empirical constants (e.g., Carson and Kirkby, 1972; Whipple and Tucker, 1999). The constants $m$ and $n$ are between 0 and 2 (Carson and Kirkby, 1972). A steady-state hillslope where overland flow drives soil transport will have a convexo-concave or convexo-planar topographic profile.

One difficulty in parameterizing the various transport laws has been obtaining quantitative, spatially-explicit measures of physical erosion across hillslopes. The mass balance approach used here and by Yoo et al. (2007) provides a means of achieving this. Of particular interest are the values of the transport coefficients (the various $K$s), which embed the effects of climate, lithology, biota, and transport mechanisms. A few researchers have begun exploring the mechanistic controls on $K$ (e.g., Gabet et al., 2000; Gabet et al., 2003; Yoo et al., 2005; Heimsath et al., 2005; Roering, 2008). However, more data is needed to understand the variability of $K$.

Another characteristic of hillslope soils that can be addressed using the spatially-explicit soil transport rates is soil residence time. Soil residence time is of interest because, just as on gentle landscapes where the degree of chemical weathering is dependent on soil age, on hillslopes the rate of chemical erosion is dependent on soil residence time (Yoo et al, 2007). Thus, the spatial variation of soil residence time on a hillslope is useful for understanding the spatial variation of soil chemistry. Previously, residence time has been calculated by dividing the soil mass in a unit area by the bedrock erosion rate (i.e. soil production rate) (e.g., Heimsath et al., 2001). However, this approach does not consider atmospheric deposition or lateral transport. Though the first is often negligible, the second has a dramatic effect on the calculation and interpretation of soil residence time.

In order to account for lateral transport in soil residence time, Yoo et al. (2007) derived a residence time equation based on the steady-state mass balance of an immobile element, as in equation 3. Here, we add atmospheric deposition as another soil input. Two components of the total residence time, $T_{Rt}$, over a distance $\Delta x$ can be defined. The first, $T_{R\phi}$, accounts for the input of an immobile element from $P$ and $A$:

$$T_{R\phi} = \frac{\rho_s C_{is} h}{C_{ir} P + C_{iA} A} , \tag{12}$$

61

and the second, $T_{RE}$, accounts for the effect of lateral transport over a distance $\Delta x$:

$$T_{RE} = \frac{\rho_s C_{is\_x+\Delta x} h \Delta x}{C_{is\_x} Q_{s\_x}},$$ (13)

where the subscript $x+\Delta x$ indicates the value at a distance $\Delta x$ below $x$. Following the same derivation as Yoo et al. (2007), $T_{Rt}$ is:

$$T_{Rt} = \frac{\rho_s C_{is\_x+\Delta x} h \Delta x}{\left(C_{ir} P \Delta x + C_{iA} A \Delta x\right) + C_{is\_x} Q_{s\_x}} = \frac{T_{RE} T_{R\phi}}{T_{R\phi} + T_{RE}}.$$ (14)

These calculations reveal variations in soil residence time over the length of the hillslope and, due to the large effect of $\tilde{Q}_s$, capture the shift from where $T_{R\phi}$ dominates the value of $T_{Rt}$ (the upper portion of the hillslope, where $\tilde{Q}_s$ is small) to where $T_{RE}$ is dominant (the lower portion of the hillslope, where $\tilde{Q}_s$ is large).

Another way of considering the "lifetime" of a hillslope soil is the total transport time, which is the time required for soil to move from the summit to a distance downslope, $x$. The total transport time is equal to $T_{Rt}$ integrated from the summit to $x$. Calculated over the same $x$ on different hillslopes, this metric enables a simpler comparison between hillslopes than the spatially-variable soil residence time.

## Cosmogenic Radionuclides

Solving equations 2, 3, and 4 requires knowledge of $P$ and whether or not the soil is in steady state. Cosmogenic radionuclides (CRN) can be used to address both problems. CRN are produced near the earth's surface by cosmic rays, and the rate of production decreases exponentially with increasing depth (Lal, 1991). The concentration of CRN in a rock reflects the time during which it has been near the surface (in the zone of CRN production), which is controlled by the rates of erosion and deposition above it. If rates of erosion and deposition are constant, such that the overlying soil is in steady state, then the CRN concentration reflects the rate of the conversion of weathered rock to soil, or $P$ in equation 1. This is often called the "denudation rate", because, if $A$ and chemical loss from the bedrock prior to its incorporation into the soil are ignored, a steady-state mass balance requires that $P$ is equal to the rate of soil loss ($\nabla \cdot \tilde{Q}_s + W$ in Eq. 1). In this paper, because we consider atmospheric input, we will avoid using "denudation rate" and refer to the erosion rate calculated from CRN concentrations as "bedrock erosion rate".

The steady-state concentration of a CRN, $C$ (atom g$^{-1}$), in the bedrock is:

$$C = P_c \left( \frac{1}{\lambda + \frac{\rho_r P}{\Lambda}} \right),$$ (15)

where $P_c$ is the CRN production rate (atom g$^{-1}$ y$^{-1}$)(corrected for any overlying soil and/or rock mass), $\lambda$ is the decay constant (y$^{-1}$), $\rho_r$ is the bulk density of the bedrock (g cm$^{-3}$), $P$ is the bedrock erosion rate (cm y$^{-1}$), and $\Lambda$ is the mean length of attenuation of the cosmic rays (g cm$^{-2}$) (Lal and Arnold, 1984). Equation 15 can be rearranged to solve for bedrock erosion rate:

$$P = \frac{\Lambda}{\rho_r}\left(\frac{P_c}{C} - \lambda\right). \tag{16}$$

Though $P$ is in units of cm y$^{-1}$ here, it can easily be converted to a mass flux for use in equation 1, as the rate of soil production from bedrock, by multiplying by the sample dry bulk density. These calculations require: (1) the rate of the conversion of bedrock to soil must be constant, (2) the soil mass must be constant ($\rho_s \partial h / \partial t = 0$), (3) the time the bedrock has been exposed to cosmic rays, $t$, is long enough that $t >> (\lambda + \rho_r P \Lambda^{-1})^{-1}$, and (4) the bedrock must have zero initial concentration of the CRNs being measured.

Pairs of CRN, such as $^{26}$Al and $^{10}$Be produced in quartz, are often analyzed because they have different response times to perturbations in steady-state conditions due to their different $P_c$ and $\lambda$ values. A comparison of the concentrations of different CRN in the same sample can reveal deviation from steady state that would not be recognized with a single nuclide. In steady state, the production rate ratio of $^{26}$Al and $^{10}$Be in quartz is 6.7 (Nishiizumi et al., 2007 after Nishiizumi et al., 1989). The ratio of the concentrations of these CRN (hereafter referred to as $^{26}$Al/$^{10}$Be) is 6.7 when erosion is rapid and decreases with decreasing erosion rate, reaching a minimum of 3.5 when erosion is zero. If the ratio is below the steady-state line on a $^{10}$Be vs. $^{26}$Al/$^{10}$Be plot, then the sample has experienced a complex exposure history ($\partial h / \partial t \neq 0$), non-uniform erosion, or experimental error (e.g., Lal, 1991). Discretion is required to interpret data from slowly eroding, ancient landscapes.

The approaches to quantifying hillslope process rates described above have been developed within the last few decades or later and represent the state of the field of hillslope geomorphology. As a result, most have not yet been widely applied (the exception is CRN-derived hillslope denudation rates) and many questions remain. In order to examine the effect of precipitation on these rates, we have selected a study area in which other variables like tectonic setting, bedrock composition, and temperature are either approximately constant or can be explicitly constrained. The sensitivity of landscapes to precipitation is likely greatest where it is a limiting factor, and, thus, we apply the approaches above to one of the driest places on Earth: the Atacama Desert.

**STUDY AREA: THE ATACAMA DESERT**
Northern Chile was selected for our study area because there is a large, long-term precipitation gradient, ranging from semiarid to hyperarid, over a region with relatively spatially-uniform uplift and areas of similar bedrock (Fig. 1). At the northern end of this precipitation gradient is the Atacama Desert, which spans a region from southern Peru into northern Chile. It is primarily located in a large, north-south trending valley, the Central Depression, bounded on the west by the Coastal Cordillera and on the east by the pre-Andean ranges (Fig. 1a). The

southern boundary of the Atacama Desert is subject to debate.  Rundel et al. (1991) suggest the present-day border lies at La Serena and the Rio Elqui (~30ºS) based on a shift in vegetation from semiarid coastal scrub to succulent desert communities, but the nearly lifeless zone for which the Atacama Desert is renowned ends near the latitude of Chañaral (~26.3ºS).

MAP along the Chilean coast decreases exponentially with decreasing latitude, from ~100 mm y$^{-1}$ at 29ºS  to 1 mm$^{-1}$ or less between 20 and 26ºS (Ericksen, 1981) (Fig. 1b).  MAP also decreases with increasing longitude, with the pre-Andean ranges wetter than the Central Depression (Houston, 2006).  The Coast Range experiences frequent fog, but the penetration of fog inland decreases rapidly with distance from the coast (Cáceras et al., 2007).  Geochemical evidence suggests that dry conditions have persisted at least periodically since the middle to late Miocene (Alpers and Brimhall, 1988; Sillitoe and McKee, 1996; Hartley and Chong, 2002; Dunai et al., 2005; Clarke, 2006; Houston, 2006; Nishiizumi et al., 2005; Rech et al., 2003; Kober et al., 2007), and possibly much earlier (Clarke, 2006; Hartley et al., 2005).  Within this long-term aridity, there have been episodes of more pluvial conditions prior to the relatively dry climate at present.  Sediment deposition rates inferred from offshore drill cores between 24ºS and 44ºS indicate that the Southern Westerlies moved north as much as 5º latitude from their current position ~24 to 16 ka, likely increasing precipitation by about an order of magnitude (Lamy et al., 2000; Hebbeln et al., 2007).  Salt cores (Bobst et al., 2001), paleowetland deposits (Rech et al., 2003), rodent middens (Betancourt et al., 2000; Latorre et al., 2002; Latorre et al., 2003), and archeological studies (Núñez et al., 2002) generally corroborate the marine sediment findings.  The wetter episodes described above have been of insufficient magnitude and duration to remove or chemical alter highly water-soluble and biologically-reactive compounds such as nitrate in the hyperarid parts of the Central Depression (Ewing et al., 2007).  Though MAP has varied, the latitudinal gradient has persisted.

Systematic shifts in biota occur with latitude due to the changes in MAP (Fig. 1c).  The hyperarid north (~19-23ºS) is a nearly abiotic landscape (Navarro-González et al., 2003; Warren-Rhodes et al., 2006) with no vascular plants.  Biota increases with increasing latitude, such that around 26ºS there are scattered fog-adapted plants, and by ~29ºS there is a succulent desert scrub ecosystem (Rundel et al., 1991).

Uplift of the Coastal Cordillera between 22 and 33ºS has averaged about 0.2 mm y$^{-1}$ over the last 100 to 800 ky (Fig. 1d).  The long profiles of rivers cutting through the Coastal Cordillera at these latitudes have convex or straight regions near the coast, indicative of a geomorphic system out of equilibrium with baselevel (Mortimer, 1980).  Hypsometric curves (the cumulative fraction of total area vs. normalized elevation) of the land surface of the Atacama Desert are generally convex (Montgomery et al., 2001), a pattern consistent with a landscape where fluvial incision is unable to match tectonic uplift.  This suggests that inland hillslopes are isolated from current marine baselevel and that local channel incision rate may differ greatly from the uplift rate.

Soils on non-eroding alluvial surfaces show extreme sensitivity to MAP in their salt composition and concentration (Ewing et al., 2006), in the degree of chemical weathering (Ewing et al., 2006; Amundson et al., 2007), and in the abundance of microbial life (Navarro-González et al., 2003; Warren-Rhodes et al., 2006).  Gypsum, anhydrite, halite, carbonate, iodate

and borate are found in alluvial soils in the northern part of the Atacama, above ~24ºS (Ericksen, 1981; Ewing et al., 2006), due in part to the deposition of material derived from marine and volcanic sources in the region (Bohlke et al., 1997; Rech et al., 2003; Michalski et al., 2004).  As precipitation increases, the salt content of alluvial soils decreases and organic matter increases (Ewing et al., 2006).

## METHODS

### Site Selection
We selected three hillslopes along a north-south transect with similar parent material (granitic) and topography (convexo-planar), each of which is bounded at the base by a bedrock-bedded channel (indicating active incision) (Fig. 2).  As a result, the primary variable causing differences between the sites is precipitation and the associated changes in vegetation (Table 1, Fig. 2a-c).  MAP increases from ~1 mm at the northernmost ("hyperarid") site, to ~10 mm at the middle ("arid") site, to ~100 mm at the southernmost ("semiarid") site (Fig. 1b).  Our initial intention was to locate hillslopes at similar elevations and distance from the coast because geography controls fog occurrence in the Atacama, with the most fog occurring at low elevations and closest to the coast (Rech et al., 2003).  However, locating hillslopes on suitable rock for CRN analysis was more important so the semiarid and arid sites are lower in elevation and closer to the coast, and thus receive more fog, than the hyperarid site (Table 1).  The importance of fog parallels the increase in MAP and should not compromise the MAP gradient.  MAT decreases slightly from north to south, from 17ºC at the hyperarid hillslope (McKay et al, 2003), to16ºC at the arid hillslope (Rundel et al., 1996), to13.5ºC at the semiarid hillslope (Squeo et al., 2006) (Table 1).   In summary, along the study transect rainfall increases by two orders of magnitude with increasing latitude, whereas temperature decreases by a factor of about 0.76.  Thus, the largest climate variable is precipitation.

The parent material is fairly uniform between the sites (Table 1).  The hyperarid hillslopes are underlain by a fine-grained, amphibole and biotite-containing granodiorite of middle Cretaceous age (Marinovic et al., 1992).  This is the most mafic and fine-grained bedrock of the three sites.  In the arid region, bedrock is a 217 Ma, coarser-grained monzogranite with several andesitic to basaltic dikes that follow regional fracture patterns but do not appear to strongly control topographic development (Godoy and Lara, 1998).  The hillslopes considered in this work do not have dikes.  Lastly, bedrock at the semiarid site is a biotite and amphibole-containing monzogranite with a grain size similar to that of the arid site.  It contains no mafic dikes and is estimated to be at least 100 Ma by K-Ar dating (Emperan and Pineda, 2000).  Bedrock fracturing is similar at all the sites (described further below) and probably affects erosion rates uniformly.

### Field Observations and Analyses
Topographic surveys of each hillslope were made using a Trimble GPS and analyzed with Golden Surfer Software (v. 8.0).  Vegetation density was measured by calculating the length fraction of a 50-m measuring tape underlain by vegetation along three transects on each hillslope.  20 to 50 soil excavations were made on each hillslope in which soil thickness was measured.  The base of the soil was identified in the excavations based on the presence of minimally expanded or perturbed bedrock textures.  Five to six of the excavations were made

along a slope-parallel transect extending from the ridge top to the bottom of the hillslope (Fig. 2d-f). These soils were described following the methods of Schoenenberger et al. (2002) and sampled by horizon for chemical analysis, bulk density determination, and textural analyses. Particle size was determined by hydrometer on sieved soil samples from which salt had been removed using a weak EDTA solution, if necessary (Bodine and Fernald, 1973). Soil, gravel, and bedrock samples were analyzed by ALS Chemex, Sparks, NV, for major element chemistry (by lithium borate fusion and ICP-AES). Soil fines (<2mm) were shaken in deionized water, and filtered, then analyzed by Dr. Ken Williams of the Lawrence Berkeley Laboratory by ion chromatography (IC) for nitrate and chloride ions.

Atmospheric deposition has previously been measured along a shorter north-south transect in the Atacama Desert by Ewing et al. (2006) using passive dust collectors. To complement and expand this data set, 3 or 4 passive collection dust traps were emplaced at each site. The traps were made of stainless steel bundt pans filled with marbles atop a wire mesh and were put on poles 1-1.5 m above the ground (Reheis and Kihl, 1995). They were located on nearby hillslopes and plains (<1 km away from the study hillslope while also as far as reasonable from roads or tracks) to capture some of the variability in deposition within the region. The traps were collected ~2 years after their deployment. Dust traps and marbles were rinsed with deionized water and the solution was filtered and measured for nitrate, chloride, and sulfate ions by IC (by Dr. Ken Williams). The silicate dust from the pans (collected on the filter) was pooled within each climate region and analyzed for major element chemistry by MS-ICP analysis at the Desert Research Institute (which is well equipped to process small samples).

Saprolite or weathered bedrock at the base of the soil was collected for CRN analysis in the excavations along the downslope transects on each hillslope. Exposed bedrock from channels adjacent to the hillslopes was also collected to measure incision rate. The samples were processed using methods described in Kohl and Nishiizumi (1992). Briefly, the bedrock samples were ground to pass through a 0.5 mm sieve. The quartz mineral grains were isolated through a series of acid dissolutions then dissolved and processed to isolate Be and Al. $^{10}Be/^{9}Be$ and $^{26}Al/^{27}Al$ were measured by accelerator mass spectrometry (AMS) at the Lawrence Livermore National Laboratory Center for Accelerator Mass Spectrometry (R. Finkel) and at the Purdue Rare Isotope Measurement Laboratory (M. Caffee) and normalized to the Nishiizumi et al. (2007) $^{10}Be$ AMS standard and the Nishiizumi (2003) $^{26}Al$ AMS standard, respectively. Accordingly, the $^{10}Be$ half-life of 1.36 My and the $^{26}Al$ half-life of 0.705 My were used. The erosion rates and exposure ages were calculated based on the scaling functions of Lal (1991), assuming 2.5% muon contribution, and using sample densities of 2.5 g cm$^{-3}$ for rock (the arid and hyperarid sites) and 1.5 g cm$^{-3}$ for saprolite (the semiarid site). Production rates (at sea level and high latitude) of 5.1 atoms $^{10}Be$ g quartz$^{-1}$ y$^{-1}$ and 34.07 atoms $^{26}Al$ g quartz$^{-1}$ y$^{-1}$ were used (Nishiizumi et al., 2007).

In order to evaluate the potential importance of overland flow as a soil transport mechanism, sprinkling experiments were performed in each precipitation zone. Sprinkling experiments were conducted over 1-m$^2$ plots. The experiments were small scale due to the need for portability. The sprinkler was a nozzle mounted on an adjustable tripod with a pressure gauge and compression stop valve to control water pressure (Wilcox et al., 1986). The water was pumped from a bucket using a 1/6 horsepower Simer Submersible Utility Pump which

produced 8-10 psi through the nozzle. Two nozzle sizes were used, a 1/8GG-4.3W fulljet brass nozzle and a 1/8GG-6.5W fulljet brass nozzle (Spraying Systems Co), which produced precipitation rates of about 6 cm/h and 55 cm/h, respectively. The plot was surrounded on three sides by a windscreen constructed of a PVC pipe frame and heavy plastic drop cloth walls. While this greatly reduced wind disturbance, the experiments were conducted at a height of about 0.5 m above the ground to avoid drift due to swirling winds. The low spraying height and pressure does not produce precipitation with the same kinetic energy as natural rainfall, and nozzles of this size tend to produce drops smaller than natural rainfall (Wilcox et al, 1986).

The sprinkling plot was bounded on the downslope side by a steel collection trough set into the ground (Dunne et al., 1980). The other sides were bounded by plastic lawn edging set 5-10 cm into the soil, as possible. The trough had a steel lip that was set into the soil to capture the surface runoff and a lid to minimize direct addition from the sprinkler. It also had a sloped bottom to send collected runoff to a spout from which it was collected at regular intervals. The times to ponding, initial runoff, and full runoff (majority of area contributing), and the duration of runoff after spray was turned off were recorded. We also noted if and when sediment was mobilized. Application rate was measured by covering the plot with plastic and measuring runoff over two one-minute intervals. Runoff samples were collected every 1 or 2 minutes, depending on runoff rate, and the total volume was measured. Sprinkling experiments were run at a minimum until several minutes after steady-state runoff was achieved, generally lasting ~10, 20, and 30 minutes. For several runs, the samples were filtered to collect the sediment mobilized in that interval. Because municipal tap water was used, the water was not sampled for chemical analyses. After each sprinkling experiment, the collection trough was removed and the face of its trench was excavated to observe how deep the water had infiltrated and if any subsurface patterns were observable. Infiltration rates were calculated by subtracting the runoff rate from the application rate.

**Modeling Hillslope Processes**

Physical and chemical erosion rates were calculated using equations 4 and 5 along an elevation transect. The degree of divergence ($l_x/l_{x+\Delta x}$), $\Delta x$, and $\nabla z$ were determined graphically from 1-m contour topographic maps of each site. $H$ and the depth-averaged values of $C_{ir}$, $C_{is}$, $\rho_s$, $\rho_r$, and $P$ measured in the 5 to 6 soils were plotted against $x$, and fitted linear or polynomial relationships between the variables and $x$ were used to interpolate between these points, producing continuous smooth trends as a function of $x$. This approach was used by Yoo et al. (2007) and is necessary to avoid fatal model instability during the iteration. Fitted linear or polynomial trends are used rather than linear interpolations between each data point because this minimizes the effects of local heterogeneity in soil and bedrock characteristics and of error inherent in the measurements. Ti was used as the immobile element, and has been shown to produce similar estimates of chemical weathering as Zr at sites in the Atacama (S.A. Ewing, pers. comm.). $A$ and $C_{iA}$ were assumed to be constant over the hillslope but different for each site, as described below.

To test the applicability of the $\nabla z$-dependent and $H\nabla z$-dependent transport models (Eqs. 8 and 9), $\tilde{Q}_s$ was plotted against $\nabla z$ and $H\nabla z$. On these plots, the slope of the linear trend is equal to the transport coefficient $K_s$ and $K_h$, respectively. $\hat{Q}_s$, $H$, and $\nabla z$ all tend to increase with $x$, thus to ensure that the transport model is not affected by the covariance of these variables with

67

distance downslope, $\tilde{Q}_s\nabla z^{-1}$ and $\tilde{Q}_s(H\nabla z)^{-1}$ were plotted against $x$ (Heimsath et al., 2005).  In these plots, the data should be homoscedastic around the $K_s$ or $K_h$ value over the entire hillslope length (i.e. vary randomly with $x$ near a horizontal line equal to $K$) if the transport model is appropriate.  The applicability of the $S_c$-dependent transport model (Eq. 10) is suggested if, when $\tilde{Q}_s$ is plotted against $\nabla z$ and $H\nabla z$, the trend is nonlinear.  To constrain this transport model, curves bracketing the data on the $\tilde{Q}_s$ vs. $\nabla z$ plots were iteratively determined, described by unique pairs of $S_c$ and $K_c$.  $K_c$ is gradient-dependent, but at $\nabla z \ll S_c$, $K_c*$ and $K_h$ should be equal.  As with the other models, the test for covariation involves plotting $\tilde{Q}_s(1-(\nabla z/S_c)^2)(H\nabla z)^{-1}$ against $x$.  The values will vary homoscedastically around $K_c$ if the model is appropriate.  For the overland flow model (Eq. 11), in an approach similar to the $S_c$-dependent model, $K_w$, $m$, and $n$ are tuned to best fit the data, then tested for covariation by plotting $Q_s(x^m\nabla z^n)^{-1}$ against $x$.

## RESULTS AND INTERPRETATION

The three hillslopes show enormous (greater than one order of magnitude) and systematic differences in 1) soil properties 2) mechanisms of soil formation and transport, and 3) the rates of these processes with MAP.  Over this small range of MAP, the soils and hillslope processes exhibit more variation than has been observed across much of the rest of the planet.

## Semiarid Hillslope

### *Observations*

The semiarid hillslope is located near La Serena and is discontinuously covered with coastal chaparral -type vegetation (Fig. 2a).  While it is related to previous studies of semiarid to humid hillslopes (e.g., Heimsath et al., 1999, 2005; Yoo et al., 2007, 2009), in that the availability of water, $CO_2$, and organic matter in the soil facilitates deep weathering and the creation of saprolite (hand excavations could not reach unweathered bedrock) (Fig. 3), it is more arid.  Soil thickness (defined at this site as the depth to saprolite) increases linearly with distance downslope, from 6.5 cm to 27 cm (Table 2, Fig. A1a).  The near surface soil is coarse sand and fine gravel which overlies a less porous, brown, finer-textured soil horizon interwoven with roots.  The uppermost horizons have moderate to weak subangular blocky structure, and below them is increasingly coarse soil with no observable structure.  In the lower soil horizons and saprolite, thick, red clay films surround in-place mineral grains, and the transition from soil to saprolite is gradual (Fig. 3).  Carbonate and other salts were not detectable in the soils.

Bioturbation appears to be the dominant mechanism of soil transport.  Cacti and shrubs cover 32% of the soil surface (Fig. 2a) and their roots, though concentrated in the upper tens of centimeters of the soil, extend into the saprolite (Fig. 3).  The vegetation supports small burrowing mammals and insects, as well as non-native grazers (including mules, horses, and goats) which trample the soil surface.  Prior to these introduced species, a population of native grazers likely played a similar role (Wheeler, 1995).  Despite the large amount of bare ground, the coarse surface appears to limit rainsplash and minimizes overland flow.  No rills were observed on the hillslope, but several burro trails along the ridge have been eroded tens of cm deep.  The sprinkling experiments showed that water infiltrates through the surface sand and flows on top of the fine brown soil beneath the surface sand.  No gravel mobilization was observed within the plot.  Infiltration rates were proportional to application rates, increasing from 2.6-15.6 cm $hr^{-1}$ as application increased from 5.7-26.5 cm $hr^{-1}$ (Table 3).  In summary, chemical

weathering (as evidenced by clay films and soil reddening) weakens the bedrock and leads to some chemical erosion, while bioturbation (as evidenced by burrows and root traces) disrupts the weathered bedrock, converts it to soil, and transports it downslope.

Bioturbation and chemical erosion decrease the soil density as the soil is formed, but much of the change in density occurs during saprolitization. Soil bulk density averages 1.38 g cm$^{-3}$ and increases linearly with distance downslope. The upper saprolite bulk density is only slightly greater and averages 1.44 g cm$^{-3}$. It varies parabolically with distance downslope, peaking ~ 20-30 m (Table 2, Fig. A1b). The similarity of bulk densities is indicative of the substantial weathering of the saprolite prior to its incorporation into the soil. Consistent with this finding, the depth-averaged soil Ti concentrations, $C_{is}$, are somewhat greater than the saprolite Ti concentrations, $C_{ir}$ (2300 ppm vs. 1700 ppm, respectively, Table 2). Second-degree polynomial trends were used to represent $C_{is}$ and $C_{ir}$ in the chemical erosion modeling, with minima between 30-40 m downslope (Fig. A1c). In contrast to the rest of the soil, the surface sand layer is Ti-poor. This could be due to the washing of fines, in which Ti is concentrated, through the large pores between the coarse, quartz-rich sand grains to the relatively fine-rich horizon below.

The primary input to the soil is from the saprolite; atmospheric input is likely small relative to this process. Average $P$ was 26 m My$^{-1}$, but $P$ varied parabolically with distance downslope (Fig. A1d), increasing from ~20 m My$^{-1}$ at the crest, peaking at ~35 m My$^{-1}$ along the shoulderslope and backslope, and then decreasing to ~26 m My$^{-1}$ at the base next to the channel (Table 2). The peak $P$ coincides with the lowest $C_{ir}$ and $C_{is}$ values, suggesting an important threshold on this hillslope, as discussed below. All dust collectors at this site were stolen. However, if $A$ were the same as in the hyperarid region (~2.6 g m$^{-2}$ y$^{-1}$, discussed below), then $A$ is less than 10% of $P$. $A$ in this region is likely smaller than in the hyperarid region because there are not similar sources of fine silicate dust or salt. Additionally, bedrock in the surrounding region is mostly felsic plutonic rock (Emperan and Pineda, 2000) and is not expected to provide atmospheric dust with a composition significantly different from the local soil which could skew $C_{is}$. For simplicity, we assume no atmospheric input and acknowledge that this makes the calculated erosion rates minimum values.

[26]Al/[10]Be ratios and [10]Be measured in the saprolite samples indicate that the exposure history is too short to test for steady state (too far left in Fig. 4) but that some samples have experienced complex exposure histories ([26]Al/[10]Be ratios below 6.68) (Table 2, Fig. 4). Additionally, the uppermost saprolite sample (SGA-1, Table 2) has an impossibly high [26]Al/[10]Be ratio of 7.45±0.64, most likely indicating an overestimate of [26]Al. The combination of the complex exposure history inferred from the [26]Al/[10]Be ratios and the variation in the rates of soil production from bedrock suggest that the hillslope soils may not be in steady state, which we discuss further below.

### *Soil Erosion and Residence Time*
Soil flux initially increases with distance downslope, $x$, then, coincident with the soil production and soil chemistry threshold noted above, remains nearly constant. Plots of depth-integrated $\tilde{Q}_s$ vs. $\nabla z$ and $H\nabla z$ (Figs. 5a, 5c) both show linear trends, with $K_s = 0.0025$ m$^2$ y$^{-1}$ and $K_h = 0.0058$ m y$^{-1}$, respectively. When tested for covariance, values of $\tilde{Q}_s \nabla z^{-1}$ increase with $x$ (Fig. 5b) whereas values of $\tilde{Q}_s(H\nabla z)^{-1}$ follow a roughly horizontal trend (Fig. 5d), but they lie

above the value for $K_h$. The critical slope produced a similar plot to Figure 5d, with $S_c = 0.8$ and $K_c$ ranging between 0.004-0.0087 m y$^{-1}$ (Fig. 5e). Because $S_c$ is large relative to the slopes observed on the hillslope, this model is indistinguishable from the $H\nabla z$-dependent one, and the test for covariation produces the same pattern (Fig. 5f). In fact, equation 9 is a special case of equation 10, applicable when $S_c \gg \nabla z$, as appears to be the case here. If the $S_c$-dependent model did apply, $\nabla z$ would become constant (i.e. planar) towards the base of the slope, rather than increase with distance downslope as it does here (Table 2, Fig. 2f). No combination of parameters in equation 11 could produce a model that fit the $\tilde{Q}_s$ values, consistent with the absence of evidence for overland flow, and is not shown here. Thus, soil flux appears to be best modeled as a function of $H\nabla z$, as is expected for most bioturbated hillslopes.

The offset between $K_h$ and $\tilde{Q}_s(H\nabla z)^{-1}$ suggests that use of the entire data set to determine $K_h$ results in an underestimate of that value. If $K_h$ is recalculated using data from only the uppermost 40 m, it increases to 0.0087 m y$^{-1}$ and is more consistent with the data in Figure 5d. There are several possible explanations for this apparent threshold near 40 m. First, it may indicate a shift in soil transport mechanisms, coincident with the geochemical and erosion rate changes described above, but there is no obvious difference observable in the field. Alternatively, the assumption of a linear dependence of $\tilde{Q}_s$ on $H$ may fail at the greater soil thicknesses towards the base of the hillslope. Lastly, part of the hillslope may not be at steady state, invalidating a fundamental assumption of the mass balance method. Variations in channel incision rate cause changes in soil thickness and $P$ which propagate upslope from the channel (Dietrich et al., 1995; Furbish and Fagherazzi, 2001; Furbish, 2003; Mudd and Furbish, 2004; Mudd and Furbish, 2007). On this hillslope, the $^{26}$Al/$^{10}$Be ratios are lowest ~45 m downslope (Table 2), suggesting that signals of changes in incision rate are propagating upslope, to which $P$ and $H$ near the footslope have already adjusted, and which the upper part of the hillslope has not yet "felt". The mass balance method calculates from upslope to downslope, so a zone of nonsteady-state conditions would affect the calculation of erosion rate values from that point to the base of the hillslope. We do not have a way to distinguish between these possibilities and acknowledge that a combination of the above scenarios is also possible.

A similar threshold of ~40 m appears in the chemical erosion rate. $W$ increases with distance downslope from ~1.7 to 10 g m$^{-2}$ y$^{-1}$, but is essentially constant below ~35 m (Fig. 6a). $W_\Phi$ is positive and the peak chemical loss from incorporated saprolite occurs on the backslope, coincident with the peak in saprolite erosion rate (Fig. 6a). This pattern is similar to that observed by Dixon et al. (2009) in the Sierra Nevada. They found that with faster erosion rates, less chemically-altered bedrock was incorporated into the soil, and this "fresher" material subsequently weathered in the soil and increased the apparent soil chemical erosion rate. Where erosion rates were slower, the bedrock was more chemically-altered prior to its incorporation into the soil and thus experienced less chemical erosion once in the soil. In contrast with $W_\Phi$, $W_S$ is negligible at the crest then shifts from negative (net gain) on the upper 40 m of the hillslope, to positive (net loss) towards the base of the slope (Fig. 6a). Yoo et al. (2007) interpreted increasing chemical gain in the downslope direction on a hillslope in Australia as the result of the lateral translocation of clay. However, in this study, particle size measurements show that clay content is actually lowest where $W_S$ shows the most net chemical gain (Fig. 6b) and an explanation is not readily available. Towards the base of the slope, where negative $W_S$ values indicate chemical loss, it is possible that more products of chemical weathering are moved into

70

the underlying saprolite and weathered bedrock. Indeed, the thickness and prominence of clay films in the saprolite in the bottom of the excavations increases with distance downslope, as does $C_{ir}$, suggesting significant chemical transport occurring below the physically-disturbed soil. In the soil, chemical erosion is a small component (less than 20%) of total soil erosion. A mass balance model that includes both saprolite and unweathered bedrock in addition to soil (e.g., Anderson et al., 2002; Yoo and Mudd, 2008; Dixon et al., 2009) would better capture the geochemical fluxes on this hillslope, but unweathered bedrock could not be sampled from the excavations.

The inclusion of $W_S$ in $W$ suggests a greater chemical loss at the base of the slope than a $W$ based on $W_\Phi$ alone does. As a result, the CDF and ECDF are similar on the upper parts of the hillslope, then diverge coincident with the change in sign of $W_S$ downslope (Fig. 6c). Whereas CDF increases then decreases, ECDF increases gradually for the first 40 m then increases nearly exponentially below that. When integrated over the entire hillslope, ECDF and CDF are both 0.19 because the positive and negative components of $W_S$ cancel each other out.

The total soil residence time, $T_{Rt}$, ranges between 245-480 years, with the shortest residence times ~40 m downslope where bedrock erosion rates peak and physical and chemical erosion rates plateau (Fig. 6d). $T_{Rt}$ is dominated by $T_{RE}$, which is expected on any soil-mantled hillslope since $P$ will always be $\leq \nabla \cdot \tilde{Q}_s$. $T_{R\phi}$ increases with distance downslope from 2,600 y to >50,000 y, while $T_{RE}$ and $T_{Rt}$ decrease from ~500 y to 300 y. Integrating over the hillslope, the total transport time is ~6,000 y, whereas if only $T_{R\phi}$ is considered, the transport time is >300 ky. If we convert the total transport time into a velocity by dividing by the hillslope length, the upper ~20 cm of soil move ~0.8 cm y$^{-1}$. This velocity is similar to calculations using field measurements on humid hillslopes (Young,1960; Fleming and Johnson, 1975). These calculations highlight the importance of considering lateral transport on soil residence time. They also suggest that the soil is physically eroded before it can be greatly chemically eroded, given the ~$10^3$ y total transport time.

## Arid Hillslope

### *Observations*
The arid hillslope lies in the midst of a broad biotic-to-abiotic transition zone, and has extremely thin soil (mostly <2 cm) and sparse biota (Fig. 2b). The lack of soil indicates that this hillslope is "weathering-limited" (i.e., soil erosion exceeds production, Carson and Kirkby, 1972) which (1) is a different situation from the semiarid site, and (2) means that it may not conform to the assumptions inherent to the soil mass balance model. Before even considering soil chemistry or the rates of hillslope processes, it is evident that some geomorphic threshold of precipitation and life has been crossed.

The soil cover, where present, is dominated by coarse sand and fine gravels that have an abrupt contact with the coarsely fractured bedrock below (Figs. 7a, 8). Road cuts in the area reveal bedrock joint systems extending at least 6 m deep. Vertical fractures in the near-surface bedrock are filled with fine, reddish-brown dust which is loose in the fractures and rarely forms films on the rock fragment faces. The bedrock shows almost no evidence of chemical weathering (only a few reddish rinds are detectable in thin section), but small accumulations of

gypsum and halite in microfractures are detectable with EDS (Fig. 7b). Based on observations during a fog event, the dust may act as a wick transporting fog water and atmospherically-derived salt into the fractured bedrock. Bedrock fragments extend vertically into the thin soil cover and the upper ends of these fragments appear rounded and slightly chemically altered (Fig. 7c). This rounding may be due to salt-driven granular disintegration as fog condensation becomes periodically available, and may be the primary way bedrock material is incorporated into the soil at this site. Vegetation covers 6% of the ground surface and is comprised of a few shrubs and very few cacti (Fig. 2b). These plants subsist on fog water and tend to grow in convergent areas (Fig. 2b). Roots and root traces were found in dust-filled fractures across the hillslopes (Fig. 7c). Over long time scales, the small bioturbative effect of vegetation is dispersed over the entire hillslope and could pry some bedrock apart and convert it to soil.

Though thin, soil thickness increases slightly downslope, from ~2 to 6.5 cm (Table 2), following a weak linear trend (Fig. A2a). The main outliers in soil thickness are soils 4 and 6. The bedrock in soil 4 was hydrothermally altered and appeared to be more susceptible to weathering, with deeper fine-fracturing of the rock and higher silt content (Fig. 8) compared to the other soils. Soil 6 was adjacent to a broad (1-2 m), flat channel at the base of the hillslope and likely accumulates material from upslope during the dry periods between the rainfall events which are capable of removing the sediment. Thus, for soil erosion modeling we use the average soil thickness of soils 1-5, which are the most representative of the entire hillslope.

The soil is less dense than the underlying rock due to the presence of the fine dust, averaging 1.2 g cm$^{-3}$. Soil bulk density decreases slightly with distance downslope (Table 2, Fig. A2b). The nature of the fractured bedrock prevented direct measurement of the density of this material, but based on the rock density (2.6 g cm$^{-3}$) and degree of fracturing, an estimate of 2.5 g cm$^{-3}$ was used in our calculations.

The redness of the dust suggests that is has been chemically weathered, and the chemical analysis confirms this. $C_{is}$ is greater than $C_{ir}$, averaging 1200 ppm vs. 550 ppm, respectively (Table 2), and both vary non-systematically with $x$ (Fig. A2c). The $C_{is}$ of most of the soils was very similar. However, soil 4 has a high $C_{is}$ compared to the other soils, possibly a result of the hydrothermal alteration. Soil 6 has a low $C_{is}$, possibly due to its proximity to the channel which might increase the removal of fines during rare overland flow events. Three different linear trends for $C_{is}$ were tested in the erosion calculations: (1) fit through all the soils, (2) fit through all the soils except 4, and (3) fit through all the soils except 4 and 6. All produce essentially the same values for $W$ and $Q_s$, so case 1 was used. Though a parabolic trend appears to have a better correlation with the data than a linear one, the high uncertainty in the measurements (standard deviation is about ±25%) do not support use of a more complex trend. $C_{ir}$ decreased with $x$ except for the uppermost soil, where $C_{ir}$ was the lowest (Fig. A2c). The trend selected for $C_{ir}$ had some effect on the pattern of $W$, but because there is so little variation in $C_{ir}$ (average±st. dev. = 550±134 ppm) and the measurement uncertainty was high (>25%), the average value was used.

The proportion of soil production from atmospheric input is likely higher in the arid region compared to the semiarid region, largely due to much lower $P$. The hillslope has nearly constant $P$, which decreases from 2.93±0.22 m My$^{-1}$ at the top to 2.61±0.11 m My$^{-1}$ at the base

(Table 2, Fig. A2d). This is an order of magnitude slower than the semiarid hillslope and reflects the changes in bedrock erosion mechanisms with decreasing precipitation and vegetation. Despite its remote location, all but one of the dust traps were stolen. The remaining dust trap was severely corroded due to exposure to the salt-bearing fog, with ~19 g of light grey material of non-atmospheric origin produced in the trap (Table 4). The large amount of material confounded accurate ICP analysis, but the data indicate high Cl and Al concentrations, with a Cl⁻ concentration 2-3 orders of magnitude larger than the hyperarid atmospheric input, and an Al/Si ratio 1.5-3 times larger (Table 4). High Cl is not surprising given the site's proximity to the ocean and the frequency of fog. The high Al relative to Si is inconsistent with the compositions of the local soils or dust inputs at the hyperarid site. Chloride solutions in contact with Al produce pitting corrosion, such as was observed in the trap, and the corrosion product is likely an aluminum oxychloride (such as $Al(OH)_2Cl$ or $Al(OH)Cl_2$) (Nguyen and Foley, 1980). The formation of the aluminum oxychloride was likely enhanced by the presence of nitrate, which also has a strong reactivity with aluminum and produces ammonium gas (Nguyen and Foley, 1980). This reactivity could explain the low nitrate concentration in the pan compared to dust collectors in the hyperarid locations discussed below (Table 4). We attempted to correct the dust collector chemistry data for the excess (non-atmospheric) Al and O using the Al/Si ratio from the hyperarid dust traps, but the results were unsatisfactory due to the large uncertainty in the original data. As such, the erosion calculations were constrained using two end-members of atmospheric inputs: (1) assuming $A = 0$, and (2) assuming $A$ equal to that at the hyperarid site ($2.59$ g m$^{-2}$ y$^{-1}$ with $C_{iA} = 1472$ ppm, Table 4). The hyperarid value of $A$ is about 40% of the average $P$ at this site. Since soil production is through some combination of bedrock erosion and atmospheric input, we rephrase the designation of "weathering-limited" to "production-limited" to better represent the inputs to the soil.

The little soil available is eroded through some combination of bioturbation and overland flow, despite the arid climate. As mentioned above, root growth dilates the soil slightly, but the effect of animals is likely more significant. Paths formed by guanacos (coastal cameloids) crisscross the hills in this region, and this trampling helps to dislodge bedrock fragments and mobilize them downslope. Although burrowing lizards and insects are present in the region, they were generally found only on the plains surrounding the hills, but not on the hills themselves due to the shallow soil cover.

Small-scale gravel sorting on the hillslopes (Fig. 7d) suggests that rare overland flow events contribute to soil transport. Sprinkling experiments revealed fast and deep infiltration, promoted by the degree of fracturing in the rock. The infiltration rate increased from 3.3-25.3 cm hr$^{-1}$ as application rate increased from 5.5-52.5 cm hr$^{-1}$ (Table 3). Only fine sediment was mobilized during the sprinkling experiments. Gravel was unaffected even at the highest application rate, but this was with a small source area. The experimental application rates exceed any recorded precipitation events (Rundel et al., 1996) which suggests that gravel transport is a rare occurrence. If bioturbation and overland flow are the primary soil transport mechanisms, then transport is likely slope-dependent in some fashion.

$^{26}$Al/$^{10}$Be ratios are mostly slightly below the expected steady-state $^{26}$Al/$^{10}$Be ratio (Table 2, Fig. 9). This indicates a complex exposure history, likely involving burial and reexposure. As discussed above, MAP has varied throughout the Quaternary and it is reasonable to expect that

73

the rates of geomorphic processes and the soil mass balance have responded to a small degree. However, because they are near the steady-state line, within error, the assumption of steady state may not be unreasonable. As discussed below, the thinness of the soil and errors associated with other inputs to the soil mass balance modeling approach are greater problems in the application of this method.

### *Soil Erosion and Residence Time*

The extreme thinness of the soil, the non-systematic variation in $C_{is}$, and the difficulty in constraining atmospheric input chemistry, make calculations of chemical and physical erosion on the arid hillslope tenuous at best. The values of $\tilde{Q}_s$ and $W$ will be minimum values since the soils are production-limited. Additionally, the analysis of the $\nabla z$-dependence of $\tilde{Q}_s$ is limited by the narrow range of $\nabla z$ on the hillslope, which ranges between 0.2 and 0.7 but is primarily 0.51±0.05. We include these calculations for completeness and acknowledge the limitations of this exercise.

On a hillslope that is production-limited, the rate of soil production will be the determining factor on soil flux across the entire hillslope. Plots of $\tilde{Q}_s$ vs. $\nabla z$ and $H\nabla z$ are similar because the soil thickness was set as constant in these calculations (Fig. 10). However, the linear fit to the data has a higher slope (i.e. a greater value of $K_s$ or $K_h$) when $A$ is included, and lower slope when it is not, because including $A$ provides more material for transport (Fig. 10). $K_s$ ranges from $7\times10^{-5}$ to $2\times10^{-4}$ $m^2$ $y^{-1}$ (depending on $A$), while $K_h$ ranges from $3.4\times10^{-3}$ to $9\times10^{-3}$ m $y^{-1}$ (Figs. 10a and c). When tested for covariance with distance downslope, plots of $\tilde{Q}_s\nabla z^{-1}$ and $\tilde{Q}_s(H\nabla z)^{-1}$ vs. $x$ (Figs. 10b and d) show that when $A$ is not included the values are nearly constant, though lower than the respective $K_s$ or $K_h$. Though these models seem to capture some elements of soil flux, the small amounts of salt observed in the soil, and the silicate dust observed in the dust trap (amidst the aluminum oxide), indicate $A$ is nonzero at the arid site. When $A$ is included, the values of $\tilde{Q}_s\nabla z^{-1}$ and $\tilde{Q}_s(H\nabla z)^{-1}$ increase with $x$ and are lower than the respective $K_s$ or $K_h$. Thus, neither the $\nabla z$- nor the $H\nabla z$-dependent model satisfactorily describes soil flux across the hillslope, particularly towards the base of the hillslope.

The steep, planar nature of the hillslope (Fig. 2g) suggests that a $S_c$-dependent transport law (Eq.10) will be a better fit. Using soil flux calculated assuming a value of $A$ equivalent to the hyperarid site (which gives maximum values for $K_c$), the data are bounded by $\tilde{Q}_s$ values calculated using $K_c = 2\times10^{-3}$ m $y^{-1}$ and $S_c = 0.55$ (left dashed line, Fig. 16a), and $K_c = 1.2\times10^{-3}$ m $y^{-1}$ and $S_c = 0.70$ (right dashed line, Fig. 10e). We have included $H$ in the equation, though it could be ignored since it is constant. The best fit to the data lies between the two, with $K_c = 1.6\times10^{-3}$ m $y^{-1}$ and $S_c = 0.65$ (solid line, Fig. 10e). The test for covariation shows that the values of $\tilde{Q}_s(1-(\nabla z/S_c)^2)(H\nabla z)^{-1}$ vary homoscedastically around the value of $K_c$ and suggests that the critical slope model may be the most appropriate (Fig. 10f).

The $S_c$-dependent model appears to constrain the data well, but the sorted surface gravels indicate that the overland flow model (Eq. 11) could be important. The data are best fit with $\tilde{Q}_s$ calculated with $K_w = 1\times10^{-5}$ m $y^{-1}$, $n = 1$, and $m = 1$ (Figs. 10g and h). However, this fit does not work well at low $\nabla z$, which corresponds to the uppermost part of the hillslope ($x < 5$ m). Braun et al. (2001) showed that for an Australian hillslope, the mechanisms that drove soil transport changed with distance downslope and a combination of transport laws best captured soil flux

across the hillslope.  The arid site may be similar.  The thinness of the soil confounded assigning a soil transport law for the top of the hill ($x < 5$ m) where soil is thinnest, but the soil transport mechanism appears to switch to overland flow on the lower parts.  This is consistent with the field observations of the occurrence of the sorted gravel bands, which start at some distance downslope of the crest.

$W$ decreases slightly with distance downslope, from 3.8 to 2.2 g m$^2$ y$^{-1}$ if $A$ is included, and from 4.2 to 3.7 g m$^2$ y$^{-1}$ if $A = 0$ (Figs. 11a-b).  Because $W_s$ is near zero, $W$ is predominantly determined by $W_\Phi$ and the assumed $A$, as expected in a production-limited system.  Assuming $A$ is equal to the hyperarid measurements halves $W$ and its components, due to the addition of atmospheric material that is relatively Ti-rich, with 1470 ppm in the atmospheric input vs. 550 ppm in the bedrock and 1200 ppm in the soil (Table 2).  Thus, the $W$ calculated assuming no atmospheric input is the maximum chemical erosion possible, and the hillslope is likely experiencing less than that value.  Additional modeling using different trends for $C_{is}$, $C_{ir}$, and $H$ produced slightly different $W$ values, but overall $W$ was small and positive (indicative of slight loss), consistent with field observations.  When $W_s$ is low, as it is here, the difference between the CDF and ECDF is small and the spatial trends of the CDF and ECDF are entirely dependent on that of the soil inputs (Fig. 11c).  However, with $A$ potentially equaling ~30% of $P$, the calculation of CDF and ECDF is dependent on $A$.  In this case, including $A$ decreases the CDF from ~0.55 to ~0.1 and changes the interpretation of the primary source of the dust from bedrock weathering to atmospheric input.  The emplacement of stainless steel dust collectors at better-hidden locations would address this question.

Soil residence time calculations are complicated by the low soil thickness and dependent on the assumption of the value for $A$.  If $A$ is equal to the hyperarid input rate, $T_{R\phi}$ decreases from 4.5 ky to 4.0 ky with $x$, $T_{RE}$ decreases more rapidly from 2.5 ky to 0.3 ky, and $T_{Rt}$ decreases from 1.6 ky to 0.3 ky (Fig. 11d).  Alternatively, if $A = 0$, then the residence times are about twice as long but follow similar patterns, with $T_{R\phi}$ decreasing from 8.7 ky to 8.4 ky, $T_{RE}$ decreasing more rapidly from 3.1 ky to 0.6 ky, and $T_{Rt}$ decreasing from 3.1 ky to 0.6 ky (not shown)   The slight decrease in soil residence time with distance downslope is similar pattern to $W$.  This concurrence is expected, since near the crest the slope gradient and $\tilde{Q}_s$ are lowest and give water the longest time to react with the soil.  Total transport time also varies by a factor of two depending on $A$, ranging from 11 ky if $A$ is equivalent to the hyperarid rate, to 22 ky if $A$ is 0.  The true value likely lies between the two.  These fairly short soil residence times and transport times leave little time for chemical weathering to occur, as calculated above.

In summary, the arid hillslope is unique along the precipitation gradient because it is production-limited and essentially soil-free.  Though some chemical weathering has occurred based on both the field observations and erosion calculations, the underlying bedrock is fresh and lacks the saprolite observed at the semiarid site.  The arid hillslope was wetter in the past and likely had soil and saprolite.  The absence of soil and saprolite on the hillslope at present suggest that the hillslope was stripped to bedrock during aridification, a process that has also been inferred to have occured in the Mojave Desert (Oberlander, 1972).

## Hyperarid Hillslope

*Observations*

The soils on the hyperarid hillslope are different from the other two sites because they contain a large proportion of salt in addition to fine silicate dust and bedrock fragments ranging from sand to cobble size (Table 5, Figs. 12 and 13). Biotic processes are essentially absent (Fig. 2c), with no plants present at all.

The soil excavations reveal a thin (~1-2 cm) layer of loose, fine-grained, silicate-rich soil at the surface which is underlain by salt-rich, porous horizons with weak to moderate polygonal structure (Fig. 12a). Below these horizons lie increasingly salt-cemented, gravel-rich horizons with coarse polygonal structure (Fig. 12b). The gravels are sharply angular and lack evidence of chemical weathering, even those on the surface. Road cuts reveal deep (>4m) fracture systems in the bedrock that are permeated with gypsum and halite, but the bedrock has not been chemically altered (Fig. 12c). Salt intrusion into rock also occurs at the microscopic scale (Fig. 12d) and likely contributes to rock disintegration.

Determining the location of the soil-bedrock interface was a challenge due to the salt intrusion into the rock and the lateral heterogeneity of the soil. We consider the relevant soil depth to be the base of the soil horizon with polygonal structure development. The contact was abrupt, marked by a distinct shift in gravel content from ≤25% in the overlying horizons to ≥50% below, though it was wavy to irregular. Soil thickness increases slightly with distance downslope from ~6 cm to a maximum of 9 cm (Table 2). A linear trend for $H$ is most appropriate given the variation observed in the excavations (Fig. A3a). The excavations on this hillslope were shallow, but a nearby road cut confirmed that fractured bedrock occurs at shallow depths on relatively steep slopes (Fig. 12c). On other, gentler hillslopes in the hyperarid region, the salt-rich soil reaches ~1 m thick.

Sulfate (as anhydrite and gypsum) is the most common salt in the soil and increased slightly with distance downslope (Table 5, Fig. 13b). Nitrate, chloride, and iodine (likely as iodate) were present in smaller amounts and vary little or randomly with distance downslope (Table 5, Fig.13c). The salt-rich horizons often have high porosity and the depth-averaged soil bulk density is consistently less than 1 g cm$^{-3}$ (Table 2). The soil bulk density decreases linearly with $x$. Bedrock bulk density also decreases linearly with $x$ (Fig. A3b), likely due to the increased degree of bedrock fracturing (and subsequent salt infilling).

Field observations suggest that salt pries apart the rock using pre-existing fractures and eventually "lifts" bedrock fragments into the soil column through salt growth and shrink-swell (Figs. 12a and c). Crystallization pressures of gypsum and halite have been modeled to be more than adequate to fracture rock (Winkler and Singer, 1972; Steiger, 2005), and many experimental studies support this (eg. Cardell et al., 2003; Viles and Goudie, 2007; Rodrigues-Navarro and Doehne, 1999). However, due to the infrequency of moisture-related salt shrink-swell under current conditions, bedrock erosion rates are extremely slow. CRN-derived bedrock erosion rates are nearly constant, increasing slightly from 0.98 to 1.20 m My$^{-1}$ with $x$ (Table 2, Fig. A3d).

These values of $P$ are among the lowest measured on Earth, equivalent to 2-2.5 g m$^{-2}$ y$^{-1}$. For comparison, $A$ is $2.59 \pm 0.21$ g m$^{-2}$ y$^{-1}$ (Table 4). As a result, the soil chemistry is strongly dependent on the chemistry of the atmospheric input. $C_{is}$ ranges from 2500 to 1000 ppm (Table 2, Fig. A3c), while $C_{ir}$ decreases linearly with distance downslope from 4000 to 2500 ppm (Fig. A3c), partly due to the increase in salt content in the underlying bedrock (Table 2). $C_{ir}$ is significantly greater than $C_{is}$, which is the opposite of what is observed in chemically eroded soils and implies significant chemical gain. $C_{iA}$ is $1470 \pm 350$ ppm (Table 4), comparable to the average $C_{is}$ ($1320 \pm 580$ ppm). The values of $C_{iA}$ and $A$ are similar to those determined by Ewing et al. (2006) in the same area and those from dust traps at a nearby site (ORH, ~70 km south) (Table 4), suggesting that $A$ is fairly uniform over the region. Though the dust traps provide only a short-term measure of atmospheric deposition, there is good agreement between the dust traps and geologic estimates for salt deposition rates (Ewing et al., 2006). The chemistry of the soil compared to the bedrock and the atmospheric input suggest that the soils are formed through the retention of atmospheric inputs, rather than the weathering of inputs from bedrock.

$C_{is}$ in the uppermost soil on the hillslope (2545 ppm) is significantly higher than the four other excavations ($1320 \pm 239$ ppm). Thus, the trend used in the erosion calculations could include uppermost soil as representative of the heterogeneity of soils on the hillslope, ignore it as an anomaly, or simply average it in with the rest. The distribution of soil salts with depth and distance downslope offers some guidance in selecting the appropriate trend for the erosion rate modeling. Field observations and soil chemistry data indicate vertical chemical transport produces the silicate rich surface horizon and salt-rich underlying horizons. The slight increase in sulfate concentration with distance downslope (Fig. 13b) requires chemical gain to increase (i.e., $W$ to become more negative). Of the three trends described above, only a linear fit through all 5 data points produces this pattern of chemical erosion when plugged into the erosion calculations.

The soil salt drives not only bedrock erosion but possibly soil erosion as well. The polygonal structure in the soil is likely formed through shrink-swell processes, although some soil cracks in northern Chile may result from earthquakes (Loveless et al., 2005; Loveless et al., 2009). Seismic shaking disturbs the soil in a non-regular way (Keefer and Moseley, 2004), but the material filling some of the larger cracks is layered, indicative of progressive crack opening and in-filling as would be expected with shrink-swell processes. The wetting events that drive soil shrinking and swelling must be extremely rare, given the preservation of salts in the soils and the lack of chemical weathering of the bedrock. Transport by clay shrink-swell is slope-dependent (e.g. Fleming and Johnson, 1975), and, though no work has been done on salt-driven soil transport, it is likely also slope-dependent.

Soil shrink-swell is not the only transport process. Surface gravels on hillslopes throughout the hyperarid region are sorted into contour-parallel bands (Fig. 14), most likely by extremely rare overland flow (discussed in Chapter 4). Transport of soil and surface gravels by overland flow would follow equation 11. Thus, it is likely that soil transport is primarily slope-dependent, but as a combination of slow creep processes and rare overland flow.

Lastly, the $^{26}$Al/$^{10}$Be ratios of the hillslope bedrock samples plot within the erosion window, within error (Fig. 15), indicating that soil thickness and erosion rate may be approaching steady state. Thus, the use of the soil mass balance approach seems reasonable.

### Soil Erosion and Residence Time

As at the arid site, analysis of the slope dependence of soil flux is limited by the small range of $\nabla z$ across the hillslope, which varies from 0.4 to 0.6. $\tilde{Q}_s$ is not linearly related to $\nabla z$ or $H\nabla z$ (Figs. 16a and c). In the tests for covariation, a strong ($r^2 = 0.80$ and 0.85, respectively) linear increase with $x$ is observed (Figs. 16b, d). Even if we exclude the four data points with the highest $\tilde{Q}_s$, which improves the linear correlation between $\tilde{Q}_s$ and $H\nabla z$, the covariation with distance downslope is not removed. Despite the poorness-of-fit, $K_s$ and $K_h$ are as much as an order of magnitude smaller than calculated for the semiarid hillslope, which indicates that significantly slower processes are at work, even at similar values of $\nabla z$. The surprising implication of the poor fit of equations 8 and 9 is that soil creep is not an important component of soil transport here, despite the evidence of significant soil shrink-swell described above.

The convexo-planar profile of the hillslope suggests that a critical slope-dependent transport law (Eq. 10) may be more appropriate. The hillslope data were bounded by models of $\tilde{Q}_s$, with $K_c = 2.5\times10^{-5}$ m y$^{-1}$ and $S_c = 0.75$ defining the high-$\nabla z$ boundary (right dashed line, Fig. 16e), and $K_c = 1\times10^{-4}$ m y$^{-1}$ and $S_c = 0.53$ defining the low-$\nabla z$ boundary (left dashed line, Fig. 16e). The best fit for the data lie somewhere between the two, and our estimate is $K_c = 5\times10^{-5}$ m y$^{-1}$ and $S_c = 0.68$ (solid line, Fig. 16e). The test for covariation (Fig. 16f) shows that the data increase slightly with $x$ and the greatest scatter is towards the base of the hillslope. Thus, while this model appears to better capture soil flux than equations 8 and 9, it may not be the best option.

The gravel sorting on the hillslopes reveals that, despite its rarity, overland flow may be an important component of soil transport. Using equation 12, $K_w = 4\times10^{-6}$ y$^{-1}$, $m = 2$, and $n = 2$ provided the best fit for the majority of the data ($x>5$ m, Fig. 16g), though in the test for covariation this model works best for $x>5$ m (Fig. 16h). The best transport model may be a combination of the $S_c$-dependent model and the overland flow model, with overland flow increasingly important towards the base of the slope.

As discussed above, the trend of $C_{is}$ was selected to produce increasing chemical gains (more negative $W$) with distance downslope. $W_\Phi$ decreased from -3.2 to -5.7 g m$^{-2}$ y$^{-1}$ and $W_s$ decreased from 0 to -6.6 g m$^{-2}$ y$^{-1}$, such that the total chemical erosion was -12 g m$^{-2}$ y$^{-1}$ at the base of the hillslope (Fig. 17a). Chemical gain has previously been measured on a hillslope in Australia, likely due to the precipitation of clay from the soil solution in soils near the base of the slope (Yoo et al., 2007). Here, salt, rather than clay, is being concentrated in a process that is likely much slower given the infrequency of soil wetting. These values imply that salt is preferentially retained on the hillslopes compared to the material derived from the bedrock, though the mechanism for this is unclear. Because $W_s$ is of similar magnitude to $W_\Phi$, CDF and ECDF values diverge with distance downslope, though both are negative (Fig. 17b). CDF values decrease from -0.5 to -1.0 while ECDF values decrease from -0.5 to -2.2. This site is the first case where CDF (and/or ECDF) values are consistently negative, highlighting the unique nature of soils in this climatic zone.

78

The soil residence time ranges from ~300-3600 y (Fig. 17c) and total transport time is ~33 ky. The shortest soil residence times are towards the base of the hillslope where they are surprisingly similar in magnitude to the semiarid site. They are surprising given the appearance of a landscape immobilized by salt, but the thinness of the soils and the steepness of the slope contribute to relatively rapid turnover. As a check, the magnitude of the soil residence time and total transport time can be explored using the soil salt inventory independent of the erosion modeling, as we do below.

The mass of salt-forming anions ($NO_3^-$, $Cl^-$, and $SO_4^{-2}$) in the soils and the rate of their input is known, thus their residence time in the soil can be calculated (Table 5). This is the same as the calculation of $T_{R\phi}$ but does not include the silicate component. Because it does not consider the lateral transport of salt, this calculation will be a maximum salt residence time. Considering only the anions of the salt avoids the complexity of salt composition in this region. Across the hillslope, the residence time of $NO_3^-$ is less than 100 y, likely due to the high solubility of nitrate enabling relatively rapid transport from the surface into the fractured bedrock below our sampling depths (Table 5). The residence time of $Cl^-$ ranges between 500-1,500 y, but halite is also highly soluble (Table 5). In contrast, sulfates are less soluble and the residence time of $SO_4^{-2}$ ranges from 6-20 ky, up to an order of magnitude greater than the bulk soil residence time (Table 5). This sulfate-based residence time must be higher than the actual residence time, thus it supports the relatively short bulk-soil residence time calculated using the soil mass balance model.

The hyperarid hillslope is unique along this precipitation gradient because it is free of biota and yet manages to sustain a soil mantle, albeit one composed primarily of salt. Though salt appears to drive some soil transport through shrink-swell, surface gravel patterning indicates that overland flow occurs. The tests of the different transport equations support that most soil transport may be through overland flow. The similarity of the soil residence time to that at the semiarid site was surprising given the appearance of hillslope inactivity, but the salt residence time supports the mass balance-derived calculation.

In summary, the three hillslopes in this study range from relatively wet and biotically-driven to extremely dry, salt-rich, and precipitation-sensitive. Below, we summarize and compare the results from the different hillslopes to examine the effect of precipitation on hillslope soil formation and to identify the MAP that defines a pedologic and geomorphic threshold .

## GEOMORPHIC AND PEDOLOGIC EFFECTS OF PRECIPITATION AND VEGETATION

Soil thickness is the first indication of the changes in the soil mass balance in response to MAP. The semiarid site has a relatively thick, chemically weathered soil, indicating a transport-limited system. This is similar to most gentle hillslopes around the world. With increasing aridity, the soil mantle disappears and the arid hillslope becomes production-limited. The soil mantle returns under even more arid conditions, as seen on the hyperarid hillslope, but this soil mantle is only partly derived from the underlying bedrock. Instead, over half of the hyperarid hillslope soil is produced through the retention of atmospheric inputs. In this case, the soil may

be considered transport-limited, although a better description may be "climate-limited", as discussed below.

These changes in soil thickness with MAP are coupled with changes in the rates and types of soil production and transport mechanisms.  Hillslope-averaged rates of soil production from bedrock, physical erosion, and chemical erosion are dependent on MAP (Fig. 18).  This plot also reveals that the mass balance approach is behaving as expected, with soil inputs ($P+A$) only slightly higher than soil outputs ($W+\nabla \cdot \tilde{Q}_s$).  Included in Figure 18 and our discussion below is data from Frog's Hollow, the gentle granitic hillslope in Australia that was the subject of Yoo et al. (2007) and the only other site where comparable measurements have been made.  Frog's Hollow is much wetter than the sites here, with MAP = 650 mm, and is located in eucalyptus savannah.

The most surprising result from this work is that $P$ on these hillslopes are strongly correlated to MAP (Fig. 19a).  Previous work has focused on erosion rates on hillslopes in semiarid to humid climates which have no dependence on MAP (Fig. 19a).  For MAP>100 mm, the variation in $P$ at a given MAP is greater than that between different MAP values.  A similar compilation, using catchment-averaged erosion rates determined from CRN in stream sediment, revealed a similar trend (von Blanckenburg et al., 2006).  The absence of a climate signal in erosion rates was attributed to the overriding importance of factors other than MAP, particularly variations in tectonic setting (i.e. local boundary conditions) and chemical erosion.  Thus, MAP~100 mm defines a geomorphic threshold between MAP-dependent and MAP-independent bedrock erosion rates.  This geomorphic threshold coincides with a threshold in net primary productivity (NPP) (Leith, 1973; Fig. 19b), which we use as a measure of the biotic influence on the landscape, and would imply that humid, vegetated landscapes are (1) more sensitive to varying boundary conditions and (2) subject to more variation in chemical erosion.  The observations along the Chilean MAP gradient presented here provide some explanation as to why this may be the case.

We begin with a brief review of the coupling between $P$ and channel incision rates, which set the hillslope basal boundary condition.  Hillslopes evolve in response to channel incision via two relationships: slope-dependent soil flux and depth-dependent $P$.  First, slope-dependent soil flux enables "communication" between the boundary condition at the base of the slope and the soils upslope from it (Kirkby, 1971; Ahnert, 1987; Armstrong, 1987; Anderson and Humphrey, 1989; Fernandes and Dietrich, 1997).  Increased incision will locally steepen the toe of the hillslope and, if soil flux is a function of slope (Eqs. 8-11, for example), increase soil flux.  Second, depth-dependent bedrock erosion enables this change in soil flux to be translated into a change in bedrock erosion.  If incision rates increase at the hillslope base, steepening slopes increase soil flux which thins the soil.  Thinner soil increases $P$ and the coupled soil erosion-hillslope form-soil thickness system moves towards a new equilibrium (e.g., Penck, 1953; Ahnert, 1970; Dietrich et al., 1995; Furbish and Fagherazzi, 2001; Furbish, 2003; Mudd and Furbish, 2004; Mudd and Furbish, 2007).  A constant incision rate can produce steady-state soil thicknesses in the upslope positions, whereas the cessation of incision leads to progressive upslope deviation from steady-state.

Hillslope boundary conditions in this study are MAP-dependent. Stream channel incision rates increased with MAP, from ~1.3 m My$^{-1}$ at the hyperarid site, to 3.7 m My$^{-1}$ at the arid site, and to 34 m My$^{-1}$ at the semiarid site (Table 1), despite similar Holocene uplift rates (Fig. 1d). A striking feature of the topographic profiles of channels in northern Chile is that they are all convex and many contain large knickpoints (Mortimer, 1980). These profiles indicate that stream incision is not in equilibrium with sea level, particularly east of the Coast Range. There is simply inadequate rainfall. As a result, the hyperarid and arid landscapes are largely isolated from changes in sea level (due to climate or tectonic uplift) because of the low MAP. As MAP increases to the south, stream channel profiles become concave (Mortimer, 1980). These profiles indicate that stream channel incision is more responsive to changes in sea level, and the signal of these changes is propagated upchannel relatively rapidly. Thus, stream channel incision rates in humid and some semiarid climates are primarily a function of tectonics and geologic factors rather than water availability, whereas in hyperarid to arid climates they are controlled by MAP and past base level conditions.

The soil transport mechanisms affect the sensitivity of a hillslope to changes in boundary condition through the transport coefficient in the soil transport law, which captures the "efficiency" of the mechanism and is independent of slope. As shown above, MAP determines vegetation (NPP) and the types of erosion mechanisms active on a hillslope. On gentle (non-landsliding) hillslopes in humid and semiarid climates, including the semiarid site in this study, soil transport is often primarily through bioturbation as burrowing and/or tree-throw. As MAP decreases, soil transport shifts from being driven by biotic mechanisms to abiotic ones, particularly overland flow and possibly some salt shrink-swell. As a result, one might expect both physical erosion rates ($\nabla \cdot \tilde{Q}_s$) and transport coefficients ($K$ values) to increase with increasing MAP.

A comparison of $\nabla \cdot \tilde{Q}_s$ values on the hillslopes demonstrates the importance of $K$. Total physical erosion rate varies depending on the length of the hillslope, so here we compare hillslope segments of similar length. The hillslope segments are ~13 m long, the length of the shortest hillslope (hyperarid), and begin at the top of each hillslope. Though $\nabla \cdot \tilde{Q}_s$ is greatest on the semiarid hillslope segment (349 g m$^{-1}$ y$^{-1}$), the hyperarid hillslope has the next largest $\nabla \cdot \tilde{Q}_s$ (93 g m$^{-1}$ y$^{-1}$) and the arid site has the lowest value (54 g m$^{-1}$ y$^{-1}$, calculated assuming $A$ is equivalent to the hyperarid site) (Table 6). This is not an effect of the difference in slope between the segments (i.e., decreasing slope with decreasing MAP) because the average slope of the 13 m-long segments increases with decreasing MAP, from 0.20 on the semiarid hillslope, to 0.44 on the arid hillslope, and to 0.52 on the hyperarid hillslope (Table 6). If $\tilde{Q}_s$ was simply a function of slope, then physical erosion would be largest on the hyperarid hillslope. Clearly, the type of process, as manifested in the $K$ value, is a critical factor in $\tilde{Q}_s$.

A challenge in comparing $K$ values is that as the transport mechanisms change with MAP, the appropriate soil transport law (Eqs. 8-11) also changes and the $K$ values are not always comparable between them. This is a particular issue for the overland flow equation, in which the units of $K_w$ are determined by $m$ and $n$. Table 6 lists the various $K$ values calculated for each transport law for each of the sites considered here. As described above, soil flux on the semiarid hillslope is $H\nabla z$-dependent, whereas at the arid and hyperarid hillslopes, soil flux is a function of $\nabla z$ and $x$, and the model is differently parameterized for each site. One way to compare between

the sites is to use the $K_c$ values from the $S_c$-dependent model which, though it was not the most satisfactory at any site, could be constrained for each. Additionally, at low slopes, $K_c$ values are directly comparable to $K_h$ values. A comparison of the $K_h$ value from the semiarid hillslope with the $K_c$ values from the arid and hyperarid hillslopes suggests that $K$ increases nearly two orders of magnitude for a two order of magnitude increase in MAP (Table 6). Though not ideal, this is the first evidence that climate is a factor controlling $K$.

Few other sites have been studied where $K$ values could be calculated, but these data suggest less variation in $K$ where MAP>100 mm. At Frog's Hollow, $K_h = 4.4 \times 10^{-3}$ m y$^{-1}$ (Yoo et al., 2007), a value between those of the semiarid and the arid hillslopes. $K_h$ has been calculated for three other, more humid hillslopes: Nunnock River, Australia (MAP = 900 mm and $K_h = 5.5 \times 10^{-3}$ m y$^{-1}$), Tennessee Valley, California (MAP = 800 mm and $K_h = 1.2 \times 10^{-2}$ m y$^{-1}$), and Point Reyes, California (MAP = 800 mm and $K_h = 5 \times 10^{-3}$ m y$^{-1}$) (Heimsath et al., 2005). These $K_h$ values are based on total soil erosion, rather than just physical erosion, but this does not affect the overall trend. Based on this data, where MAP>100 mm $K_h$ values fall in a narrow range between 4 to $6 \times 10^{-3}$ m y$^{-1}$. However, where MAP<100 mm, $K_h$ values are $\leq 8.7 \times 10^{-3}$ m y$^{-1}$, but likely as much as an order of magnitude smaller than at the semiarid hillslope (Fig. 19c). The range in $K_h$ values at higher MAP is likely due primarily to the variation in the organisms driving bioturbation and stabilizing the soil (Gabet et al., 2003; Istanbulluoglu and Bras, 2006). Tennessee Valley is unique in that the bedrock is metasedimentary rather than granitic as at the other sites. MAP, vegetation, and soil transport processes at Tennessee Valley are similar to those at Point Reyes, thus this geologic difference may explain its substantially higher $K_h$ value.

The other $K$ value in need of discussion is from the semiarid site, where the $K_h$ is higher than all the other semiarid and humid hillslopes except for Tennessee Valley. The difference appears to be the onset of significant chemical erosion on hillslopes where MAP>>100 mm. The hillslope-averaged ECDF of the semiarid hillslope in this study, 0.19, compared to 0.44 at Frog's Hollow (Yoo et al., 2007), the only other site where hillslope-averaged ECDF values have been calculated (Table 6). These ECDF values indicate that the proportion of soil erosion due to chemical erosion doubles, though average bedrock erosion rates are similar, ranging from 8 to 52 g m$^{-1}$ y$^{-1}$ on the semiarid hillslope and from 33 to 53 g m$^{-1}$ y$^{-1}$ at Frog's Hollow. The average slope of the hillslopes is similar (0.18 for Frog's Hollow vs. 0.20 for the semiarid hillslope), therefore, the semiarid hillslope must have a much larger $K$ value to maintain a steady-state soil.

The effect of the MAP-dependence of $\nabla \cdot \tilde{Q}_s$ and $W$ is that soil residence time is MAP-dependent, too. Again, considering only the upper 13 m of each hillslope, the total transport time increases from 1100 y, to 8800 y, to 35000 y, at the semiarid, arid, and hyperarid hillslopes, respectively (Table 6). With such a short residence time, the semiarid hillslope is able to respond faster to changes in boundary condition than the arid or hyperarid hillslopes, and its boundary condition is more sensitive to variations in sea level than the others.

On a global scale, these results suggest that the rate of soil production from bedrock in humid and semiarid climates is more sensitive to tectonic, climatic (i.e., temperature, snowfall, seasonality) and vegetation differences than in arid and hyperarid climates where MAP is the critical factor. Indeed, the hyperarid landscape shows such MAP-sensitivity that, rather considering it "transport-limited" as one would based solely on the presence of a soil mantle, it

would be better described as "climate-limited". Additionally, the hyperarid hillslope highlights the role of atmospheric deposition as another soil production mechanism under certain conditions. The salt component produces opposing effects on soil production from bedrock similar to vegetation, in that it breaks apart the bedrock and contributes to soil transport, but also adds cohesion and stability to the soil. Unfortunately, the absence of atmospheric input rate data for the arid and semiarid sites limits the evaluation of the role of MAP in affecting atmospheric deposition. Nevertheless, these results demonstrate that where the rate of soil production from bedrock and atmospheric deposition rates are within an order of magnitude of each other, ignoring atmospheric deposition would significantly change the calculation of chemical and physical erosion.

In summary, a geomorphic and pedologic threshold lies near MAP = 100 mm. At this point, chemical erosion is low compared to more humid hillslopes, such that physical erosion is the primary soil loss mechanism but life still "drives" the landscape through bioturbation. This landscape is sensitive to tectonically- or climatically-driven changes in boundary condition due to adequate water to drive stream incision and short hillslope soil residence times. As precipitation decreases, vegetation decreases and abiotic processes, especially overland flow, are increasingly important to soil transport. Channels in arid regions will be sensitive to MAP and unable to reach steady state with current base level. At the hyperarid extreme of this climatic gradient: (1) soil production through atmospheric input is as important as that through bedrock erosion, (2) vegetation and biotically-driven geomorphic processes are absent, (3) the soils experience chemical gain rather than loss, and (4) hillslope soil processes are abiotic and extremely sensitive to MAP. Though Dietrich and Perron (2006) found no topographic signature of life, the results presented here suggest that life has a distinct effect on the rates of hillslope soil processes. One metric of this is the transport coefficient, which is sensitive to MAP where MAP<100 mm, and possibly sensitive to differences in vegetation and other soil properties where MAP>100 mm.

## CONCLUSIONS

The Atacama Desert is a unique natural laboratory for the study of hillslope soil characteristic and process rates near the hyperarid limit of life. On three granitic hillslopes along a precipitation gradient (and a corresponding biotic gradient), we measured the rate of soil production through bedrock erosion and atmospheric deposition, then calculated physical and chemical erosion rates using a mass balance model and soil chemical data. These soil production and erosion rates reveal a threshold in geomorphic and pedologic processes near MAP=100 mm. When MAP is below this threshold, these processes are extremely sensitive to climate and the landscape is abiotic. When MAP is above this threshold, the landscape is sensitive to tectonic conditions and variations in biota.

This work is the first to demonstrate that the transport coefficients in the soil transport laws are sensitive to MAP, though more data are needed to constrain how, particularly in vegetated regions where MAP and biota both affect soil transport mechanisms. The comparison of ECDF and CDF shows that lateral soil transport must be considered in order to understand the spatial distribution of chemical and physical erosion on a hillslope. This lateral component is also required to calculate meaningful soil residence times. Though more work than spot measurements or catchment-averaged values, this transect-based approach provides the data

necessary to test soil transport laws and develop more mechanistic models of soil transport processes.

## ACKNOWLEDGEMENTS

## REFERENCES CITED

Ahnert, F. 1970. Functional relationships between denudation, relief, and uplift in large mid-latitude drainage basins. American Journal of Science, 268(3): 243-263.

Ahnert, F. 1987. Approaches to dynamic equilibrium in theoretical simulations of slope development. Earth Surface Processes and Landforms, 12(1): 3-15.

Alpers, C.N., Brimhall, G.H. 1988. Middle Miocene climatic change in the Atacama Desert, Northern Chile - Evidence from supergene mineralization at La Escondida. Geological Society of America Bulletin, 100(10): 1640-1656.

Amundson, R., Ewing, S., Michalski, G., Thiemens, M., Kendall, C., Nishiizumi, K., McKay, C., Chong, G. 2007. The climatic and biotic thresholds on soil elemental cycling along an and to hyperarid rainfall gradient. Geochimica et Cosmochimica Acta, 71(15): A22-A22.

Anderson, R.S., Humphrey, N.F. 1989. Interaction of weathering and transport processes in the evolution of arid landscapes. Quantitative Dynamic Stratigraphy: 349-361.

Anderson, R.S. 2002. Modeling the tor-dotted crests, bedrock edges, and parabolic profiles of high alpine surfaces of the Wind River Range, Wyoming. Geomorphology, 46(1-2): 35-58.

Armstrong, A.C. 1987. Slopes, boundary conditions, and the development of convexo-concave forms – some numerical experiments. Earth Surface Processes and Landforms 12: 17-30.

Betancourt, J.L., Latorre, C., Rech, J.A., Quade, J., Rylander, K.A. 2000. A 22,000-year record of monsoonal precipitation from Northern Chile's Atacama Desert. Science, 289(5484): 1542-1546.

Bobst, A.L., Lowenstein, T.K., Jordan, T.E., Godfrey, L.V., Ku, T.L., and Luo, S.D. 2001. A 106 ka paleoclimate record from drill core of the Salar de Atacama, northern Chile. Palaeogeography Palaeoclimatology Palaeoecology, 173(1-2): 21-42.

Bodine, M.W., Fernalld, T.H. 1973. EDTA dissolution of gypsum, anhydrite, and Ca-Mg carbonates. Journal of Sedimentary Petrology, 43(4): 1152-1156.

Böhlke, J.K., Ericksen, G.E., Revesz, K. 1997. Stable isotope evidence for an atmospheric origin of desert nitrate deposits in northern Chile and southern California, USA. Chemical Geology, 136(1-2): 135-152.

Braun, J., Heimsath, A.M., Chappell, J. 2001. Sediment transport mechanisms on soil-mantled hillslopes. Geology, 29(8): 683-686.

Cáceres, L., Gómez-Silva, B., Garró, X., Rodríguez, V., Monardes, V., McKay, C.P. 2007. Relative humidity patterns and fog water precipitation in the Atacama Desert and biological implications. Journal of Geophysical Research-Biogeosciences, 112(G4).

Cardell, C., Rivas, T., Mosquera, M., Birginie, J., Moropoulou, A., Prieto, B., Silva, B., Van Grieken, R. 2003. Patterns of damage in igneous and sedimentary rocks under conditions simulating sea-salt weathering. Earth Surface Processes and Landforms, 28(1): 1-14.

Carson, M.A., Kirkby, M.J. 1972. Hillslope form and process. University Press, Cambridge [Eng.], viii, 475 p. pp.

Clarke, J.D.A. 2006. Antiquity of aridity in the Chilean Atacama Desert. Geomorphology, 73(1-2): 101-114.

Culling, W.E.H.1963. Soil creep and the development of hillside slopes, Journal of Geology 71:127–161.

Dahlgren, R.A., Boettinger, J.L., Huntington, G.L., Amundson, R.G. 1997. Soil development along an elevational transect in the western Sierra Nevada, California. Geoderma, 78(3-4): 207-236.

Dietrich, W.E., Reiss, R., Hsu, M.L., Montgomery, D.R. 1995. A process-based model for colluvial soil depth and shallow landsliding using digital elevation data. Hydrological Processes 9: 383-400.

Dietrich, W.E., Perron, J.T. 2006. The search for a topographic signature of life. Nature, 439(7075): 411-418.

Dixon, J.L., Heimsath, A.M., Amundson, R. 2009. The critical role of climate and saprolite weathering in landscape evolution. Earth Surface Processes and Landforms. DOI: 10.1002/esp.1836.

Dunai, T.J., Gonzalez-Lopez, G.A., Juez-Larre, J., Carrizo, D. 2005. Preservation of (early) Miocence landscapes in the Atacama Desert, northern Chile. Geochimica et Cosmochimica Acta, 69(10): A161-A161.

Dunne, T., Dietrich, W.E., Brunengo, M.J. 1980. Simple, portable equipment for erosion experiments under artificial rainfall. Journal of Agricultural Engineering Research, 25(2): 161-168.

Dupré, B., Dessert, C., Oliva, P., Goddéris, Y., Viers, J., François, L., Millot, R., Gaillardet, J. 2003. Rivers, chemical weathering and Earth's climate. Comptes Rendus Geoscience, 335: 1141-1160.

Emparan C, Pineda G. 2000. La Serena – La Higuera. Region de Coquimbo. Servicio Nacional de Geología y Minería. Geologic map No. 18, 1:100,000, Santiago.

Encinas, A., Hervé, F., Villa-Martínez, R., Nielsen, S.N., Finger, K.L., Peterson, D.E. 2006. Finding of a Holocene marine layer in Algarrobo (33 degrees 22 ' S), central Chile. Implications for coastal uplift. Revista Geologica De Chile, 33(2): 339-345.

Ericksen, G.E. 1981. Geology and origin of the Chilean nitrate deposits. Geological Society Professional Paper 1188. United States Government Printing Office: Washington.

Ewing, S., Michalski, G., Thiemens, M., Quinn, R., Macalady, J., Kohl, S., Wankel, S., Kendall, C., McKay, C.P., Amundson, R. 2007. Rainfall limit of the N cycle on Earth. Global Biogeochemical Cycles, 21: GB3009.

Ewing, S.A., Sutter, B., Owen, J.J., Nishiizumi, K., Sharp, W., Cliff, S.S., Perry, K., Dietrich, W.E., McKay, C.P., Amundson, R. 2006. A threshold in soil formation at Earth's arid-hyperarid transition. Geochimica et Cosmochimica Acta, 70(21): 5293-5322.

Fernandes, N.F., Dietrich, W.E. 1997. Hillslope evolution by diffusive processes: The timescale for equilibrium adjustments. Water Resources Research, 33(6): 1307-1318.

Fleming, R.W., Johnson, A.M. 1975. Rates of seasonal creep of silty clay soil. The Quarterly Journal of Engineering Geology, 8: 1-29.

Furbish, D.J. 2003. Using the dynamically coupled behavior of land-surface geometry and soil thickness in developing and testing hillslope evolution models. Prediction in geomorphology. American Geophysical Union, Washington, 169-181 pp.

Furbish, D.J., Fagherazzi, S. 2001. Stability of creeping soil and implications for hillslope evolution. Water Resources Research, 37(10): 2607-2618.

Gabet, E.J. 2000. Gopher bioturbation: Field evidence for non-linear hillslope diffusion. Earth Surface Processes and Landforms, 25(13): 1419-1428.

Gabet, E.J., Reichman, O.J., Seabloom, E.W. 2003. The effects of bioturbation on soil processes and sediment transport. Annual Review of Earth and Planetary Sciences, 31: 249-273.

Gilbert, G.K. 1877. Geology of the Henry Mountains (Utah). U.S. Geographical and Geological Survey of the Rocky Mountains Region, Washington, D.C.

Godoy, E., Lara, L. 1998. Hojas Chañaral y Diego de Almagro, Región de Atacama. Servicio Nacional de Geología y Minería, Geologic map of Chile No. 5-6, 1:100,000, Santiago.

Govers, G., Poesen, J. 1998. Field experiments on the transport of rock fragments by animal trampling on scree slopes. Geomorphology, 23: 193-203.

Greenway, D.R. 1987. Vegetation and slope stability. *In* Anderson, M.G., Richards, K.S. (Eds.) Slope Stability. Wiley, Chichester, 187-230 pp.

Hack, J.T.1957. Studies of longitudinal profiles in Virginia and Maryland, USGS Professional Papers 294-B, Washington DC, pp. 46–97.

Hartley, A.J., Chong, G. 2002. Late Pliocene age for the Atacama Desert: Implications for the desertification of western South America. Geology, 30(1): 43-46.

Hartley, A.J., Chong, G., Houston, J., Mather, A.E. 2005. 150 million years of climatic stability: evidence from the Atacama Desert, northern Chile. Journal of the Geological Society, 162: 421-424.

Hebbeln, D., Lamy, F., Mohtadi, M., Echtler, H. 2007. Tracing the impact of glacial-interglacial climate variability on erosion of the southern Andes. Geology, 35(2): 131-134.

Heimsath, A.M., Dietrich, W.E., Nishiizumi, K., Finkel, R.C. 1999. Cosmogenic nuclides, topography, and the spatial variation of soil depth. Geomorphology, 27(1-2): 151-172.

Heimsath, A.M., Ehlers, T.A. 2005. Quantifying rates and timescales of geomorphic processes. Earth Surface Processes and Landforms, 30(8): 917-921.

Hewawasen, T. 2003. Quantifying erosion in the tropical highlands of Sri Lanka over different time scales using cosmogenic nuclide and river load data. Ph.D. thesis, University of Bern, Bern.

Houston, J. 2006. Variability of precipitation in the Atacama desert: Its causes and hydrological impact. International Journal of Climatology, 26(15): 2181-2198.

Istanbulluoglu, E., Bras, R.L. 2006. On the dynamics of soil moisture, vegetation, and erosion: Implications of climate variability and change. Water Resources Research, 42(6).

Jenny, H. 1941. Factors of Soil Formation. McGraw-Hill Book Company, Inc.: New York.

Keefer, D.K., Moseley, M.E. 2004. Southern Peru desert shattered bv the great 2001 earthquake: Implications for paleoseismic and paleo-El Nino-Southern oscillation records. Proceedings of the National Academy of Sciences of the United States of America, 101(30): 10878-10883.

Kirkby, M.J. 1971. Hillslope process-response models based on the continuity equation. Institute of British Geographers Special Publication 3: 15-30.

Kirkby, M. 1990. The landscape viewed through models. Zeitschrift fur Geomorphologie, 79: 63-81.

Kirkby, M.J. 1967. Measurement and theory of soil creep. Journal of Geology, 75(4): 359-378.

Kober, F., Ivy-Ochs, S., Schlunegger, F., Baur, H., Kubik, P.W., Wieler, R. 2007. Denudation rates and a topography-driven rainfall threshold in northern Chile: Multiple cosmogenic nuclide data and sediment yield budgets. Geomorphology, 83(1-2): 97-120.

Kohl, C.P., Nishiizumi, K. 1992. Chemical isolation of quartz for measurement of in situ-produced cosmogenic nuclides. Geochimica et Cosmochimica Acta, 56(9): 3583-3587.

Kump, L.R., Brantley, S.L., Arthur, M.A. 2000. Chemical weathering, atmospheric $CO_2$, and climate. Annual Reviews of Earth and Planetary Science, 28: 611-667.

Lal, D., Arnold, J.R. 1985. Tracing quartz through the environment. Proceedings of the Indian Academy of Science(Earth Planetary Science Section) 94: 1-5.

Lal, D. 1991. Cosmic-ray labeling of erosion surfaces – in situ nuclide production-rates and erosion models. Earth and Planetary Science Letters, 104(2-4): 424-439.

Lamy, F., Klump, J., Hebbeln, D., Wefer, G. 2000. Late Quaternary rapid climate change in northern Chile. Terra Nova, 12(1): 8-13.

Latorre, C., Betancourt, J.L., Rylander, K.A., Quade, J. 2002. Vegetation invasions into absolute desert: A 45 000 yr rodent midden record from the Calama-Salar de Atacama basins, northern Chile (lat 22º-24ºS). Geological Society of America Bulletin, 114(3): 349-366.

Latorre, C., Betancourt, J.L., Rylander, K.A., Quade, J., Matthei, O. 2003. A vegetation history from the arid prepuna of northern Chile (22-23 degrees S) over the last 13,500 years, pp. 223-246.

Le Roux, J.P., Gomez, C., Venegas, C., Fenner, J., Middleton, H., Marchant, M., Buchbinder, B., Frassinetti, D., Marquardt, C., Gregory-Wodzicki, K.M., Lavenu, A. 2005. Neogene-Quaternary coastal and offshore sedimentation in north central Chile: Record of sea-level changes and implications for Andean tectonism, pp. 83-98.

Le Roux, J.P., Olivares, D.M., Nielsen, S.N., Smith, N.D., Middleton, H., Fenner, J., Ishman, S.E. 2006. Bay sedimentation as controlled by regional crustal behaviour, local tectonics and eustatic sea-level changes: Coquimbo Formation (Miocene-Pliocene), Bay of Tongoy, central Chile. Sedimentary Geology, 184(1-2): 133-153.

Leith, H.. 1973. Primary Production: Terrestrial Ecosystems. Human Ecology 1: 303–322.

Leonard, E.M., Wehmiller, J.F. 1992. Low uplift rates and terrace reoccupation inferred from mollusk aminostratigraphy, Coquimbo Bay area, Chile. Quaternary Research, 38(2): 246-259.

Loveless, J.P., Allmendinger, R.W., Pritchard, M.E., Garroway, J.L., Gonzalez, G. 2009. Surface cracks record long-term seismic segmentation of the Andean margin. Geology, 37(1): 23-26.

Loveless, J.P., Hoke, G.D., Allmendinger, R.W., Gonzalez, G., Isacks, B.L., Carrizo, D.A. 2005. Pervasive cracking of the northern Chilean Coastal Cordillera: New evidence for forearc extension. Geology, 33(12): 973-976.

Marinovic, N., Smoje, I., Maksaev, V., Hervé, M., Mpodozis, C. 1992. Hoja Aguas Blancas, Región de Antofagasta. Servicio Nacional de Geología y Minería, Geologic map of Chile No. 70, 1:100,000, Santiago.

Marquardt, C., Lavenu, A., Ortlieb, L., Godoy, E., Comte, D. 2004. Coastal neotectonics in Southern Central Andes: uplift and deformation of marine terraces in Northern Chile (27 degrees S). Tectonophysics, 394(3-4): 193-219.

McKay, C.P., Friedmann, E.I., Gomez-Silva, B., Caceres-Villanueva, L., Andersen, D.T., Landheim, R. 2003. Temperature and moisture conditions for life in the extreme arid

region of the Atacama Desert: Four years of observations including the El Nino of 1997-1998. Astrobiology, 3(2): 393-406.

McKean, J.A., Dietrich, W.E., Finkel, R.C., Southon, J.R., Caffee, M.W. 1993. Quantification of soil production and downslope creep rates from cosmogenic Be-10 accumulations on a hillslope profile. Geology, 21(4): 343-346.

Michalski, G., Bohlke, J., Thiemens, M. 2004. Long term atmospheric deposition as the source of nitrate and other salts in the Atacama Desert, Chile: New evidence from mass-independent oxygen isotopic compositions. Geochimica et Cosmochimica Acta, 68(20): 4023-4038.

Molnar, P., Anderson, R.S., Anderson, S.P. 2007. Tectonics, fracturing of rock, and erosion. Journal of Geophysical Research-Earth Surface, 112(F3).

Montgomery, D.R., Balco, G., Willett, S.D. 2001. Climate, tectonics, and the morphology of the Andes. Geology, 29(7): 579-582.

Mortimer, C. 1973. The Cenozoic history of the southern Atacama Desert, Chile. Journal of the Geological Society of London 129: 505-526.

Mortimer, C. 1980. Drainage evolution in the Atacama Desert of northern Chile. Revista Geológica de Chile 11: 3-28.

Mudd, S.M., Furbish, D.J. 2006. Using chemical tracers in hillslope soils to estimate the importance of chemical denudation under conditions of downslope sediment transport. Journal of Geophysical Research-Earth Surface, 111(F2).

Mudd, S.M., Furbish, D.J. 2007. Responses of soil-mantled hillslopes to transient channel incision rates. Journal of Geophysical Research-Earth Surface, 112(F3).

Navarro-Gonzalez, R., Rainey, F., Molina, P., Bagaley, D., Hollen, B., de la Rosa, J., Small, A., Quinn, R., Grunthaner, F., Caceres, L., Gomez-Silva, B., McKay, C.P. 2003. Mars-like soils in the Atacama Desert, Chile, and the dry limit of microbial life. Science 302: 1018-1021.

Nguyen, T.H., and Foley, R.T. 1980. The chemical nature of aluminum corrosion. Journal of the Electrochemical Society 127: 2563-2566.

Nishiizumi, K., Winterer, E.L., Kohl, C.P., Klein, J. 1989. Cosmic ray production rates of 10Be and 26Al in quartz from glacially polished rocks. Journal of Geophysical Research 94: 17,907-17,915.

Nishiizumi, K. 2003, Preparation of 26Al AMS standards: Nuclear Instruments & Methods in Physics Research Section B, v. B223-224, p. 388-392.

Nishiizumi, K., Caffee, M.W., Finkel, R.C., Brimhall, G., Mote, T. 2005. Remnants of a fossil alluvial fan landscape of Miocene age in the Atacama Desert of northern Chile using cosmogenic nuclide exposure age dating. Earth and Planetary Science Letters, 237(3-4): 499-507.

Nishiizumi, K., Imamura, M., Caffee, M.W., Southon, J.R., Finkel, R.C., McAninch, J. 2007. Absolute calibration of Be-10 AMS standards. Nuclear Instruments & Methods in Physics Research Section B-Beam Interactions with Materials and Atoms, 258(2): 403-413.

Nunez, L., Grosjean, M., Cartajena, I. 2002. Human occupations and climate change in the Puna de Atacama, Chile. Science, 298(5594): 821-824.

Oberlander, T.M. 1972. Morphogenesis of granitic boulder slopes in Mojave Desert, California. Journal of Geology 80: 1-20.

Onda, Y. 1992. Influence of water storage capacity in the regolith zone on hydrological characteristics, slope processes, and slope form. Zeitschrift Fur Geomorphologie, 36(2): 165-178.

Ortlieb, L., Barrientos, S., Guzman, N. 1996. Coseismic coastal uplift and coralline algae record in northern Chile: The 1995 Antofagasta earthquake case. Quaternary Science Reviews, 15(8-9): 949-960.

Ota, Y., Paskoff, R. 1993. Holocene deposits on the coast of north-central Chile - radiocarbon ages and implications for coastal changes. Revista Geologica De Chile, 20(1): 25-32.

Owen, J.J., Amundson, R., Dietrich, W.E., Nishiizumi, K., Sutter, B., and Chong, G. *in revision*. The sensitivity of hillslope soil production to precipitation. Earth Surface Processes and Landforms.

Penck W. 1953. Morphological analysis of land forms. Czech H, Boswell KC (trans). Macmillan: London.

Quezada, J., Gonzalez, G., Dunai, T., Jensen, A., Juez-Larre, J. 2007. Pleistocene littoral uplift of northern Chile: Ne-21 age of the upper marine terrace of Caldera-Bahia Inglesa area. Revista Geologica De Chile, 34(1): 81-96.

Rech, J., Quade, J., Hart, W. 2003. Isotopic evidence for the source of Ca and S in soil gypsum, anhydrite and calcite in the Atacama Desert, Chile. Geochimica et Cosmochimica Acta, 67(4): 575-586.

Reheis, M.C., Kihl, R., 1995. Dust deposition in southern Nevada and California, 1984-1989 - relations to climate, source area, and source lithology. Journal of Geophysical Research-Atmospheres, 100(D5): 8893-8918.

Riebe, C.S., Kirchner, J.W., Finkel, R.C. 2003. Long-term rates of chemical weathering and physical erosion from cosmogenic nuclides and geochemical mass balance. Geochimica et Cosmochimica Acta, 67(22): 4411-4427.

Riebe, C.S., Kirchner, J.W., Finkel, R.C. 2004. Erosional and climatic effects on long-term chemical weathering rates in granitic landscapes spanning diverse climate regimes. Earth and Planetary Science Letters, 224(3-4): 547-562.

Riebe, C.S., Kirchner, J.W., Granger, D.E., Finkel, R.C. 2001. Minimal climatic control on erosion rates in the Sierra Nevada, California. Geology, 29(5): 447-450.

Rodriguez-Navarro, C., Doehne, E. 1999. Salt weathering: Influence of evaporation rate, supersaturation and crystallization pattern. Earth Surface Processes and Landforms, 24(3): 191-209.

Roering, J.J. 2004. Soil creep and convex-upward velocity profiles: Theoretical and experimental investigation of disturbance-driven sediment transport on hillslopes. Earth Surface Processes and Landforms, 29(13): 1597-1612.

Roering, J.J. 2008. How well can hillslope evolution models "explain" topography? Simulating soil transport and production with high-resolution topographic data. Geological Society of America Bulletin, 120(9-10): 1248-1262.

Roering, J.J., Kirchner, J.W., Dietrich, W.E. 1999. Evidence for nonlinear, diffusive sediment transport on hillslopes and implications for landscape morphology. Water Resources Research, 35(3): 853-870.

Rundel, P.W., Dillon, M.O., Palma, B., Mooney, H.A., Gulmon, S.L., Ehleringer, J.R. 1991. The phytogeography and ecology of the coastal Atacama and Peruvian deserts. Aliso 13: 1-49.

Rundel, P.W., Dillon, M.O., Palma, P. 1996. Flora and vegetation of Pan de Azucar National Park in the Atacama Desert of northern Chile. Gayana Botánica 53: 295-315.

Saillard, M., Hall, S.R., Audin, L., Farber, D.L., Herail, G., Martinod, J., Regard, V., Finkel, R.C., Bondoux, F. 2009. Non-steady long-term uplift rates and Pleistocene marine terrace development along the Andean margin of Chile (31ºS) inferred from Be-10 dating. Earth and Planetary Science Letters, 277(1-2): 50-63.

Schoenenberger, P.J., Wysocki, D.A., Benham, E.C., Broderson, W.D. 2002. Field book for describing and sampling soils. Natural Resources Conservation Service, National Soil Survey Center, Lincoln, NE.

Sillitoe, R.H., McKee, E.H. 1996. Age of supergene oxidation and enrichment in the Chilean porphyry copper province. Economic Geology and the Bulletin of the Society of Economic Geologists, 91(1): 164-179.

Squeo, F.A., Aravena, R., Aguirre, E., Pollastri, A., Jorquera, C.B., Ehleringer, J.R. 2006. Groundwater dynamics in a coastal aquifer in north-central Chile: Implications for groundwater recharge in an arid ecosystem. Journal of Arid Environments, 67(2): 240-254.

Steiger, M. 2005. Crystal growth in porous materials - I: The crystallization pressure of large crystals. Journal of Crystal Growth, 282(3-4): 455-469.

Stuut, J.B.W., Lamy, F. 2004. Climate variability at the southern boundaries of the Namib (Southwestern Africa) and Atacama (northern Chile) coastal deserts during the last 120,000 yr. Quaternary Research, 62(3): 301-309.

Syvitski, J.P.M., Milliman, J.D. 2007. Geology, geography, and humans battle for dominance over the delivery of fluvial sediment to the coastal ocean. The Journal of Geology, 115: 1-19.

Viles, H., Goudie, A. 2007. Rapid salt weathering in the coastal Namib desert: Implications for landscape development. Geomorphology, 85(1-2): 49-62.

von Blanckenburg, F. 2006. The control mechanisms of erosion and weathering at basin scale from cosmogenic nuclides in river sediment. Earth and Planetary Science Letters, 242(3-4): 223-239.

von Blanckenburg, F., Hewawasam, T., and Kubik, P.W. 2004. Cosmogenic nuclide evidence for low weathering and denudation in the wet, tropical highlands of Sri Lanka. Journal of Geophysical Research 109, F03008. doi:10.1029/2003JF000049.

Warren-Rhodes, K.A., Rhodes, K., Pointing, S., Ewing, S., Lacap, D., Gomez-Silva, B., Amundson, R., Friedmann, E., McKay, C. 2006. Hypolithic cyanobacteria, dry limit of photosynthesis, and microbial ecology in the hyperarid Atacama Desert. Microbial Ecology 52: 389-398.

Wheeler, J.C. 1995. Evolution and present situation of the South-American camelidae. Biological Journal of the Linnean Society, 54(3): 271-295.

White, A.F., Blum, A.E. 1995. Effects of climate on chemical weathering in watersheds. Geochmica et Cosmochimica Acta 59: 1729-1747.

White, A.F., Blum, A.E., Bullen, T.D., Vivit, D.V., Schulz, M., Fitzpatrick, J. 1999. The effect of temperature on experimental and natural chemical weathering rates of granitoid rocks. Geochemica et Cosmochimica Acta 63: 3277-3291.

Wilcox, B.P., Wood, M.K., Tromble, J.T., and Ward, T.J. 1986, A hand-portable single nozzle rainfall simulator designed for use on steep slopes: Journal of Range Management, v. 39, no. 4, p. 375-377.

Winkler, E., Singer, P. 1972. Crystallization pressure of salts in stone and concrete. Geological Society of America Bulletin, 83(11): 3509-3513.

Yair, A. 1995. Short and long term effect of bioturbation on soil erosion, water resources and soil development in an arid environment. Geomorphology, 13: 89-99.

Yoo, K., Amundson, R., Heimsath, A.M., Dietrich, W.E. 2005. Process-based model linking pocket gopher (Thomomys bottae) activity to sediment transport and soil thickness. Geology, 33(11): 917-920.

Yoo, K., Amundson, R., Heimsath, A.M., Dietrich, W.E., Brimhall, G.H. 2007. Integration of geochemical mass balance with sediment transport to calculate rates of soil chemical weathering and transport on hillslopes. Journal of Geophysical Research-Earth Surface, 112(F2).

Young, A. 1960. Soil movement by denudational processes on slopes. Nature (188)4745: 120-122.

**Table 1.** Site characteristics.

| | MAP (mm) | MAT (average, range) (ºC) | elevation (masl) | distance inland (km) | plant density (% area) | bedrock | channel incision rate (m My$^{-1}$) | mean hillslope erosion rate (m My$^{-1}$) | main pedogenic processes |
|---|---|---|---|---|---|---|---|---|---|
| **Semiarid** | 100 | 13.5, 8-21[a] | 380 | 15 | 32 | monzogranite | 33.8 ± 1.7 | 27.1 ± 2.4 | bioturbation, chemical weathering |
| **Arid** | 10 | 16, 11-27[b] | 690 | 21 | 6 | monzogranite | 3.7 ± 0.1 | 2.72 ± 0.16 | salt prying, chemical weathering |
| **Hyperarid** | <1 | 17, 0-32[c] | 1170 | 50 | 0 | granodiorite | 1.3 ± 0.3 | 0.97 ± 0.04 | salt shrink-swell |

[a]Squeo et al. (2006)

[b]Rundel et al. (1996)

[c]McKay et al. (2003)

[d] in <2mm fraction

[e]does not include surface gravels

**Table 2.** Soil properties (first half) and cosmogenic radionuclide data (second half).

| sample ID | sample type | distance downslope, $x$ (m) | CRN sample depth (cm) | slope-normal soil thickness, $H$ (cm) | slope (m m$^{-1}$) | soil density, $\rho_s$ (g cm$^{-3}$) | soil [Ti], $C_{is}$ (ppm) | saprolite or bedrock density, $\rho_r$ (g cm$^{-3}$) | bedrock [Ti], $C_{ir}$ (ppm) |
|---|---|---|---|---|---|---|---|---|---|
| *Semiarid (29.77˚S, 71.08˚W, 377 masl)* | | | | | | | | | |
| SGA-1 | hillslope saprolite | 7.7 | 7 | 6.7 | 0.29 | 1.34 | 2579 | 1.40 | 1439 |
| SGA-2 | hillslope saprolite | 15.4 | 10 | 9.4 | 0.36 | 1.40 | 2562 | 1.46 | 2098 |
| SGA-3 | hillslope saprolite | 25.4 | 15 | 13.8 | 0.42 | 1.43 | 2065 | 1.52 | 1619 |
| SGA-4 | hillslope saprolite | 33.2 | 14 | 13.0 | 0.40 | 1.39 | 2122 | 1.47 | 1619 |
| SGA-06-28 | hillslope saprolite | 38.2 | 22 | 20.3 | 0.41 | 1.41 | na | na | na |
| SGA-06-17 | hillslope saprolite | 44.4 | 17 | 15.9 | 0.38 | 1.36 | na | na | na |
| SGA-06-16 | hillslope saprolite | 49.6 | 24 | 22.2 | 0.41 | 1.28 | na | na | na |
| SGA-5 | hillslope saprolite | 50.2 | 30 | 27.0 | 0.48 | 1.44 | 2124 | 1.35 | 1918 |
| SGA05-14b | channel bedrock | 59.2 | 0 | 0 | na | na | na | na | na |
| *Arid (26.28˚S, 70.49˚W, 687 masl)* | | | | | | | | | |
| CH-1 | hillslope bedrock | 0 | 2.5 | 2.4 | 0.21 | 1.32 | 1178 | 2.50 | 360 |
| CH-2 | hillslope bedrock | 2.3 | 2 | 1.9 | 0.40 | 1.55 | 1179 | 2.50 | 719 |
| CH-3 | hillslope bedrock | 6.3 | 2 | 1.8 | 0.51 | 1.15 | 1079 | 2.50 | 599 |
| CH-4 | hillslope bedrock | 10.7 | 4 | 3.6 | 0.51 | 1.16 | 1701 | 2.50 | 659 |
| CH-5 | hillslope bedrock | 14.3 | 2 | 1.7 | 0.67 | 1.07 | 1272 | 2.50 | 480 |
| CH-6 | hillslope bedrock | 17.3 | 3.5 | 3.1 | 0.53 | 1.18 | 849 | 2.50 | 480 |
| CH-7 | channel bedrock | 19.1 | 0 | 0 | na | na | na | na | na |
| *Hyperarid (24.13˚S, 69.99˚W, 1170 masl)* | | | | | | | | | |
| YH-05-16c | hillslope bedrock | 0 | 4.5 | 4.2 | 0.40 | 0.81 | 2524 | 2.48 | 4011 |
| YH-17-4 | hillslope bedrock | 2.5 | 5 | 4.7 | 0.34 | 0.83 | 1047 | 2.41 | 3961 |
| YH-18-4 | hillslope bedrock | 5.0 | 24 | 21.6 | 0.49 | 0.52 | 1364 | 2.55 | 3999 |
| YH-19-C | hillslope bedrock | 8.8 | 9 | 7.6 | 0.62 | 0.46 | 1620 | 2.07 | 2911 |
| YH-20-C | hillslope bedrock | 12.2 | 7 | 5.9 | 0.65 | 0.54 | 1247 | 1.93 | 2608 |
| YH-05-44b | channel bedrock | 14.6 | 0 | 0 | na | na | na | na | na |

**Table 2 continued.**

| sample ID | depth-corrected values | | | | | | $^{10}$Be erosion | $^{26}$Al erosion | average erosion | |
|---|---|---|---|---|---|---|---|---|---|---|
| | $^{10}$Be (atom g$^{-1}$) | +/- | $^{26}$Al (atom g$^{-1}$) | +/- | $^{26}$Al/$^{10}$Be | +/- | (m My$^{-1}$) | (m My$^{-1}$) | (m My$^{-1}$) | +/- |
| *Semiarid (29.77˚S, 71.08˚W, 377 masl)* | | | | | | | | | | |
| SGA-1 | 2.74E+05 | 6.59E+03 | 2.04E+06 | 1.68E+05 | 7.45 | 0.64 | 23 | 18 | 20 | 1.7 |
| SGA-2 | 1.79E+05 | 5.00E+03 | 1.30E+06 | 8.10E+04 | 7.25 | 0.50 | 35 | 32 | 33 | 2.3 |
| SGA-3 | 1.96E+05 | 5.48E+03 | 1.10E+06 | 7.29E+04 | 5.61 | 0.40 | 32 | 37 | 35 | 2.7 |
| SGA-4 | 1.72E+05 | 4.66E+03 | 1.22E+06 | 5.74E+04 | 7.08 | 0.39 | 36 | 34 | 35 | 1.9 |
| SGA-06-28 | 2.54E+05 | 1.29E+04 | 1.28E+06 | 9.98E+04 | 5.04 | 0.47 | 24 | 32 | 28 | 5.3 |
| SGA-06-17 | 2.94E+05 | 2.06E+04 | 1.75E+06 | 1.15E+05 | 5.95 | 0.57 | 21 | 23 | 22 | 1.5 |
| SGA-06-16 | 3.64E+05 | 2.04E+04 | 2.27E+06 | 1.55E+05 | 6.25 | 0.55 | 17 | 17 | 17 | 0.8 |
| SGA-5 | 3.45E+05 | 9.02E+03 | 2.36E+06 | 2.16E+05 | 6.84 | 0.65 | 18 | 17 | 17 | 1.7 |
| SGA05-14b | 1.13E+05 | 8.09E+03 | 7.08E+05 | 4.67E+04 | 6.24 | 0.61 | 33 | 35 | 34 | 1.7 |
| *Arid (26.28˚S, 70.49˚W, 687 masl)* | | | | | | | | | | |
| CH-1 | 1.44E+06 | 3.40E+04 | 8.01E+06 | 3.11E+05 | 5.57 | 0.25 | 2.7 | 3.0 | 2.9 | 0.2 |
| CH-2 | 1.38E+06 | 3.25E+04 | 7.72E+06 | 3.60E+05 | 5.61 | 0.29 | 2.9 | 3.1 | 3.0 | 0.2 |
| CH-3 | 1.37E+06 | 3.29E+04 | 7.73E+06 | 2.76E+05 | 5.63 | 0.24 | 2.9 | 3.1 | 3.0 | 0.2 |
| CH-4 | 1.56E+06 | 4.47E+04 | 8.98E+06 | 5.11E+05 | 5.76 | 0.37 | 2.4 | 2.6 | 2.5 | 0.1 |
| CH-5 | 1.65E+06 | 4.63E+04 | 9.10E+06 | 3.18E+05 | 5.53 | 0.25 | 2.3 | 2.6 | 2.4 | 0.2 |
| CH-6 | 1.59E+06 | 7.30E+04 | 9.29E+06 | 4.70E+05 | 5.85 | 0.40 | 2.4 | 2.5 | 2.4 | 0.1 |
| CH-7 | 1.10E+06 | 2.79E+04 | 6.61E+06 | 3.39E+05 | 6.00 | 0.34 | 3.6 | 3.8 | 3.7 | 0.1 |
| *Hyperarid (24.13˚S, 69.99˚W, 1170 masl)* | | | | | | | | | | |
| YH-05-16c | 4.64E+06 | 2.10E+05 | 2.50E+07 | 1.33E+06 | 5.39 | 0.38 | 0.95 | 0.95 | 0.95 | 0.05 |
| YH-17-4 | 5.14E+06 | 6.30E+04 | 2.67E+07 | 7.70E+05 | 5.19 | 0.16 | 0.83 | 0.85 | 0.84 | 0.02 |
| YH-18-4 | 4.78E+06 | 8.23E+04 | 2.46E+07 | 7.77E+05 | 5.14 | 0.19 | 0.91 | 0.97 | 0.94 | 0.04 |
| YH-19-C | 4.63E+06 | 5.79E+04 | 2.61E+07 | 9.15E+05 | 5.64 | 0.21 | 0.95 | 0.88 | 0.91 | 0.05 |
| YH-20-C | 4.11E+06 | 6.90E+04 | 2.17E+07 | 6.35E+05 | 5.28 | 0.18 | 1.1 | 1.2 | 1.1 | 0.05 |
| YH-05-44b | 3.57E+06 | 8.85E+04 | 1.47E+07 | 8.93E+05 | 4.11 | 0.27 | 1.3 | 2.1 | 1.7 | 0.51 |

**Table 3.** Sprinkling experiment data.

| sprinkling experiment | slope (m m$^{-1}$) | application rate (cm hr$^{-1}$) | steady state runoff rate (cm hr$^{-1}$) | steady state infiltration rate (cm hr$^{-1}$) | duration of runoff (min) |
|---|---|---|---|---|---|
| semiarid 1 | 0.18 | 5.7 | 1.5 | 2.6 | 9.75 |
| semiarid 2 | 0.42 | 6.5 | 0.5 | 4.1 | 25 |
| semiarid 3 | 0.42 | 26.5 | 10.5 | 15.6 | 2 |
| arid 1 | 0.38 | 5.7 | 1.3 | 4.2 | 12 |
| arid 2 | 0.38 | 5.5 | 2.0 | 3.3 | 10 |
| arid 3 | 0.38 | 52.5 | 28.9 | 25.3 | 3 |
| hyperarid 1 | 0.21 | 58.7 | 16.1 | 33.5 | 8 |
| hyperarid 2 | 0.34 | 5.7 | 0.5 | 4.3 | 9 |
| hyperarid 3 | 0.27 | 5.2 | 0.1 | 4.2 | 32 |

**Table 4.** Dust collector data for the arid hillslope (CH), the hyperarid site (YH), and two other sites in the hyperarid region (ORH and Ewing et al., 2006).

| dust trap ID | silicate dust input rate (gm$^{-2}$y$^{-1}$) | Al/Si | NO$_3^-$ input rate (gm$^{-2}$y$^{-1}$) | Cl$^-$ input rate (gm$^{-2}$y$^{-1}$) | SO$_4^{-2}$ input rate (gm$^{-2}$y$^{-1}$) | total input rate (gm$^{-2}$y$^{-1}$) | Ti (ppm) | ± (ppm) |
|---|---|---|---|---|---|---|---|---|
| *arid region* | | | | | | | | |
| CH-3* | 20.196 | 1.35 | 0.011 | 1.024 | 0.025 | 21.256 | 396 | 21 |
| *hyperarid region* | | | | | | | | |
| YH-1 | 1.162 | 0.87 | 0.637 | 0.077 | 0.958 | 3.980 | 1373 | 40 |
| YH-2 | 1.009 | 0.72 | 0.500 | 0.031 | 0.923 | 3.457 | 1861 | 43 |
| YH-3 | 1.018 | 0.63 | 0.449 | 0.042 | 0.967 | 3.481 | 1182 | 34 |
| YH average | 1.063 | 0.74 | 0.529 | 0.050 | 0.949 | 3.639 | 1472 | 39 |
| YH st. deviation | 0.086 | 0.12 | 0.097 | 0.024 | 0.023 | 0.295 | 350 | |
| *nearby hyperarid sites* | | | | | | | | |
| ORH-1 | 1.572 | 0.47 | 0.260 | 0.004 | 0.543 | 3.942 | 1794 | 35 |
| ORH-2 | 1.127 | 0.41 | 0.335 | 0.003 | 0.568 | 3.155 | 1899 | 43 |
| ORH-3 | 1.509 | 0.44 | 0.195 | 0.003 | 0.552 | 3.760 | 2345 | 57 |
| ORH average | 1.403 | 0.44 | 0.263 | 0.004 | 0.554 | 3.619 | 2013 | 45 |
| ORH st. deviation | 0.241 | 0.03 | 0.070 | 0.000 | 0.013 | 0.412 | 292 | |
| Ewing et al. (2006) | 2.032 | na | 0.759 | 0.098 | 1.319 | 4.701 | 1637 | na |

*silicate input rate is high due to corrosion of dust collector

**Table 5.** Soil salt concentration and residence time on the hyperarid hillslope.

| soil ID | distance downslope (m) | concentration | | | | residence time | | |
|---|---|---|---|---|---|---|---|---|
| | | $SO_4^{-2}$ (ppm) | $NO_3^-$ (ppm) | $Cl^-$ (ppm) | I (ppm) | $SO_4^{-2}$ (y) | $NO_3^-$ (y) | $Cl^-$ (y) |
| YH-16 | 0.00 | 16489 | 374 | 713 | 47 | 6020 | 33 | 571 |
| YH-17 | 2.49 | 16920 | 252 | 1206 | 41 | 19220 | 35 | 1436 |
| YH-18 | 4.97 | 21245 | 451 | 544 | 67 | 14466 | 42 | 503 |
| YH-19 | 8.76 | 18141 | 445 | 1150 | 58 | 10514 | 46 | 1219 |
| YH-20 | 12.23 | 21570 | 422 | 819 | 66 | 12890 | 33 | 681 |

**Table 6.** Comparison of erosion rates, CDF and ECDF values, and *K* values. The shaded boxes indicate the soil transport models that did not describe the data well.

| Site | MAP (mm) | Average slope | Average bedrock erosion rate $(gm^{-2}y^{-1})$ | *for upper 13 m* | | | | *entire hillslope* | |
|---|---|---|---|---|---|---|---|---|---|
| | | | | Chemical gain $(gm^{-1}y^{-1})$ | Chemical loss $(gm^{-1}y^{-1})$ | Soil flux at bottom $(gm^{-1}y^{-1})$ | Transport time (y) | CDF | ECDF |
| Hyperarid | 2 | 0.52 | 2.16 | -56 | 0 | 93 | 35,000 | -0.57 | -0.93 |
| Arid | 10 | 0.44 | 6.77 | 0 | 44 | 54 | 8,800 | 0.34 | 0.33 |
| Semiarid | 100 | 0.20 | 33.2 | 0 | 48 | 349 | 1,100 | 0.17 | 0.12 |
| Frog Hollow | 650 | 0.18 | 46.7 | na | na | na | na | 0.65 | 0.66 |

| Site | $K_s$ $(m^2y^{-1})$ | $K_h$ $(my^{-1})$ | $K_c$ $(my^{-1})$ | $S_c$ | $K_w$ | n | m |
|---|---|---|---|---|---|---|---|
| Hyperarid | 0.0004 | 0.0032 | 0.0002-0.001 | 0.56-0.75 | $4 \times 10^{-6}$ $y^{-1}$ | 2 | 2 |
| Arid | 0.0002 | 0.009 | 0.0012-0.002 | 0.55-0.7 | $1 \times 10^{-5}$ $my^{-1}$ | 1 | 1 |
| Semiarid | 0.00252 | 0.0087 | 0.005-0.0087 | ≥0.8 | na | na | na |
| Frog Hollow | na | 0.0044 | na | na | na | na | na |

na = not available

**Figure 1.** (a) A shaded relief map showing site locations (created with GeoMapApp v.1.7.8). Only in the hyperarid region were the two hillslopes sufficiently apart (~70 km) to necessitate separate markers on the map. (b) Average mean annual precipitation (MAP) increases with longitude (Worldclimate.com). (c) Plant density (measured in this study) follows MAP and increases with longitude. (d) Coastal uplift rates have been uniform across the study area in the Holocene. Uplift data compiled from Leonard and Wehmiller (1992), Ota et al. (1995), Ortlieb et al. (1996), Marquardt et al. (2004), Le Roux et al. (2005, 2006), Encinas et al. (2006), Quezada et al. (2007), and Saillard et al. (2009).



97
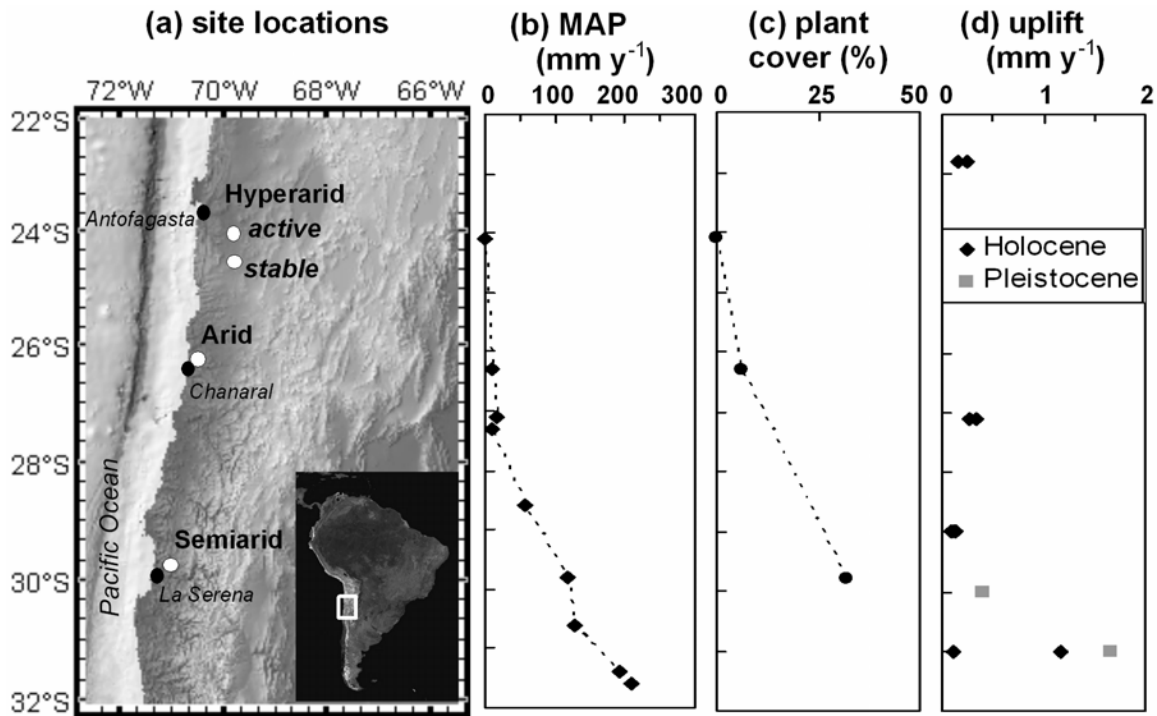
**Figure 2.** Photographs (a, b, c), topographic maps (d, e, f), and topographic profiles (g, h, i) of the semiarid, arid, and hyperarid hillslopes, respectively. Topographic maps show soil excavation locations (black squares) and channel bedrock sampling locations (open squares). The semiarid channel was sampled ~30 m upstream and is not shown. The contour interval of the topographic maps is 1 m, though scale varies as shown.
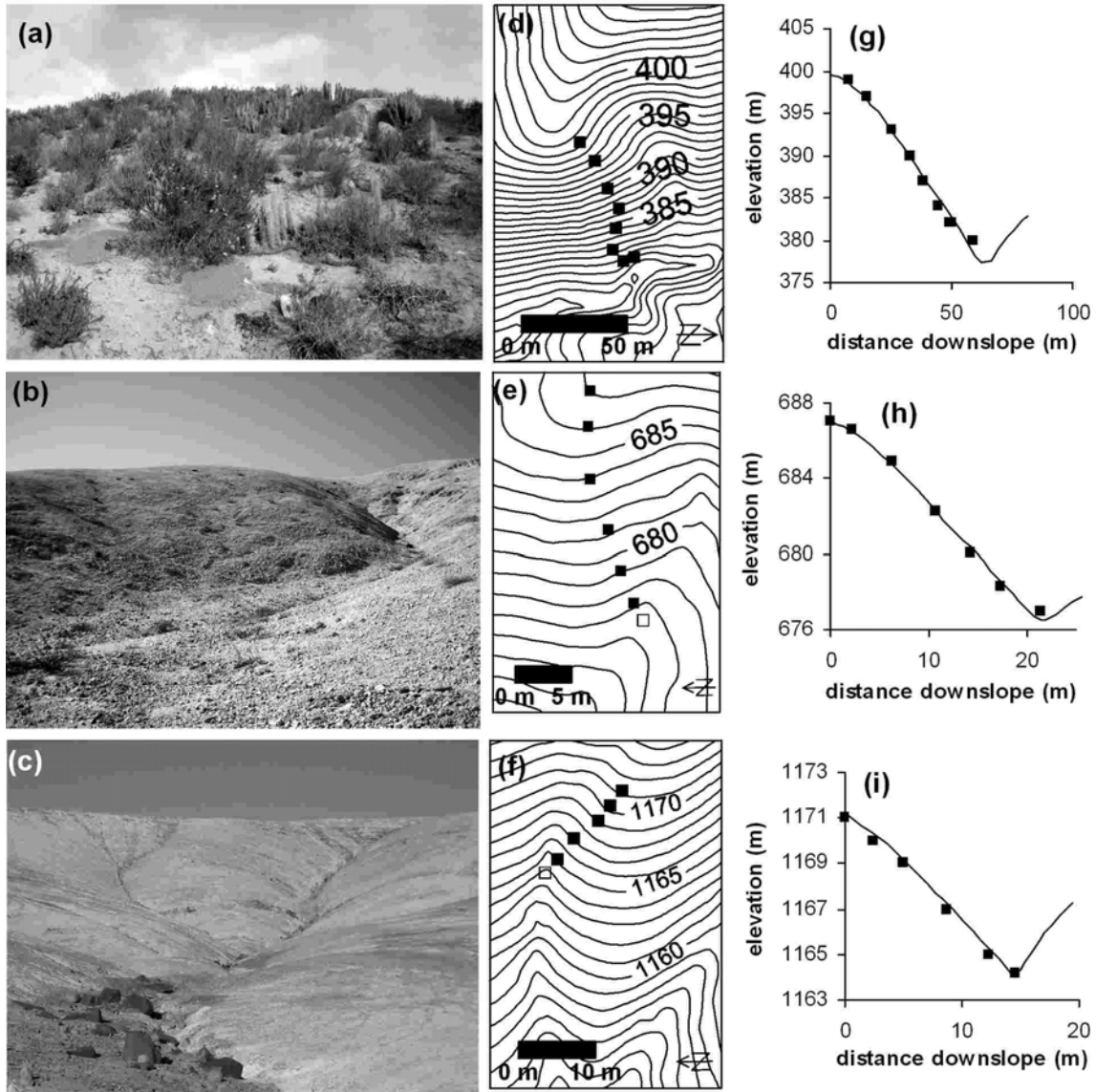
**Figure 3.** Semiarid hillslope soil has a sandy, gravelly surface overlying finer material. Roots and burrows are most common in the upper ~20 cm. Clay films are thicker and more common with increasing depth indicating deep chemical weathering.
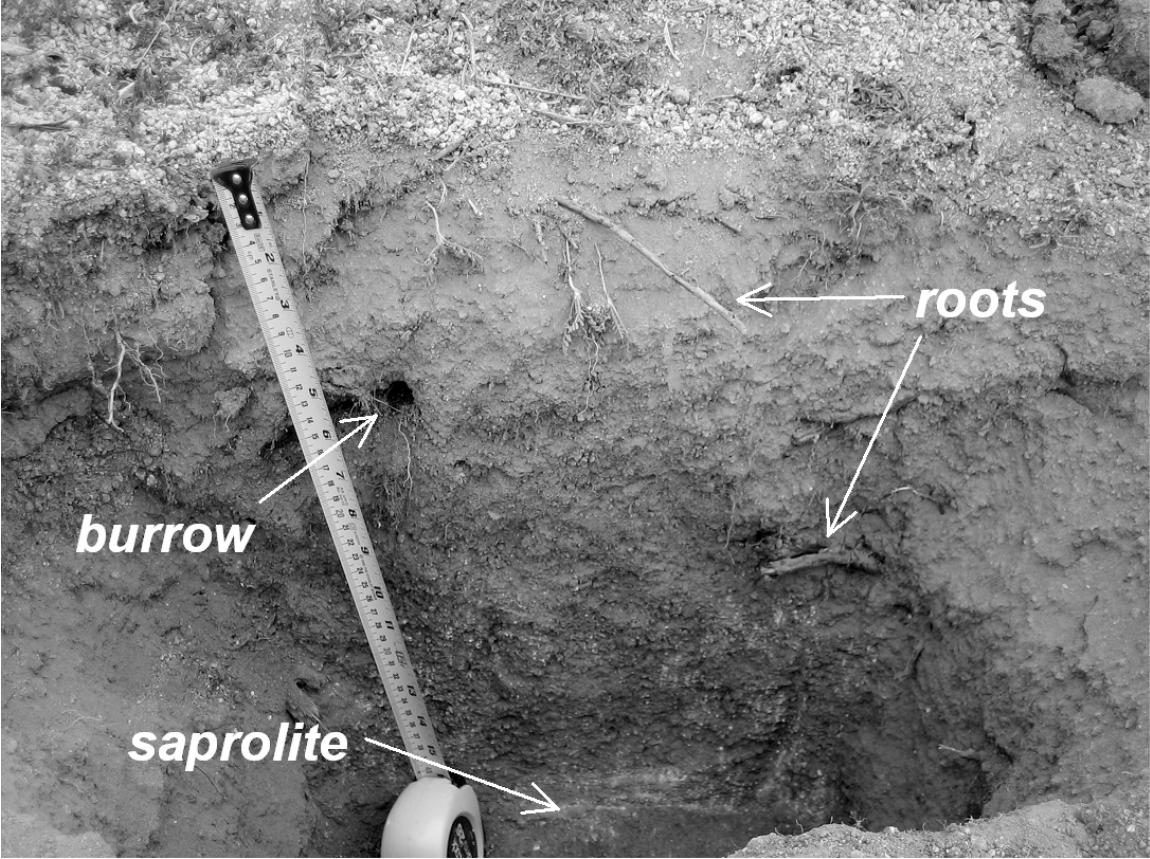
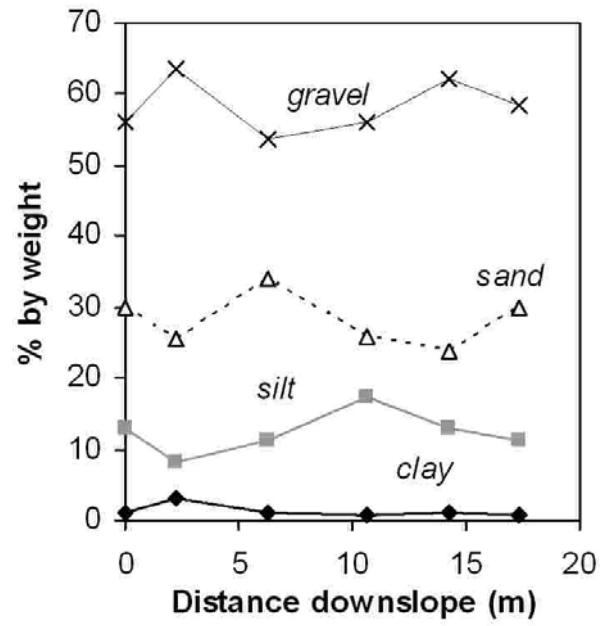**Figure 4.** Semiarid hillslope CRN data (adjusted to sea level and high latitude) on a $^{26}$Al/$^{10}$Be vs. $^{10}$Be concentration plot. Surface gravel samples generally plot farther from the steady state erosion line than the bedrock samples, indicating complex exposure history or non-steady state conditions. The error bars of one surface gravel sample (SGA-06-1-G, Table 3) extend off the plot and are due to large error in the measurement of $^{26}$Al.
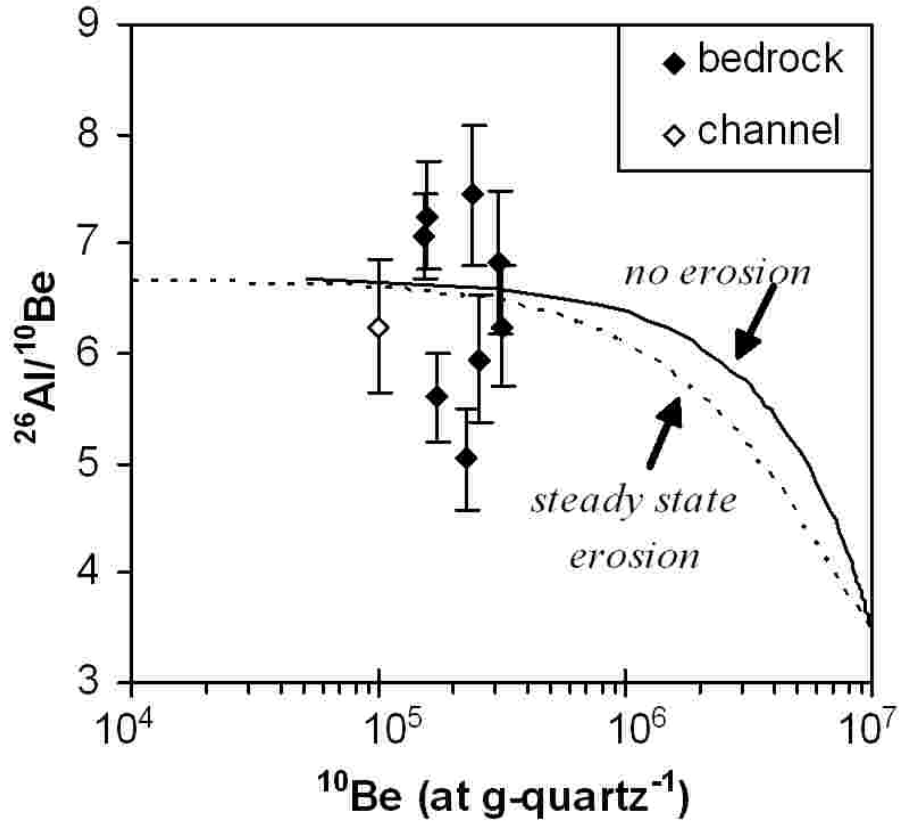
**Figure 5.** Tests of soil transport laws and covariation for the semiarid hillslope. (a) and (b) linear, slope-dependent equation (Eq. 8). The correlation between soil flux and slope is linear but there is some scatter at the highest soil fluxes, corresponding to locations >35 m from the ridge. The test for covariation shows that there is remaining variation with distance downslope and that the slope-dependent model is not appropriate. (c) and (d) slope- and depth-dependent equation (Eq. 9). Soil flux is linearly correlated to the depth-slope product, though again there is scatter at the highest soil fluxes. The two trend lines are fits to all the data ($K_h = 0.0058$ m y$^{-1}$) and to only the upper 40 m ($K_h = 0.0087$ m y$^{-1}$). The data are approximately horizontal but higher than the $K_h$ suggested by the fit to all the data (0.0058 m y$^{-1}$), and are closer to the $K_h$ calculated for the upper 40 m. (e) and (f) critical slope-dependent model (Eq. 10). Low-$\nabla z$ $K_c$ values are similar to $K_h$ and this model is nearly identical to the $H\nabla z$-dependent model because $S_c$ is large relative to the range of gradients on the hillslope. (figure on next page)

**Figure 5 continued.**
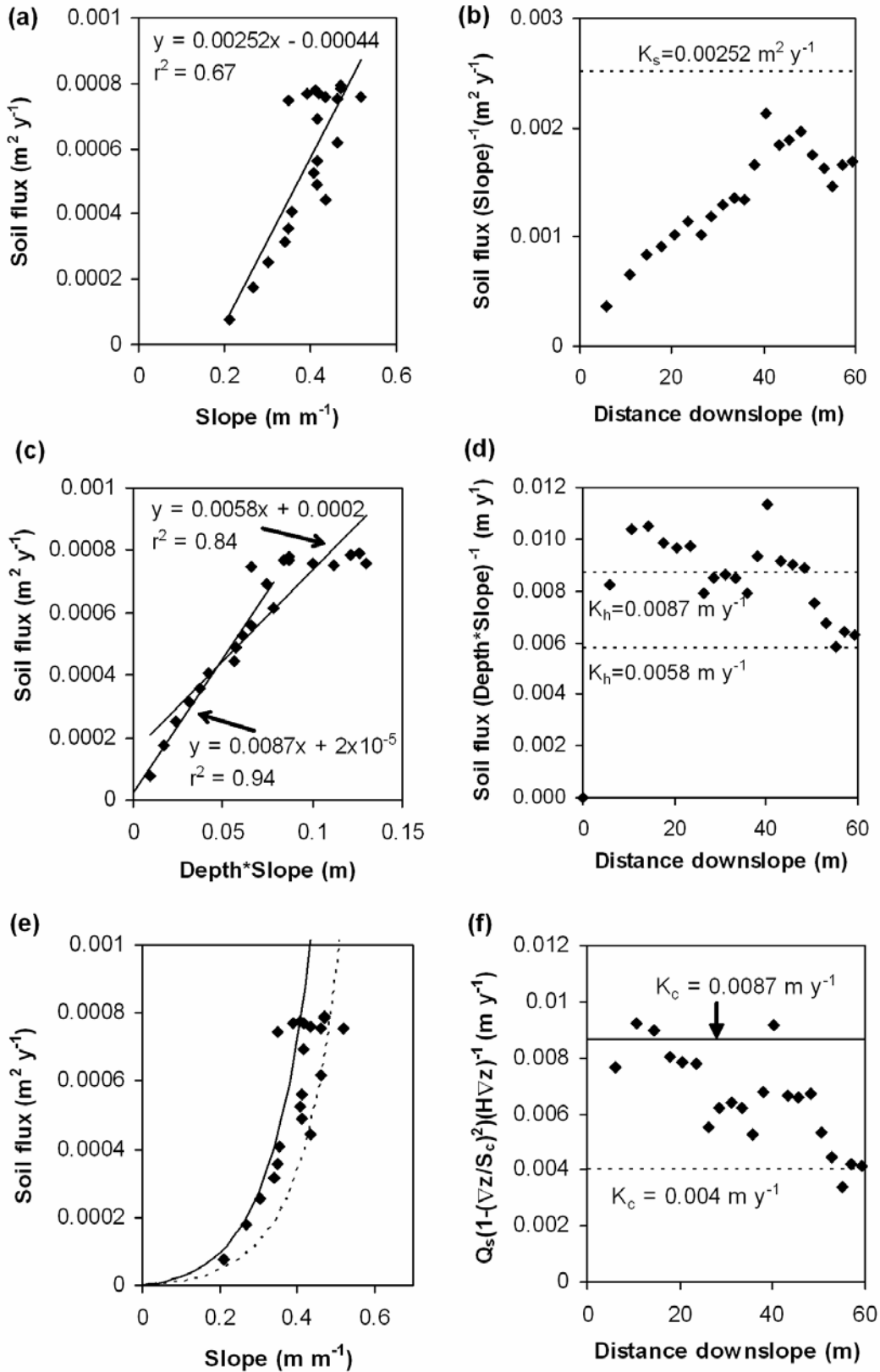
**Figure 6.** (a) Total chemical erosion ($W_{total}$), vertical chemical erosion ($W_{\phi}$), and lateral chemical erosion ($W_s$) vs. distance downslope on the semiarid hillslope. Near 40 m, the lateral erosion component shifts from negative (gain) to positive (loss). Total chemical erosion indicates chemical loss over the length of the hillslope. (b) Depth-averaged soil particle size on the semiarid hillslope vs. distance downslope. Fines content increases slightly with distance downslope and gravel content follows a trend similar to the bedrock erosion rate. (c) Semiarid CDF and ECDF are similar for the first 40 m of the hillslope then diverge, with the CDF suggesting decreasing chemical erosion relative to saprolite input whereas the ECDF indicates the opposite. (d) Semiarid hillslope soil residence times decrease slightly with distance downslope but are generally ~300 y.
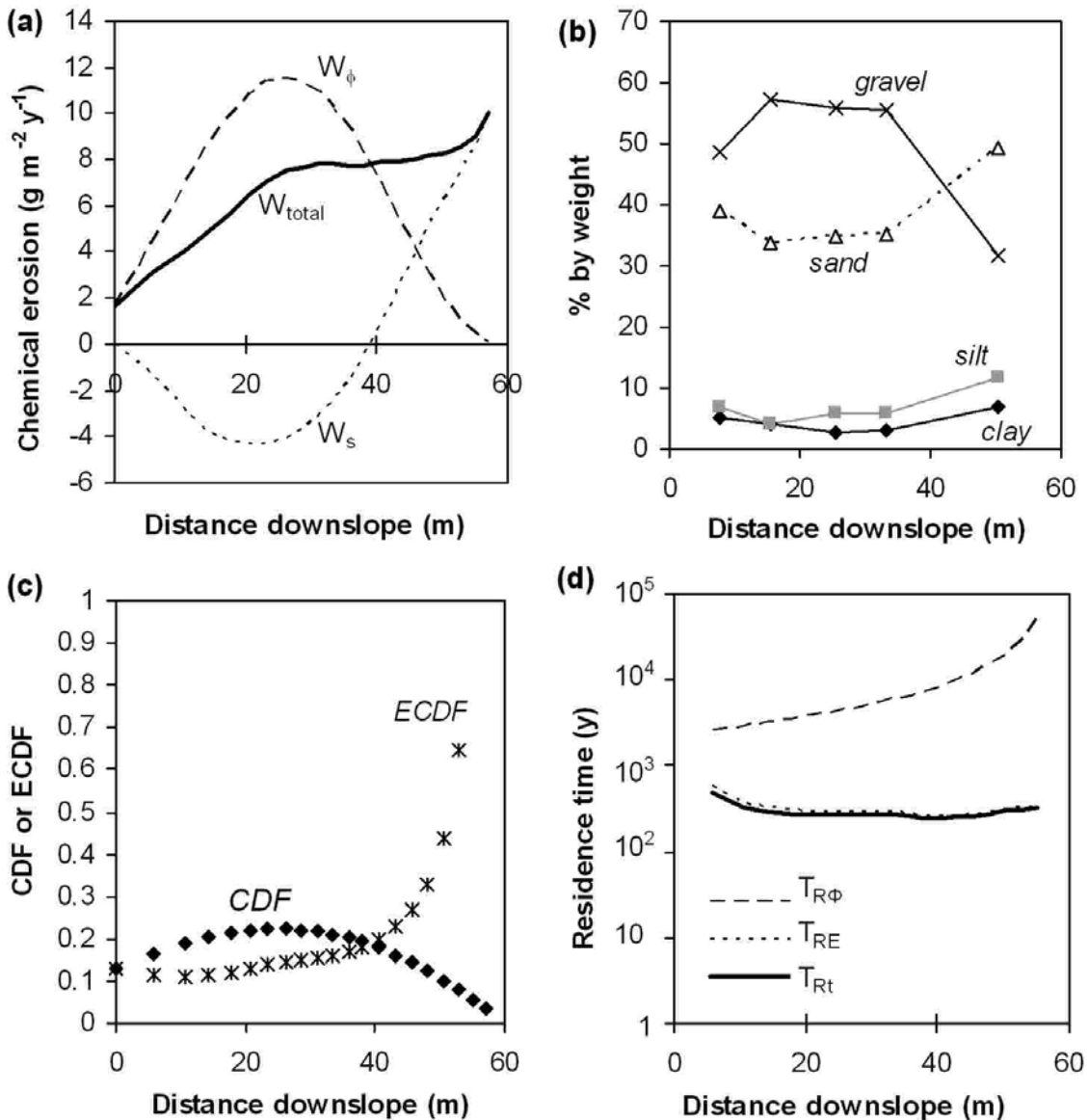
**Figure 7.** (a) The arid hillslope has an extremely thin soil cover overlying fractured bedrock. (b) Microfractures in the near-surface bedrock contain gypsum and halite, but show little evidence of chemical weathering. (c) The tops of the bedrock fragments extending into the soil are rounded. Root traces follow fractures into the underlying bedrock. (d) Surface gravels on a nearby hillslope have been sorted into bands. The coarser gravels have been colonized by lichens and appear dark.
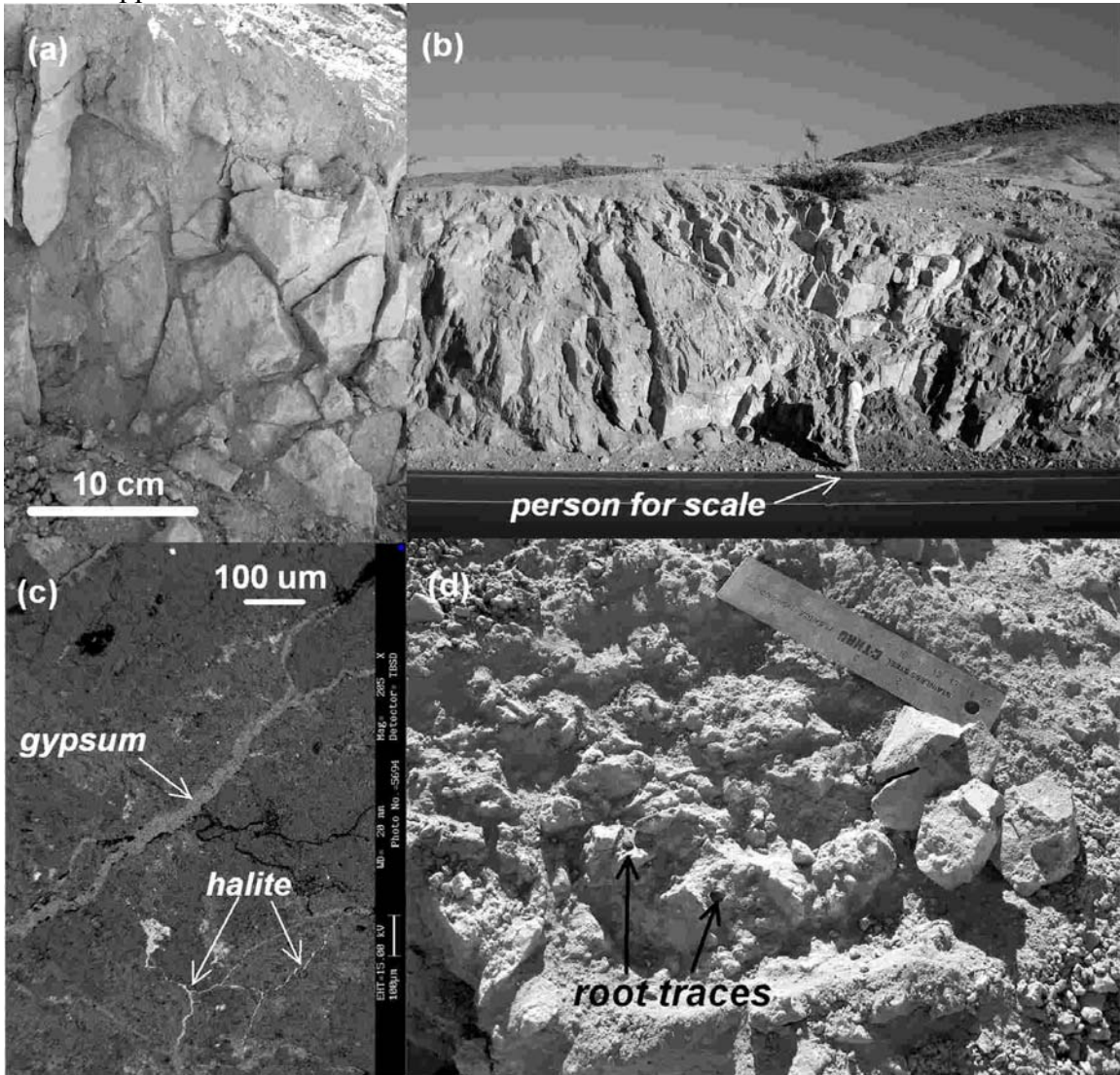
**Figure 8.** Depth-averaged particle size of the arid hillslope soils vs. distance downslope.

**Figure 9.** Arid hillslope CRN data (adjusted to sea level and high latitude) on a $^{26}$Al/$^{10}$Be vs. $^{10}$Be concentration plot. The data all plot near or just below the steady state erosion line, indicating simple exposure history close to steady state.
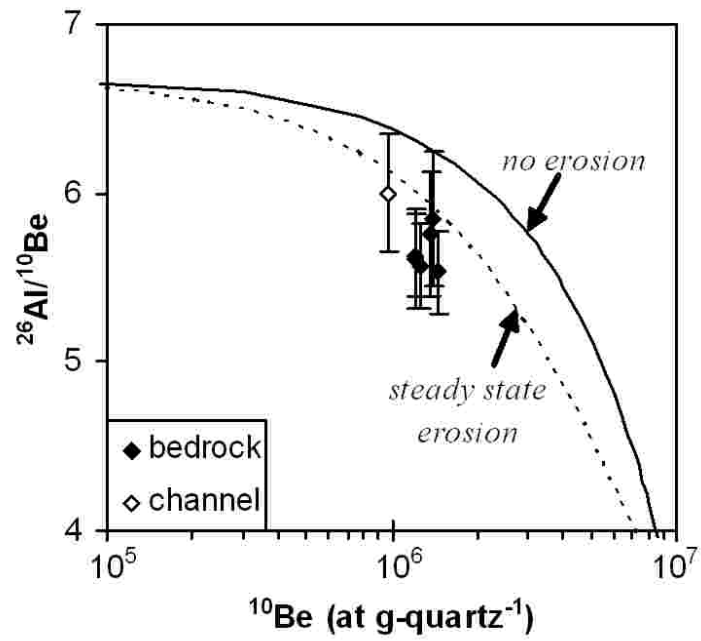
**Figure 10.** Tests for arid hillslope soil transport equation and covariation with distance downslope. (a) and (b) linear slope-dependent model (Eq. 8). As must be the case, when $A$ is included, the soil flux increases and the value of $K_s$ (0.0002 $m^2y^{-1}$) is greater than when there is no $A$ ($K_s = 0.00007$ $m^2y^{-1}$). The test for covariation shows that there is remaining variation with distance downslope and that the slope-dependent model is not adequate. (c) and (d) slope- and depth-dependent equation (Eq. 9). Because the soil thickness has been modeled as constant, the same patterns are produced in this test as in (a) and (b). (e) and (f) critical slope-dependent transport law (Eq. 10). The data are bounded by dashed lines defined by $K_c = 0.002$ and $S_c = 0.55$ (left dashed line), and $K_c = 0.0012$ and $S_c = 0.70$ (right dashed line). The solid line is defined using $K_c = 0.0016$ and $S_c = 0.65$. The test for covariation shows that the data vary homoscedastically around the middle $K_c$ value. (g) and (h) overland flow transport law (Eq. 11). In the best fit, $K_w = 1x10^{-5}$ m $y^{-1}$, $n = 1$, and $m = 1$, and this model appears to be most applicable towards the base of the slope based on the covariation with $x$. (figure on next page)

**Figure 10 continued.**
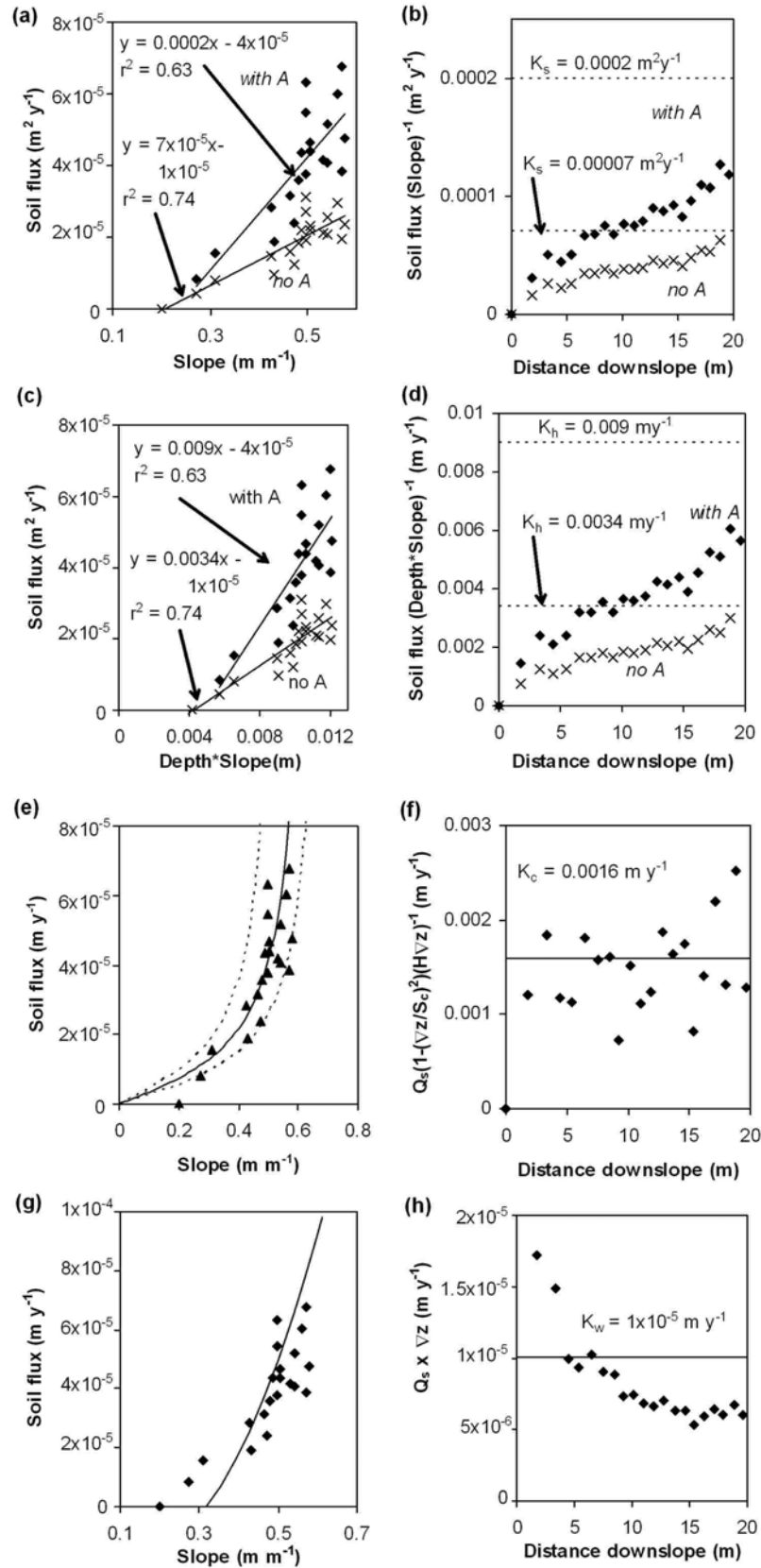
**Figure 11.** (a) and (b) Chemical erosion on the arid hillslope vs. distance downslope, calculated with atmospheric input and without, respectively. In both cases, chemical erosion is greatest at the top of the hillslope. (c) CDF and ECDF values are similar, whether calculated with atmospheric input or without, but the inclusion of atmospheric input greatly reduces their values. (d) Arid hillslope soil residence times calculated with atmospheric input. $T_{RE}$ and $T_{Rt}$ overlap each other at 0 y, whereas $T_{R\phi}$ decreases slightly with distance downslope.
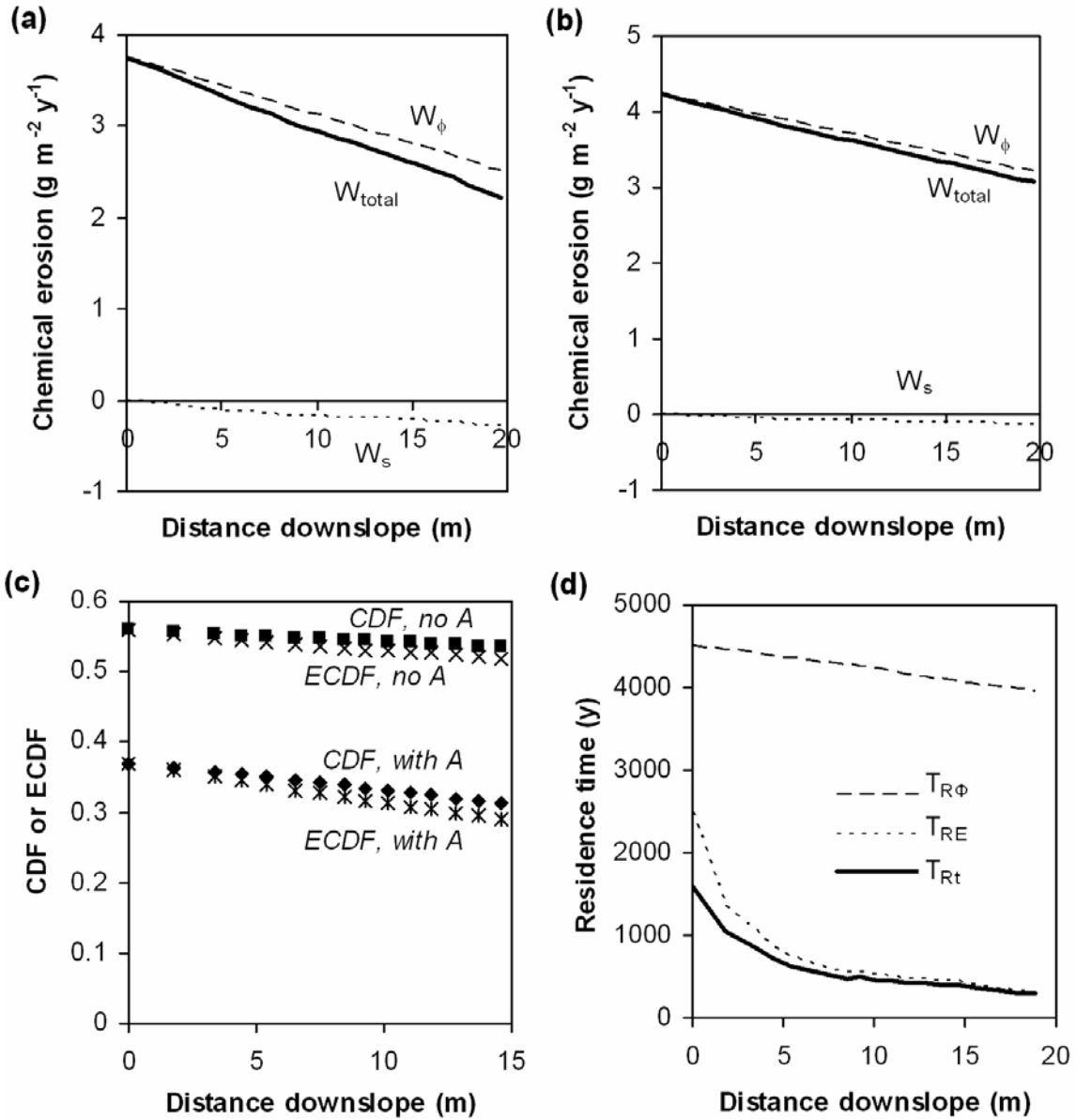
**Figure 12.** (a) Soils on the hyperarid hillslope are thin and gypsum-rich. (b) Gypsum, halite, and nitrate penetrate into the underlying bedrock and produces coarse polygons. The black lines indicate the gravel-poor boundaries between the polygons in the foreground. Central polygon is ~1.5 m across. (c) More of the bedrock is exposed in a road cut through a nearby hillslope which has a similarly thin soil (<15 cm) on top of salt-infused bedrock. A rock hammer is lying on the soil surface. (d) SEM-EDS image of a bedrock fragment thin section showing halite and nitrate in a microcrack. The surface is unweathered.
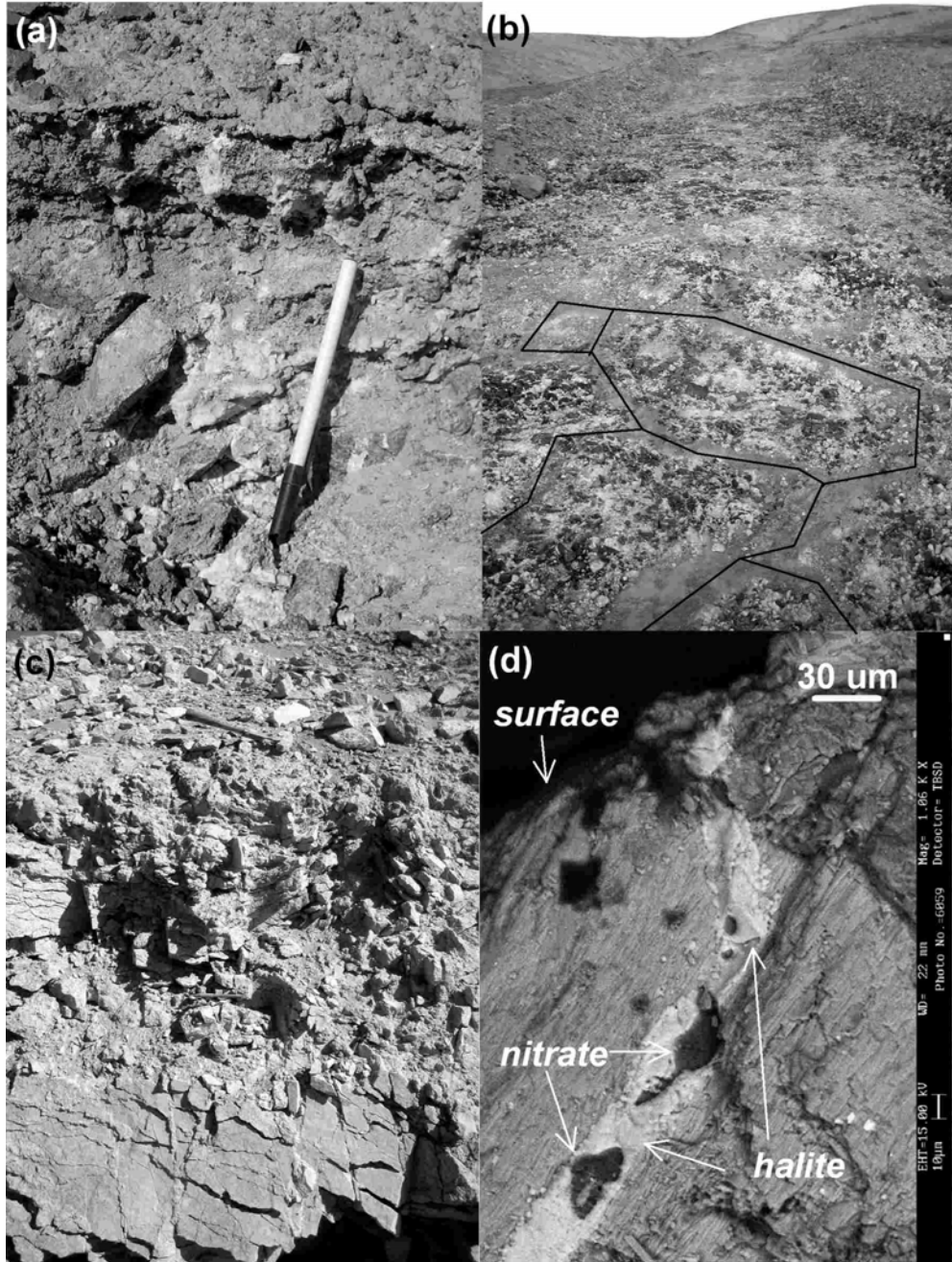
**Figure 13.** (a) Sand content increases slightly with distance downslope, while clay and silt fractions stay nearly constant. Gravel content (not including surface gravels) decreases. (b) Depth-averaged soil sulfate concentration increases slightly with distance downslope. (c) Nitrate, chloride, and iodine concentrations vary randomly or are nearly constant. Note that sulfate is on a different scale and more than an order of magnitude greater than chloride, nitrate, and iodate.
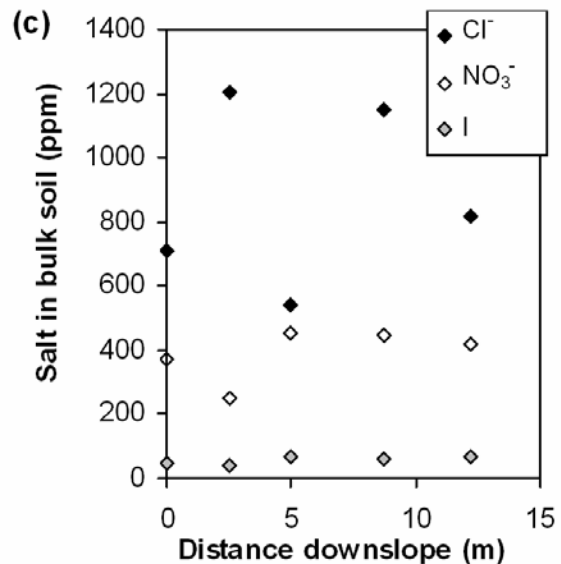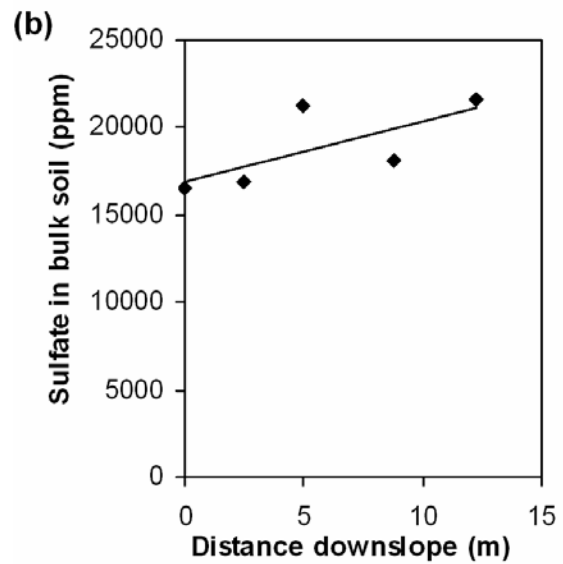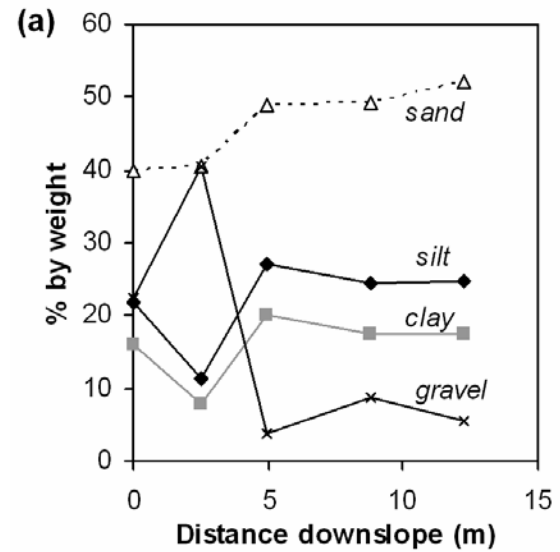
**Figure 14.** (a) Contour-parallel bands of darkly-varnished, sorted gravels on a hillslope in the hyperarid region. (b) View upslope of a gravel band showing the particle sorting.
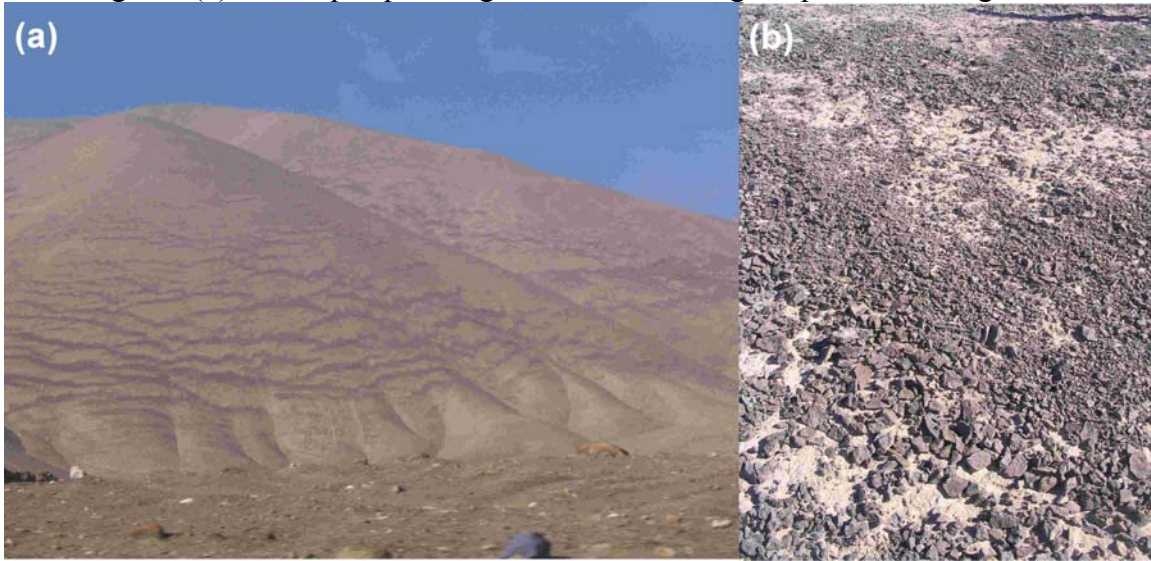
**Figure 15.** Hyperarid hillslope CRN data (adjusted to sea level and high latitude) on a $^{26}$Al/$^{10}$Be vs. $^{10}$Be concentration plot. The bedrock plot within the steady-state erosion window, within error, while the channel sample lies below the steady-state erosion line.
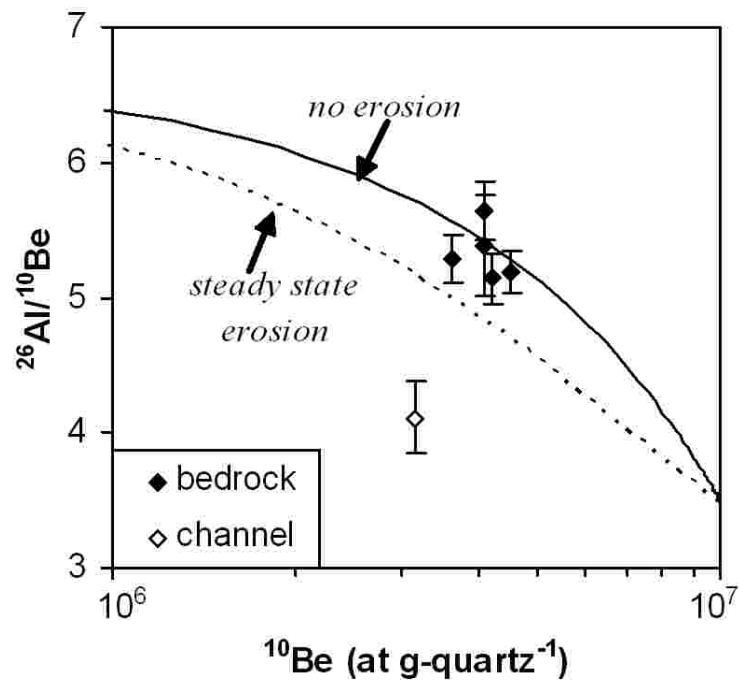
**Figure 16.** Tests for hyperarid hillslope soil transport law and covariation. (a) and (b) the linear slope-dependent equation (Eq. 8). Physical erosion is not strongly correlated to slope gradient and the test for covariation shows that the slope-dependent model is not adequate. (c) and (d) the slope- and depth-dependent equation (Eq. 9). Because the soil thickness varies so little, the plots testing the equation 9 are similar to (a) and (b) and do not show a good fit. (e) and (f) the critical slope-dependent transport law (Eq. 10). Lines were calculated using $H = 0.07$ m (the average soil thickness). The right dashed boundary is defined by $K_c = 2.5 \times 10^{-5}$ m y$^{-1}$, the left dashed boundary is defined by $K_c = 1 \times 10^{-4}$ m y$^{-1}$ and $S_c = 0.53$, and the solid line is defined by $K_c = 5 \times 10^{-5}$ m y$^{-1}$ and $S_c = 0.68$. The test of covariation based on the solid line shows the values mostly vary homoscedastically around the $K_c$ value. (g) and (h) the overland flow transport law (Eq. 11), which was best constrained with $K_w = 4 \times 10^{-6}$ y$^{-1}$, $n = 2$, and $m = 2$. This model appears to be most applicable towards the base of the slope. (figure on next page)
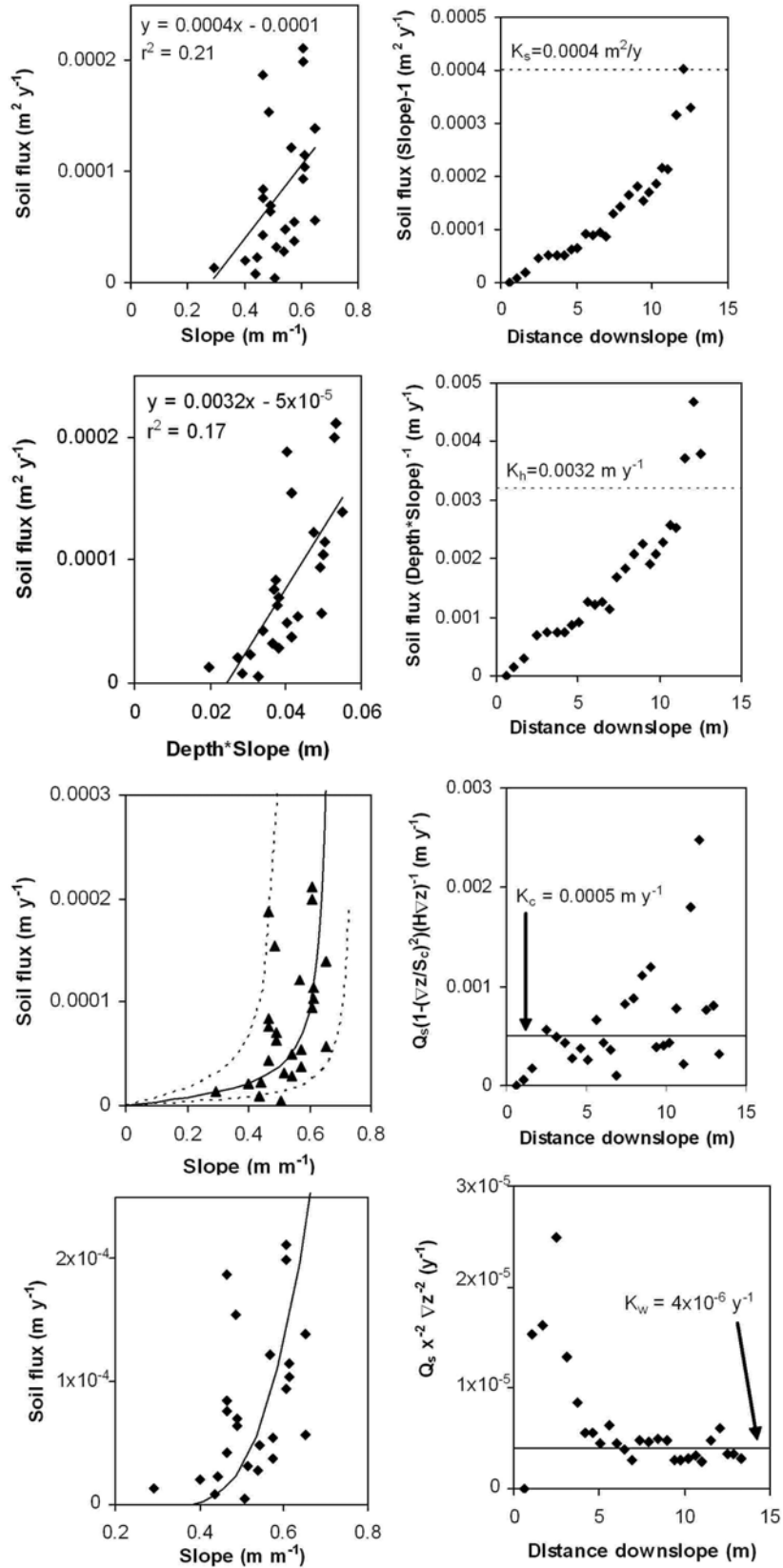
**Figure 16 continued.**

**Figure 17.** (a) Chemical erosion on the hyperarid site shows increasing gain (more negative) with distance downslope. Though the component due to weathering of incoming material ($W_\phi$) is fairly steady, $W_s$ decreases substantially and indicates that lateral leaching of the soil decreases with distance downslope. (b) CDF and ECDF are similar near the top of the hillslope but increasingly diverge with distance downslope. (c) Soil residence time vs. distance downslope.
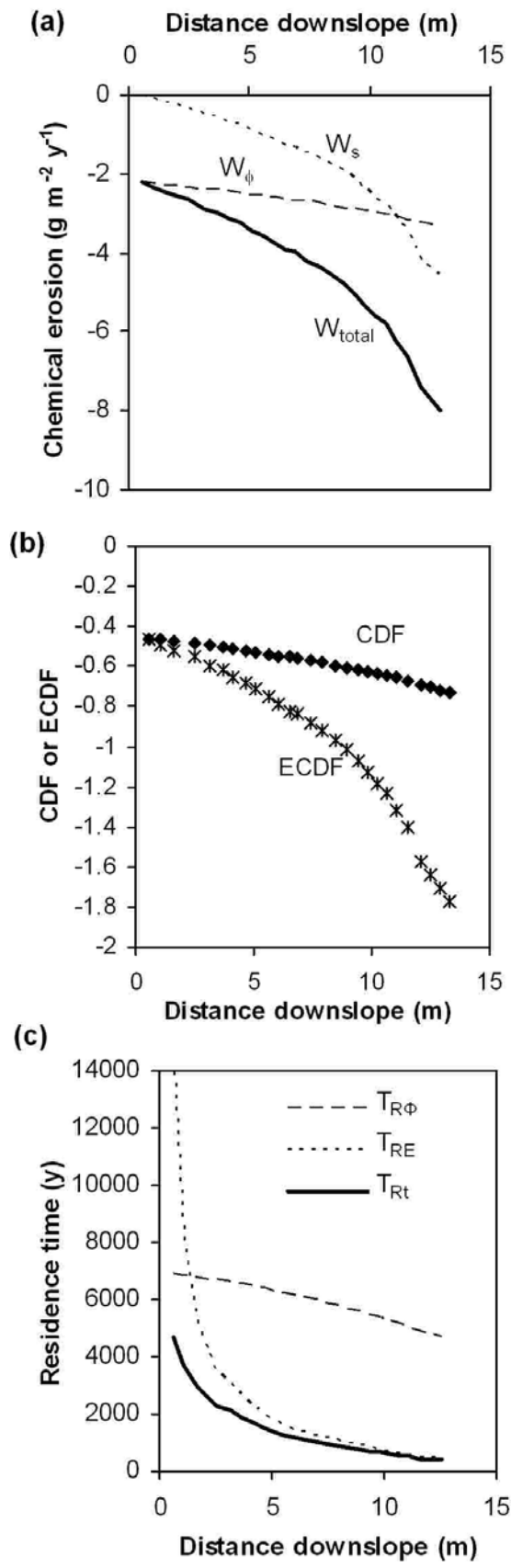
**Figure 18.** Soil flux and chemical erosion summed over the upper 13 m of each hillslope for the hyperarid, arid, and semiarid hillslopes of this study and the Frog Hollow hillslope (Yoo et al., 2007).
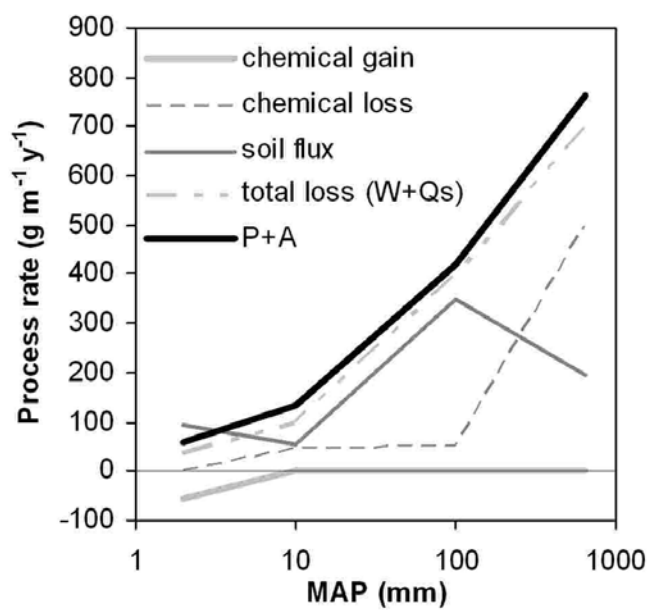
**Figure 19.** (a) Hillslope bedrock erosion rates as a function of MAP. Data are limited to bedrock erosion rates calculated by measuring CRN in granitic bedrock at the soil-bedrock interface, except for the data of Hewawasen et al. (2003), Riebe et al. (2004a), and von Blanckenburg et al. (2004), which were calculated from localized samples of hillslope soils. If the soil is well-mixed then erosion rates calculated from the soil should be similar to rates calculated from bedrock. The grey trendline is through the data from this study (white circles). (b) NPP as a function of MAP (Leith, 1973) shows some dependence on MAP at lower MAP (<500 mm). (c) low-gradient $K_c$ values (which are comparable to $K_h$ values) of the Atacama sites are strongly correlated to MAP, whereas at MAP>100 mm, $K_h$ values show no correlation. Frog's Hollow (open triangle) has a low $K_h$ value due to high chemical erosion. Tennessee Valley (open square) has a high $K_h$ value because it is in sandstone rather than granite.
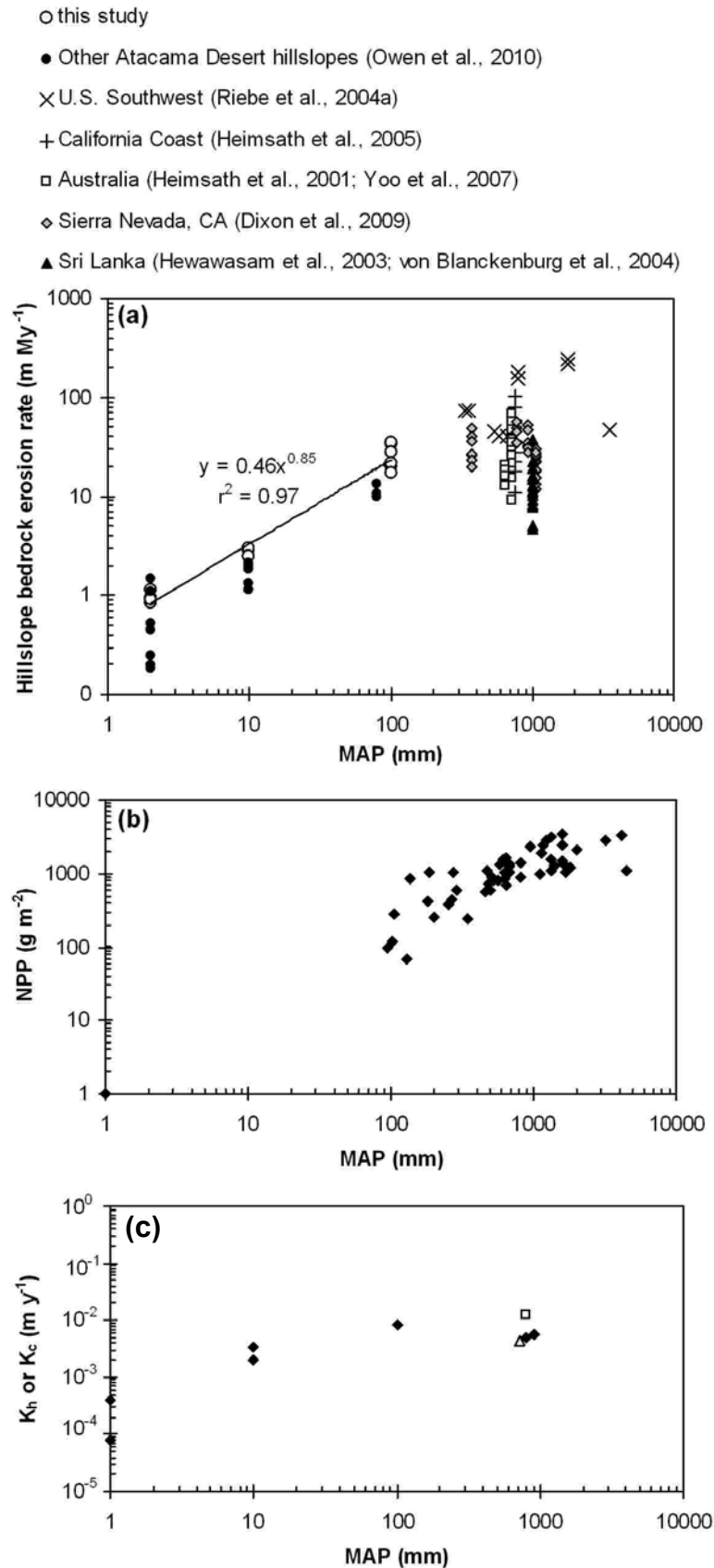


118

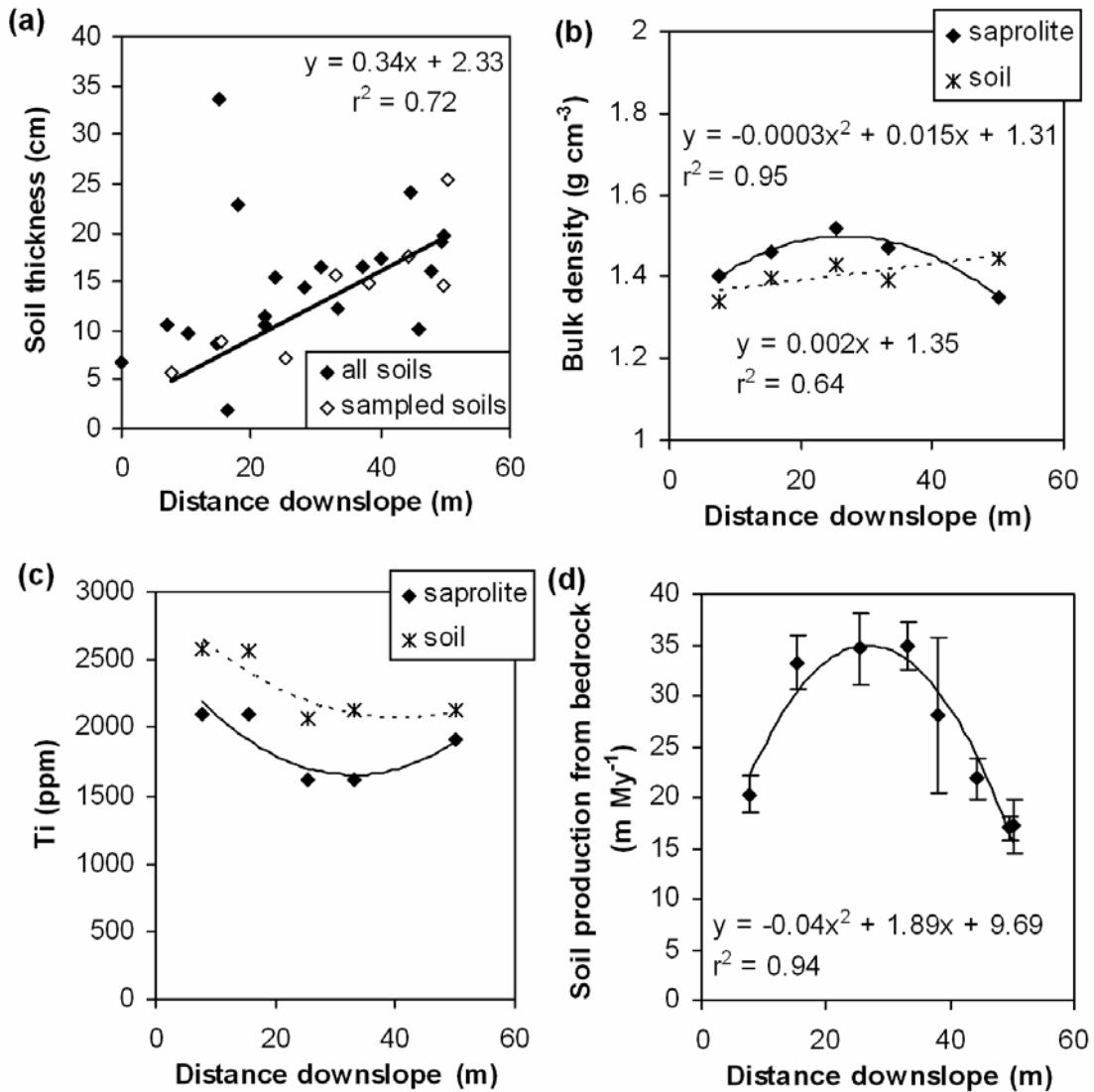**Figure A1.** Semiarid hillslope soil transect data showing trend lines used to interpolate values along the length of the hillslope for input into the calculation of $Q_s$ and $W$. (a) slope-normal soil thickness measured in all the excavations (trend line is through the sampled soil data). (b) soil and saprolite bulk density. (c) soil and saprolite [Ti] ($C_{is}$ and $C_{ir}$). $C_{is} = 0.54x^2 - 43.75x + 2950$ ($r^2 = 0.83$) and $C_{ir} = 0.84x^2 - 55.24x + 2564$ ($r^2 = 0.78$). (d) The rate of soil production from saprolite.

**(a)**

Soil thickness (cm) vs Distance downslope (m)

$y = 0.34x + 2.33$
$r^2 = 0.72$

♦ all soils
◊ sampled soils

**(b)**

Bulk density (g cm$^{-3}$) vs Distance downslope (m)

♦ saprolite
✳ soil

$y = -0.0003x^2 + 0.015x + 1.31$
$r^2 = 0.95$

$y = 0.002x + 1.35$
$r^2 = 0.64$

**(c)**

Ti (ppm) vs Distance downslope (m)

♦ saprolite
✳ soil

**(d)**

Soil production from bedrock (m My$^{-1}$) vs Distance downslope (m)
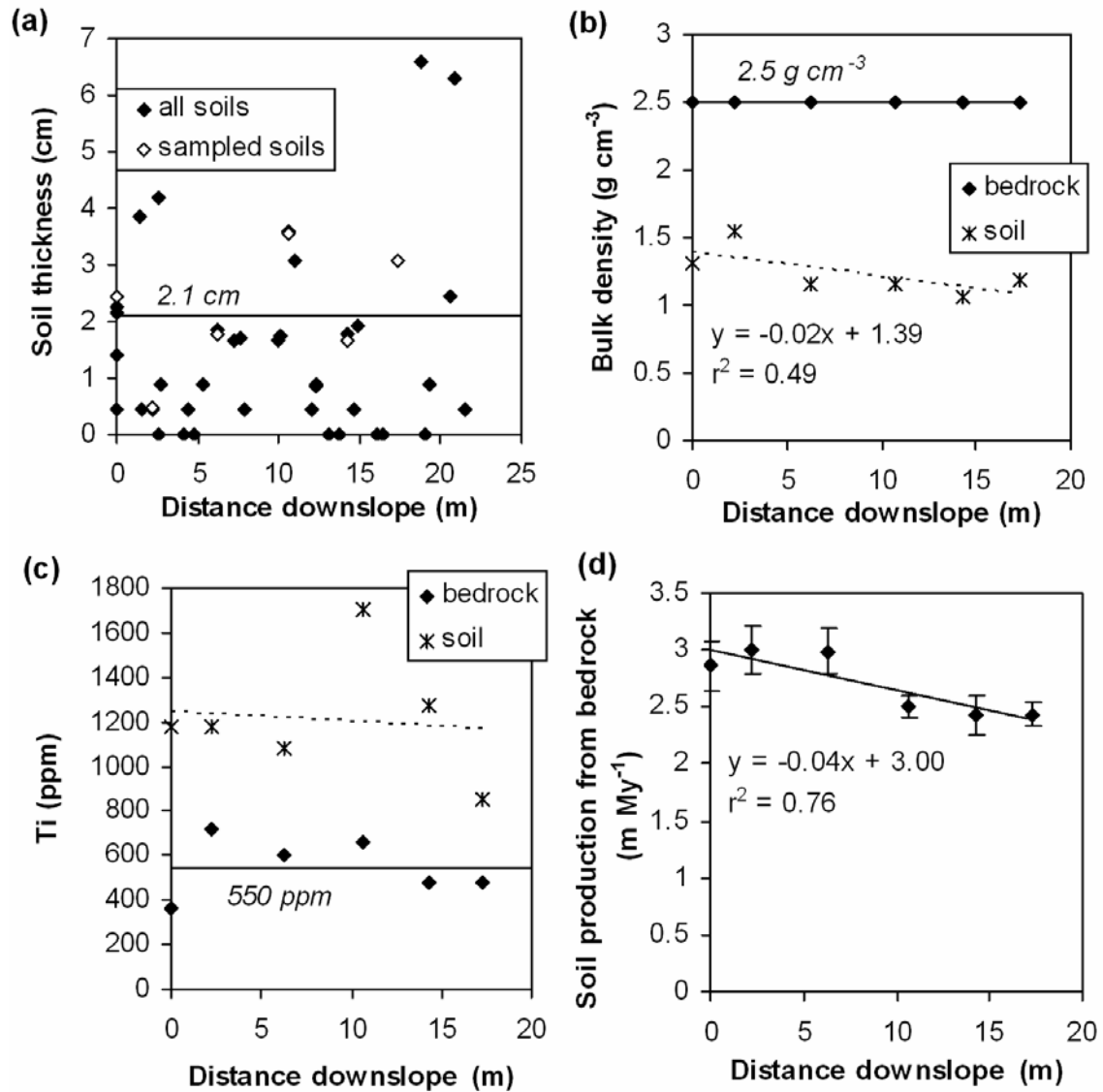
$y = -0.04x^2 + 1.89x + 9.69$
$r^2 = 0.94$

119

**Figure A2.** Arid hillslope soil transect data showing trend lines used to interpolate values along the length of the hillslope for input into the calculation of $Q_s$ and $W$. (a) slope-normal soil thickness, (b) soil and bedrock bulk density, (c) $C_{is}$ and $C_{ir}$, and (d) the rate of soil production from bedrock. In figure (c), $C_{is}$ = -4x +1246 ($R^2$ = 0.01) and average $C_{ir}$ = 550 ppm.

**Figure A3.** Hyperarid hillslope soil transect data showing trend lines used to interpolate values along the length of the hillslope for input into the calculation of $Q_s$ and $W$. (a) slope-normal soil thickness, (b) soil and bedrock bulk density, (c) soil and bedrock [Ti], and (d) rate of soil production from bedrock. In (c), $C_{is} = -130x + 4237$ ($r^2 = 0.86$) and $C_{ir} = -58x + 1893$ ($r^2 = 0.24$).
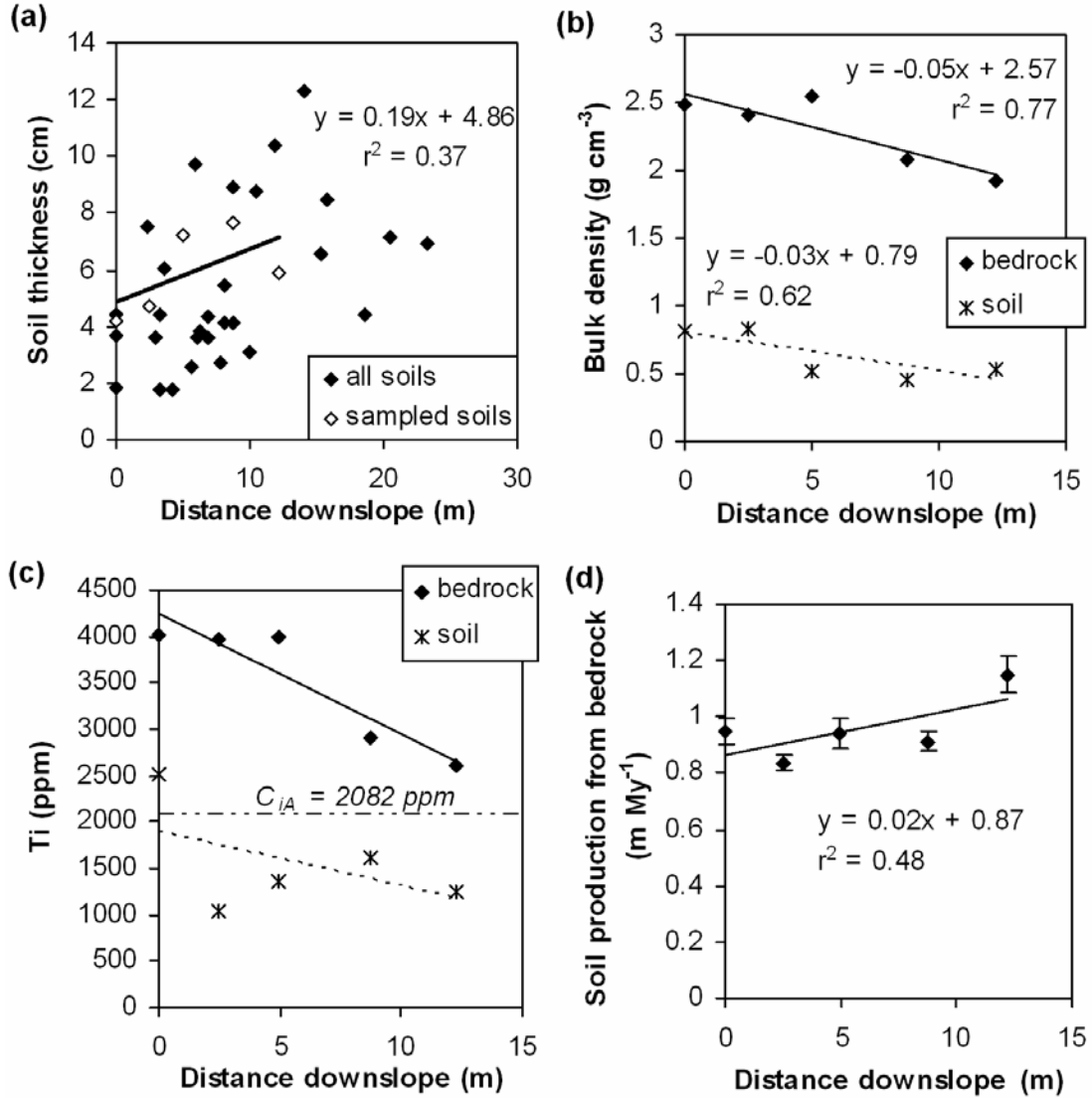
# Chapter 4

## The Zebra Stripes of the Atacama Desert: Fossil Evidence of Overland Flow

**Abstract**

Some hillslopes in the hyperarid region of the Atacama Desert of northern Chile have surface gravels which have formed distinct, contour-parallel bands which we call "zebra stripes" (due to the contrast between the darkly-varnished gravels and the light-colored, salt-rich soil). The zebra stripes are sorted such that the coarsest gravels are at the downslope front. How and when the zebra stripes formed are perplexing questions, particularly in a region experiencing prolonged hyperaridity. Using GoogleEarth, satellite imagery, and field observations, we report the first quantitative observations of zebra stripes in order to test hypotheses of the mechanisms and timing of their formation. We consider soil shrinking and swelling, seismic shaking, and overland flow as possible formation mechanisms and find that overland flow is the most likely. Based on cosmogenic radionuclide concentrations in surface gravel and bedrock, as well as salt deposition rates from the atmosphere and content in the soils, we propose that the salt-rich soils began accumulating >0.5-1 Ma and the zebra stripes formed in the last $10^3$-$10^5$ y. The zebra stripe pattern has been preserved due to the self-stabilization of the gravels within the stripes and the continued absence of life (which would disturb the surface, as seen at a wetter site the south). The accumulation of the salt-rich mantle and the formation of zebra stripes suggest a profound climatic change occurred sometime between the late Pliocene and early Holocene.

## INTRODUCTION

The hyperarid Atacama Desert contains an array of both familiar and unique landform features of great antiquity. Some of the most visually striking features are contour-parallel bands of sorted gravels on gently-sloping hillslopes (Fig. 1). We refer to these as "zebra stripes" because the gravels, coated with a dark varnish, contrast sharply with the underlying sulfate-rich soils, and form distinct bands. In contrast, the subhorizontal alluvial fans adjoining these slopes are often covered by a more continuous, commonly interlocking desert pavement. Zebra stripes appear to be a feature unique to the Atacama Desert, since nothing similar has been reported to date from other deserts on Earth, despite extensive study of surface gravels in Arizona (Abrahams et al., 1986; Abrahams et al., 1992), New Mexico (Wilcox et al., 1997), California (Clark, 1972; Castle and Youd, 1972; McFadden et al., 1987; Anderson et al., 2002; Sylvester et al., 2002), the Namib Desert (Van der Wateren and Dunai, 2001), and the Negev Desert (Yair, 1983, 1990; Yair and Kossovsky, 2002; Kuhn et al, 2004; Matmon et al., 2009).

Zebra stripes may be a special case of disturbed desert pavement on hillslopes in the Atacama Desert. Desert pavement is a layer of coarse fragments that forms on low-gradient landforms in arid to hyperarid regions (McFadden et al., 1998). It is characterized by a single layer of rock fragments which overlie a sometimes vesicular, always nearly gravel-free soil horizon whose thickness varies depending on the age of the surface, rate of atmospheric dust and solute input, climate, and topography (e.g. McFadden et al., 1987, 1998; Al-Farraj and Harvey, 2000; Anderson et al., 2002; Wood et al., 2005; Adelsberger and Smith, 2009). Desert pavement "floats" on the accumulation of atmospherically-derived salt and dust such that the surface clasts experience constant exposure from the time the geomorphic surface is formed (McFadden et al., 1998). This continuous exposure has been demonstrated using cosmogenic radionuclide ($^3$He)

dating of volcanic surfaces and pavement clasts in the Mojave Desert, CA (Wells et al., 1995). Desert pavement is often poorly developed, if at all, on moderately to steeply sloping surfaces due to sporadic overland flow or other disturbance (Wood et al., 2005; Adelsburger and Smith, 2009). Desert pavement patterns appear to at least partially preserve the topography and gravel distribution prior to the accumulation of the atmospherically-derived material (Wood et al., 2005). In Chile, bar and swale features persist in desert pavements on Miocene landforms, attesting to both the importance of initial gravel distribution and its persistence over millions of years under favorable conditions.

The zebra stripes may be formed through the disruption of desert pavement and persist on the hillslope due to the continuing hyperaridity and minimal subsequent disturbance. However, the process of zebra stripe formation is unknown. How and when the zebra stripes formed, and why they persist, are interesting questions involving the coupling between geomorphology and climate. In this paper, we (1) make the first quantitative observations of these features (and their associated hillslopes and soils), (2) consider an array of hypotheses of zebra stripe formation, and (3) conclude that zebra stripes were likely produced by ancient overland flow and have been preserved under hyperarid conditions.

**PHYSIOGRAPHY, SEISMICITY, AND CLIMATE OF THE ATACAMA DESERT**

The Atacama Desert spans a region from southern Peru into northern Chile. The largely lifeless zone for which the Atacama is renowned extends south to ~26.3ºS, near Chañaral. It is primarily located in the north-south trending Central Depression, bounded on the west by the Coast Range and on the east by the pre-Andean ranges (Fig. 3).

Seismic records indicate that there is some latitudinal variation in earthquake activity, corresponding to different segments of the subducting Nazca plate. There are two flat-slab regions between 2-15ºS and 27-33ºS which subduct at an angle of 5-10º, whereas the rest of the plate subducts at an angle of ~30º (Jordan et al., 1983). Seismicity is more frequent and intense over the flat-slab regions, but the entire region is seismically active (Jordan et al., 1983). The positive correlation between historic seismicity and Neogene crustal deformation suggests that current stress regimes are similar to those that drove Andean uplift (Jordan et al., 1983), thus the boundaries between regions of differing seismicity have likely been constant for over 20 My. Data compiled by Goes (1996) indicate several earthquakes of magnitudes ≥ 7 have occurred in northern Chile during the last 100 years, but available records are too sparse to determine a recurrence interval of these large events. Nevertheless, most of northern Chile has likely experienced large earthquakes since the Neogene, and if seismic shaking were producing zebra stripes then their formation would be ongoing through today.

Present-day mean annual precipitation (MAP) in Chile decreases exponentially with decreasing latitude, from ~100 mm y$^{-1}$ at 29ºS to 1 mm$^{-1}$ or less between 20 and 26ºS (Ericksen, 1981). MAP also decreases with increasing longitude, with the pre-Andean ranges generally wetter than the Central Depression (Houston, 2006). The Coast Range is subjected to frequent fog, but the penetration of fog inland decreases rapidly with distance from the coast (Cáceras et al., 2007). Precipitation seasonality changes with latitude: rainfall shifts from winter Pacific Westerlies in the south to summer Atlantic easterlies in the north, with the inflection point near Iquique (~20.5ºS) (Houston, 2006). Geochemical evidence suggests that dry conditions have

persisted at least periodically since the middle to late Miocene (Alpers and Brimhall, 1988; Sillitoe and McKee, 1996; Hartley and Chong, 2002; Dunai et al., 2005; Clarke, 2006; Houston, 2006; Nishiizumi et al., 2005; Rech et al., 2006; Kober et al., 2007), and possibly much earlier (Clarke, 2006; Hartley et al., 2005).

Within this long-term aridity, there have been episodes of more pluvial conditions which have been correlated to orbital forcing and ENSO (the El Niño-Southern Oscillation).  Sediment deposition rates inferred from offshore drill cores between 24°S and 44°S indicate that the Southern Westerlies moved north as much as 5° latitude from their current position ~24 to 16 ka, likely increasing precipitation by about an order of magnitude (Lamy et al., 2000; Hebbeln et al., 2007).  The increased sediment deposition, and inferred increased precipitation, recorded in the sediment cores corresponds to a precessional maxima (Stuut and Lamy, 2004).  Salt cores (Bobst et al., 2001), paleowetland deposits (Rech et al., 2003), rodent middens (Betancourt et al., 2000; Latorre et al., 2002; Latorre et al., 2003), and archeological studies (Núñez et al., 2002) generally corroborate the marine sediment findings.  Discrepancies between these studies may occur when the study sites are located near the border between winter and summer precipitation zones (Houston and Hartley, 2003) which have opposite responses to El Niño conditions, discussed more below (Houston, 2006).  The wetter episodes described above have been of insufficient magnitude and duration to remove or chemically alter highly water-soluble and biologically-reactive compounds such as nitrate in the hyperarid parts of the Central Depression (Ewing et al., 2007).

None of the records mentioned above are of fine enough resolution to identify individual storms.  Unfortunately, historical precipitation records in northern Chile date back to the 1900's at the earliest and are limited to monthly records from a few coastal towns (Worldclimate.com).  There are essentially no data on the intensity of the rare storm events (Ortlieb, 1995), although these are the most geomorphologically significant.  However, the records do provide some constraints on the regional distribution of precipitation, the recurrence intervals of particularly wet years, and the conditions that promote them.  Precipitation on the northern Chilean coast and Central Valley occurs primarily in the winter (May-October), whereas on the coast north of ~20-22°S and in the Andes occurs primarily in summer (November-April) (Houston and Hartley, 2003; Houston, 2006).  Along the northern Chilean coast, annual rainfall>10 mm recurs on decadal to century timescales (Houston, 2006).  Wetter years in this region correspond to El Niño events (whereas in the northern, summer-precipitation zone, wetter years correspond to La Niña), but not all El Niño phases result in wetter conditions (Houston, 2006; Magilligan and Goldstein, 2001; Vargas et al., 2006).  A study of atmospheric conditions coinciding with the northern Chile events indicates that, in addition to El Niño conditions, high latitude (~40-60°S) tropospheric anomalies were necessary to redirect precipitation-producing air masses (Vargas et al., 2006).

The largest storm for which there is hourly intensity data occurred in Antofagasta (Fig. 3) in 1991 (an El Niño year) and caused debris flows (Vargas et al., 2000).  Precipitation averaged 0.5 to 1.4 cm/h and peaked at 2.4 cm/h (Vargas et al., 2000).  Thus, the best proxy for storm intensity near our area of study appears to be the sedimentary records of flooding and debris flows in Antofagasta.  Since 1930, storm events triggering debris flows have coincided with the winter period of the development phase of El Niño and the arrival of frontal systems from the

north (Vargas et al., 2006). Debris flow deposits near Antofagasta date back to ~23.5 ka and include 45 deposits since ~5.5 ka. Between ~8.4 ka and 5.3 ka there is a conspicuous lack of alluvial deposition in both southern Peru and northern Chile, after which debris flow activity simultaneously began in both regions (Vargas et al., 2006). This pattern is consistent with that derived from other records in the northern Andes, that there were limited ENSO effects until ~5.7 ka (Vargas et al., 2006). If high-intensity precipitation in this region is generally correlated with El Niño-like conditions, then periods in the more distant past with El Niño-like conditions might also have produced large storms or higher rainfall. These might include the periods of high erosion that recur on precessional timescales discussed above, as well as the mid-Pliocene warm period (~3.3 to 3.0 Ma) (eg. Bonham et al., 2009). Foraminifera assemblages, $\delta^{18}O$ values and magnesium to calcium ratios of foraminifera shells, and the alkenone unsaturation index of organic matter in ocean sediment all suggest El Niño-like conditions during the Pliocene warm period (Ravelo et al., 2006; Dowsett and Robinson, 2009). Since El Niño conditions alone are not enough to produce higher precipitation in northern Chile, and it is the building phase (winter-spring) of El Niño when precipitation peaks, it is not clear if conditions during the mid-Pliocene warm period would produce large storms in conjunction with increased precipitation (Bonham et al., 2009). However, the mid-Pliocene was likely the most pluvial period prior to the mid to late Pleistocene (~0.5-0.1 Ma), when current ENSO conditions were established (Cane, 2005).

In summary, large rainfall events in northern Chile are extremely rare today, but may have been more common during wetter periods in the past. Because soil formation in the Atacama is so precipitation-dependent, particularly salt accumulation and distribution through the soil (Ewing et al., 2006), hillslope soil characteristics may help constrain the timing of zebra stripe formation.

**HYPOTHESES OF ZEBRA STRIPE FORMATION**

Here, we present three possible mechanisms of zebra stripe formation: salt shrink-swell, seismic shaking, and overland flow, and propose that each of these scenarios would produce different regional distribution of zebra stripes, gravel patterns on hillslopes, and hillslope soil characteristics, which could be distinguished in the field.

Beaty (1983), the first to mention these features in scientific literature, called them "tiger stripes" and proposed that the stripes are formed due to the shrinking and swelling of the ubiquitous salts in the soil. Soil transport by clay shrink-swell on hillslopes is a slope-dependent process (e.g. Kirkby, 1967) and unless there is some underlying heterogeneity in the soil, it would not be expected to concentrate surface gravels into bands. However, soils on stable landforms in this region have dramatic polygonal structure that exists at cm to m scale (Fig. 2, Ewing et al., 2006), and the cracks associated with polygons are sometimes manifested on the surface through variations in particle size. If polygonal soil structure occurs on the hillslopes, then gravels could be concentrated along their boundaries, and the gravel lines would extend in all directions with little or no sorting of the gravels. If soil shrink-swell was the cause, we would expect (1) zebra stripes to occur on any hillslopes wherever there is adequate salt in the soil to create polygonal structure (and to be absent where soil is salt-poor), (2) zebra stripe location to correspond to underlying soil structure, (3) zebra stripe spacing to increase with curvature, (4) poor sorting of gravels within bands, and (5) continuing zebra stripe formation under present conditions.

Disturbance of desert pavement by seismic shaking has been observed in the Mojave Desert, CA, on a gently-sloping interfluve (Michael et al., 2002; Haff, 2005), in the Anza-Borrego Desert, CA, where stones on ridge tops were most likely to move (Clark, 1972; Castle and Youd, 1972), and on the slopes of the Pisgah Crater, CA, where rocks rolled downslope and soils slumped (Sylvester et al., 2002). While no similar observations of quake-driven soil movement have been made in the Atacama Desert, earthquake-shattered ground observed in northern Chile and southern Peru (Keefer and Moseley, 2004; Loveless et al., 2005; Loveless et al., 2009) demonstrates the potential for seismic shaking to be an important geomorphic process in the region. Clark's observations (1972) indicate that topography magnified ground shaking in some cases, and topographic focusing of seismic waves by even small (~15 m) hillslopes is well established (Bard, 1982; Bouchon et al., 1996a,b). Clark (1972) also suggests that bedrock type, through its effect on clast shape and abundance, is an important factor in clast movement. Particles mobilized downslope as a dry flow will segregate by size such that larger particles accumulate farther downslope (e.g. Savage and Lun, 1988; Boutreaux, 1998), which could produce size-sorting within each zebra stripe. The distinct banding could be produced by the slumping of surface materials, followed by particle sorting as described above. However, though gravel-free lineations occurred following a 7.1 M earthquake in the Mojave, they were independent of topography (Haff, 2005). Seismic shaking might also be implicated in soil development and gravel sorting within a zebra stripe through the "brazil nut effect", in which mixtures of particles shaken vertically will separate according to particle size (Schröter et al., 2006). Though this process has not been definitively observed in nature, it has been suggested as a means of producing Mima mounds in Washington (Berg, 1990). If zebra stripes were produced by seismic shaking, we would expect (1) zebra stripes to occur in other seismically-active regions (though possibly dependent on underlying geology), (2) zebra spacing to be greatest at the tops of hills where seismic energy is greatest, (3) gravels to coarsen downslope within each zebra stripe, (4) correlation between zebra stripe location and microtopography (produced by slumping), and (5) evidence of faulting and/or slumping to be preserved within the soil.

Our last hypothesis considers overland flow, and is thus perhaps the most intriguing given the region's prolonged hyperaridity. Though present conditions are largely rain-free, bedrock-bedded channels adjacent to zebra-striped hillslopes suggest sporadic overland flow occurs (enough to remove eolian material), and recent debris flow deposits near the coast indicate that some storms generate overland flow capable of transporting large clasts (Vargas et al., 2006). Sediment transport by overland flow is a function of both the source area contributing runoff and the slope gradient (Horton, 1945), which should produce gravel patterns distinct from those proposed for the other possible processes discussed above. Horton (1945) proposed a 'belt of no erosion' extending from the top of gently convex hillslopes to some critical distance in which gravels are not mobilized due to the low contributing area and low slope. The 'belt of no erosion' has been challenged by Yair and Klein (1973). However, their study plots were well below the crest of the hillslopes and had nearly uniform slopes over their length. Thus, a belt of no erosion would not be expected within the limits of their study areas. If overland flow forms zebra stripes, and because we are considering entire hillslopes, we would expect undisturbed desert pavement on the top of the hillslope. In contrast, both salt shrink-swell and seismic shaking would disturb the pavement fabric on the top of hillslopes.

Because sediment transport by overland flow is a function of both distance downslope (related to source area) and gradient, if the flow is continuous down the slope gravels might not be expected to form bands. However, roll waves or discontinuous flow might produce banding. Roll waves are intermittent surges and ripples in sheet flow that cause the depth of the water to oscillate at fairly regular intervals (if water supply is constant). Through their slightly greater shear stress relative to the rest of the flow, roll waves could entrain coarse material into overland flow if there is enough water present and if the gradient is large enough (Horton, 1938; Mayer, 1959). Since the transition to roll waves is rapid, even a short, intense rainstorm might be adequate to produce roll waves capable of mobilizing many of the largest gravels which would not be mobilized otherwise. After perhaps only a few seconds, as the deeper flow out-paced some coarse particles, these would begin to stop moving. The immobile coarse particles would create flow instability around them, which would cause other coarse particles to come to rest adjacent to them and impede the flow of finer gravels. Increasingly fine material would accumulate upslope from the dam. This process may be similar to that forming bedload sheets in streams (e.g., Nelson et al., 2009) and could produce laterally-continuous (along-contour) features.

Intense rainstorms in arid and hyperarid environments tend to be short and infiltration rates may be high, making continuous overland flow from hill crest to footslope infrequent. On hillslopes with high infiltration rates, Horton (1945) observed increased surface disturbance by raindrop impacts, due to the lower flow depth. This disturbance could mix fine material into a semifluid mass which can then flow *en masse* as a "cloudburst flood" (Horton, 1945). If the cloudburst involved is of high enough intensity and short enough duration, then bands of abruptly transported gravels could form on slopes which are steep enough. Sorting of clasts within debris flows by particle size, such that coarse material is concentrated at the front of the flow, is widely recognized (e.g. Whipple and Dunne, 1992; Major and Iverson, 1999), and it could be that gravels on zebra striped hillslopes are sorted by similar mechanisms.

If overland flow is responsible for zebra stripe formation, and if the flow is continuous, then the distance between zebra stripes would increase with distance downslope. The gravels within each zebra stripe would also coarsen downslope. If zebra stripe formation is through sheet flow, we expect zebra stripes to only form on divergent parts of the hill and to become increasingly irregular or absent on convergent parts, particularly if rills are present.

In addition to (1) undisturbed desert pavement on hilltops, and (2) the characteristic spacing and sorting described above, if zebra stripes were produced by overland flow we would also expect (3) their regional distribution to be climate-dependent and (4) possibly bedrock-dependent. The climate-dependency could be in the intensity and duration of the rainstorms, as well as in the types of soils formed under different climatic conditions, which would affect infiltration rates. As with seismic shaking, bedrock type has an important effect on clast size and shape that could affect clast transport and sorting.

Soil shrink-swell, seismic shaking, and overland flow should produce distinct gravel patterns, soil characteristics, and regional distributions of zebra stripes. In order to test the above hypotheses, we use seismic and climatic data from northern Chile, high-resolution satellite imagery, and field observations.

**APPROACH AND METHODS**

GoogleEarth was used to identify the regional extent of zebra-striping in northern Chile and to explore other parts of the world where they might occur. Because the resolution of GoogleEarth is poor in some regions, field observations were made of zebra stripe occurrence in northern Chile from the coast to the Andean foothills between ~18.4ºS to 23.6ºS. Less intensive observations were made as far south as La Serena (~29ºS).

A study of the correlation between bedrock geology and zebra stripe occurrence was performed using the digital 1:100,000 Antofagasta geologic map (González and Niemeyer, 2005) and GoogleEarth. Of the digital geologic map coverage in northern Chile, this map had the most consistent high resolution imagery in GoogleEarth and was within the heart of the region where zebra stripes occur. In a subsection of the map spanning 23.5 to 24ºS and 70 to ~70.3ºW, polygons were drawn around (1) all hillslopes and (2) hillslopes with zebra stripes. This area excluded most of the Coast Range, where zebra stripes do not occur, so as to maximize the geologic signal and minimize the geographic one. The hillslope and zebra stripe polygons were overlaid on the geologic map using ArcView v.9.3 (ESRI) and the area of each geologic unit within the hillslope region and the zebra-striped region was calculated using tools within the software.

Our primary field site (OR) was a convexo-planar hillslope near Oficina Rosario, 70 km south of Antofagasta and 50 km inland (Fig. 3). It was selected because it is well within the zebra-striped area, easily accessible (just off the Pan-American Highway), and representative of hillslopes in the region. The hillslope is composed of fine-grained granodiorite and abutted by mostly Pliocene alluvium accumulating within an internally drained basin containing localized salar deposits (Marinovic et al., 1992). The hillslope was surveyed using a Trimble differential GPS, with data points collected approximately every 2 m. The topographic data were analyzed with Golden Surfer Software (v. 8.0) and converted to a 3.6-m grid by krigging. This grid size was found to best capture the general topography using the same approach as Heimsath et al. (1999), and neither overly smoothes, nor puts too much weight on, small features that could be due to survey error. A secondary field site, CH, was located near Chañaral (Fig. 3) on a hillslope formed from monzogranite. This hillslope was also surveyed, and soils were described and infiltration rates measured, as discussed below. However, only qualitative observations of zebra stripes were made.

The distribution of zebra stripes on OR was analyzed using a 25 km$^2$ Quickbird satellite image (Digital Globe, Inc.) with 0.6-m resolution. This resolution is fine enough to clearly show zebra stripes on the study hillslope (Fig. 4). The Quickbird imagery was overlaid with the topography data using Golden Surfer Software (v. 8.0). Zebra stripe fronts were digitized to analyze the relationship between zebra stripe distribution and topographic characteristics (gradient, curvature, and distance downslope). The spacing between zebra stripe fronts (defined by the abrupt transition from dark gravels to light soil) was determined along 8 transects on the Quickbird image which extended from the top of the hillslope to the north, northeast, east, southeast, south, southwest, west, and northwest (Fig. 4).

As another way to measure the distance between zebra stripe fronts and describe particle size within zebra stripes, gravel size and percent gravel coverage (%GC) were estimated in the field along several downslope transects on OR.  Five 50-m transects were located on OR (G-1, G-2, G-3, and G-4, Fig. 4, transect 5 could not be located on our topographic map accurately enough to correlate it with topographic characteristics),  a 50-m transect (G-6) was located on a saddle between OR and an adjacent hillslope to the west, and a 100-m transect (G-7) was located on the adjacent hillslope.  Gravel sizes were estimated visually according to 5 classes: 1) fine (average intermediate diameter, D, ~1-2 cm), 2) fine and medium (D~1-5 cm), 3) medium (D~2-5 cm), 4) medium and coarse (D~2-10+ cm) or mix (D~1-10+ cm), and 5) coarse (D~5-10+ cm).  Thus, each transect was divided into 40-70 bands of distinct gravel size and coverage.  To test the accuracy of our size descriptions, pebble counts of eight consecutive bands in G-2 were made.  Zebra stripe fronts were defined along these transects using a length index, LI, where LI = size class × gravel cover fraction.  Zebra stripe fronts were defined as bands where $LI \geq 2.4$.  The results of the LI analysis were in good agreement with visual estimates and other more subjective metrics, but the LI analysis is preferred for being more objective.

In order to characterize the underlying soils, five soil excavations were made along a downslope transect on OR (Fig. 4).  Soil thickness was measured in each excavation, with the bedrock-soil interface defined where rock fragments exceeded 85%.  The soils along the downslope transect were described following the methods of Schoenenberger et al. (2002) and were sampled by horizon for analysis of chemical composition, bulk density, and particle size.  Major element chemistry of soil, gravel, and bedrock samples was analyzed by ALS Chemex, Sparks, NV, by lithium borate fusion and ICP-AES.  Soil fines (<2mm) were shaken for one hour in deionized water and filtered, then analyzed by Dr. Ken Williams of the Lawrence Berkeley Laboratory by ion chromatography for nitrate and chloride ions.  Because sulfate is difficult to fully dissolve, total S measured in the soil was converted to sulfate, assuming no S content in the bedrock which the chemical analyses support.  Particle size was determined using a  hydrometer on sieved soil samples from which salt had been removed using a weak EDTA solution (Bodine and Fernald, 1973).

To constrain the exposure history of the zebra stripes, surface gravels and bedrock from the soil-bedrock interface were collected from each soil pit on OR1 for analysis of the cosmogenic radionuclides (CRN) $^{10}$Be and $^{26}$Al.  The samples were processed using methods described in Kohl and Nishiizumi (1992).  Briefly, the samples were ground to pass through a 0.5 mm sieve.  The quartz mineral grains were isolated through a series of acid dissolutions then dissolved and processed to isolate Be and Al.  $^{10}$Be/$^9$Be and $^{26}$Al/$^{27}$Al were measured by accelerator mass spectrometry (AMS) at the Lawrence Livermore National Laboratory Center for Accelerator Mass Spectrometry and at the Purdue Rare Isotope Measurement Laboratory and normalized to the Nishiizumi et al. (2007) $^{10}$Be AMS standard and the Nishiizumi (2003) $^{26}$Al AMS standard, respectively.  Accordingly, the $^{10}$Be half-life of 1.36 My and the $^{26}$Al half-life of 0.705 My were used. Erosion rates and exposure ages were calculated based on the scaling functions of Lal (1991) and assuming 2.5% muon contribution.  Production rates (at sea level and high latitude) of 5.1 atoms $^{10}$Be g quartz$^{-1}$ y$^{-1}$ and 34.1 atoms $^{26}$Al g quartz$^{-1}$ y$^{-1}$ were used (Nishiizumi et al., 2007).

The hillslope soils are a mixture of bedrock-derived rock fragments and atmospherically-derived dust and salt. The age of the zebra stripe formation can be constrained by calculating the amount of the salt in the soil and dividing by the atmospheric deposition rate to determine a minimum time of salt accumulation. This calculation is a minimum time because there has likely been incomplete retention of deposited material as well as some loss of material downslope. Atmospheric deposition at a nearby site (70 km north) has previously been measured by Ewing et al. (2006) using passive dust collectors and geologic averages which were found to be similar despite averaging over 1 year and 2 My, respectively ($4\pm2$ g m$^2$ y$^{-1}$). To complement and expand this data set, 3 passive collection dust traps were set near OR. The dust traps were made of aluminum bundt pans filled with marbles atop a wire mesh and were put on poles 1-1.5 m above the ground (Reheis and Kihl, 1995). Dust and aerosols were collected for ~2 years. Traps and marbles were rinsed with deionized water and the solution was filtered. The solution was analyzed for nitrate, chloride, and sulfate ions by Dr. Ken Williams of the Lawrence Berkeley Laboratory by ion chromatography. The silicate dust from the pans (collected on filters) was analyzed for major element chemistry by MS-ICP analysis at the Desert Research Institute.

Overland flow is produced when precipitation exceeds infiltration, so infiltration rates are needed to determine under what conditions overland flow is possible. Infiltration rates were measured in three sprinkling experiments and four infiltrometer experiments on OR, and 3 sprinkling experiments on CH. Sprinkling experiments were small scale due to the need for portability. The sprinkler was a nozzle mounted on an adjustable tripod with a pressure gauge and compression stop valve to control water pressure (Wilcox et al., 1986). The water was pumped from a bucket using a 1/6 horsepower Simer Submersible Utility Pump which produced 8-10 psi through the nozzle. Two nozzle sizes were used: a 1/8GG-4.3W fulljet brass nozzle (4.3W) and a 1/8GG-6.5W fulljet brass nozzle (6.5W), both from Spraying Systems Co. The nozzles produced precipitation rates of about 6 cm/h and 55 cm/h, respectively, but application was not uniform. The sites are subject to strong diurnal winds so a windscreen was constructed with a PVC pipe frame and heavy plastic drop cloth walls. While this greatly reduced wind disturbance, the experiments were conducted at a height of about 0.5 m above the ground to avoid drift due to swirling winds. Due to the low spraying height and pressure, the spray did not have the same kinetic energy as natural rainfall, and nozzles of this size tend to produce drops smaller than natural rainfall (Wilcox et al., 1986). The lower kinetic energy likely decreases the mobilization of fine sediment, but since we are most interested in the mobilization of gravels this should not negatively affect our interpretations.

Each sprinkling experiment was performed on a 1 m$^2$ plot that was bounded on the downslope side by a steel collection trough set into the ground (Dunne et al., 1980). The other sides of the plot were bounded by plastic lawn edging set 5-10 cm into the soil. The trough had a steel lip that was set into the soil to capture the surface runoff and a lid to minimize direct addition from the sprinkler. The trough had a sloped bottom to send collected runoff to a spout from which it was collected at regular intervals. Time to runoff, time to steady-state runoff (when the runoff rate was nearly constant for 4-5 sequential measurements), and duration of runoff after spray was turned off were recorded. We also noted if and when sediment was mobilized. Application rate was measured by covering the plot with plastic and measuring runoff over two one-minute intervals. The application rate and runoff rate were corrected for

direct input of water into the collection trough by measuring the water collected prior to runoff initiation on the plot.

Runoff samples were collected every 1 or 2 minutes, depending on runoff rate, and the total volume was measured.  Sprinkling experiments were run at a minimum of 9-27 minutes after steady-state runoff was achieved, lasting ~10-30 minutes overall.  For several runs, the samples were filtered to collect the sediment mobilized in that interval.  Because we used municipal tap water, the water was not sampled for chemical analyses.  After each sprinkling experiment, the collection trough was removed and the face of its trench was excavated to observe how deep the water had infiltrated and if any subsurface patterns were observable.  Infiltration rates were calculated by subtracting the runoff rate from the application rate.

Single-ring cylinder infiltrometers provide a simple means of getting a localized measure of maximum soil infiltration rates and were used to confirm the infiltration rates determined from sprinkling experiments.  Our infiltrometer was a plastic cylinder of 11 cm in diameter which is comparable to that used by Yair and Klein (1973), even though it is smaller than what is commonly recommended (Bouwer, 1986).  The pipe was driven 5-7 cm into the soil, depending on the subsurface conditions, and the disturbed contact between the soil and the pipe was sealed with quick-setting bathroom caulk.  The infiltrometer was filled to the lip with water and the water level was maintained at a constant level.  The time it took to add additional one-liter volumes of water was recorded for 45 minutes to 1 hour.  At the end of the experiment, the time for the remaining water to drain into the soil was recorded.  Following the experiment, the infiltrometer was removed and a cross-section parallel to the flow path was excavated to see how the water moved through the subsurface.

## RESULTS AND INTERPRETATION
### Regional zebra stripe distribution
Zebra stripes are visible in GoogleEarth within a 400 km-long, 20 to 50 km-wide zone between 21º 46' S and 25º 29' S (Fig. 3), an extent confirmed by field observations.  These boundaries do not correlate with changes in subduction style that would suggest variations in seismicity are controlling zebra stripe occurrence.  Instead, the boundaries of this zone coincide with subtle variations in climate.

The northern boundary lies near the present-day transition from winter rainfall (south of ~22ºS) to summer rainfall (north of ~20ºS) (Houston, 2006), suggesting zebra stripes may be produced only by winter rainfall.  Precipitation data are not of fine enough resolution to determine if this is due to differences in rainfall intensity or timing, and the location of the rainfall transition may have shifted in concert with the northward movement of the Westerlies.  However, the spatial correlation of zebra stripe occurrence with this rainfall transition strongly implicates rainfall, and presumably overland flow, in zebra stripe formation.  Hillslopes well north of the zebra stripe range are mantled with salt-rich soils, indicating that the presence of salt alone is not enough to produce zebra stripes.  Zebra stripe occurrence is patchy across the Central Depression, gradually disappearing to the east in the pre-Andean ranges.  This eastern boundary may be related to the increase in precipitation with increasing elevation, but it is the least distinct and thus the most difficult to interpret.  The western boundary is 20 to 40 km inland from the coast, on the east side of the Coastal Cordillera.  The hillslopes in the Coastal Cordillera

131

at these latitudes have little to no soil mantle, only a thin, loose gravel cover.  The debris flow deposits near Antofagasta suggest the hillslopes have low infiltration rates and produce substantial overland flow capable of removing surface gravels, salt, and soil from the hillslope.

The southern extent of large-scale zebra stripes that are visible in GoogleEarth is ~80 km north of Chañaral, corresponding to the disappearance of salt from hillslope soils under wetter, though still arid to hyperarid, conditions.  However, on CH a few (<5% of hillslope area) fine (10-cm scale bands, composed of coarse sand) zebra stripes were observed (Fig. 5).  These stripes are too small to be visible in GoogleEarth, and without a salty soil-mantle or the accumulation of desert varnish on the surface gravels for contrast, these small stripes are only visible upon close inspection in the field.

Zebra striping is discontinuous and appears to be affected by underlying geology.  In the area of the Antofagasta geologic map in which we performed our spatial analysis, the hillslopes have developed on a variety of bedrock types: felsic to intermediate plutonic rock (~45%), sandstones and schist (~18%), Miocene to Pliocene gravels and alluvium (~17%), and small zones of mafic igneous rocks (total ~16%).  Hillslopes composed of monzogranite and diorite were generally the least likely to have zebra stripes, while schist, gabbro, and certain monzogranites were the most likely (Table 1).  The boundaries between zebra-striped areas and those with few to no zebra stripes are strongly correlated with contacts between the underlying geologic units and can be abrupt (Fig. 6).  However, mineral grain size and bulk chemistry inferred from rock type do not seem to affect the degree of zebra striping (Table 1), nor is there any correlation with age, dike concentration, or degree of faulting.  For example, the Cretaceous Piedra Grande unit has two components, a monzogranite, Kigr(c), which is about 80% striped and a granodiorite, Kigr(a), which has <1% striping.  These units are next to each other and nearly identical in age and geologic history, thus rock type appears to be the primary variable, but it is not clear why.  As another example, the hillslopes formed on two monzogranites, Kirg(c) and Jsg(c) are 82% and 4% zebra-striped, respectively.  Without additional fieldwork examining gravel size, gravel shape, soil properties, and topography of different hillslopes within the region, we cannot explain the above observations.  Still, the apparent importance of underlying geology in zebra stripe formation is consistent with either the seismic or overland flow hypotheses in which gravel size and shape are controlling factors.

**Gravel distribution on hillslopes**
At OR, and throughout the zebra-striped region, the most distinct zebra stripes are several meters long (along-contour), about 1-3 m wide (parallel to slope), and separated by relatively gravel-free areas (Figs. 1 and 4).  When viewed up close, the zebra stripes are not as continuous along-contour as they appear in the Quickbird imagery (in which they reach lengths of  50+ m).  The zebra stripe fronts, where coarser-grained zones of high gravel concentration abruptly transition to low-gravel zones downslope, are often gently bowed downslope or upslope and do not follow topographic contours perfectly (Figs. 1 and 4).  The crest of OR has been disturbed by vehicle traffic, but the gravels on top of a hillslope adjacent to OR form a tight pavement.  This pavement begins opening up ~5 m from the crest and forms clear stripes ~10 m from the crest.  Similarly, zebra stripes on OR begin ~13 to 40 m from the hill crest, initiating closer to the crest on the northwest and southeast sides where the hillslope gradient increases most rapidly (Fig. 7a).  Plan (horizontal) curvature appears to affect zebra stripe occurrence, while profile (vertical)

132

curvature does not (Figs. 7b and 7c).  Zebra stripe fronts are not associated with either a profile curvature value (or range) or a change in profile curvature.  Instead, zebra stripes are best developed where plan curvature is divergent and less common in convergent regions where there are more rills (dark blue areas, Fig. 7c).

The distance between zebra stripe fronts increases downslope along the eight transects in the Quickbird image (Figs. 8 and A1).  The average wavelength increases from 4.6±1.5 m within 40 m of the crest, to 7.4±3.3 m 40-120 m from the crest.  The increase is weakest along the transect extending to the west, which is likely due to its short length and its termination at the saddle between OR and the adjacent hillslope.  Field estimates of gravel size and gravel cover along several transects reveal greater complexity in the gravel cover than can be observed in the satellite imagery or from a distance in the field (Fig. 9).  The average distance between zebra stripes calculated from the field observations is 3.2±1.5 m.  This value is similar to the average of the upper part of the hillslope from the Quickbird imagery, but slightly smaller due in part to the lower resolution of the Quickbird imagery (0.6 m) compared to the field data.

Particle sorting is usually strong within zebra stripes, with a coarse, tightly packed front downslope of finer, more scattered particles (Fig. 1c).  The gravels are not stacked – the stripes are a single grain deep.  The fronts are often distinct, but in some cases have been degraded (discussed below).  A plot of grain size and gravel cover vs. distance along one transect shows the periodic nature of the zebra stripes and the sorting within zebra stripes, but also captures the complexity of the gravel cover (Fig. 9).  Tests of our estimates of gravel size against pebble counts (Fig. 10) demonstrate that our size classes capture relative gravel sizes, and that the gravels become coarser with distance downslope.   The complexity in %GC along the hillslope transects suggests possible disturbance following initial zebra stripe formation.

The distribution of zebra stripes on the hillslopes suggests the stripes were formed by overland flow.  The increase in distance between fronts continues downslope of the peak in average gradient (~60 m), which would not occur if zebra stripes were produced by curvature-dependent salt shrink-swell.  It is also inconsistent with our predictions for the patterns produced by seismic shaking, which would have the greatest distance between fronts at the top of the hill where the shaking is topographically enhanced.  This pattern indicates both slope and contributing area are important factors in zebra stripe formation and, in conjunction with the zone where gravels have not been mobilized at the crest of the adjacent slope, strongly supports the overland flow hypothesis.  Because contributing area is a factor, this implies that the overland flow can be continuous from crest to footslope.  However, the absence of an accumulation of gravels at the base of the slope indicate that the gravels are not being transported all the way down the slope, nor are the surface gravels being refreshed with gravel from the soil.  Instead they are likely transported relatively short distances.  Lastly, particle sorting within zebra stripes is not likely to be produced by soil shrink-swell (discussed further below), but could be produced by seismic shaking or overland flow.

**Soil and gravel properties at OR**
Soil properties in the Atacama Desert are precipitation-dependent and vary systematically with latitude.  The persistent hyperaridity at Oficina Rosario has driven the

formation of abiotic soils rich in atmospherically-derived salts, while the slightly wetter conditions at Chañaral are capable of removing almost all material from the hillslope.

At OR, the soils are composed of gypsum, nitrate, halite, and some fine silicate dust, mixed with angular bedrock fragments ranging from gravel to cobble size (Fig. 1d, Table 2).  On average, the soil has low gravel content (0 to 40%), high salt content in the fine fraction (1.5 to 4% gypsum, 0.2% halite, ~300 ppm nitrate), and a sandy-loam fine silicate fraction (~68% sand, ~17% silt, and ~15% clay) (Table 2).  The salt is mainly atmospherically-derived.  The rates of atmospheric deposition calculated from the dust traps are presented in Table 3.  The average rate at OR is comparable to that calculated at sites ~70 km north.

Across the hillslope, the soil profiles share a similar horizonation (Fig. 11).  The surface gravels sit on top of 1-2 cm of light brown, soft, vesicular, platy, slightly salt-cemented dust that is nearly gravel-free (By1).  Below the platy horizon is a 2 cm-thick horizon of soft, white, gravel-free, vesicular salt and dust (By2).  Below the By2 horizon is a horizon of more vesicular, gravel-poor salt and dust, with strong prismatic structure,  mottled brown and white color, and stronger salt cementation, with veins of indurated white gypsum.  With increasing depth, some prisms have 40-60% gravel, and salt cementation is even stronger.  Gravels within the soil are angular and lack evidence of chemical weathering or saprolitization.  The concentration of gravels in parts of the salt-cemented polygons suggests that salt shrink-swell is an important force incorporating rock from the bedrock into the soil.  The boundaries between prisms are cracks filled with brown, salt-cemented sand and some gravels.  Slickensides on the faces of some prisms (e.g., Fig. 11e) suggest substantial movement within the soil.  The sandy fill is weakly laminated (e.g., Fig. 11c) which may be caused by progressive crack opening and in-filling.  These cracks can be up to tens of cm wide, penetrate deep into the soil, and are found on both gently-sloping surfaces (Fig. 2a) and hillslopes.  Though some soil cracks and rock fractures may be linked to earthquakes (Loveless et al., 2005; Keefer et al., 2004), the majority of cracks are likely formed by shrink-swell events.  Rock fragment content increases rapidly, though unevenly, beneath the prismatic horizons.  The road cut of the Pan American Highway at the base of OR (downslope of ORH-1, Fig. 4) reveals salt-filled cracks extending >3 m into the fractured bedrock.

These soils are similar to the upper horizons in an excavation examined on an ancient alluvial terrace located 70 km north of OR (Ewing et al., 2006).  Despite the difference in local gradient (1% on the terrace vs. 20-35% on OR), soils at each location have platy surface horizons 3-4 cm thick overlying soil with increasingly larger prismatic structure, with large vertical cracks penetrating deep (70 to >90 cm) into the soil.  The salt-cemented prisms have greater bulk density than the surface, and localized, irregular, horizontal sheets of strongly-cemented salt are found towards the upper parts of these horizons.  Unlike the horizontal landscapes, there is no surface expression of the salt prisms, such as microtopography or gravel concentration.

Soil thickness is extremely heterogeneous across the hillslope, as suggested in Figures 11b and 11e.  As another example, the photo in Figure 1e is of a side face of the ORH-4 excavation and shows much deeper salt-rich soil accumulation compared to the upslope face of the excavation (Fig. 11a).  This is likely due to the heterogeneous action of the salt prisms.  Despite this variation, on average both the depth to soil with >5% gravel content and the

thickness of the horizons with coarse prismatic structure increase with distance downslope (Table 2, Fig. 11), suggesting some downslope transport of salt and fine material by some combination of overland flow and soil shrink-swell. Indeed, the concentrations of $NO_3^-$, $Cl^-$, and $SO_4^{-2}$ in soil fines (<2mm) by horizon increase with depth and with distance downslope (Table 3), as would be expected for some aqueous transport of salts through the soil. One other possible explanation for the increasing soil thickness with distance downslope is windblown sediment. A small salar is located in the valley a few tens of km northeast of OR, and some sediment has accumulated there. Strong diurnal winds occur in the valley and dust devils and windblown trash attest to their transporting power. If the soil towards the base of the hillslope was thicker due to windblown dust, the soil would be expected to be sandier than the soil towards the top of the hillslope. Sand content of the soil does increase with distance downslope, but this appears to mainly be due to the higher concentration of sand-filled cracks rather than a systematic increase in sand throughout the soil. Thus, while wind is an active force in this region, it seems to have homogeneously affected soil composition and the increase in soil thickness downslope is primarily produced through other soil transport processes.

In contrast to the underlying soils, the upper 3-4 cm of the soil profiles across the hillslope are very similar in appearance, gravel content, and salt concentration (Fig. 11, Table 2). The lack of disturbance despite the large underlying prisms suggest that this material may have accumulated during a recent phase of hyperaridity during which the underlying soil was fairly stable (not shrinking and swelling). For a minimum estimate of the duration of this period, the total mass of $SO_4^{-2}$ in the By1 and By2 horizons of each soil excavation (Table 2) was divided by the rate of sulfate deposition ($0.554\pm0.013$ g m$^2$ y$^{-1}$, Table 4). Ewing et al. (2006) found that at their site, salt deposition rates from dust traps agreed well with geologically-averaged rates, calculated from soils on horizontal stream terraces of known age, thus it is a reasonable approximation to use the rate calculated from the dust trap as the long-term deposition rate. We focus on $SO_4^{-2}$ because it is the least soluble of the salts measured and thus the inventory in the soils is likely to be the most complete compared to $NO_3^-$ and $Cl^-$.

The uppermost 3-4 cm of the soils have between 2-6 ky worth of sulfate, while the upper parts of the profiles where gravel content is <5% have between 8-691 ky worth of sulfate, and the entire measured soil profiles contain 71-692 ky worth of sulfate (Table 2). If the surface gravels have been floating on accumulating salt and dust as a desert pavement, then the sulfate suggests the surface gravels have been separated from the bedrock surface for at least $10^4$-$10^5$ years, and from the prismatic horizons for $10^3$-$10^4$ years. This is a rough measure for several reasons: the incomplete retention of sulfate in the soil (unlike soils on horizontal surfaces in the hyperarid region), the downslope transport of soil (providing another source of salt to the lower soils in addition to atmospheric deposition), and the possible continued pushing of gravels towards the surface or their loss into cracks. However, the consistency of the upper 3-4 cm values is consistent with our interpretation of a relatively stable and uniform accumulation period during the last 2-6 ky. If the zebra stripes formed before this period and have floated on the accumulating soil ever since, then the process of soil accumulation is somewhat different from that of the desert pavement hypothesis of McFadden et al. (1998). In their model, dust is trapped between the surface gravels and is worked underneath them to produce a gravel-free soil. On a zebra striped-hill there are large areas with sparse gravel cover which would not be expected to accumulate soil. However, field observations indicate that small cracks in the surface crust on

135

the top of the soil could act as small traps for dust and salt.  Additionally, the fog carries salt and may produce some soil through wet deposition.  Thus, the continued accumulation of soil despite patchy surface gravel cover is reasonable.

Most surface gravels on OR are 1 to 3 cm in diameter (intermediate axis), though much larger gravels (>10 cm) are also present (Figs. 9, 10).  They are angular, except for the largest cobbles and boulders (which are ventifacted and sometimes have concentric sheets separating from them), and most are varnished.  The gravels appear randomly oriented, though the shortest axis is usually oriented perpendicular to the surface.  159 gravels were collected along a 1.5 m transect, all axes were measured, and the gravel morphology was classified following Sneed and Folk (1958).  Most gravels are bladed (23%) (shaped similar to shoe boxes, with each axis different from the others but not dramatically so), but are increasingly platy (shaped like a tile) and very-bladed (shaped like a checkbook) as grain size increases from fine to coarse (Fig. 12).  These morphologies indicate that the gravels, especially the larger ones, are likely sliding rather than rolling downslope during overland flow events, consistent with observations of disturbed desert pavement in the Mojave Desert (Haff, 2005).

Though most gravels are loosely resting on the surface, some surface gravels ($\leq$10%) are strongly cemented into the soil and some gravels sit atop salt pedestals (Fig. 1e).  Pedestals occur under medium to coarse gravels when they are isolated (in areas of low %GC) or at the downslope front of a zebra stripe.  Dissolution features on the surface of the surrounding soil suggests that the pedestals form when rain produces enough runoff to move, dissolve, and/or collapse the fine material of the surface soil, but inadequate to mobilize gravels.  This is similar to the mechanisms proposed by Bunte and Poesen (1993, 1994).  At zebra stripe fronts, pedestals appear to be produced by flow cascading over larger gravels and creating small-scale scour pools.  This process undermines gravels and destabilizes them and could promote migration of zebra stripes along the hillslope, or at least cause some of the complexity in gravel cover observed along the field transects.  The undermining of surface gravels appears to be the only process disturbing them – the absence of most life means that the surface is not trampled.  Additionally, the presence of rills suggests that modern overland flow can be continuous over the hillslope, and yet the zebra stripes are largely undisturbed.   The zebra stripes may be self-stabilizing, which we explore further below.

The porosity of the soil salt and prevalence of cracks on OR results in a high infiltration rate in the present-day soil.  During sprinkling experiments, steady-state infiltration was 4.2 to 42.6 cm h$^{-1}$ as precipitation increased from 5.2 to 58.7 cm h$^{-1}$ (Table 4), suggesting infiltration is proportional to precipitation.  The maximum infiltration is high for barren ground, suggesting the plastic edging bounding the study plots may have disturbed the surface and enabled higher infiltration.  However, infiltrometer tests confirm the potential for such high infiltration rates, with values ranging from 26 to 134 cm h$^{-1}$ (Table 5).  They also suggest subsurface control on infiltration, with the lowest rates observed where near-surface salt cementation was strongest and most continuous (Table 5).  Consistent with this interpretation, rills on OR do not incise below ~ 4 cm, where there is often an abrupt transition in soil bulk density associated with a change in the degree of salt cementation.  The infiltration rate has probably varied as the soil developed, particularly as salts were accumulated and redistributed through the soil, changing bulk density and flow paths.  Under current conditions, rainfall would need to exceed ~3 cm h$^{-1}$ in order to

generate overland flow, and likely need to be higher to produce a flow capable of mobilizing gravels. This rainfall intensity is possible in the current climate, based on the peak intensity of 2.4 cm h$^{-1}$ recorded in Antofagasta (the only precipitation intensity data available for the region), but extremely rare.

Despite the relatively high infiltration rates (compared to modern precipitation intensity data), observations of the soils and surface gravels on OR suggest that the most likely formation process is overland flow. The lack of continuity between the zebra stripes and the underlying salt prisms suggest that salt shrink-swell is not driving zebra stripe formation. Seismic shaking strong enough to mobilize gravels would likely disturb soil structure, which was not observed. The particle size analysis and soil chemistry suggest the soils could promote gravel mobilization by overland flow through surface sealing and by smoothing the surface.

Surface sealing refers to a rainfall-induced surface seal, formed by the compaction of the upper mm to cm of the soil by raindrop impacts and dependent on soil texture, porosity, and rainfall energy (Mualem and Assouline, 1996). This compaction changes the hydraulic properties of the soil, generally decreasing infiltration rates as the surface soil becomes denser (Mualem and Assouline, 1996). However, if rainfall becomes strong enough it can disrupt the seal and may increase infiltration rates. On OR, the upper few cm of soil are fairly low-density (~1 g cm$^{-3}$, Table 2) and are composed of silicate dust loosely cemented with atmospherically-derived salts. Initial raindrop impacts could decrease the infiltration rate of the soil and promote runoff, though the effectiveness of this seal would likely decrease once overland flow deep enough to mobilize gravels occurred (because of the disturbance to the bed). The surface seal can be enhanced by the dispersion of clays by sodium (Mualem and Assouline, 1996, and references therein). The surface soil is likely ~1000-2000 ppm NaCl and 200-600 ppm NaNO$_3$ (assuming Na$^+$ is the cation balancing the Cl$^-$ and NO$_3^-$ measured in Table 2), thus adequate sodium is available to disperse clays in solution. Both the fineness of the surface soil and its salt content could contribute to surface sealing, decreasing infiltration and enhancing overland flow.

In order to mobilize a surface gravel, overland flow must achieve a critical shear stress. The critical shear stress increases with increasing friction angle, a.k.a. the particle angle of repose (Wiberg and Smith, 1987; Torri and Poesen, 1988; Poesen and Torri, 1989; Kirchner et al., 1990; Torri and Poesen, 1990; Lamb et al., 2008). The friction angle is a function of the diameter of the particle of interest, $D_i$, relative to the diameter of the particles beneath it, $D_b$, such that the friction angle is larger if $D_i$ approaches $D_b$ and smaller if $D_i >> D_b$. On OR, $D_b \approx 0.1$ cm while $D_i$ ranges from 1-10+ cm, thus the friction angle is very low for most surface gravels (those which are not embedded in the soil).

Modern overland flow, though continuous over the hillslope as evidenced by the active rills, does not appear to be capable of significantly disturbing the zebra stripes. This is not unexpected since surface gravels that are closely packed will be more resistant to mobilization by overland flow compared to solitary surface gravels (Bunte and Poesen, 1994). On OR, the surface gravels were likely initially randomly distributed (i.e. scattered) across the hillslope. The relatively smooth surface would enable the mobilization of even the largest gravels, and this effect could be enhanced by surface sealing. Large gravels induce greater local turbulence in the flow (e.g., Bunte and Poesen, 1994) and when large gravels come in proximity to each other their

effect on flow can decrease shear stress enough to cease moving. This would likely create a line of coarser gravels along-contour (perpendicular to the flow) which would also block the transport of smaller gravels downslope. As the gravels accumulate, the flow is no longer capable of mobilizing the coarsest gravels and the zebra stripe is fixed in place. Thus, the zebra stripes, once formed, are very stable and are only disturbed by undercutting at the zebra front and the concentrated flow in rills. If this is the correct process, then it may also explain why some hillslopes with seemingly ample gravel do not develop stripes. There may be a maximum surface gravel cover above which overland flow cannot reach adequate velocities to mobilize the gravel. Likewise, there may be a minimum required amount of surface gravel necessary to produce the interactions that lead to zebra stripe formation. Larger-scale sprinkling experiments would be useful in addressing this problem.

**Zebra stripe chronology at OR using cosmogenic radionuclide analysis**

Though salt deposition rates provide some constraint on the history of the zebra stripes at OR, they are limited by the incomplete retention of salt in the soil and variations in thickness due to downslope transport. The timing of desert pavement and zebra stripe formation on OR can also be approached using CRN concentrations. CRN concentration in rock is, among other things, a function of the production rate of the CRN, the depth (or depth history) of the sample, and the erosion rate of the sample. Thus, possible exposure and erosion histories of surface gravel and bedrock can be explored by modeling CRN concentration as a function of time,

$$N = N_0 e^{-\lambda t} + P_0 e^{-h\rho_s \Lambda^{-1}} \left( \rho_r \varepsilon \Lambda^{-1} + \lambda \right)^{-1} \left( 1 - e^{-t\left( \rho_r \varepsilon \Lambda^{-1} + \lambda \right)} \right), \quad (1)$$

where $N$ is the CRN concentration (atom $g^{-1}$), $N_0$ is the initial CRN content of the sample, $\lambda$ is the decay constant ($y^{-1}$), $t$ is time (y), $P_0$ is production rate corrected for sample latitude and elevation, $h$ is the soil thickness (cm), $\rho_s$ is the bulk soil density (g $cm^{-3}$), $\Lambda$ is the cosmic ray attenuation length (g $cm^{-2}$), $\rho_r$ is the bulk density of the rock (g $cm^{-3}$), and $\varepsilon$ is the rock erosion rate (cm $y^{-1}$) (Granger and Muzikar, 2001).

As discussed in section 2, CRN analysis was used to test if the gravels forming desert pavement in the Mojave Desert have been continuously exposed, and therefore "floating", since the formation of the surface (Wells et al., 1995). Using a similar approach, we tested three possible scenarios for the surface gravels (cases 1-3) and three for the underlying bedrock (cases 4-6). Case 1 is the simplest: constant exposure ($h=0$) and no erosion ($\varepsilon =0$). This would apply to a gravel that has continuously floated on the soil surface, as in the desert pavement formation mechanism of McFadden et al. (1998). In case 2, the gravels float on the soil surface ($h=0$), but are subject to constant, low erosion ($\varepsilon =8\times10^{-5}$ g $cm^{-2}$ $y^{-1}$, or ~0.3 m $My^{-1}$), where erosion is driven by wind abrasion, thermal fracturing, or salt-prying. The gravel within and between the salt prisms on OR suggest that there could be transport of gravel to the surface from the underlying bedrock. For case 3 we model rock undergoing constant erosion ($\varepsilon =2.5\times10^{-5}$ g $cm^{-2}$ $y^{-1}$, or ~1 m $My^{-1}$) at a constant depth ($h=90$ cm) such that $N$ is at steady state, then at $t=0$ the gravel is moved instantaneously to the surface ($h=0$) and no longer erodes ($\varepsilon =0$). Though instantaneous movement is impossible in nature, this provides a simple end-member case that does not require assumptions of the gravel velocity towards the surface. The erosion rate in case 3 is based on the average bedrock erosion rate calculated from [10]Be concentrations for the 5 excavations, and the erosion rate in case 2 is assumed to be about 60% lower due to the

decreased intensity of erosion processes at the surface. We propose cases for the underlying bedrock as well because it may contain information on the development of the soil and the origin of the gravel. In case 4, we test the steady-state hillslope model, in which bedrock erosion and soil thickness are constant ($\varepsilon$ =2.5×10$^{-5}$ g cm$^{-2}$ y$^{-1}$ and $h$=90 cm). In case 5, the bedrock is initially exposed at the surface and eroding at a constant rate ($\varepsilon$ =2.5×10$^{-5}$ g cm$^{-2}$ y$^{-1}$ and $h$=0) such that $N$ is at steady state, then at $t$=0 there is instantaneous burial and continued constant erosion ($\varepsilon$ =2.5×10$^{-5}$ g cm$^{-2}$ y$^{-1}$ and $h$=90 cm). Similar to case 5, in case 6 the bedrock begins exposed at the surface and eroding constantly ($\varepsilon$ =2.5×10$^{-5}$ g cm$^{-2}$ y$^{-1}$ and $h$=0), but at $t$=0 is then buried instantaneously and erosion ceases ($\varepsilon$ =0 and $h$=90 cm). Again, instantaneous burial is impossible and though we could attempt to convert our atmospheric deposition rate to a soil accumulation rate by assuming a bulk density of the deposited material, the case presented here provides a simple end-member. These cases are end members of a spectrum of exposure and erosion histories and are not expected to exactly match our measurements, particularly since the accumulation of soil and changes in erosion rate are gradual processes rather than instantaneous. A wide range of variable combinations can produce the same $N$, thus attempting more refined models (such as accounting for gradual soil accumulation) is not particularly illuminating.

Surface gravel and bedrock $^{26}$Al and $^{10}$Be concentrations, exposure ages, and erosion rates are summarized in Table 6. The exposure ages are calculated assuming no erosion and the erosion rates are calculated assuming constant exposure history. The quartz in the bedrock at OR has a high Al content, making the measurement of $^{26}$Al more difficult and thus prone to larger error. For our modeling we use $\lambda_{Be}$=5.097×10$^{-7}$ y$^{-1}$, $P_{0\_Be}$=10.68 atoms Be g$^{-1}$ y$^{-1}$, $\lambda_{Al}$=9.763×10$^{-7}$ y$^{-1}$, $P_{0\_Al}$=71.31 atoms Al g$^{-1}$ y$^{-1}$, $\rho_s$ =1.2 g cm$^{-3}$ (the depth-average of the five soil excavations, though this is approximate given the heterogeneity observed in the soil), $\rho_r$ =2.65 g cm$^{-3}$, and $\Lambda$=165 g cm$^{-2}$.

Figures 13a and b show $^{10}$Be and $^{26}$Al concentrations over time for the surface gravel cases compared to the measured values in the surface gravels from the four upper soil excavations (surface gravel was not analyzed for ORH-1). The most likely exposure and erosion history for each sample is identified using the intercepts of the models with the measured values. For the surface gravels, any of the cases are possible, but the models do provide some constraint on the timing of the surface exposure. Based on $^{10}$Be, the surface gravels highest up on the slope (ORH-4), have the shortest exposure histories (~0.5 My). Surface gravels on the rest of the hillslope have similar $^{10}$Be concentrations (~9×10$^{6}$ atom g$^{-1}$) and longer exposure times (0.5-1 My). If the gravels originated at the top of the hillslope and were progressively moved downslope, gravel exposure age would increase significantly with distance downslope. The consistency in gravel $^{10}$Be content suggests that the gravels are locally sourced, and have experienced similar exposure histories which include sustained exposure at the surface and little, if any, erosion. The CRN-derived exposure times exceed the soil accumulation time based on the salt inventory (70-650 ky), so the surface gravels have likely floated at or near the surface while the soil accumulated, rather than transported to the surface during or following salt accumulation. The $^{26}$Al data indicate that the surface gravels have exposure ages between 0.25-0.75 My, but counter to the $^{10}$Be results, gravels with the longest exposure are towards the top of the hillslope. It is not entirely clear why the $^{26}$Al and $^{10}$Be results are so different, but the greater sensitivity of $^{26}$Al to changes in the balance between production and decay or erosion (due to the faster decay rate of $^{26}$Al) suggests that there may have been some cycling of gravels in the upper

parts of the soil.  Both CRN suggest that the surface gravels are locally-sourced from the underlying bedrock and have experienced similar exposure histories across the hillslope, with little downslope transport.

The use of amalgamated samples of surface gravels produces CRN concentrations that are average values.  Measuring CRN in individual surface gravels could provide more constraint on the gravels' histories, particularly for comparing fine and coarse gravels.  However, this analysis is limited by the CRN concentration in the gravels but may become possible as measurement methods are improved.

Figures 13c and d show $^{10}$Be and $^{26}$Al concentrations for the bedrock cases over time compared to the measured values for the bedrock in the soil excavations.  Based on the $^{10}$Be concentrations in the bedrock, the bedrock must have been buried and eroding very slowly, if at all, (case 6) for 0.5-1.5 My.  The uppermost excavation has the lowest $^{10}$Be concentration which suggests it may still be eroding, or was eroding more recently than the samples from downslope.  The downslope bedrock samples do not vary systematically downslope, but the models suggest that the CRN content reflects exposure near the surface prior to burial, and that burial has been occurring for 0.5-1.5 My.  $^{26}$Al concentrations suggest the bedrock has been buried and eroding (case 5 or 6) for between 0.5-1 My.  However, the variation of $^{26}$Al concentrations downslope does not match that of the $^{10}$Be concentrations.  This discrepancy could be the result of complex exposure histories for the bedrock, or from the difficulty in measuring $^{26}$Al concentration.  Nevertheless, these results suggest that the bedrock has been buried for at least 0.5 My, consistent with the surface gravels having been exposed (and non-eroding) for a similar time.

If the soil has formed primarily through the accumulation of atmospheric inputs, with some contribution from the underlying rock, then rock fragments within the soil would be expected to have higher CRN concentrations closer to the surface.  Accordingly, $^{10}$Be and $^{26}$Al concentrations in soil gravels generally decrease with increasing depth in most of the excavations (except ORH-2 where the bedrock CRN are too high), with the bedrock samples often having the lowest concentrations (Table 6).  These trends suggests that the rock fragments within the soil have also been subjected to burial with limited, if any, transport downslope.  Overall, these calculations suggest that the hillslope bedrock was once exposed at the surface and was then buried.  During burial, the bedrock erosion rate must have decreased, possibly to 0, and the bedrock has experienced this burial for ~0.25-1 My.

Despite our simplifications, these calculations suggest that the gravels now on the soil surface have been continually exposed while the bedrock has been buried, exactly as has been proposed for desert pavement formation.  These results are surprising because not only do they suggest that the surface gravels on these hillslopes are "floating" on atmospherically-derived salt and dust, just as on horizontal surfaces, but that these gravels have been essentially in place (within a few m) for as long as $10^6$ y.

**Zebra stripes at CH**
Unlike OR, hillslopes near Chañaral are almost entirely soil-free and salt-free, and a few plants are present.  The soil cover on CH, where present, is dominated by coarse sand and fine gravels mixed with fine reddish-brown dust, and has an abrupt contact with the coarsely

140

fractured bedrock below (Fig. 5c). The bedrock shows almost no evidence of chemical weathering, with only a few reddish rinds detectable in thin section. Infiltration rates determined from sprinkling experiments ranged from 3.3-25.3 cm h$^{-1}$, comparable to the rates at OR, and were proportional to sprinkling rate (Table 4). Due to the thinness of the soil, capturing all runoff from the plot was extremely difficult and it is likely that our infiltration rates were overestimated. Additionally, the soil was too thin to use an infiltrometer effectively.

Zebra stripes are rare on CH and of smaller scale than those on OR (Figs. 5a and 5b). They are most often present on steep slopes with little evidence of animal traffic (the area is sparsely populated with guanacos, a coastal cousin of the llama). Zebra stripes are absent where animal tracks are common. They are more irregular and thinner than the ones on OR. The zebra stripes coarsen towards the downslope front as at OR, but the gravels rarely exceed 1 cm in diameter. Nowhere are the 10+ cm-diameter gravels observed. The absence of large gravels may be related to fog- and salt-driven weathering processes which produce finer material compared to the salt-prying at OR (Owen et al., 2010). Though the gravels sit on top of the dusty soil, they are not perched on pedestals nor embedded in the soil. These zebra stripes could not have formed through soil shrink-swell because there is not adequate soil present, nor is it likely that they formed through seismic shaking since they are so irregular. Thus, the zebra stripes at CH, though much smaller than those at OR, probably form through a similar process during overland flow. They are more likely to be disturbed by animal trampling but the smaller size of the gravels involved means that they are easier to re-form. Whereas the zebra stripes on OR are stable, the zebra stripes on CH may be relatively transient.

The conditions at CH provide some constraint on the history of OR prior to zebra stripe formation. Hillslopes south of CH are mantled with a chemically-weathered soil mantle, and presumably a similar soil mantle covered both CH and OR when the climate was semiarid (likely mid-Pliocene, as discussed in section 3). However, none of this chemically-weathered material is found on either hillslope today, indicating that the hillslope was stripped to bedrock prior to the accumulation of the salt-rich soil in the case of OR. At CH, fractured bedrock of similar size to the surface gravels on OR is only cm from the surface. Below, we combine field observations and the geochronology from the soil salt and CRN to propose a history for the formation of zebra stripes on OR and identify the necessary condition for their formation.

**CONDITIONS FOR AND CHRONOLOGY OF ZEBRA STRIPE FORMATION**
Zebra stripe formation and persistence appear to require specific conditions in order to occur: 1) surface gravels must be present within certain (but unknown) limits on concentration, 2) the gravels must be of the right shape and size (geologic control), 3) the soil surface must be much finer than the gravels themselves, 4) the slope and contributing area must be high enough to produce flow fast enough to mobilize the gravels (but not so high that the gravels can't stop before reaching the base of the slope), and 5) disturbance by animals or vegetation must be minimal. Though some of these conditions are met in other parts of the world, the hyperarid region of the Atacama Desert appears to be the only place where all occur as a consequence of the climatic history of the region.

The Atacama Desert and regions to its south have experienced increasing aridity for the last 2-9 My, as outlined in section 3. Today, the precipitation gradient causes variation in

hillslope soils which may mirror the development of the soil mantle on OR during this long-term aridification. Semiarid hillslopes near La Serena (~29ºS) are mantled with chemically-weathered soil and support desert vegetation (Fig. 14a). OR was likely last semiarid during the mid-Pliocene warm period ~3 Ma. The lack of any remnant chemically-altered soil or bedrock on CH and OR today indicates that the landscape was stripped of this material as MAP decreased (Fig. 14b). Our CRN modeling suggests the bedrock on OR has experienced burial for at least 0.5 My, and the removal of the chemically-weathered material must have pre-dated the onset of burial. When salt began accumulating on OR, it likely pried rock fragments from the bedrock and created a layer of relatively coarse gravels on the surface (Fig. 14c). With further salt accumulation, many of these gravels floated on the surface and the soil developed a cover of scattered, non-sorted surface gravels (Fig. 14d). The hyperarid region is dry enough that the accumulation of atmospheric material likely formed desert pavement across the landscape, on the hillslopes as well as on horizontal surfaces. However, on the hillslopes the accumulation of soil would effectively "expand" the surface, opening up the pavement so there is more space between the surface gravels than in a typical desert pavement. As mentioned above, the spacing of gravels is an important factor in their interaction with overland flow. It may be that there is a critical threshold in soil accumulation necessary to spread the surface gravels an enable mobilization by overland flow.

Wetting and drying events produced the coarse prismatic structure observed in the deeper parts of the soil, as well as decreased the overall infiltration rate of the soil as the salt was concentrated into denser horizons. The prismatic soils required at least 100-200 ky to accumulate based on our salt deposition calculations, and probably much longer given the incomplete retention of atmospheric inputs. As mentioned above, salt shrink-swell on the scale of the large prisms would likely have disturbed the soil surface and any gravel sorting that may have occurred. Thus, we propose that the zebra stripes observed today post-date the formation of the salt prisms.

The zebra stripes formed as described at the end of section 5.3, starting with surface gravels scattered randomly across the hillslope on a bed of fine, salty soil. Their formation likely occurred incrementally over the course of several storms, rather than in one large event, with coarser gravels interacting with each other within the flow and creating contour-parallel bands (Figs. 14 e, f). However, exactly when this occurred, whether before or after the accumulation of the uppermost horizons of the soil, is uncertain.

During the last $10^3$-$10^5$ y, OR has experienced sustained hyperardity during which the porous surface layer (upper ~4 cm) accumulated. Within a similar time period, debris flow deposits near Antofagasta indicate storms capable of generating overland flow occurred approximately once a century (Vargas et al., 2006). The infiltration rate of the present-day soil is about equal to or greater than the highest intensity rainfall recorded in the region, which produced damaging debris flows in Antofagasta (Vargas et al., 2000). Thus, recent conditions are adequate to mobilize gravels, but the development of rills cutting across the zebra stripes and the observation of few disturbed surface gravels on the hillslope suggest that the zebra stripes have been in place at least centuries, if not millennia.

**CONCLUSIONS**

The zebra stripes on hillslopes in the Atacama Desert may be a unique feature found nowhere else on Earth.  Cosmogenic radionuclide analysis indicates that atmospherically-derived salts and dust have floated the surface gravels and buried the bedrock for at least 0.5-1 My.  The process is comparable to the formation of desert pavement found in arid regions throughout the world, but is unusual on hillslopes, particularly for such a long period of time.  The regional occurrence of zebra stripes, their distribution on hillslopes, and the soil and rock properties associated with them suggest that the zebra stripes were produced by overland flow.  Though overland flow capable of mobilizing gravels is likely possible under modern climate conditions, we propose that the zebra stripes formed centuries or millennia ago and have been preserved by their self-stabilization and the absence of other disturbances, particularly life.

While we have asked "Why are there zebra stripes in the Atacama Desert?", a complementary puzzle is "Why aren't they in other hyperarid regions on Earth?"  Their apparent absence may be due to bedrock, precipitation history or seasonality, or soil characteristics.  Though we have identified some of the important characteristics required for their formation, further field work in the Atacama Desert, particularly larger-scale sprinkling experiments, would improve our initial constraints.  Similar studies in other hyperarid deserts would also help clarify "why not", and provide important context for interpreting hillslope surface deposits on other terrestrial planets.

**ACKNOWLEDGEMENTS**

**References**

Abrahams, A. D., Parsons, A. J., and Luk, S. H., 1986, Resistance to overland-flow on desert hillslopes: Journal of Hydrology, v. 88, no. 3-4, p. 343-363.

Abrahams, A.D., Parsons, A.J., and Hirsch, P.J., 1992, Field and laboratory studies of resistance to interrill overland flow on semiarid hillslopes, southern Arizona. In: Overland flow: Hydraulics and erosion mechanics. Parsons, A.J. and Abrahams, A.D. eds. UCL Press, London, p. 1-23.

Adelsberger, K.A., and Smith, J.R., 2009, Desert pavement development and landscape stability on the Eastern Libyan Plateau, Egypt: Geomorphology, v. 107, p. 178-194.

Al-Farraj, A., and Harvey, A. M., 2000, Desert pavement characteristics on wadi terrace and alluvial fan surfaces: Wadi Al-Bih, UAE and Oman: Geomorphology, v. 35, no. 3-4, p. 279-297.

Alpers, C. N., and Brimhall, G. H., 1988, Middle Miocene climatic change in the Atacama Desert, Northern Chile - Evidence from supergene mineralization at La Escondida: Geological Society of America Bulletin, v. 100, no. 10, p. 1640-1656.

Anderson, K., Wells, S., and Graham, R., 2002, Pedogenesis of vesicular horizons, Cima Volcanic Field, Mojave Desert, California: Soil Science Society of America Journal, v. 66, no. 3, p. 878-887.

Bard, P. Y., 1982, Diffracted waves and displacement field over two-dimensional elevated topographies: Geophysical Journal of the Royal Astronomical Society, v. 71, no. 3, p. 731-760.

Beaty, C. 1983, Tiger Striping; A curious form of surficial patterning in the Atacama Desert, N. Chile, GSA Annual Meeting Abstracts with Programs 15: 387.

Berg, A. W., 1990, Formation of mima mounds - a seismic hypothesis: Geology, v. 18, no. 3, p. 281-284.

Betancourt, J. L., Latorre, C., Rech, J. A., Quade, J., and Rylander, K. A., 2000, A 22,000-year record of monsoonal precipitation from Northern Chile's Atacama Desert: Science, v. 289, no. 5484, p. 1542-1546.

Bobst, A. L., Lowenstein, T. K., Jordan, T. E., Godfrey, L. V., Ku, T. L., and Luo, S. D., 2001, A 106 ka paleoclimate record from drill core of the Salar de Atacama, northern Chile: Palaeogeography Palaeoclimatology Palaeoecology, v. 173, no. 1-2, p. 21-42.

Bodine, M. W., and Fernalld, T. H., 1973, EDTA dissolution of gypsum, anhydrite, and Ca-Mg carbonates: Journal of Sedimentary Petrology, v. 43, no. 4, p. 1152-1156.

Bonham, S. G., Haywood, A. M., Lunt, D. J., Collins, M., and Salzmann, U., 2009, El Nino-Southern Oscillation, Pliocene climate and equifinality: Philosophical Transactions of the Royal Society a-Mathematical Physical and Engineering Sciences, v. 367, no. 1886, p. 127-156.

Bouchon, M., and Barker, J. S., 1996, Seismic response of a hill: The example of Tarzana, California: Bulletin of the Seismological Society of America, v. 86, no. 1, p. 66-72.

Bouchon, M., Schultz, C. A., and Toksoz, M. N., 1996, Effect of three-dimensional topography on seismic motion: Journal of Geophysical Research-Solid Earth, v. 101, no. B3, p. 5835-5846.

Boutreaux, T, 1998, Surface flows of granular mixtures: II. Segregation with grains of different size: The European Physical Journal B, v. 6, p. 419-424.

Bouwer, H. 1986, Intake rate: Cylinder infiltrometer, *in* Methods of Soil Analysis, Part 1. Physical and Mineralogical Methods.  Agronomy Monograph no. 9 (2nd ed.).  American Society of Agronomy-Soil Science Society of America, p. 825-844.

Bunte, K., and Poesen, J., 1993, Effects of horseshoe vortex erosion on sediment yield from soils covered by rock fragments: Zeitschrift Fur Geomorphologie, v. 37, no. 3, p. 327-335.

Bunte, K., and Poesen, J., 1994, Effects of rock fragment size and cover on overland-flow hydraulics, local turbulence and sediment yield on an erodible soil surface: Earth Surface Processes and Landforms, v. 19, no. 2, p. 115-135.

Cáceres, L., Gómez-Silva, B., Garró, X., Rodríguez, V., Monardes, V., and McKay, C. P., 2007, Relative humidity patterns and fog water precipitation in the Atacama Desert and biological implications: Journal of Geophysical Research-Biogeosciences, v. 112, no. G4. doi:10.1029/2006JG000344.

Cane, M. A., 2005, The evolution of El Nino, past and future: Earth and Planetary Science Letters, v. 230, no. 3-4, p. 227-240.

Castle, R.O., and Youd, T.L, 1972, Engineering Geology, *in*: The Borrego Mountain Earthquake of April 9, 1968: Geological Survey Professional Paper 787, p.158-174.

Clark, M.M, 1972, Collapse Fissures along the Coyote Creek fault. *in*: The Borrego Mountain Earthquake of April 9, 1968: Geological Survey Professional Paper 787, p. 190-207.

Clarke, J. D. A., 2006, Antiquity of aridity in the Chilean Atacama Desert: Geomorphology, v. 73, no. 1-2, p. 101-114.

Dowsett, H. J., and Robinson, M. M., 2009, Mid-Pliocene equatorial Pacific sea surface temperature reconstruction: a multi-proxy perspective: Philosophical Transactions of the Royal Society a-Mathematical Physical and Engineering Sciences, v. 367, no. 1886, p. 109-125.

Dunai, T. J., Gonzalez-Lopez, G. A., Juez-Larre, J., and Carrizo, D., 2005, Preservation of (early) miocence landscapes in the Atacama Desert, northern Chile: Geochimica Et Cosmochimica Acta, v. 69, no. 10, p. A161-A161.

Dunne, T., Dietrich, W. E., and Brunengo, M. J., 1980, Simple, portable equipment for erosion experiments under artificial rainfall: Journal of Agricultural Engineering Research, v. 25, no. 2, p. 161-168.

Ericksen, GE., 1981, Geology and origin of the Chilean nitrate deposits: Geological Society Professional Paper 1188, p. 37.

Ewing, S., Michalski, G., Thiemens, M., Quinn, R., Macalady, J., Kohl, S., Wankel, S., Kendall, C., Mckay, C., and Amundson, R., 2007, Rainfall limit of the N cycle on Earth: Global Biogeochemical Cycles, v. 21, no. 3, p. -.

Ewing, S. A., Sutter, B., Owen, J., Nishiizumi, K., Sharp, W., Cliff, S. S., Perry, K., Dietrich, W., McKay, C. P., and Amundson, R., 2006, A threshold in soil formation at Earth's arid-hyperarid transition: Geochimica Et Cosmochimica Acta, v. 70, no. 21, p. 5293-5322.

Goes, S. D. B., 1996, Irregular recurrence of large earthquakes: An analysis of historic and paleoseismic catalogs: Journal of Geophysical Research-Solid Earth, v. 101, no. B3, p. 5739-5749.

González, G. and Niemeyer, H, 2005, Cartas Antofagasta y Punta Tetas, Región de Antofagasta. Servicio Nacional de Geología y Minería, Geologic Map of Chile No. 89, 1:100 000, 1 sheet, 35 p.

Granger, D. E., and Muzikar, P. F., 2001, Dating sediment burial with in situ-produced cosmogenic nuclides: theory, techniques, and limitations: Earth and Planetary Science Letters, v. 188, no. 1-2, p. 269-281.

Haff, P. K., 2005, Response of desert pavement to seismic shaking, Hector Mine earthquake, California, 1999: Journal of Geophysical Research-Earth Surface, v. 110, no. F2.

Hartley, A. J., and Chong, G., 2002, Late Pliocene age for the Atacama Desert: Implications for the desertification of western South America: Geology, v. 30, no. 1, p. 43-46.

Hartley, A. J., Chong, G., Houston, J., and Mather, A. E., 2005, 150 million years of climatic stability: evidence from the Atacama Desert, northern Chile: Journal of the Geological Society, v. 162, p. 421-424.

Hebbeln, D., Lamy, F., Mohtadi, M., and Echtler, H., 2007, Tracing the impact of glacial-interglacial climate variability on erosion of the southern Andes: Geology, v. 35, no. 2, p. 131-134.

Heimsath, A. M., Dietrich, W. E., Nishiizumi, K., and Finkel, R. C., 1999, Cosmogenic nuclides, topography, and the spatial variation of soil depth: Geomorphology, v. 27, no. 1-2, p. 151-172.

Horton, R.E,1938, Rain wave-trains: Transactions, American Geophysical Union, p. 368-374.

Horton, R.E., 1945, Erosional development of streams and their drainage basins: Geological Society of America Bulletin, v. 15, p. 393-404.

Houston, J., 2006, Variability of precipitation in the Atacama desert: Its causes and hydrological impact: International Journal of Climatology, v. 26, no. 15, p. 2181-2198.

Houston, J., and Hartley, A., 2003, The central andean west-slope rainshadow and its potential contribution to the origin of hyper-aridity in the Atacama desert: International Journal Of Climatology, v. 23, no. 12, p. 1453-1464.

Jordan, T. E., Isacks, B. L., Allmendinger, R. W., Brewer, J. A., Ramos, V. A., and Ando, C. J., 1983, Andean tectonics related to geometry of subducted Nazca plate: Geological Society of America Bulletin, v. 94, no. 3, p. 341-361.

Keefer, D. K., and Moseley, M. E., 2004, Southern Peru desert shattered bv the great 2001 earthquake: Implications for paleoseismic and paleo-El Nino-Southern oscillation records: Proceedings of the National Academy of Sciences of the United States of America, v. 101, no. 30, p. 10878-10883.

Kirchner, J. W., Dietrich, W. E., Iseya, F., and Ikeda, H., 1990, The variability of critical shear-stress, friction angle, and grain protrusion in water-worked sediments: Sedimentology, v. 37, no. 4, p. 647-672.

Kirkby, M. J., 1967, Measurement and theory of soil creep: Journal of Geology, v. 75, no. 4, p. 359-378.

Kober, F., Ivy-Ochs, S., Schlunegger, F., Baur, H., Kubik, P. W., and Wieler, R., 2007, Denudation rates and a topography-driven rainfall threshold in northern Chile: Multiple cosmogenic nuclide data and sediment yield budgets: Geomorphology, v. 83, no. 1-2, p. 97-120.

Kohl, C. P., and Nishiizumi, K., 1992, Chemical isolation of quartz for measurement of *in situ*-produced cosmogenic nuclides: Geochimica Et Cosmochimica Acta, v. 56, no. 9, p. 3583-3587.

Kuhn, N. J., and Yair, A., 2004, Spatial distribution of surface conditions and runoff generation in small arid watersheds, Zin Valley Badlands, Israel: Geomorphology, v. 57, no. 3-4, p. 183-200.

Lal, D., 1991, Cosmic-ray labeling of erosion surfaces – *in situ* nuclide production-rates and erosion models: Earth and Planetary Science Letters, v. 104, no. 2-4, p. 424-439.

Lamb, M. P., Dietrich, W. E., Aciego, S. M., DePaolo, D. J., and Manga, M., 2008, Formation of Box Canyon, Idaho, by megaflood: Implications for seepage erosion on Earth and Mars: Science, v. 320, no. 5879, p. 1067-1070.

Lamy, F., Klump, J., Hebbeln, D., and Wefer, G., 2000, Late Quaternary rapid climate change in northern Chile: Terra Nova, v. 12, no. 1, p. 8-13.

Latorre, C., Betancourt, J. L., Rylander, K. A., and Quade, J., 2002, Vegetation invasions into absolute desert: A 45 000 yr rodent midden record from the Calama-Salar de Atacama basins, northern Chile (lat 22 degrees-24 degrees S): Geological Society of America Bulletin, v. 114, no. 3, p. 349-366.

Latorre, C., Betancourt, J. L., Rylander, K. A., Quade, J., and Matthei, O., 2003, A vegetation history from the arid prepuna of northern Chile (22-23 degrees S) over the last 13,500 years, p. 223-246.

Loveless, J. P., Allmendinger, R. W., Pritchard, M. E., Garroway, J. L., and Gonzalez, G., 2009, Surface cracks record long-term seismic segmentation of the Andean margin: Geology, v. 37, no. 1, p. 23-26.

Loveless, J. P., Hoke, G. D., Allmendinger, R. W., Gonzalez, G., Isacks, B. L., and Carrizo, D. A., 2005, Pervasive cracking of the northern Chilean Coastal Cordillera: New evidence for forearc extension: Geology, v. 33, no. 12, p. 973-976.

146

Magilligan, F. J., and Goldstein, P. S., 2001, El Nino floods and culture change: A late Holocene flood history for the Rio Moquegua, southern Peru: Geology, v. 29, no. 5, p. 431-434.

Major, J. J., and Iverson, R. M., 1999, Debris-flow deposition: Effects of pore-fluid pressure and friction concentrated at flow margins: Geological Society of America Bulletin, v. 111, no. 10, p. 1424-1434.

Marinovic, N., Smoje, I., Maksaev, V., Hervé, M., Mpodozis, C.,1992, Hoja Aguas Blancas, Región de Antofagasta. Servicio Nacional de Geología y Minería, Geologic map of Chile No. 70, 1:100 000, 1 sheet, 150 p.

Matmon, A., Simhai, O., Amit, R., Haviv, I., Porat, N., McDonald, E., Benedetti, L., and Finkel, R., 2009, Desert pavement-coated surfaces in extreme deserts present the longest-lived landforms on Earth: Geological Society of America Bulletin, v. 121, no. 5-6, p. 688-697.

Mayer, P.G.,1959, Roll waves and slug flows in inclined open channels: Journal of the Hydraulics Division, ASCE, v. 85, p. 99-140.

McFadden, L. D., McDonald, E. V., Wells, S. G., Anderson, K., Quade, J., and Forman, S. L., 1998, The vesicular layer and carbonate collars of desert soils and pavements: formation, age and relation to climate change: Geomorphology, v. 24, no. 2-3, p. 101-145.

McFadden, L. D., Wells, S. G., and Jercinovich, M. J., 1987, Influences of eolian and pedogenic processes on the origin and evolution of desert pavements: Geology, v. 15, no. 6, p. 504-508.

Michael, A. J., Ross, S. L., and Stenner, H. D., 2002, Displaced rocks, strong motion, and the mechanics of shallow faulting associated with the 1999 Hector Mine, California, earthquake: Bulletin of the Seismological Society of America, v. 92, no. 4, p. 1561-1569.

Mualem, Y., and Assouline, S., 1996, Soil sealing, infiltration and runoff, *in*: Issar, A.S., and Resnick, S.D., eds., Runoff, Infiltration and Subsurface Flow of Water in Arid and Semi-Arid Regions. Kluwer Academic Publishers, the Netherlands, p. 131-181.

Nelson, P.A., Venditti, J.G., Dietrich, W.E., Kirchner, J.W., Ikeda, H., Iseya, F., and Sklar, L.S., 2009, Response of bed surface patchiness to reductions in sediment supply: Journal of Geophysical Research, v. 114, FO2005, doi:10.1029/2008JF001144.

Nishiizumi K., 2003, Preparation of [26]Al AMS standards: Nuclear Instruments & Methods in Physics Research Section B, v. B223-224, p. 388-392.

Nishiizumi, K., Caffee, M. W., Finkel, R. C., Brimhall, G., and Mote, T., 2005, Remnants of a fossil alluvial fan landscape of Miocene age in the Atacama Desert of northern Chile using cosmogenic nuclide exposure age dating: Earth and Planetary Science Letters, v. 237, no. 3-4, p. 499-507.

Nishiizumi, K., Imamura, M., Caffee, M. W., Southon, J. R., Finkel, R. C., and McAninch, J., 2007, Absolute calibration of Be-10 AMS standards: Nuclear Instruments & Methods in Physics Research Section B-Beam Interactions with Materials and Atoms, v. 258, no. 2, p. 403-413.

Núñez, L., Grosjean, M., and Cartajena, I., 2002, Human occupations and climate change in the Puna de Atacama, Chile: Science, v. 298, no. 5594, p. 821-824.

Ortlieb, J., 1995, Eventos El Niño y episodios lluviosos en el Desierto de Atacama: El registro de los últimos dos siglos. Bulletin de l'Institut Français d'Etudes Andines, v. 24, no. 3, p. 519-537.

Ortlieb, L., Zazo, C., Goy, J. L., Hillaire Marcel, C., Ghaleb, B., and Cournoyer, L., 1996, Coastal deformation and sea-level changes in the northern Chile subduction area (23

degrees S) during the last 330 ky: Quaternary Science Reviews, v. 15, no. 8-9, p. 819-831.

Owen, J.J., Amundson, R., Dietrich, W.E., Nishiizumi, K., Sutter, B., and Chong, G. *in revision.* The sensitivity of hillslope soil production to precipitation. Earth Surface Processes and Landforms.

Poesen, J. W. A., and Torri, D., 1989, Mechanisms governing incipient motion of ellipsoidal rock fragments in concentrated overland-flow: Earth Surface Processes and Landforms, v. 14, no. 6-7, p. 469-480.

Ravelo, A. C., Andreasen, D. H., Lyle, M., Lyle, A. O., and Wara, M. W., 2004, Regional climate shifts caused by gradual global cooling in the Pliocene epoch: Nature, v. 429, no. 6989, p. 263-267.

Rech, J., Quade, J., and Hart, W., 2003, Isotopic evidence for the source of Ca and S in soil gypsum, anhydrite and calcite in the Atacama Desert, Chile: Geochimica Et Cosmochimica Acta, v. 67, no. 4, p. 575-586.

Reheis, M. C., and Kihl, R., 1995, Dust deposition in southern Nevada and California, 1984-1989 - relations to climate, source area, and source lithology: Journal of Geophysical Research-Atmospheres, v. 100, no. D5, p. 8893-8918.

Savage, S. B., and Lun, C. K. K., 1988, Particle-size segregation in inclined chute flow of dry cohesionless granular solids: Journal of Fluid Mechanics, v. 189, p. 311-335.

Schoenenberger, P.J., Wysocki, D.A., Benham, E.C., and Broderson, W.D., eds., 2002, Field book for describing and sampling soils, Version 2.0. Natural Resources Conservation Service, National Soil Survey Center, Lincoln, NE.

Schroter, M., Ulrich, S., Kreft, J., Swift, J. B., and Swinney, H. L., 2006, Mechanisms in the size segregation of a binary granular mixture: Physical Review E, v. 74, no. 1.

Sillitoe, R. H., and McKee, E. H., 1996, Age of supergene oxidation and enrichment in the Chilean porphyry copper province: Economic Geology and the Bulletin of the Society of Economic Geologists, v. 91, no. 1, p. 164-179.

Sneed, E.D, and Folk, R.L., 1958, Pebbles in the lower Colorado River, Texas. A study in particle morphogenesis: Journal of Geology, v. 66, p. 114-150.

Stuut, J. B. W., and Lamy, F., 2004, Climate variability at the southern boundaries of the Namib (Southwestern Africa) and Atacama (northern Chile) coastal deserts during the last 120,000 yr: Quaternary Research, v. 62, no. 3, p. 301-309.

Sylvester, A. G., Burmeister, K. C., and Wise, W. S., 2002, Faulting and effects of associated shaking at Pisgah Crater volcano caused by the 16 October 1999 Hector Mine earthquake (M-w 7. 1), Central Mojave Desert, California: Bulletin of the Seismological Society of America, v. 92, no. 4, p. 1333-1340.

Torri, D, Biancalani, R., and Poesen, J., 1990, Initiation of motion of gravels in concentrated overland flow: Cohesive forces and probability of entrainment: Catena Supplement, v. 17, p. 79-90.

Torri, D., and Poesen, J., 1988, Incipient motion conditions for single rock fragments in simulated rill flow: Earth Surface Processes and Landforms, v. 13, no. 3, p. 225-237.

Van der Wateren, F.M., and Dunai T.J,, 2001, Late Neogene passive margin denudation history - Cosmogenic isotope measurements from the central Namib desert: Global and Planetary Change, v. 30, no. 3-4, p. 271-307.

Vargas, G., Ortlieb, L., and Rutllant, J., 2000, Aluviones históricos en Antofagasta y su relación con eventos El Niño/Oscilación del Sur: Revista Geológica de Chile, v. 27, no. 2, p. 157-176.

Vargas, G., Rutllant, J., and Ortlieb, L., 2006, ENSO tropical-extratropical climate teleconnections and mechanisms for Holocene debris flows along the hyperarid coast of western South America (17º-24º S): Earth and Planetary Science Letters, v. 249, no. 3-4, p. 467-483.

Wells, S. G., McFadden, L. D., Poths, J., and Olinger, C. T., 1995, Cosmogenic $^3$He surface-exposure dating of stone pavements - Implications for landscape evolution in deserts: Geology, v. 23, no. 7, p. 613-616.

Whipple, K. X., and Dunne, T., 1992, The influence of debris-flow rheology on fan morphology, Owens Valley, California: Geological Society of America Bulletin, v. 104, no. 7, p. 887-900.

Wiberg, P. L., and Smith, J. D., 1987, Calculations of the critical shear-stress for motion of uniform and heterogeneous sediments: Water Resources Research, v. 23, no. 8, p. 1471-1480.

Wilcox, B. P., Newman, B. D., Brandes, D., Davenport, D. W., and Reid, K., 1997, Runoff from a semiarid ponderosa pine hillslope in New Mexico: Water Resources Research, v. 33, no. 10, p. 2301-2314.

Wilcox, B.P., Wood, M.K., Tromble, J.T., and Ward, T.J., 1986, A hand-portable single nozzle rainfall simulator designed for use on steep slopes: Journal of Range Management, v. 39, no. 4, p. 375-377.

Wood, Y. A., Graham, R. C., and Wells, S. G., 2005, Surface control of desert pavement pedologic process and landscape function, Cima Volcanic field, Mojave Desert, California: Catena, v. 59, no. 2, p. 205-230.

Yair, A., 1983, Hillslope hydrology water harvesting and areal distribution of some ancient agricultural systems in the northern Negev Desert: Journal of Arid Environments, v. 6, no. 3, p. 283-301.

Yair, A., 1990, Runoff generation in a sandy area - the Nizzana sands, western-Negev, Israel: Earth Surface Processes and Landforms, v. 15, no. 7, p. 597-609.

Yair, A., and Klein, M., 1973, The influence of surface properties on flow and erosion processes on debris covered slopes in an arid area: Catena, v. 1, p. 1-18.

Yair, A., and Kossovsky, A., 2002, Climate and surface properties: hydrological response of small and and semi-arid watersheds: Geomorphology, v. 42, no. 1-2, p. 43-57.

Table 1. CALCULATED ZEBRA STRIPED AREAS AND DESCRIPTION OF ROCK UNITS.

| Symbol | Major rock units | Mineral grainsize | Rock fabric or other features | Hill area (km$^2$) | Zebra area (km$^2$) | % Zebra coverage |
|---|---|---|---|---|---|---|
| Jiqm | Metamorphosed diorite | Medium to coarse | Locally foliated | 39.2 | 0 | 0 |
| Jmg | Diorite and granodiorite | Medium to coarse | Locally foliated | 46.3 | 0 | 0 |
| Jsg(f) | Monzogranite, granodiorite, quartz-rich diorite | Medium to coarse | Locally foliated | 32.4 | 0 | 0 |
| Jsg(b) | Monzogranite, syenogranite | Medium to coarse | Phaneritic | 74.6 | 0.2 | 0.3 |
| Kigr(a) | Granodiorite | Medium | Spherical inclusions of quartz diorite | 17.7 | 0.1 | 0.4 |
| Jcd | Monzodiorite and diorite | Fine to medium | Phaneritic | 52.4 | 1.0 | 1.9 |
| Mg | Gravels | Various | Well-rounded clasts | 49.5 | 1.1 | 2.2 |
| Jsg(c) | Monzogranite, granodiorite | Medium | Speckled | 14.9 | 0.6 | 4.2 |
| Jsmv | Tonalite | Fine to medium | Phaneritic | 4.3 | 0.4 | 10.1 |
| Jsg(d) | Syenogranite, monzodiorite | Coarse | Many veins of diorite and rhyolite | 5.0 | 0.5 | 10.7 |
| Jsg(e) | Tonalite, granodiorite | Fine to medium | Many diorite veins | 6.0 | 0.7 | 12.2 |
| Jln | Andesite, some basalt and sandstone | Various | Variety of textures (porphyretic to breciated) | 94.3 | 25.3 | 26.8 |
| MPla | Gravels | Various | Partially cemented by sulfate and halite | 118.2 | 34.6 | 29.3 |
| Jsg(a) | Monzogranite, syenogranite, tonalite | Medium to coarse | Phaneritic | 76.5 | 34.7 | 45.4 |
| Dst(a) | Quartz-rich sandstone, shale | Fine | Slightly meta-morphosed | 55.9 | 28.6 | 51.2 |
| Trqp | Tonalite | Medium to coarse | Marked foliation | 101.5 | 70.4 | 69.4 |
| Dst(b) | Slate, schist | Mostly fine | Moderately metamorphosed | 109.9 | 88.7 | 80.7 |
| Kigr(c) | Monzogranite | Medium to coarse | Locally foliated | 51.6 | 42.4 | 82.2 |
| Kist | Gabbro | Fine to medium | Sheared texture | 5.4 | 4.7 | 87.0 |

Data from González and Niemeyer (2005). Area was calculated in ArcMap v.3 (ESRI). Geologic units are sorted by increasing zebra stripe coverage.

Table 2. SOIL CHARACTERISTICS, SALT CONTENT, AND YEARS OF SALT BY HORIZON AT OFICINA ROSARIO.

| Sample ID | Depth (cm) | Soil bulk density (g cm$^{-3}$) | Gravel fraction | Clay fraction | Silt fraction | Sand fraction | NO$_3^-$ (ppm) | Cl$^-$ (ppm) | SO$_4^{-2}$ (ppm) | NO$_3^-$ (y) | Cl$^-$ (y) | SO$_4^{-2}$ (y) |
|---|---|---|---|---|---|---|---|---|---|---|---|---|
| | | | | — Particle size of fine fraction — | | | — Concentration in fine fraction — | | | — Years of salt by horizon — | | |
| *Soil 4, x=21.6 m* | | | | | | | | | | | | |
| ORH-05-4-1 | 2 | 0.8 | 0.05 | 0.19 | 0.21 | 0.60 | 159 | 654 | 6,000 | 9 | 2,800 | 200 |
| ORH-05-4-2 | 4 | 0.17 | 0 | 0.18 | 0.04 | 0.77 | 103 | 1,378 | 318,000 | 1 | 1,300 | 2,000 |
| ORH-05-4-3 | 7 | 0.32 | 0.1 | 0.13 | 0.08 | 0.79 | 156 | 916 | 439,500 | 5 | 2,200 | 6,900 |
| ORH-05-4-4 | 23 | 1.43 | 0.8 | NA | NA | NA | 1,197 | 2,349 | 541,500 | 200 | 30,000 | 45,000 |
| ORH-05-4-5 | 36 | 1.37 | 0.9 | 0.36 | 0.18 | 0.46 | 123 | 1,014 | 540,000 | 8 | 5,100 | 17,000 |
| | | depth-averaged = | | 0.29 | 0.15 | 0.55 | | | total= | 230 | 42,000 | 71,000 |
| *Soil 3, x=34.9 m* | | | | | | | | | | | | |
| ORH-05-3-1 | 1 | 1.22 | 0 | 0.16 | 0.14 | 0.70 | 204 | 1,236 | 16,800 | 9 | 4,300 | 400 |
| ORH-05-3-2 | 3 | 0.16 | 0 | 0.18 | 0.03 | 0.78 | 769 | 979 | 333,000 | 9 | 900 | 2,000 |
| ORH-05-3-3 | 9 | 0.41 | 0.05 | 0.08 | 0.15 | 0.77 | 183 | 927 | 400,500 | 16 | 6,200 | 17,000 |
| ORH-05-3-4 | 36 | 1.37 | 0.8 | 0.19 | 0.13 | 0.68 | 134 | 792 | 492,000 | 38 | 17,000 | 66,000 |
| ORH-05-3-5 | 69 | 1.39 | 0.9 | 0.23 | 0.21 | 0.56 | 159 | 1,050 | 460,500 | 28 | 14,000 | 38,000 |
| | | depth-averaged = | | 0.20 | 0.17 | 0.64 | | | total = | 100 | 42,000 | 123,000 |
| *Soil 2, x=54.7 m* | | | | | | | | | | | | |
| ORH-05-2-1 | 1 | 1.29 | 0.05 | 0.12 | 0.18 | 0.70 | 143 | 288 | 4,500 | 7 | 1,000 | 100 |
| ORH-05-2-2 | 3.5 | 0.16 | 0 | 0.09 | 0.10 | 0.81 | 140 | 1,092 | 337,500 | 2 | 1,300 | 2,500 |
| ORH-05-2-3 | 24 | 0.33 | 0 | 0.07 | 0.12 | 0.80 | 193 | 748 | 319,530 | 50 | 14,000 | 39,000 |
| ORH-05-2-4 | 68 | 1.34 | 0.04 | 0.14 | 0.10 | 0.76 | 123 | 864 | 418,500 | 260 | 138,000 | 427,000 |
| ORH-05-2-5 | 75 | 1.3 | 0 | 0.07 | 0.07 | 0.86 | 964 | 1,445 | 162,600 | 330 | 37,000 | 27,000 |
| | | depth-averaged = | | 0.11 | 0.10 | 0.78 | | | total = | 660 | 192,000 | 496,000 |
| *Soil 18, x=65.6 m* | | | | | | | | | | | | |
| ORH-05-18-1 | 1 | 1.12 | 0.05 | 0.14 | 0.19 | 0.67 | 257 | 1,310 | 48,000 | 10 | 4,000 | 900 |
| ORH-05-18-2 | 3.5 | 0.31 | 0 | 0.15 | 0.09 | 0.76 | 145 | 948 | 367,500 | 4 | 2,100 | 5,100 |
| ORH-05-18-3 | 8 | 0.55 | 0.05 | 0.08 | 0.11 | 0.81 | 224 | 1,023 | 370,500 | 20 | 6,800 | 16,000 |
| ORH-05-18-4 | 37 | 1.5 | 0.05 | 0.12 | 0.08 | 0.79 | 153 | 1,256 | 490,500 | 240 | 147,000 | 366,000 |
| ORH-05-18-5 | 73 | 1.29 | 0.3 | 0.15 | 0.09 | 0.75 | 145 | 2,743 | 519,000 | 180 | 252,000 | 304,000 |
| | | depth-averaged = | | 0.13 | 0.09 | 0.77 | | | total = | 450 | 412,000 | 692,000 |
| *Soil 1, x=87.7 m* | | | | | | | | | | | | |
| ORH-05-1-1 | 1 | 0.89 | 0 | 0.13 | 0.11 | 0.76 | 578 | 968 | 84,000 | 20 | 2,400 | 1,300 |
| ORH-05-1-2 | 3 | 0.34 | 0 | 0.12 | 0.06 | 0.82 | 406 | 890 | 354,000 | 10 | 1,700 | 4,300 |
| ORH-05-1-3 | 13 | 0.5 | 0 | 0.19 | 0.09 | 0.72 | 442 | 610 | 408,000 | 84 | 8,600 | 37,000 |
| ORH-05-1-4 | 57 | 1.16 | 0.05 | 0.03 | 0.11 | 0.87 | 404 | 1,012 | 277,500 | 740 | 139,000 | 243,000 |
| ORH-05-1-5 | 76 | 1.24 | 0.28 | 0.06 | 0.10 | 0.85 | 1,177 | 905 | 296,100 | 760 | 43,000 | 91,000 |
| ORH-05-1-6 | 115 | 1.22 | 0.08 | 0.18 | 0.31 | 0.51 | 6,730 | 18,072 | 221,100 | 11,000 | 2,240,000 | 175,000 |
| ORH-05-1-7 | 137 | 1.34 | 0.48 | 0.16 | 0.28 | 0.56 | 17,742 | 10,451 | 384,000 | 10,000 | 454,000 | 106,000 |
| | | depth-averaged = | | 0.11 | 0.19 | 0.70 | | | total = | 23,000 | 2,890,000 | 656,000 |

Years of salt = salt concentration * horizon thickness * bulk density * (1-gravel fraction) / atmospheric input rate, NA = not available, x = distance downslope

Table 3. DUST AND SALT DEPOSITION RATES.

| Dust trap ID | Silicate dust input rate ($gm^{-2}y^{-1}$) | $NO_3^-$ input rate ($gm^{-2}y^{-1}$) | $Cl^-$ input rate ($gm^{-2}y^{-1}$) | $SO_4^{-2}$ input rate ($gm^{-2}y^{-1}$) | Total input rate ($gm^{-2}y^{-1}$) |
|---|---|---|---|---|---|
| ORH-1 | 1.572 | 0.260 | 0.004 | 0.543 | 3.942 |
| ORH-2 | 1.127 | 0.335 | 0.003 | 0.568 | 3.155 |
| ORH-3 | 1.509 | 0.195 | 0.003 | 0.552 | 3.760 |
| ORH average | 1.403 | 0.263 | 0.004 | 0.554 | 3.619 |
| ORH st. deviation | 0.241 | 0.070 | 0.000 | 0.013 | 0.412 |
| Nearby sites | | | | | |
| YH-1 | 1.162 | 0.637 | 0.077 | 0.958 | 3.980 |
| YH-2 | 1.009 | 0.500 | 0.031 | 0.923 | 3.457 |
| YH-3 | 1.018 | 0.449 | 0.042 | 0.967 | 3.481 |
| YH average | 1.063 | 0.529 | 0.050 | 0.949 | 3.639 |
| YH st. deviation | 0.086 | 0.097 | 0.024 | 0.023 | 0.295 |
| Ewing et al. (2006) | 2.032 | 0.759 | 0.098 | 1.319 | 4.701 |

"ORH" are from Oficina Rosario. "YH" are from a site 70 km north, near that of Ewing et al. (2006), and are included for comparison.

Table 4. SPRINKLING EXPERIMENT CONDITIONS AND RESULTS.

| Site | Test | Slope ($m\ m^{-1}$) | Application rate ($cm\ h^{-1}$) | Steady-state runoff ($cm\ h^{-1}$) | Steady-state infiltration ($cm\ h^{-1}$) | Duration of sprinkling (MM:SS) | Time until runoff (MM:SS) |
|---|---|---|---|---|---|---|---|
| Oficina Rosario | 1 | 0.21 | 58.7 | 16.1 | 42.6 | 08:00 | 00:17 |
| Oficina Rosario | 2 | 0.34 | 5.7 | 0.5 | 5.2 | 18:20 | 08:00 |
| Oficina Rosario | 3 | 0.27 | 5.2 | 0.1 | 4.2 | 36:00 | 04:00 |
| Chañaral | 1 | 0.38 | 5.7 | 1.3 | 4.1 | 18:00 | 06:00 |
| Chañaral | 2 | 0.38 | 5.5 | 2.0 | 3.7 | 13:00 | 02:00 |
| Chañaral | 3 | 0.38 | 52.5 | 28.9 | 25.3 | 03:30 | 00:30 |

Steady state was inferred to occur when the values of runoff and infiltration rates became fairly stable and is the average of the last 4-5 minutes of the experiment.

Table 5. INFILTROMETER EXPERIMENT CONDITIONS AND RESULTS.

| Test | Subsurface conditions | Surface gravel | Slope ($m\ m^{-1}$) | Average infiltration rate ($cm\ h^{-1}$) |
|---|---|---|---|---|
| 2 | Generally soft, hard gypsum @ 24 cm deep | Mostly absent | 0.36 | 134.3 |
| 3 | Hard gypsum | Very gravelly | 0.31 | 26.6 |
| 5 | Half sandy, half hard gypsum | Very gravelly | 0.29 | 30.6 |
| 6 | Sandy gypsum to 26 cm deep, then hard | Absent | 0.27 | 145.4 |

Tests 1 and 4 are not reported due to breaches in the seal between the infiltrometer and the soil.

Table 6. COSMOGENIC RADIONUCLIDE DATA FOR OFICINA ROSARIO SURFACE GRAVELS, SOIL ROCK FRAGMENTS, AND BEDROCK.

| Sample ID | Sample depth | $^{10}$Be concentration | $^{26}$Al concentration | $^{26}$Al/$^{10}$Be | $^{10}$Be exposure age | $^{26}$Al exposure age | $^{10}$Be erosion rate |
|---|---|---|---|---|---|---|---|
| | (cm) | ($10^6$ atom g$^{-1}$) | ($10^6$ atom g$^{-1}$) | | (ky) | (ky) | (m My$^{-1}$) |
| Soil 4, x=21.6 m | | | | | | | |
| ORH05-4-G | 0 | 6.69 ± 0.13 | 38.79 ± 1.78 | 5.80 | 744 ± 18 | 764 ± 52 | 0.73 |
| ORH-4-4 | 10 | 7.94 ± 0.10 | 30.20 ± 0.89 | 3.80 | 921 ± 14 | 539 ± 21 | 0.56 |
| ORH-06-4 | 36 | 7.08 ± 0.12 | 34.82 ± 1.66 | 4.92 | 797 ± 17 | 654 ± 44 | 0.67 |
| ORH-06-42 | 95 | 4.13 ± 0.17 | 18.10 ± 1.38 | 4.38 | 425 ± 19 | 288 ± 25 | 1.39 |
| Soil 3, x=34.9 m | | | | | | | |
| ORH05-3-G | 0 | 9.32 ± 0.25 | 13.08 ± 1.15 | 1.40 | 1140 ± 41 | 200 ± 19 | 0.43 |
| ORH-3-4 | 35 | 6.84 ± 0.10 | 11.66 ± 0.72 | 1.70 | 766 ± 14 | 176 ± 12 | 0.70 |
| ORH-06-3 | 57 | 5.38 ± 0.23 | 28.33 ± 3.50 | 5.27 | 575 ± 28 | 497 ± 79 | 0.99 |
| Soil 2, x=54.7 m | | | | | | | |
| ORH05-2-G | 0 | 9.35 ± 0.29 | 27.00 ± 3.15 | 2.89 | 1150 ± 48 | 469 ± 70 | 0.42 |
| ORH-2-4 | 9 | 6.94 ± 0.08 | 21.49 ± 0.93 | 3.10 | 783 ± 11 | 354 ± 18 | 0.69 |
| ORH-06-2 | 92 | 11.43 ± 0.25 | 285.63 ± 18.41 | 24.99 | 1530 ± 51 | 0 | 0.28 |
| Soil 18, x=65.6 m | | | | | | | |
| ORH05-18G | 0 | 8.66 ± 0.23 | 24.98 ± 2.03 | 2.88 | 1040 ± 36 | 427 ± 43 | 0.48 |
| ORH-18-4 | 7 | 6.80 ± 0.12 | 17.80 ± 0.87 | 2.62 | 766 ± 16 | 285 ± 16 | 0.70 |
| ORH-06-18 | 75 | 5.12 ± 0.18 | 19.24 ± 2.18 | 3.76 | 548 ± 22 | 312 ± 41 | 1.04 |
| Soil 1, x=87.7 m | | | | | | | |
| ORH-1-5 | 57 | 6.44 ± 0.15 | 10.24 ± 0.84 | 1.59 | 723 ± 20 | 155 ± 14 | 0.76 |

Exposure age and erosion rate were calculated by K. Nishiizumi. Concentration has been corrected for sample elevation and latitude but not for sample depth. x is distance downslope from the crest of the hill.

**Figure 1.** Examples of "zebra stripes" - the dark grey bands of varnished, sorted gravels which run along contour. (a) Zebra stripes on the hillslope studied near Oficina Rosario (OR), viewed from the north. Light grey lines coming downslope from the top of the hill are tire tracks which reveal the salt-rich soil. (b) Zebra stripes on another hillslope ~70 km north of OR, showing strong dependence on distance downslope. (c) Close up of gravel sorting within a zebra stripe on OR. View is upslope. Gravels in the foreground are 4-10 cm in diameter and fine upslope towards a relatively gravel-free zone. The surface of the underlying soil is very smooth and light-colored due to the presence of sulfate salts. (d) Example of soil profile on OR showing grey, angular rock fragments in a matrix of white gypsum-cemented fines. Brown vertical feature on the right side is a sand-filled crack. Excavation is 1 m deep. (e) Two gravels (~3-cm diameter) have been moved upslope to reveal pedestals of salt and dust.



154
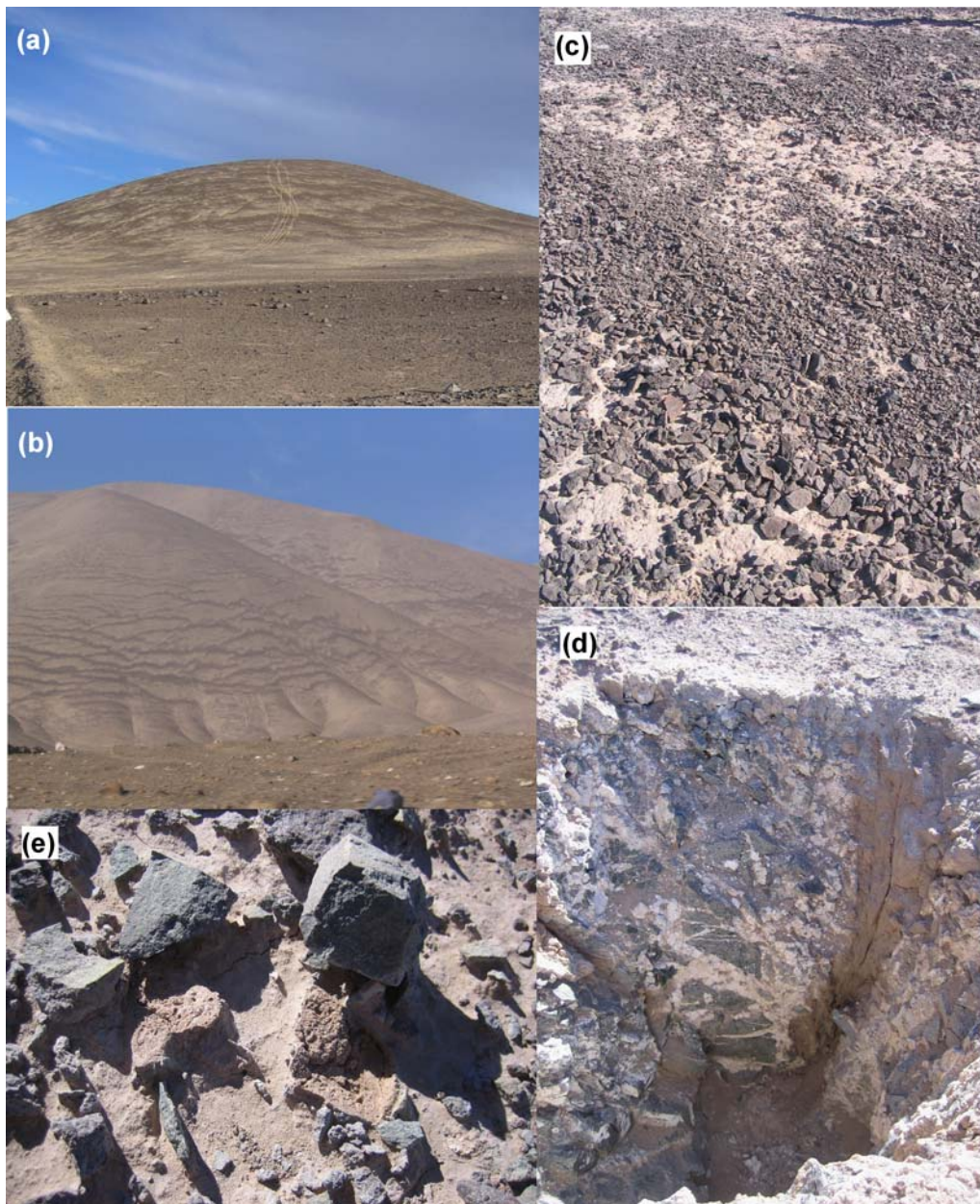
**Figure 2.** **(a)** Soil profile in Miocene gravel deposits exposed in a railroad cut and showing the ~1.5 m-tall, 0.5-1 m-diameter polygons formed through salt shrinking and swelling. **(b)** Concentrations of gravels on the surface trace the cracks bordering the underlying polygons. Rock hammer in foreground for scale.
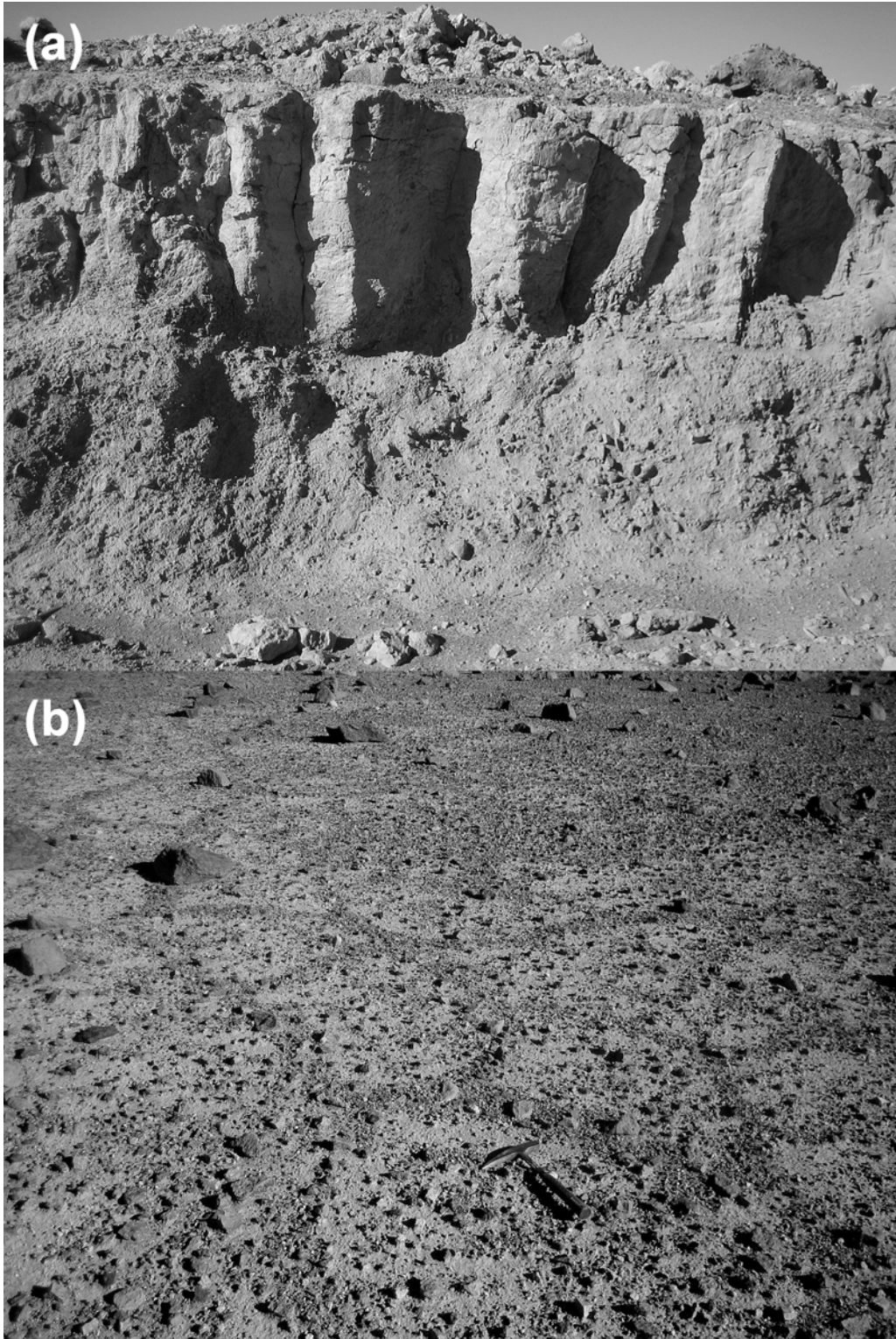
**Figure 3.** Topography of northern Chile showing major physiological features (Coast Range, Central Depression, and Andes). Black circles mark locations of OR and CH. White circles mark large cities for reference. Dashed line demarcates approximate extent of zebra stripes. Map created with GeoMapApp v.1.7.8.

156
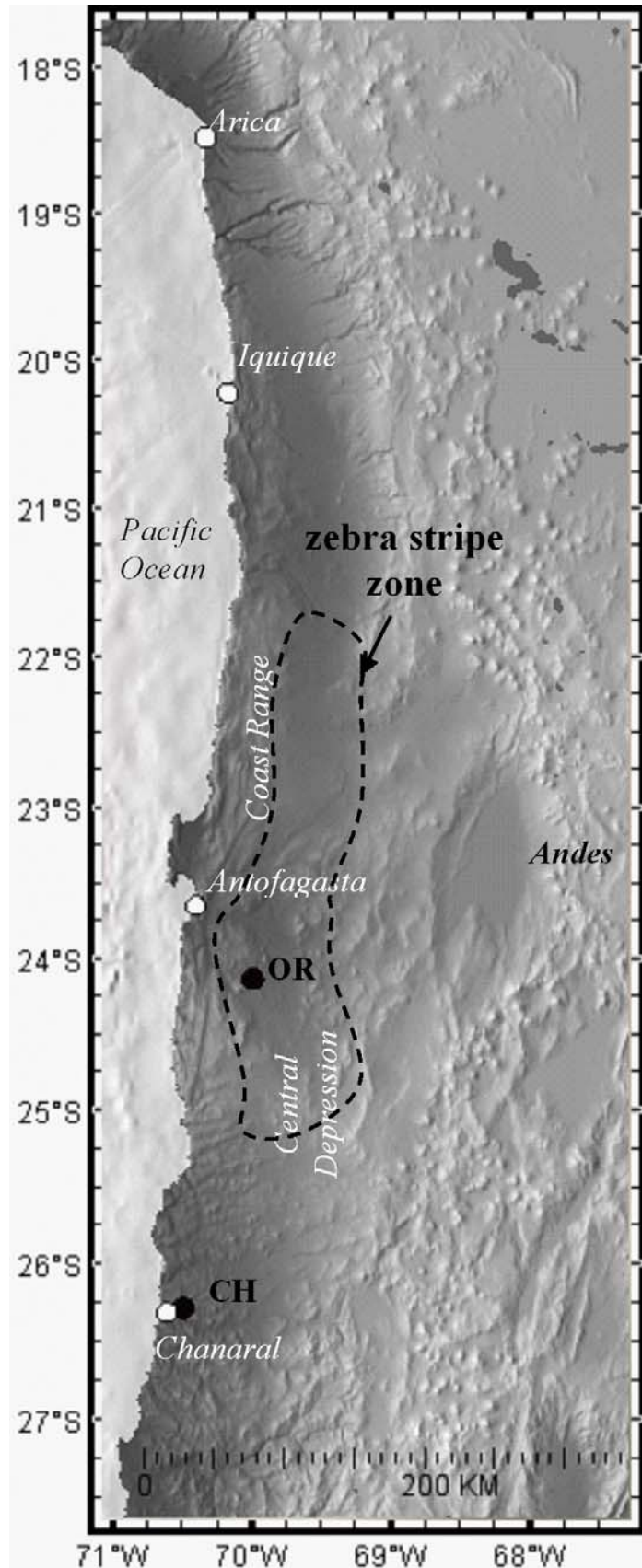
**Figure 4.** Quickbird imagery showing locations of soil excavations (black squares labeled 1, 18, 2, 3, 4), gravel description transects (G-1, G-2, G-3, G-4), and zebra front transects (black lines extending N, NE, E, SE, S, SW, W, NW from top of hill). Contour interval is 5 m. Dark diagonal line in upper right corner is the Pan American highway and the two light grey lines running parallel to it are bulldozed roads. Two shallow channels run along the southern and western boundaries of the hillslope. An area of concentrated rilling is visible on the east-southeast face downslope of G-2, and a large rill extends farther up the hill to the north of this area.
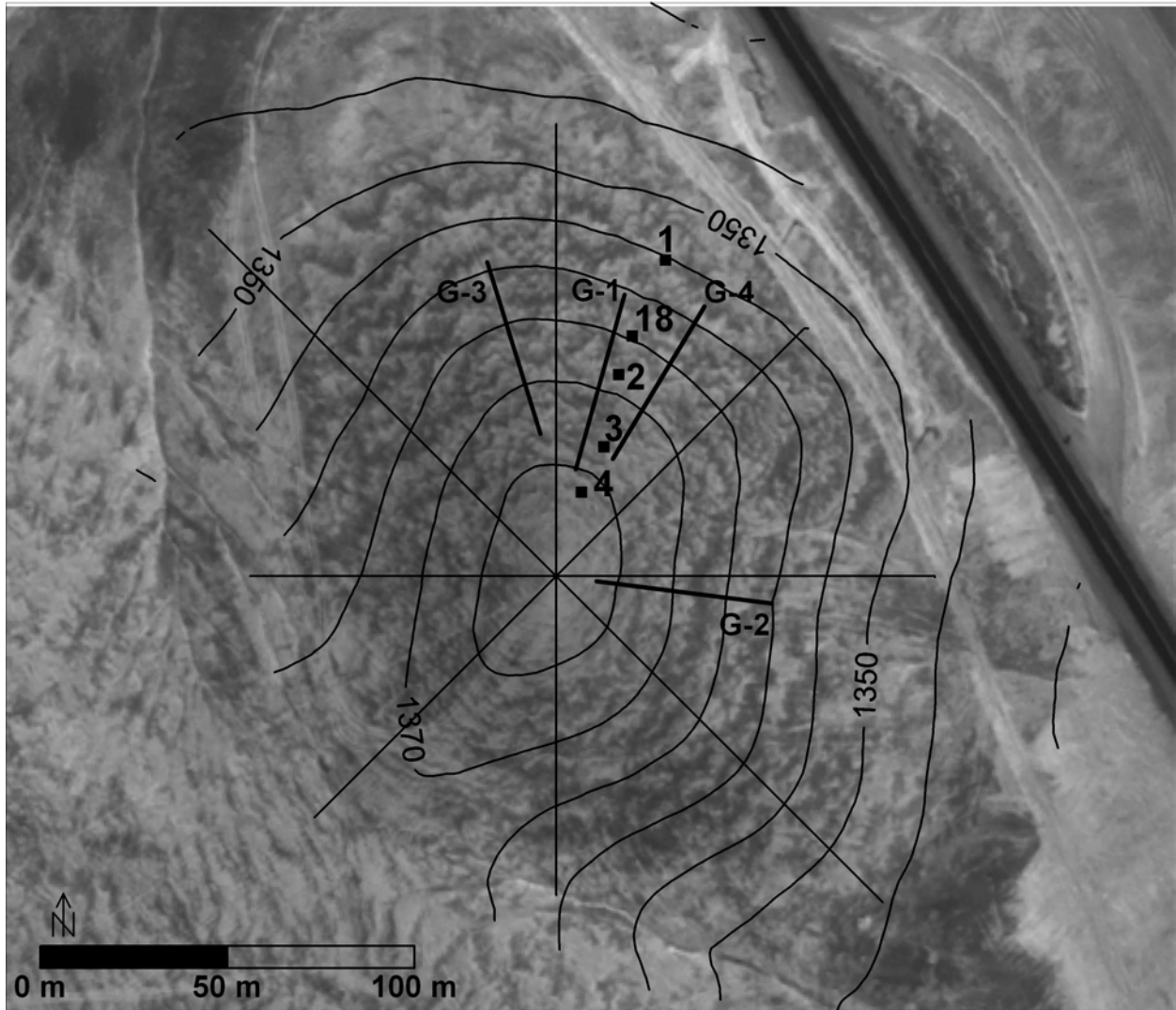
**Figure 5.** (a) Example of the smaller zebra stripes at CH. In some cases, the fine gravels (the coarsest material) have been colonized by lichens, producing the darker grey banding on the hillslope. (b) A close up of a zebra stripe, looking upslope, with a ~10-cm long lip balm tube for scale. As at OR, particles coarsen downslope, but they are much smaller and the stripe is shorter along-contour. (c) A soil profile on CH showing the thinness of the gravelly soil mantle (~1 cm here) and the fracturing of the underlying bedrock. Fine red dust fills the fractures.
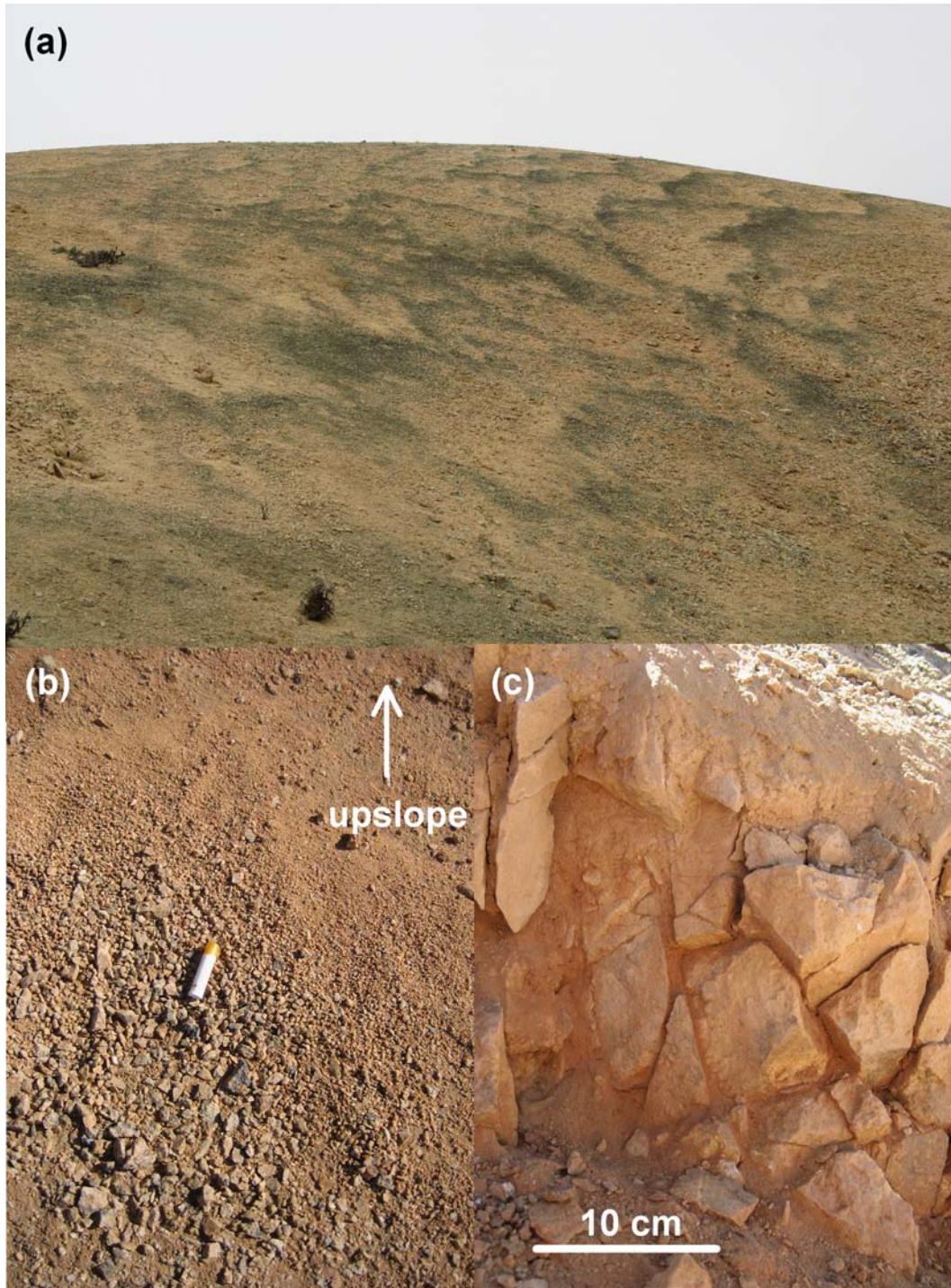
**Figure 6.** GoogleEarth image showing a sharp boundary between hillslopes that have zebra stripes and those that don't, located near 23.56º S, 70.13º W. Upper left portion is Jsg(b) monzogranite and has no zebra stripes while the lower right is Dst(b) slate and schist and has zebra stripes. The dark material along the right border is Quaternary alluvium.
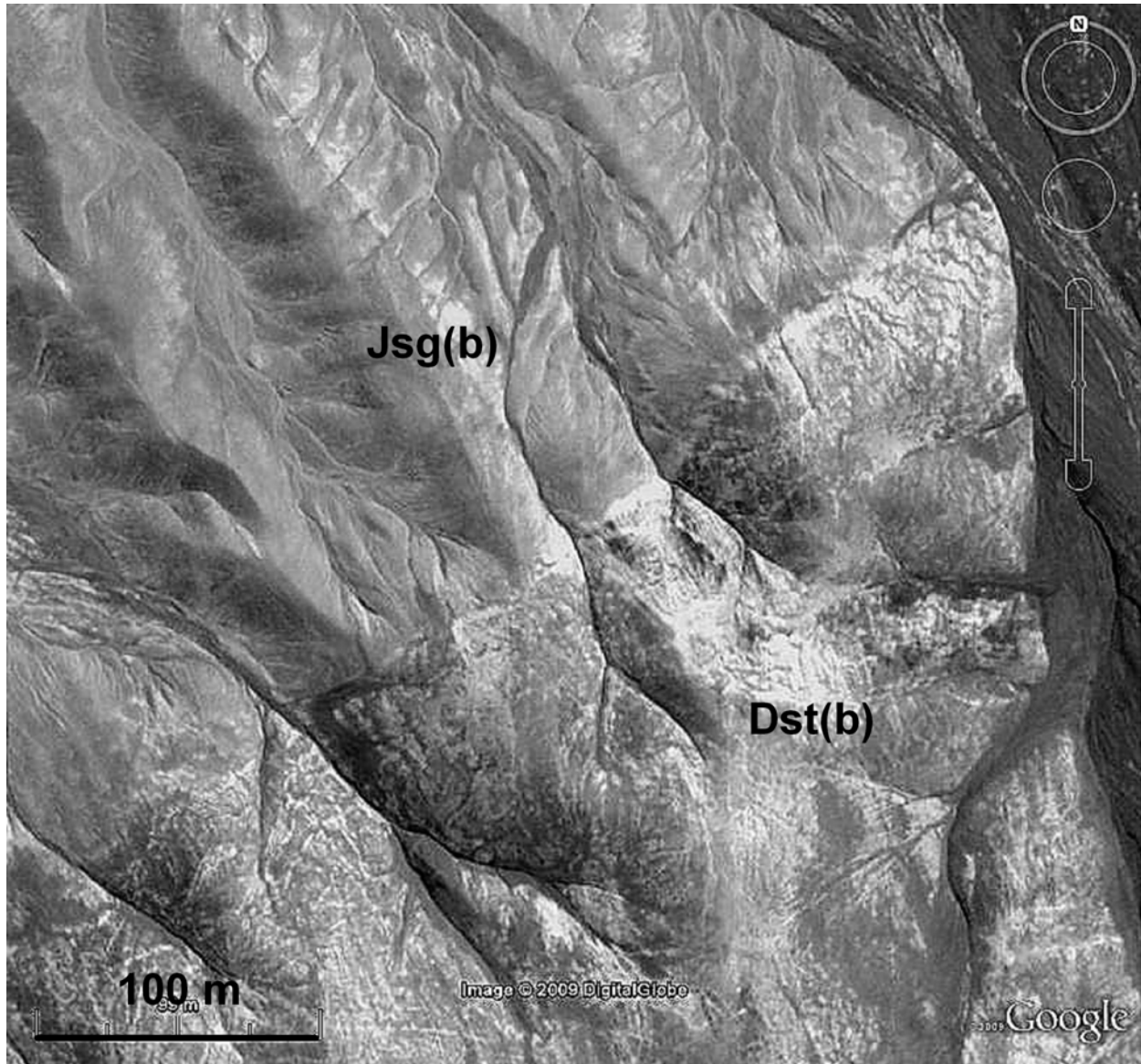
**Figure 7.** Gradient (a), plan curvature (b), and profile curvature (c) on OR based on 3.6 m-grid topography data. Black dots mark zebra stripe fronts identified by eye in the Quickbird imagery. On the gradient map, red is horizontal and blue is steepest. On the curvature maps, green and blue (positive numbers) indicate convergent areas, red and purple (negative numbers) are divergent, and white is planar.
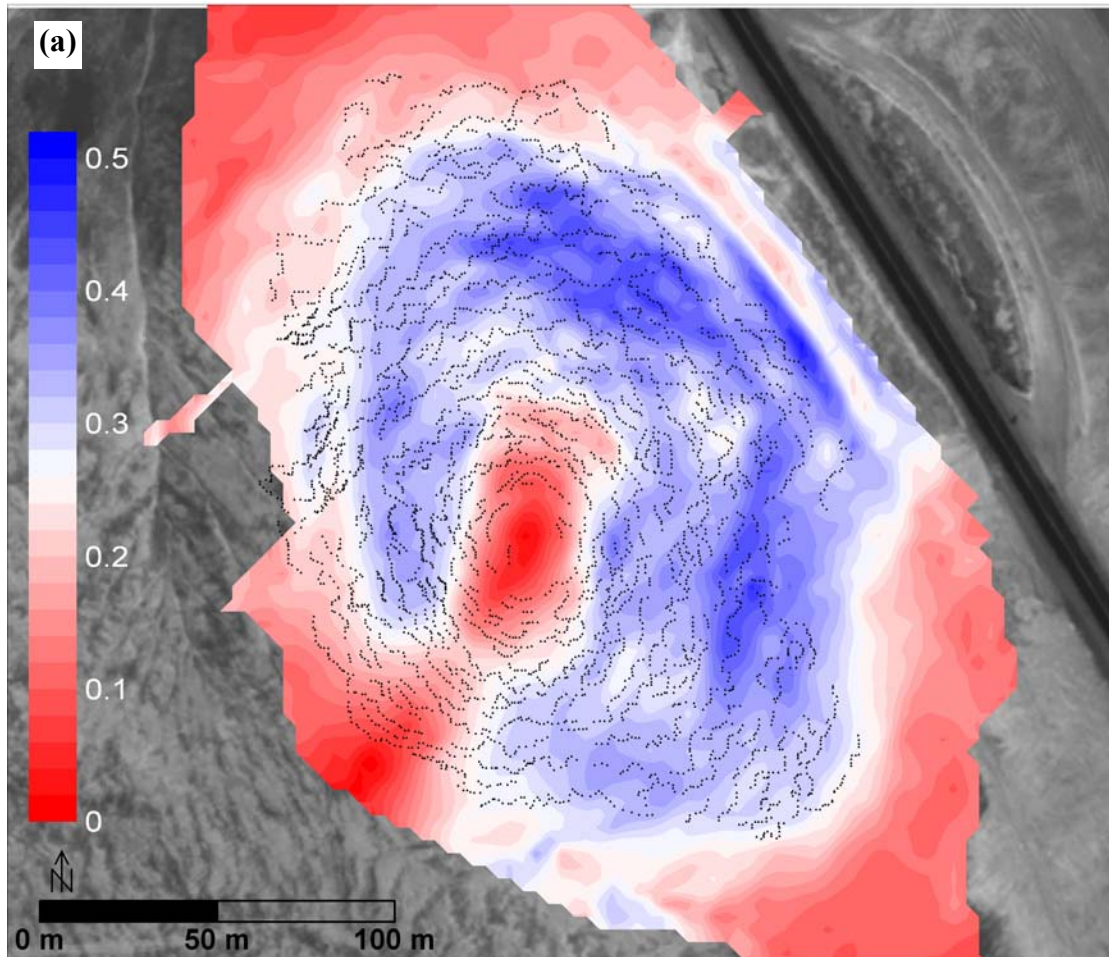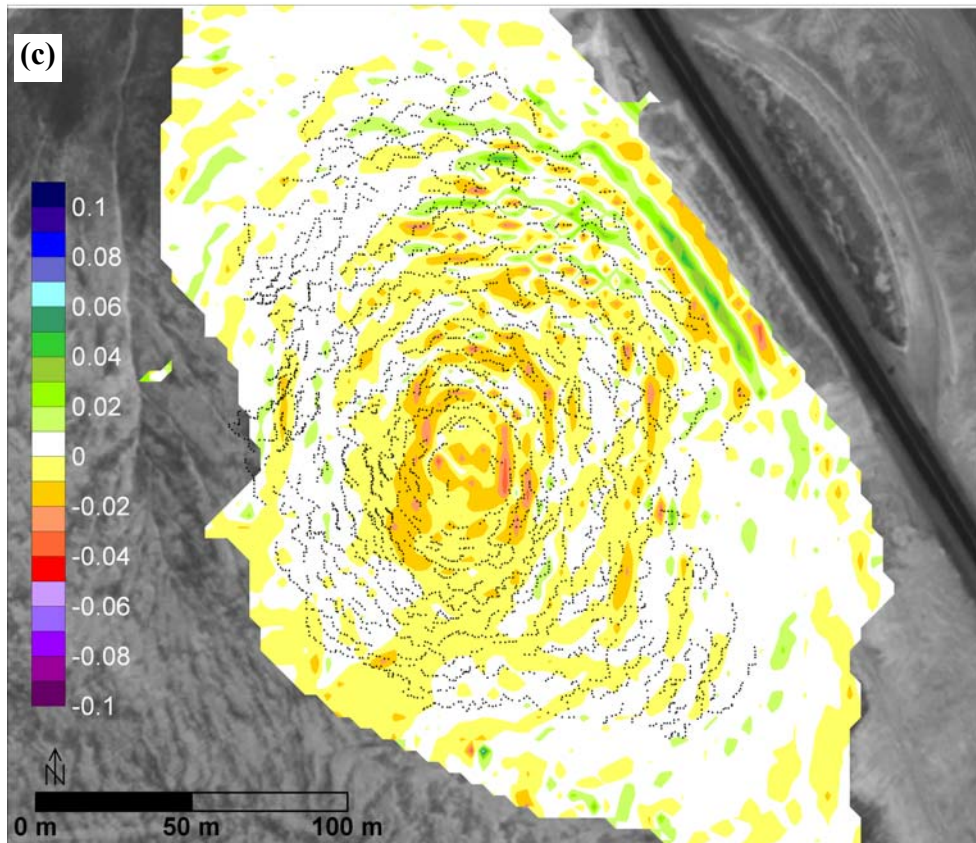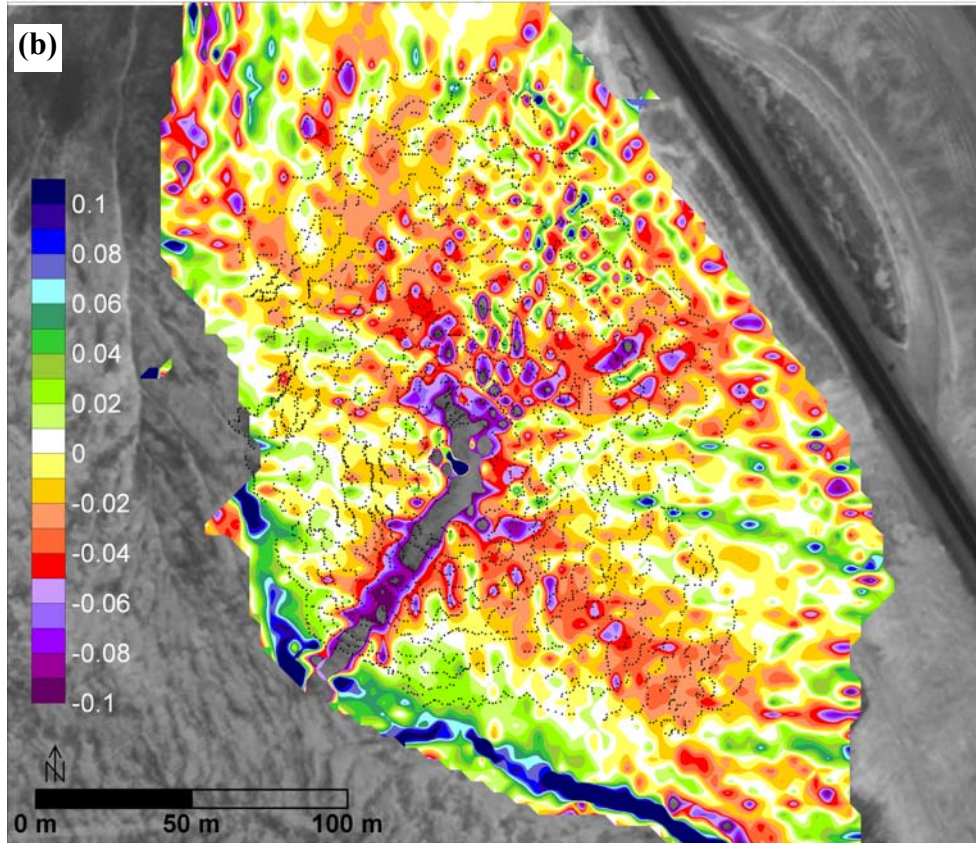
**Figure 8.** Distance between zebra fronts identified along the ordinal transects on the Quickbird imagery and along the field transects increases with distance downslope. The field data capture a finer wavelength than the Quickbird imagery, which is limited by resolution. Plots of individual transects are in Fig. A1.
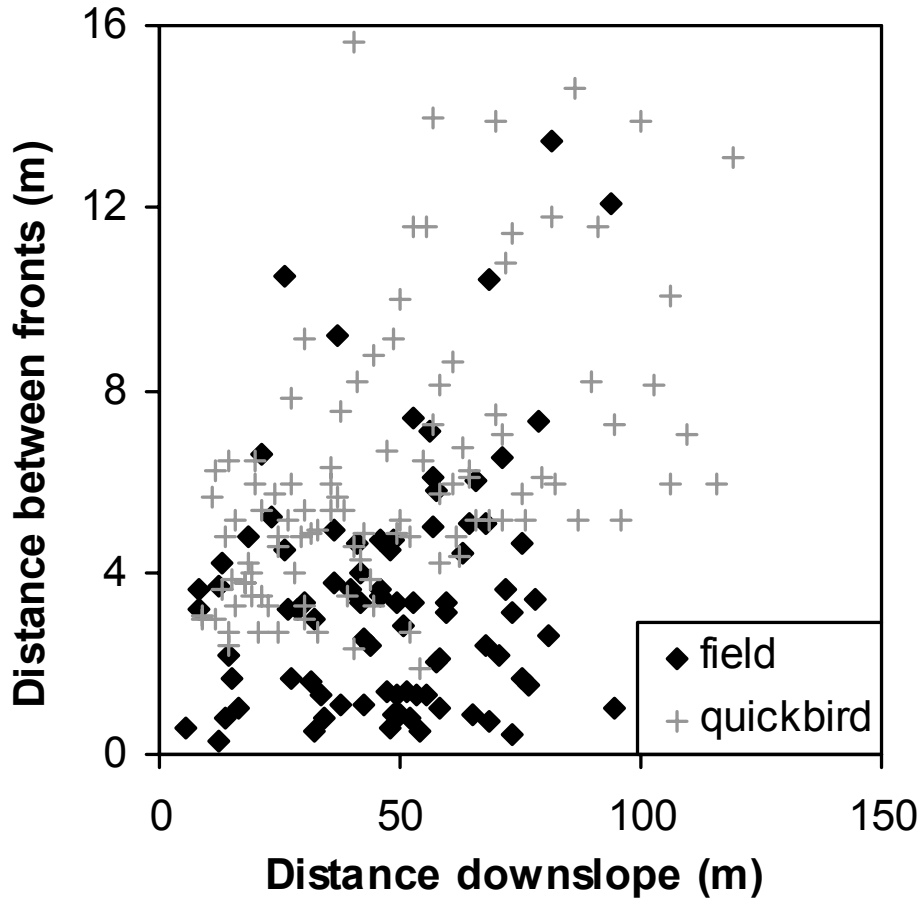
**Figure 9.** Gravel size class and gravel cover vs. distance along transect G-4. Size classes are 1=1-2 cm-diameter, 2=1-5 cm, 3=2-5 cm, 4=2-10+ cm, and 5=5-10+ cm. Vertical dashed lines indicate the locations of zebra stripe fronts based on the length index (size class x gravel cover≥2.4). The segments from 0-4 m and 20-22.5 m show the typical trend of increasing gravel size and cover towards the zebra stripe front.
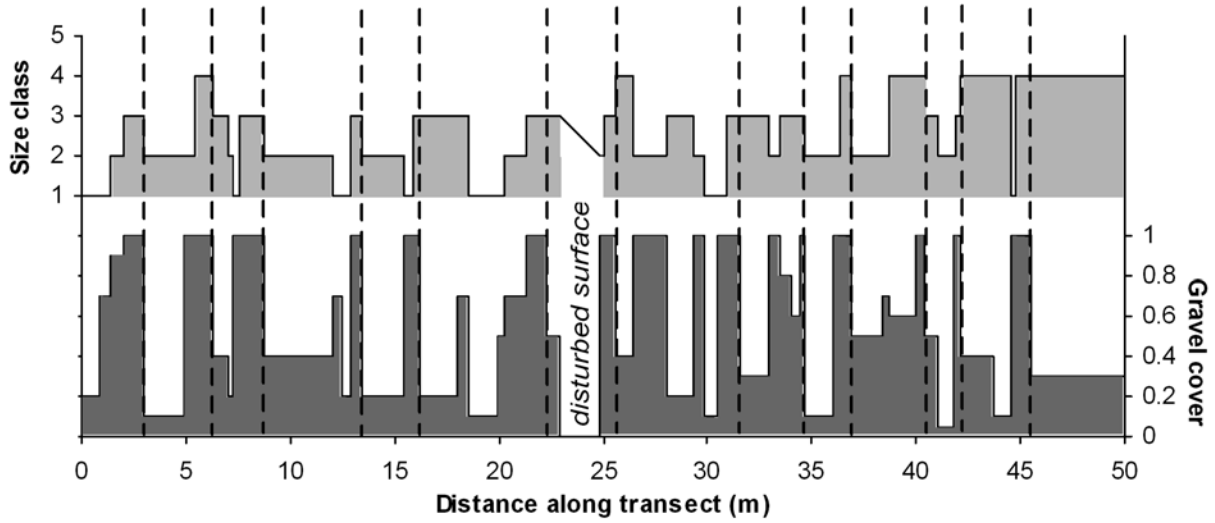
**Figure 10.** A comparison of the particle size of eight consecutive bands from transect G-2 (from upslope to downslope) estimated visually in the field and measured with a ruler. The measured values were recorded on a phi scale and show the four downslope bands are coarser than the four upslope bands.
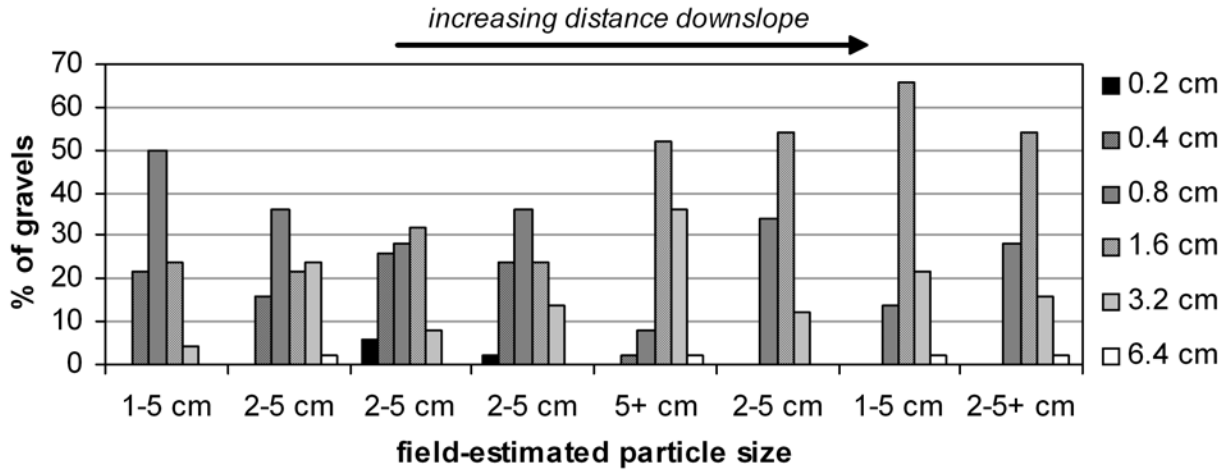
**Figure 11.** Soil profiles along a downslope transect on OR, with soil thickness on the right axes and soil horizon classifications (Taxonomy) on the left axes. From upslope to downslope (a) ORH-4, (b) ORH-3, (c) ORH-2, (d) ORH-18, and (e) ORH-1. Stippled areas are sandy while white areas are predominantly indurated sulfate. The soils are extremely heterogeneous, with irregular boundaries with the underlying fractured bedrock. Though (a) suggests the shallowest soils are towards the crest of the hill, Fig. 1d is a photo of one of the along-slope faces of the same excavation (the drawing is of the upslope face) and shows that the salt-rich soil reaches almost 1 m-thick. Large (20-50 cm-diameter) polygonal blocks, similar to those on horizontal surfaces (Fig. 2), are found across the hillslope, as are vertical, sand-filled cracks. Overlying the polygons is 2-4 cm of soft, porous, sulfate-rich soil, capped with a sandy crust. (figure on next page)
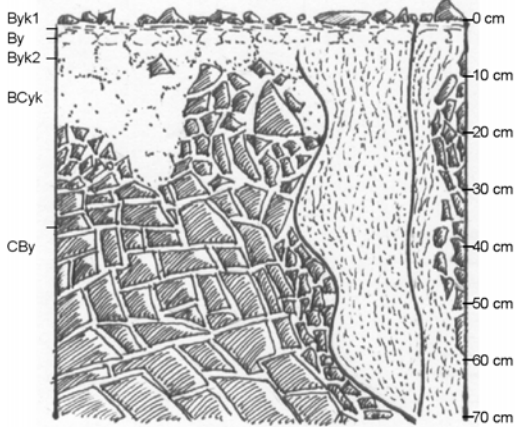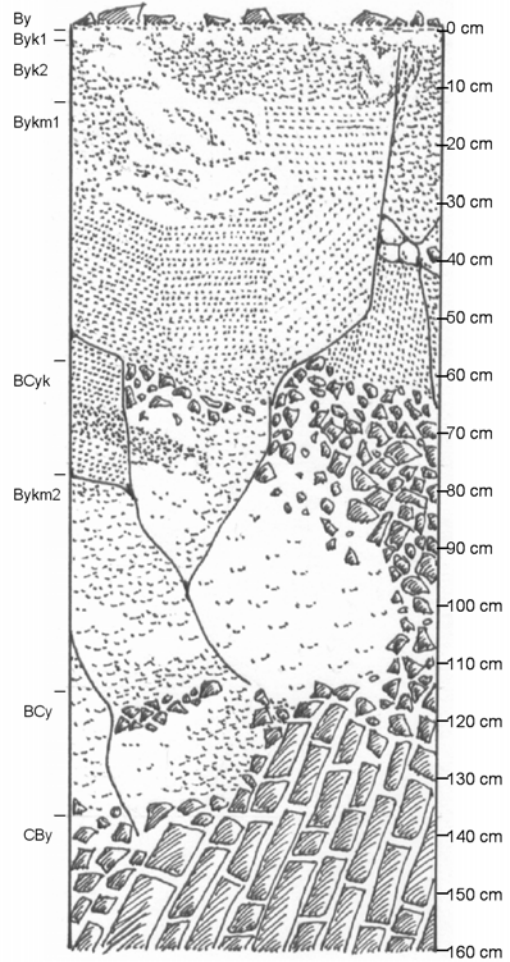
**Figure 11 continued.**

**Figure 12.** Triple-plot of gravel morphology for 159 clasts along a 1.5 m transect.  a, b, and c are the long, intermediate, and short axes, respectively.  Fields are divided into equant/compact (C), a=b=c; platy (P), a=b>c; elongate (E), a>b≅c; bladed (B), a>b>c.  V designates "very".  The one cobble measured is VP. Coarse gravels (n=52) are VB (23%), P (19%), and B (17%). Medium gravels (n=96) are mostly B (25%).  Fine gravels (n=8) are E and B (both 38%). Gravels are generally increasingly platy and bladed with increasing size.

**Figure 13.** (a) [10]Be concentration and (b) [26]Al concentration vs. time for the three surface gravel exposure cases (1-3), compared to the CRN concentrations in the surface gravels. Case 1 models constant exposure at the surface with no erosion, case 2 models constant exposure at the surface with low erosion, and case 3 models steady-state erosion at depth then instantaneous exposure at surface with no erosion. Though all the cases are possible, the [10]Be concentrations suggest the gravels have been exposed at the surface at least 0.5 My with little to no erosion, and the [26]Al concentrations suggest a shorter and more complex exposure history. (c) [10]Be concentration and (d) [26]Al concentration vs. time for the three bedrock exposure history cases (4-6), compared to the CRN concentrations in the bedrock. The bedrock is harder to constrain, but both CRN suggest the bedrock has been buried with some erosion for >0.5 My. (continued on next page)
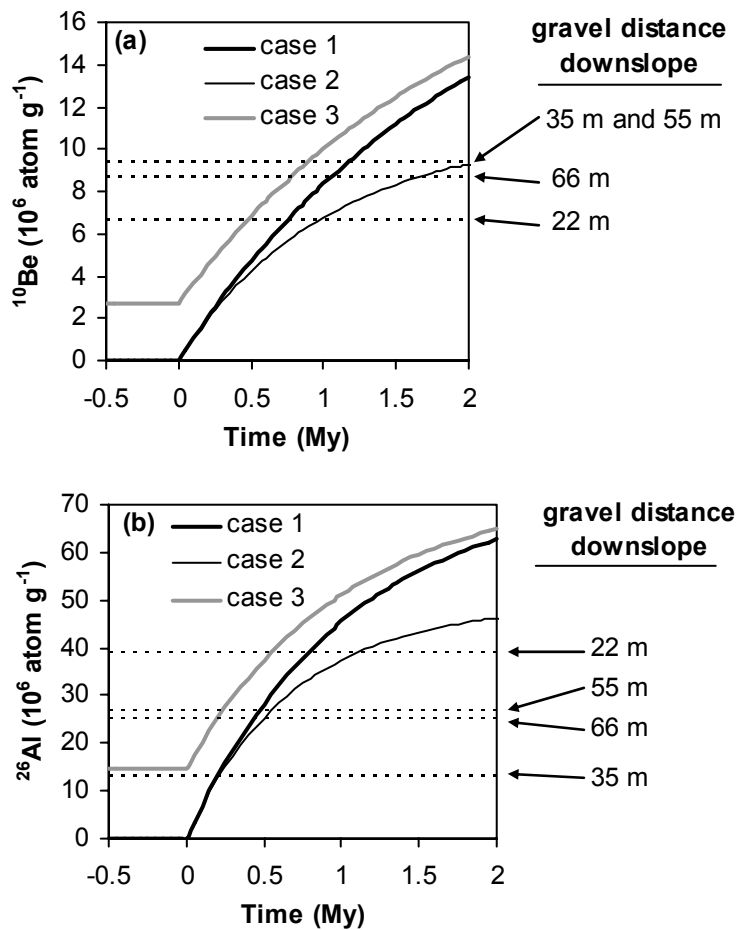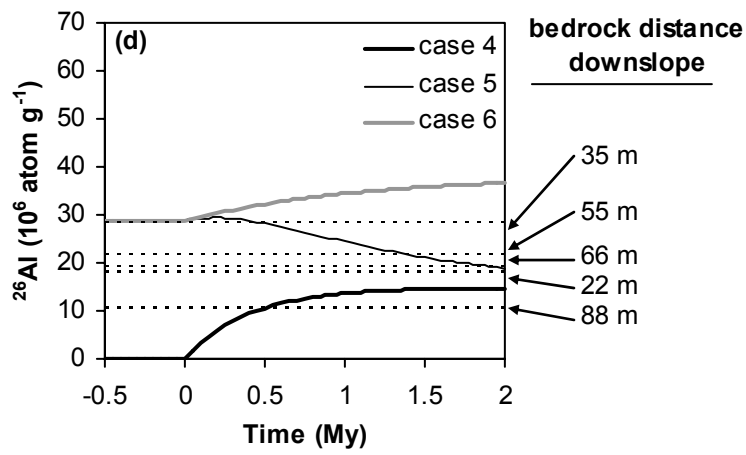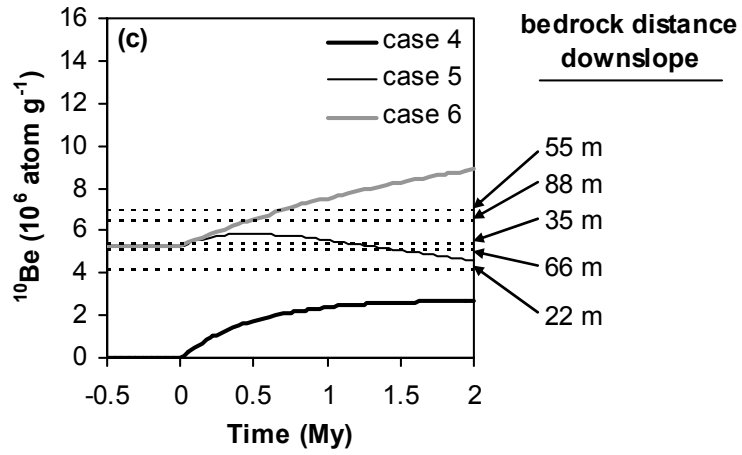
**Figure 13 continued.**

**Figure 14.** Proposed soil history on the OR hillslope. (a) >3 Ma: semiarid conditions. (b) ~0.5-3 Ma: transition to arid conditions, removal of soil and saprolite. (c) 0.5-1 Ma: salt begins to accumulate in fine fractures. (d) <0.5-1 Ma: salt accumulates and begins prying larger rock fragments from bedrock. (e) ~0.01-0.5 Ma: accumulation of salt-rich soil, development of scattered desert pavement, development of polygonal soil structure. During large rainfall events $10^5$-$10^3$ ya, gravels are mobilized. Large gravels interact. (f) $10^5$-$10^3$ ya: Gravels come to rest in sorted stripes and self-stabilize.
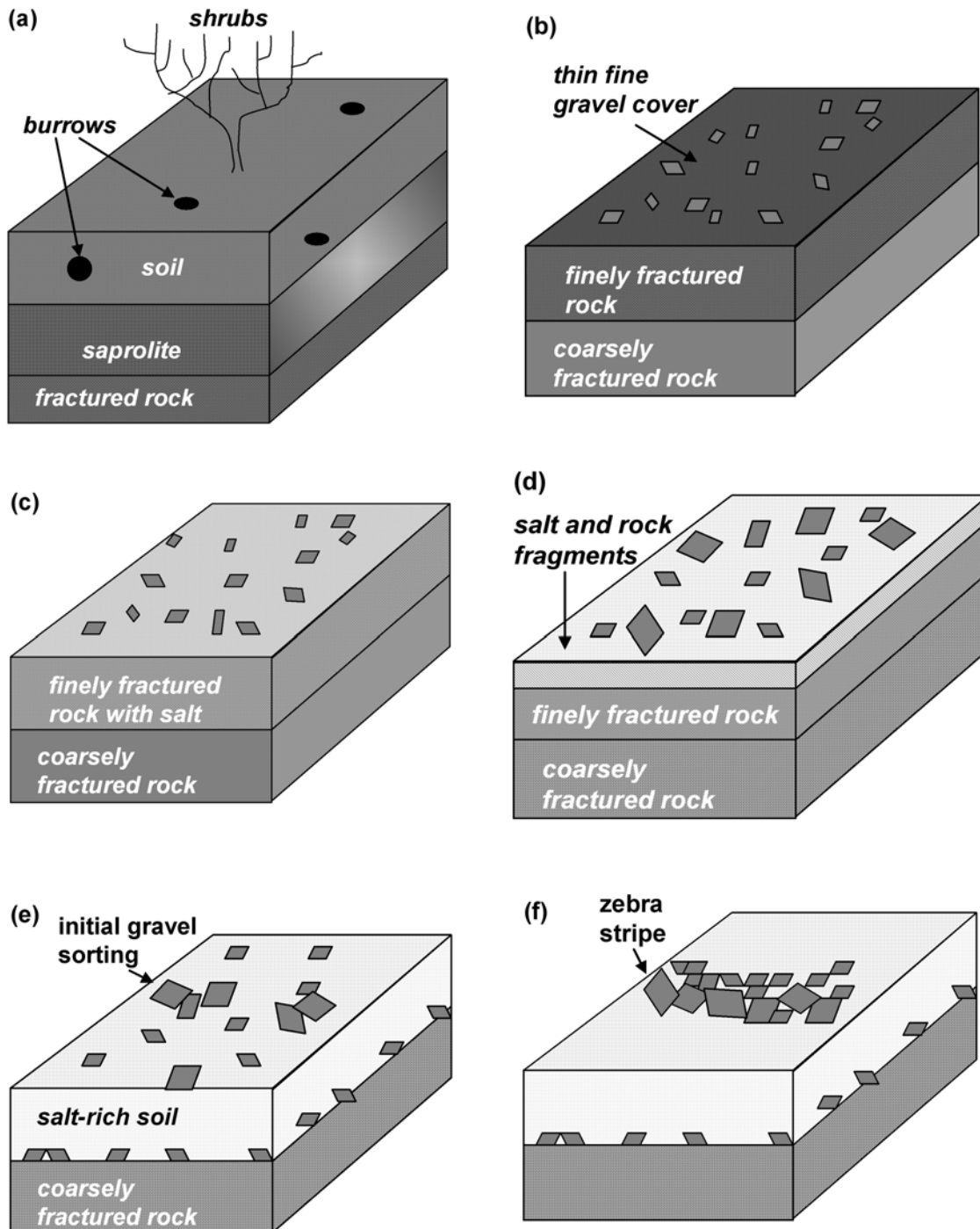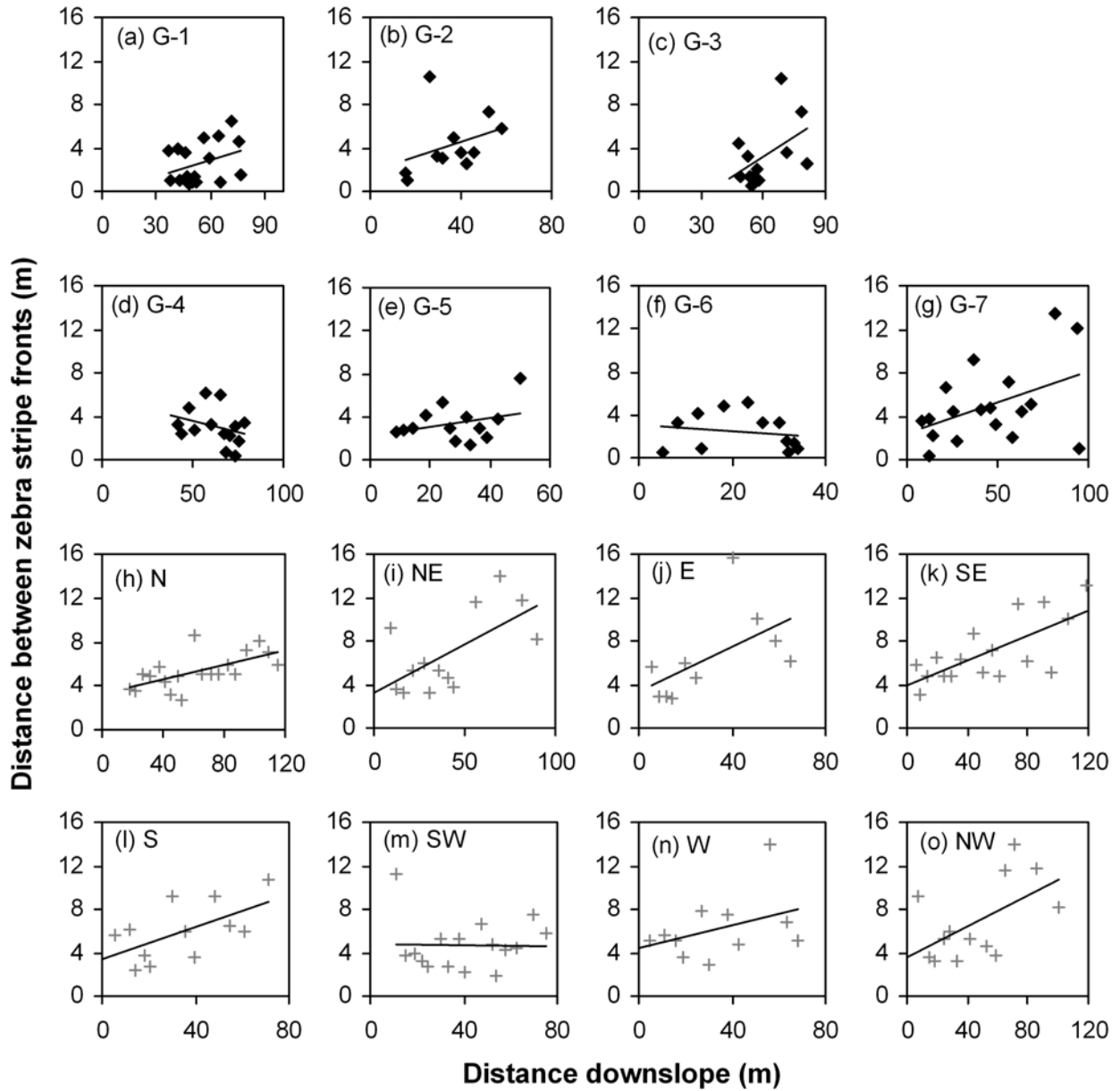
**Figure A1.** Plots of individual zebra front transects measured in the field (a-g) and in the Quickbird imagery (h-o), as shown in Figure 4.

# Chapter 5

## Conclusions

The goal of this thesis was to expand current geomorphic and pedologic understanding of arid and hyperarid hillslopes. The results of a combination of considerable field work, laboratory measurements, and modeling confirmed some hypotheses of the behavior of geomorphic processes in response to decreasing precipitation, but challenged some others. Most importantly, these observations define a geomorphic and pedologic precipitation threshold, occurring near a mean annual precipitation (MAP) rate of 100 mm. As shown in Chapter 2, this coincides with the transition from biotic to abiotic processes driving soil formation and transport, at MAP between 10 to100 mm, and correlates with changes in NPP, transport coefficients, and the soil mass balance (Fig. 1). Previous work (Reibe et al., 2004; von Blanckenburg et al., 2006) has shown that where MAP≥100 mm, soil production rates are independent of precipitation, or at least that the precipitation signal is obscured by the effects of other factors such as tectonic setting, bedrock properties, and temperature. Additionally, there was little data on soil transport laws, or the effect of precipitation on those transport laws. This work showed that at MAP<100 mm, the rate of soil production from bedrock and transport laws are strongly correlated with MAP.

Chapters 2 and 3 presented an examination of some of the factors controlling soil characteristics and the rates of soil formation and transport. I applied cosmogenic radionuclide (CRN) analysis and the mass balance approach of Yoo et al., (2007) to calculate the rates of soil production from bedrock, physical erosion, and chemical erosion. In combination with field observations, these calculations reveal how the mechanisms and rates of hillslope formation and transport change with precipitation in ways not previously observed on more humid hillslopes. Incising channels at the base of hillslopes caused soils to be thinner and soil production rates from bedrock to be faster compared to hillslopes bounded by non-eroding landforms. These results provide some of the first field support for theoretical models of hillslope development. However, unlike previous studies, the effect of boundary condition was small compared to the effect of precipitation. Soils transitioned from relatively thick, chemically-weathered, salt-free, and bioturbated at the semiarid site, to less than 2 cm-thick, minimally chemically-weathered, and affected by both bioturbation and overland flow at the arid site, to thick, salt-rich, and produced and transported through abiotic processes. The rate of soil production from bedrock decreased with decreasing precipitation, and was soil thickness-dependent in the semiarid region but was apparently independent of soil thickness in drier climates. The semiarid hillslopes have soils and soil production rates similar to those observed and calculated on semiarid and humid hillslopes around the world, but the arid and hyperarid hillslopes are significantly different. As testament to the unique conditions in the hyperarid region, surface gravels on hillslopes have been sorted by overland flow into contour-parallel bands ("zebra stripes"), which have been preserved for at least several hundred years, if not tens of thousands. Chapter 4 presented a compilation of the first field investigation of zebra stripes, and identified some of the factors that seem important to their occurrence and preservation, including prolonged hyperaridity, the near-absence of life, salt-rich soils, and possibly certain bedrock types and precipitation seasonality.

172

The work described in this thesis was designed to begin answering questions about the effect of decreasing MAP on pedologic and geomorphic processes and the coupling between them. However, it has only scratched the surface. Though the hillslopes selected for this work appear representative of hillslopes in their respective climate zones, study of additional hillslopes would provide a sense of the variability of hillslope processes within each region. In the hyperarid region, the two hillslopes suggest that soil production from bedrock may be similar across the landscape despite variations in slope, soil thickness, and distance from the coast. Data from these hillslopes also indicate that the soil production from bedrock is independent of soil thickness, but more hillslopes need to be studied to confirm this and answer the question of why this is the case. The factors affecting zebra stripe occurrence must also be tested, to understand their distribution in the Atacama, and their apparent absence in other deserts on Earth. In the arid region, constraint of atmospheric input is necessary to better calculate erosion rates, and it would be useful to know how long the hillslopes have been soil-free. At the semiarid site, considering the chemical erosion that occurs during the conversion of bedrock into saprolite would be an important next step in understanding soil formation in this region.

I defined 100 mm as the MAP threshold at which significant changes in soil chemistry, formation, and transport occur, but it is not well-constrained. More work on arid and hyperarid hillslopes, particularly calculations of soil production from bedrock, erosion rates, and transport laws and coefficients, would help to better define the precipitation threshold. This is important because not all of the geomorphic and pedologic shifts occur together. The comparison between the semiarid site and the site of Yoo et al. (2007) in Chapter 3 suggests that chemical erosion decreases dramatically at some MAP slightly greater than 100 mm. The transition to bioturbation-free hillslopes appears to occur below a MAP of 10 mm. A major challenge in this is the limited amount of precipitation data available for the Atacama Desert, and a similar study where precipitation is better constrained would be informative. Thus, rather than an absolute threshold, I have begun narrowing a range of MAP over which these transitions occur and have provided a framework for studying these processes which could be applied to other arid hillslopes.

Much of the recent interest in the Atacama Desert is because of its suitability as an analogue for Mars (e.g., Marlow et al., 2008). Both have soils rich in sulfates which show the effect of water-driven pedogenesis (Amundson et al., 2008), have gentle, abiotic hillslopes (Perron and Dietrich, 2006), and were wetter in the past (e.g., Bibring et al., 2006; Hartley and Chong, 2002). It is my hope that the results presented in this dissertation provide context for the interpretation of hillslope soils on Mars and other terrestrial planets, just as studies of fluvial systems on Earth have informed the interpretation of the fluvial geomorphology of Titan and Mars (e.g., Burr et al., 2006; Perron et al., 2006; Lamb et al., 2006).

**References**

Amundson, R., Ewing, S., Dietrich, W., Sutter, B., Owen, J., Chadwick, O., Nishiizumi, K., Walvoord, M., McKay, C. 2008. On the *in situ* aqueous alteration of soils on Mars. Geochimica et Cosmochimica Acta 72: 3845-3864.

Bibring J.-P., Squyres S. W. and Arvidson R. E. 2006. Merging views on Mars. Science 313: 1899–1901.

Burr, D.M., Emery, J.P., Lorenz, R.D., Collins, G.C., Carling, P.A. 2006. Sediment transport by liquid surficial flow: Application to Titan. Icarus 181: 235-242.

Dietrich, W.E., Perron, J.T. 2006. The search for a topographic signature of life. Nature, 439: 411-418.

Hartley, A.J., Chong, G. 2002. Late Pliocene age for the Atacama Desert: Implications for the desertification of western South America. Geology, 30(1): 43-46.

Lamb, M. P., Howard, A., Johnson, J., Whipple, K., Dietrich, W. E., Perron T. 2006 Can springs cut canyons into rock? Journal of Geophysical Research 111: E07002.

Marlow, J.J., Martins, Z., and Sephton, M.A. 2008. Mars on Earth: soil analogues for future Mars missions. Astronomy & Geophysics, 49: 2.20-2.23.

Perron, J.T., Lamb, M.P., Koven, C.D., Fung, I.Y., Yager, E. 2006. Valley formation and methane precipitation rates on Titan. Journal of Geophysical Research 111: E11001.

Yoo, K., Amundson, R., Heimsath, A.M., Dietrich, W.E., Brimhall, G.H. 2007. Integration of geochemical mass balance with sediment transport to calculate rates of soil chemical weathering and transport on hillslopes. Journal of Geophysical Research-Earth Surface, 112(F2).